

FINAL TECHNICAL REPORT

For research supported by
AFOSR Contract No. F49620-98-1-0033
for period 10/1/97 to 9/30/00

Experimental Investigations with a 5-kW-Class Laboratory- Model Closed-Drift Hall Thruster

Prepared by

Alec D. Gallimore⁽¹⁾, Brian E. Gilchrist⁽²⁾,
R. Paul Drake⁽³⁾, Frank S. Gulczinski⁽⁴⁾, and James M. Haas⁽⁴⁾

Department of Aerospace Engineering
Department of Electrical Engineering and Computer Science
Department of Nuclear Engineering and Radiological Science
University of Michigan
Ann Arbor, MI 48109

Work Supported by

Air Force Office of Scientific Research
Program Monitor: Dr. Mitat Birkan

⁽¹⁾ Associate Professor, Co-Principal Investigator, Department of Aerospace Engineering

⁽²⁾ Associate Professor, Co-Principal Investigator, Department of Electrical Engineering and Computer Science

⁽³⁾ Professor, Co-Principal Investigator, Department of Nuclear Engineering and Radiological Science

⁽⁴⁾ Graduate Research Assistant, Department of Aerospace Engineering

APPROVED FOR PUBLIC RELEASE; DISTRIBUTION UNLIMITED

January 2001

20010309 009

REPORT DOCUMENTATION PAGE

AFRL-SR-BL-TR-01-

0169

Public reporting burden for this collection of information is estimated to average 1 hour per response, including the time for reviewing instructions needed, and completing and reviewing this collection of information. Send comments regarding this burden estimate or any other aspect of the burden to Washington Headquarters Services, Directorate for Information Operations and Reports, 1215 Jefferson Davis Highway, Suite 121, Arlington, VA 22202-4000. DOD Form 1040-01-003 (Rev. 07-04-01)

1. AGENCY USE ONLY (Leave blank)			2. REPORT DATE January 31, 2001	3. REPORT TYPE AND Final Technical Report, 10/1/97 to 9/30/00	4. TITLE AND SUBTITLE Experimental Investigations with a 5-kW-Class Laboratory- Model Closed-Drift Hall Thruster	5. FUNDING NUMBERS F49620-98-1-0033
6. AUTHOR(S) A. D. Gallimore, B. E. Gilchrist, R. P. Drake, F. S. Gulczinski, and J. M. Haas			7. PERFORMING ORGANIZATION NAME(S) AND ADDRESS(ES) University of Michigan Attn: Kathryn DeWitt DRDA, 3003 South State St. Wolverine Towers, Room 1053 Ann Arbor, MI 48109-1274			
8. PERFORMING ORGANIZATION REPORT NUMBER			9. SPONSORING / MONITORING AGENCY NAME(S) AND ADDRESS(ES) AFOSR/NA 801 North Randolph Road, Room 732 Arlington VA 22203-1977			
10. SPONSORING / MONITORING AGENCY REPORT NUMBER			11. SUPPLEMENTARY NOTES 12a. DISTRIBUTION / AVAILABILITY STATEMENT Approved for Public Release; Distribution Unlimited			
AIR FORCE OFFICE OF SCIENTIFIC RESEARCH (AFOSR) NOTICE OF FINAL 10128CDR TECHNICAL REPORT HAS BEEN REVIEWED AND IS APPROVED FOR PUBLIC RELEASE LAW AFR 100-12. DISTRIBUTION IS UNLIMITED.						
13. ABSTRACT (Maximum 200 Words) This final technical report summarizes research conducted at the Plasmadynamics and Electric Propulsion Laboratory (PEPL) to characterize the internal and plume plasma of a closed-drift Hall thruster (CDT). The project was composed of the following segments: 1) a 5-kW-class CDT (P5) was built and characterized in terms of performance and plume divergence; 2) the molecular-beam mass spectrometer (MBMS) was used to measure the ion energy distribution function and charge state throughout the P5 plume; 3) laser-induced fluorescence was used to measure the ion velocity and temperature in the near-field plume; 4) a 35 GHz microwave interferometer was developed to measure plasma oscillations and electron density in the plume; and 5) the near-field and internal plasma of the P5 were characterized using the High-speed Axial Reciprocating Probe (HARP) system developed for this effort. The HARP system enabled, for the first time, the insertion and removal of probes from a CDT discharge channel while minimizing perturbation to thruster operation. The magnetic field, electron temperature, ion number density, plasma and floating potential, and Hall current were mapped throughout the P5 discharge chamber at two operating conditions. Thruster perturbation, determined by monitoring discharge current, was less than 10% for the majority of measurements.						
14. SUBJECT TERMS Hall thruster; (Electric) Propulsion; Plasma physics				15. NUMBER OF PAGES 262 16. PRICE CODE		
17. SECURITY CLASSIFICATION OF REPORT UNCLASSIFIED	18. SECURITY CLASSIFICATION OF THIS PAGE UNCLASSIFIED	19. SECURITY CLASSIFICATION OF ABSTRACT UNCLASSIFIED	20. LIMITATION OF ABSTRACT NONE			

NSN 7540-01-280-5500

FINAL TECHNICAL REPORT

For research supported by
AFOSR Contract No. F49620-98-1-0033
for period 10/1/97 to 9/30/00

Experimental Investigations with a 5-kW-Class Laboratory- Model Closed-Drift Hall Thruster

Prepared by

Alec D. Gallimore⁽¹⁾, Brian E. Gilchrist⁽²⁾,
R. Paul Drake⁽³⁾, Frank S. Gulczinski⁽⁴⁾, and James M. Haas⁽⁴⁾

Department of Aerospace Engineering
Department of Electrical Engineering and Computer Science
Department of Nuclear Engineering and Radiological Science
University of Michigan
Ann Arbor, MI 48109

Work Supported by

Air Force Office of Scientific Research
Program Monitor: Dr. Mitat Birkan

⁽¹⁾ Associate Professor, Co-Principal Investigator, Department of Aerospace Engineering

⁽²⁾ Associate Professor, Co-Principal Investigator, Department of Electrical Engineering and Computer Science

⁽³⁾ Professor, Co-Principal Investigator, Department of Nuclear Engineering and Radiological Science

⁽⁴⁾ Graduate Research Assistant, Department of Aerospace Engineering

APPROVED FOR PUBLIC RELEASE; DISTRIBUTION UNLIMITED

January 2001

TABLE OF CONTENTS

	Page
Abstract	iii
Nomenclature	iv
 CHAPTER	
1 Introduction	1
1.1 Electric Propulsion Overview	2
1.2 Closed Drift Thruster (CDT) Overview	6
1.3 Summary of Internal CDT Research	9
1.4 Contribution of Research	14
References for Chapter 1	17
 2 Facilities and Diagnostics - Air Force Research Laboratory	20
2.1 Vacuum Chamber – Chamber 6	21
2.2 Thruster – SPT-70	23
2.3 Probe	23
2.4 Positioning System	24
2.5 Spectrometer	25
References for Chapter 2	27
 3 Experimental Results – AFRL	29
3.1 Electrostatic Probe – CDT Interaction	29
3.2 Electrostatic Probe Thermal Model	32
3.3 Probe Construction Considerations	37
References for Chapter 3	39
 4 Facilities and Diagnostics - Plasmadynamics and Electric Propulsion Laboratory (PEPL)	40
4.1 Vacuum Chamber – Large Vacuum Test Facility (LVTF)	40
4.2 Thruster – P5	42
4.2.1 P5 Design Considerations	42
4.2.2 P5 Performance Validation	52
4.3 High-speed Axial Reciprocating Probe System – (HARP)	59
4.4 Probes	64
4.4.1 Emissive Probe	64
4.4.2 Double Langmuir Probe	70
4.4.3 Hall Current Probe	80
4.4.4 Magnetic Field Probe	81
References for Chapter 4	82

5	Internal and Near Field Plasma – PEPL	84
5.1	Probe Data	84
5.1.1	Plasma and Floating Potential	85
5.1.2	Ion Number Density and Electron Temperature	96
5.1.3	Radial and Axial Magnetic Field – Vacuum	106
5.1.4	Hall Current	117
5.2	Discussion of Probe Data	122
5.2.1	Plasma and Floating Potential	127
5.2.2	Electron Temperature – Ion Number Density	137
	References for Chapter 5	146
6	Internal and Near Field Data Analysis	147
6.1	Hall Current	147
6.2	Self-Fields	151
6.3	Hall Parameter	154
6.4	Thrust	168
6.4.1	Electrostatic Analysis	168
6.4.2	Electromagnetic Analysis	170
6.4.3	Jet Thrust	174
6.5	Beam Current	176
6.6	Comparison with Numerical Simulation	186
	References for Chapter 6	197
7	Summary and Future Work	199
7.1	Summary of Experimental Results and Data Analysis	199
7.1.1	HARP	199
7.1.2	P5	200
7.1.3	Propellant Acceleration	200
7.1.4	Propellant Ionization	201
7.1.5	Role of Hall Current	202
7.1.6	Thruster Macro-Properties	202
7.1.7	Experimental – Numerical Comparison	203
7.2	Future Work	204
7.2.1	Additional Thruster Conditions	204
7.2.2	Internal LIF	205
7.2.3	Plasma Magnetic Field Measurements	205
7.2.4	Next Generation Hall Thruster	205
	References for Chapter 7	207
Appendices		208
A.	Ion number density profiles beyond the radial confines of the discharge channel	209
B.	Electron temperature profiles beyond the radial confines of the discharge channel	232
C.	Plasma potential profiles beyond the radial confines of the discharge channel	255

ABSTRACT

This final technical report summarizes research conducted at the Plasmadynamics and Electric Propulsion Laboratory (PEPL) to characterize the internal and plume plasma of a closed-drift Hall thruster (CDT). The project was composed of the following segments: 1) a 5-kW-class CDT (P5) was built and characterized in terms of performance and plume divergence; 2) the molecular-beam mass spectrometer (MBMS) was used to measure the ion energy distribution function and charge state throughout the P5 plume; 3) laser-induced fluorescence was used to measure the ion velocity and temperature in the near-field plume; 4) a 35 GHz microwave interferometer was developed to measure plasma oscillations and electron density in the plume; and 5) the near-field and internal plasma of the P5 were characterized using the High-speed Axial Reciprocating Probe (HARP) system developed for this effort. The HARP system enabled, for the first time, the insertion and removal of probes from a CDT discharge channel while minimizing perturbation to thruster operation. The magnetic field, electron temperature, ion number density, plasma and floating potential, and Hall current were mapped throughout the P5 discharge chamber at two operating conditions. Thruster perturbation, determined by monitoring discharge current, was less than 10% for the majority of measurements.

NOMENCLATURE

A_d	Collection area, directed ion flux	[m ²]
A_p	Probe surface area	[m ²]
A_s	Sheath area	[m ²]
A_1	Arbitrary constant	[\cdot]
A_2	Arbitrary constant	[\cdot]
B	Magnetic field vector	[G]
<i>B</i>	Scalar magnetic field	[G]
C_p	Specific heat	[J/kg·K]
<i>d</i>	Probe diameter	[m]
E	Electric field vector	[V/m]
<i>E</i>	Scalar electric field	[V/m]
F	Force	[N]
<i>f</i>	Particle flux	[1/m ² ·s]
<i>g</i>	Gravitational constant	[m/s ²]
I	Current vector	[A]
<i>I</i>	Scalar current	[A]
I_{sat}	Ion saturation current	[A]
I_{sp}	Specific Impulse	[s]
j	Current density vector	[A/m ²]
<i>j</i>	Scalar current density	[A/m ²]
K	Kinetic energy	[N·m]

l	Probe length	[m]
M	Ion mass	[kg]
M_{fin}	Final propellant mass	[kg]
M_{init}	Initial propellant mass	[kg]
m	Electron mass	[kg]
\dot{m}_a	Propellant mass flow rate	[sccm]
n	number density	[1/m ³]
n_e	Electron number density	[1/m ³]
n_i	Ion number density	[1/m ³]
n_n	Neutral number density	[1/m ³]
n_0	Charged particle density outside sheath	[1/m ³]
P/A	Power density	[W/m ²]
P_c	Collisional probability	[1/m_Pa]
P_D	Thruster discharge power	[W]
p_o	Discharge channel pressure	[Pa]
q	Electron charge	[C]
Q	Collision cross section	[m ²]
Q_{ei}	Electron-ion collision cross section	[m ²]
Q_{en}	Electron-neutral collision cross section	[m ²]
r	Probe radius	[m]
r_I	Radial distance for self-field calculations	[m]
T	Thrust	[N]
$\bar{\bar{T}}$	Coordinate transformation tensor	[$-$]

T_e	Electron temperature	[K]
T_{ev}	Electron temperature	[eV]
T_{max}	Melting temperature	[K]
t_{bulk}	Probe melting time	[s]
U_e	Propellant exit velocity	[m/s]
\mathbf{V}	Particle velocity vector	[m/s]
V	Scalar particle velocity	[m/s]
V_{ExB}	Electron drift velocity	[m/s]
\bar{v}	Electron thermal speed	[m/s]
Z	Ion charge state	[$-$]
θ	Field direction	[$^{\circ}$]
ϕ	Potential	[V]
ν_t	Total collision frequency	[1/s]
$\bar{\sigma}$	Conductivity tensor	[1/ μ m]
σ_0	Scalar conductivity	[1/ μ m]
Ω	Hall parameter	[$-$]
ω_e	Electron cyclotron frequency	[1/s]
∇	Volumetric element	[m 3]

CHAPTER 1

INTRODUCTION

Hall thruster research has been on going since the early 1960's when both the United States and the former Soviet Union began investigating its use for spacecraft propulsion. Early problems encountered in the US brought the research to a halt as resources were diverted to what was then considered more promising technology, namely ion engines¹. Work continued to progress in the former Soviet Union, however, culminating with the first use of a Hall thruster on board a Soviet Meteor spacecraft in 1972². Over the next two decades over one hundred Soviet Hall thrusters were successfully flown. With the end of the Cold War, the technology was transferred to the West for performance verification and flight qualification. Initial qualification efforts in the early 1990's concentrated on the 1.35 kW SPT-100^{3,4,5,6}. Since then, the unique performance capabilities of the Hall thruster have spurred research and development into thrusters covering a wide range of power levels. For example, the Busek BHT-200, employed by the Air Force Research Laboratory (AFRL) in their study of Hall thruster clusters, operates as low as 150 W⁷. At the other end of the power spectrum is the 50 kW TM-50, developed by TsNIIMASH in Russia, which has been demonstrated at NASA GRC in 1999 at a power level of 25 kW⁸. The first Western flight of a Hall thruster was the RHETT2/EPDM TAL (Thruster with Anode Layer) on the NRO STEx spacecraft in

October 1999⁸. Both Loral and Lockheed Martin are currently working to integrate Hall thrusters into spacecraft for on-orbit functions⁹.

1.1 Electric Propulsion Overview

Hall thrusters belong to a group of propulsion devices collectively referred to as electric propulsion. Electric propulsion derives its name from the fact that it uses electrical energy to accelerate a propellant to high exhaust velocities. This is in contrast to chemical rockets, which must rely on the energy stored in the chemical bonds of its propellant. While chemical propulsion is capable of producing much higher thrust, its reliance on chemical energy severely limits the exhaust velocity. When discussing thruster performance, it is common to refer to its specific impulse, which is the exhaust velocity divided by the gravitational acceleration at sea level, g (~9.8 m/s). Typical specific impulse values for chemical rockets fall in the range of 200-300 s. Electric propulsion, on the other hand, is limited mainly by the available, on-board, electrical energy. Depending on the type of thruster, specific impulse values above 5000 s can be achieved.

Exhaust velocity is an important figure of merit for propulsion devices because it is essentially a measure of the fuel efficiency. This can be seen clearly by examining the rocket equation

$$\frac{M_{init}}{M_{fin}} = e^{\Delta V / U_e} \quad \text{Eq. 1-1}$$

where M_{init} is the initial spacecraft mass including the propellant, M_{fin} is the spacecraft mass minus the consumed propellant, U_e is the exhaust velocity of the propellant stream, and ΔV is a measure of the energy needed for a given mission. Equation 1-1 shows that for a given ΔV , larger exhaust velocities reduce the mass ratio, i.e. the necessary propellant mass. Thus electric propulsion enables the completion of a given mission using less propellant than a chemical rocket but generally at the expense of longer trip times. This translates into cost savings in a number of ways. By reducing the propellant mass budget for a given mission, a smaller, and hence cheaper, launch vehicle can be used. Another option is to use the mass savings for additional, usable payload. Conversely, for the same propellant mass as that required for a chemical rocket, the mission lifetime of the spacecraft can be extended. As an example, for a typical geostationary communications satellite, the propellant budget for north/south stationkeeping can be reduced by replacing the chemical thrusters with an electric propulsion system. The result is a 15% increase in net payload.

Electric propulsion devices are subdivided into three categories, reflecting the method of acceleration: electrothermal, electrostatic, and electromagnetic. Electrothermal thrusters use electrical energy to heat a propellant, which is then expanded out of a nozzle to produce thrust. There are two primary types of electrothermal thrusters, the resistojet and the arcjet. As its name implies, the resistojet heats the propellant using a resistively heated element. The arcjet, on the other hand, forms a much higher temperature arc around which the propellant is injected. Both thrusters generally use hydrazine derivatives as propellant, an artifact of their being retrofitted to existing chemical

propellant feed systems. Electrothermal thrusters offer the lowest specific impulse of electric propulsion devices but still provide several hundred seconds beyond the best chemical rockets.

Electrostatic thrusters rely on large potential fields to accelerate an ionized gas. The Hall thruster and the ion engine are two examples of this class of thruster. The ion engine relies on an internal cathode and set of ring magnets to ionize an injected propellant, usually xenon. The ionized particles are then accelerated through a large potential by a series of closely spaced grids and neutralized by an external cathode. The ion engine typically has a specific impulse range of 1000-5000 s but has a small thrust to area ratio dictated by space-charge considerations. Hall thrusters, sometimes referred to as gridless ion engines, use magnetic fields to trap electrons, setting up a large potential drop. This process will be discussed in more detail in the next section. Because the plasma remains quasi-neutral, there are no space-charge limitations in the Hall thruster and exhaust velocity is limited only by available power and material considerations.

The third class of electric propulsion devices, electromagnetic, use crossed electric and/or magnetic forces to accelerate propellant. The primary example is the magnetoplasmadynamic (MPD) thruster. The MPD uses a large current to create a magnetic field in a plasma. The resulting magnetic field then interacts with the applied current creating a $\mathbf{j} \times \mathbf{B}$ force that accelerates the plasma. The MPD operates at very high power levels, kilowatts to megawatts, and provides the highest thrust of all the electric propulsion devices at comparatively moderate specific impulses¹⁰. Another example is

the pulsed plasma thruster (PPT), which uses a high voltage discharge to ablate, and subsequently accelerate, material from the surface of a solid block of Teflon. Figure 1.1 below illustrates the current flight specific impulse range achieved by the different types of electric propulsion devices. Laboratory model thrusters have pushed these upper limits even higher; Hall thrusters¹¹ and ion engines¹² have been demonstrated at specific impulse levels of 8000 s and 200000 s, respectively. However, these high specific impulses were achieved using non-standard propellants during very short duration tests. Typical values for a chemical propulsion system are included in Figure 1.1 for reference.

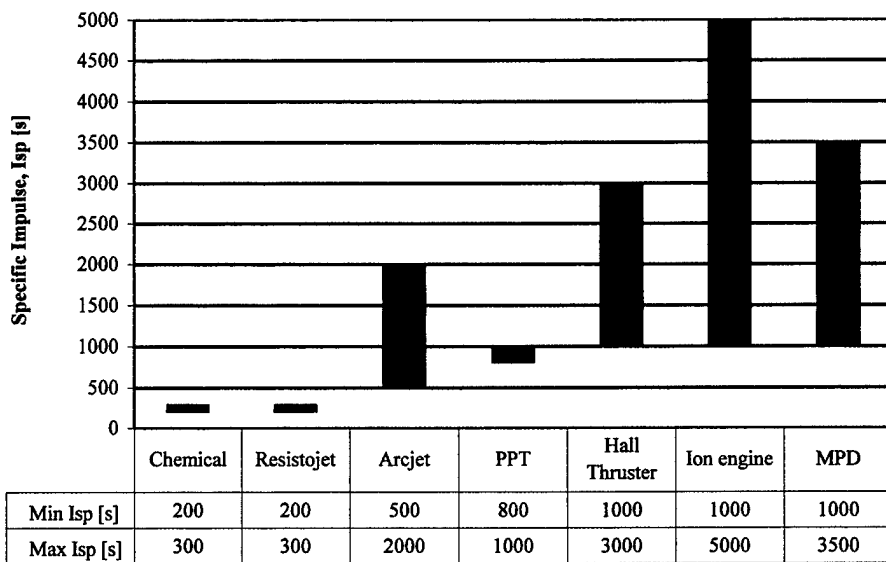


Figure 1.1 Typical specific impulse range of the various types of electric propulsion devices. Typical chemical propulsion values are included for comparison.

1.2 Closed Drift Thruster (CDT) Overview

The Hall thruster, also referred to as a Closed Drift Thruster (CDT), is a coaxial device in which orthogonal electric and magnetic fields are employed to ionize an inert gas, such as xenon, and accelerate the resulting ions to produce thrust. The main components of the CDT are shown in Figure 1.2.

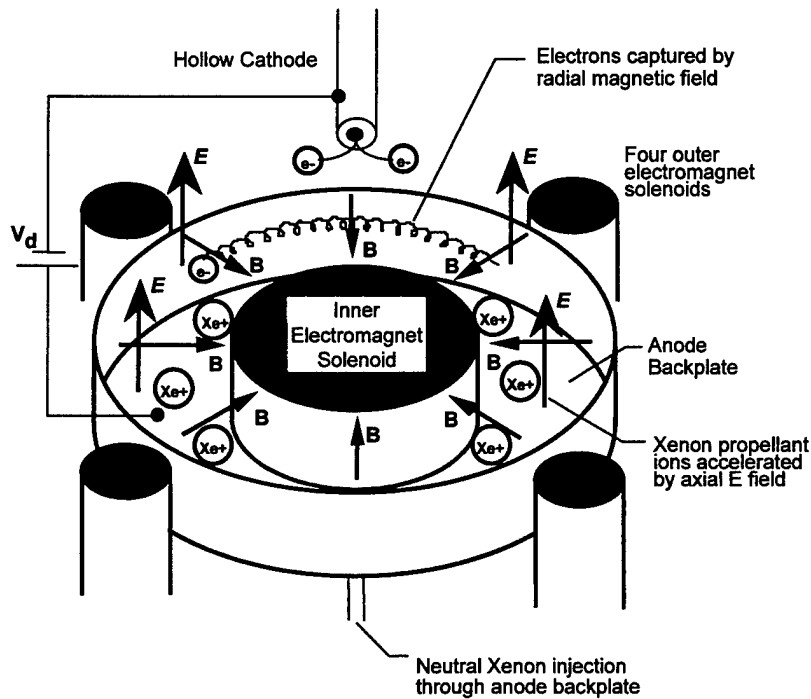


Figure 1.2 Components of a typical Hall thruster.

The magnetic field that is produced by an electromagnet is channeled between an inner ferromagnetic core (pole piece) and outer ferromagnetic ring (pole pieces are not shown in the figure). The electromagnet circuit is typically composed of a single central magnet coil in parallel with a series of outer magnet coils, the number of which may range from one to eight, depending on the particular thruster. In the case of low power thrusters, permanent magnets have also been used. Though separate power supplies can be used to

energize the electromagnet coils, the number of turns in each is usually set so the electromagnet establishes the proper magnetic field strength when it is operated in series with the discharge supply. This configuration results in an approximately radial magnetic field with a peak strength of a few hundred Gauss near the exit of the engine. The field strength is sufficiently low that only the electrons are magnetized. The radial magnetic field exhibits a bell-shaped axial profile with the peak situated near the exit. Most of the acceleration takes place near the region of peak magnetic field strength.

An axial electric field is provided by applying a voltage between the anode and the cathode. As the electrons stream upstream toward the anode from the cathode, their motion is impeded by the magnetic field. Because of the orientations of the electric and magnetic fields, the electrons drift in the **ExB** direction, forming an azimuthal Hall current. These electrons also ionize propellant atoms that are injected through the anode and which are subsequently accelerated by the axial electric field. This emerging ion flux is then neutralized by electrons from the external cathode. From an electrostatic point-of-view, the magnetic field suppresses the axial mobility of the electrons while exerting essentially no effect on the ions. This enables the plasma to support an axial electric field with a potential difference close to the applied voltage between the electrodes. Thus, the bulk of the ions are accelerated to kinetic energies within 80% of the applied discharge voltage. Moreover, the mixture of electrons and ions in the acceleration zone means that the plasma is electrically neutral, and as such, is not space-charge limited in ion current density as in the case of a gridded ion thruster. This combination of processes accounts for the CDT's high thrust efficiency and thrust density. The electromagnetic point-of-

view is simply that the azimuthal Hall current interacts with the radial applied magnetic field and accelerates the plasma axially through the $\mathbf{j} \times \mathbf{B}$ force.

There are two types of Hall thrusters: the stationary plasma thruster (SPT) (sometimes referred to as a magnet layer Hall thruster) which has a relatively long, ceramic discharge channel, and the thruster with anode layer (TAL) which employs a more shallow, metal discharge channel. Figure 1.3 illustrates the difference between the two thruster types.

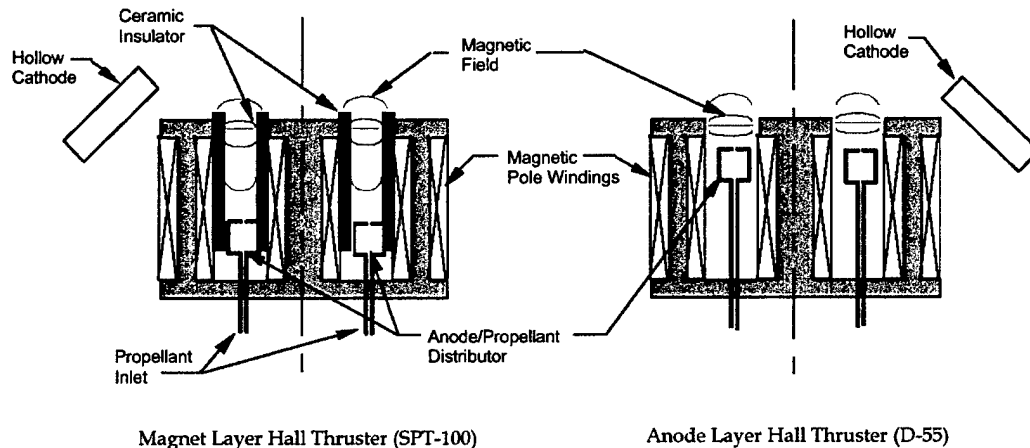


Figure 1.3 Comparison of SPT- and TAL-type Hall thrusters¹³.

While the performance characteristics of the two thrusters types are very similar, the length and material properties of the channel wall result in a significantly different structure of the acceleration zone. In the SPT, electrons experience a large applied potential and gain energy as they stream upstream from the external cathode to the anode at the back of the discharge channel. While this axial motion is impeded by the applied radial magnetic field, the electrons are essentially free to move radially along these same

magnetic field lines. The electrons then impact the ceramic walls. Because of the large secondary electron coefficient of the ceramic, these “hot” impacting electrons are replaced by relatively “cold” secondary electrons. The net effect is that the temperature of the electrons is moderated, resulting in a long, smooth acceleration zone. It is for this reason that SPT-type thrusters are often referred to as closed-drift thrusters with extended acceleration zones. The TAL, on the other hand, has conducting discharge channel walls with a very low secondary electron emission coefficient. The channel walls are held at cathode potential, reducing the number of impacting electrons. The net effect here is a much larger electron temperature, which supports a very sharp jump in the plasma potential. This narrow acceleration zone forms near the anode, hence the name thruster with anode layer.

1.3 Summary of Internal CDT Research

The Hall thruster arrived in the West as a relatively mature technology, having undergone years of refinement through its use on Soviet spacecraft. As such, the primary focus in the early years of US testing was on verifying performance and investigating issues of thruster/spacecraft interaction. This early work was conducted primarily at the Jet Propulsion Laboratory and at NASA Lewis Research Center. An overview of this research can be found in previous works^{13,14}. Regarding internal measurements, the earliest available experimental data is somewhat limited in that it comes entirely from translated Russian journal articles.

One of the earliest sets of electrostatic probe data came from Morozov¹⁵ where he measured the plasma potential and ion current density using several different working gases, including xenon, at voltages and currents as large as 1000 V and 15 A. These data indicated a very long acceleration zone, spanning nearly 75% of the discharge channel and extending several centimeters downstream of the exit plane. Ionization occurred primarily in the anode region with the ions being accelerated along most of the channel. An interesting feature was the presence of a large anode potential drop, for which no explanation was given. The ion stream was well formed near the anode, interacting very little with the walls. In the second half of the channel, ion interaction with the walls increased resulting in an increased axial electron current to compensate for the lost charge. Both plasma potential and ion current were essentially symmetric about the channel centerline.

Askhabov¹⁶ conducted measurements of electron temperature, number density, and floating potential in a direct-flow version of a Hall accelerator with extended acceleration zone. The direct-flow version used a booster volume at the entrance to the discharge channel providing an entrance area for the working gas that was 90% of the channel area. Plasma expanded to fill this booster volume as discharge voltage was increased, however, the basic behavior of the measured plasma parameters in the channel was the same as that for a traditional Hall accelerator.

Bishaev¹⁷ performed a comprehensive set of two-dimensional measurements that included directed ion current, electron temperature, number density, and plasma potential.

These data showed considerably different results from those of Morozov¹⁵. No large anode potential drop was observed and the plasma potential remained constant over the first 75% of channel, indicating a much shorter acceleration zone than previously observed. The data indicated that the channel consisted of two zones. The first zone extended from the anode to approximately half way along the channel and was characterized by a low density, low temperature plasma. There was very little ion production in this region, the electric field was essentially zero, and ion motion was predominantly toward the anode and walls. The second zone, starting approximately half way along the discharge channel and extending to the exit, was labeled the region of ionization and acceleration. This zone was characterized by sharp axial gradients in potential, temperature, and charged particle density. Ions underwent significant acceleration and formed a coherent beam directed along the thruster axis.

More recently, Barkalov¹⁸ investigated the azimuthal electron drift current inherent to all Hall accelerators. Using a series of inductive pickups along the inside and outside of the discharge channel, various aspects of the azimuthal electron current were determined. Discharge current was kept constant. The total Hall current increased nearly linearly with increasing discharge voltage, ranging from 1.2 to 2.4 times the discharge current, which was kept constant. It was also shown that the centroid of the azimuthal current shifted from the exit plane toward the anode with increasing voltage, stabilizing at a distance equivalent to 30% of the length of the discharge channel from the anode.

Outside of the former Soviet Union, internal data is rather limited. Guerrini¹⁹ measured electron temperature, number density, and plasma potential using electrostatic probes along the centerline of the discharge channel of an SPT-50. From the axial profiles of these parameters, they ascertained three regions along the channel: a pre-ionization zone near the anode where ionization and ion current are weak and plasma potential is high, an ionization zone midway along the channel where ionization and ion current increase and electron temperature is high, and an acceleration zone where plasma potential drops and ion current increases. The probe was inserted from the front of the thruster and oriented along the axis.

Hargus^{20,21} has performed optical and probe based internal measurements on a laboratory model Hall thruster. Ion and neutral velocity were measured using Laser Induced Fluorescence (LIF) with nonresonant signal detection while plasma potential was measured using an emissive probe. This provided information on propellant energy deposition, electric field strength, electron temperature, and flow divergence. A slit cut through the discharge channel wall provided both probe and optical access. The results indicated that the plasma potential remained nearly constant over 80% of the channel length, dropping sharply near the exit plane. Electron temperature followed the plasma potential profile downstream of the exit plane, with a peak value of approximately 20 eV a few millimeters upstream of the exit plane. Further upstream the temperature dropped to its downstream value before rising slightly near the anode.

Raitses²² investigated axial floating potential profiles as a function of discharge voltage in a laboratory model Hall thruster. Measurements were made at a single radial location, 1 mm from the external wall, with a probe inserted axially from the front of the thruster. The results showed that floating potential depended mainly on the magnetic field and remained constant with changing mass flow.

The aforementioned Russian internal data provided a great deal of information on the ionization and acceleration mechanisms inside a Hall accelerator. In particular, Morozov¹⁵ and Bishaev¹⁷ provided fully two-dimensional data sets so that radial as well as axial profiles of the plasma parameters can be studied. However, the data suffer from several significant limitations. No performance data for any of the Hall accelerators is specified. Further, very little information is provided concerning the construction of the various Hall accelerators from which the data is obtained. Internal plasma parameters are very sensitive to both discharge channel material and the structure of the magnetic field. Discharge channel material is not specified by any of the Russian authors. Magnetic field data is either not provided or is provided along the channel centerline only; in many cases, the centerline magnetic field values have been normalized to protect proprietary magnetic circuit designs. Regarding the non-Russian data, without exception it is one-dimensional and does not provide any information on radial profiles of the various plasma parameters.

Of primary importance regarding all previous data is that the use of electrostatic probes tends to significantly perturb the plasma when inserted into the thruster. Hargus²¹

reported discharge current variations of 150% above nominal when using the emissive probe over a range of voltages; at higher voltages, perturbation to thruster operation was so great as to make probe measurements impossible. Askhabov¹⁶ mentions perturbations at moderate voltages but fails to specify the extent of the perturbation and which sets of data the perturbation affected. This raises doubt as to the validity of the measurement. Neither Bashaev¹⁷, nor Guerrini¹⁹, nor Morozov¹⁵ gave any indication of the extent of thruster perturbation during their measurements.

1.4 Contribution of Research

The research presented in this dissertation involved the characterization of the plasma in the discharge channel of a Hall thruster. While the Hall thruster has been demonstrated to offer significant performance advantages for orbit raising and stationkeeping missions, issues of material erosion and beam divergence, and their effect on overall efficiency remain. The principal goal of this thesis was to provide a comprehensive set of two-dimensional internal plasma parameters in order to better understand the underlying physics of the Hall thruster, in particular the ionization and acceleration mechanisms. Inherent to the principal goal was to perform these measurements on a well-defined (dimensions, magnetic field structure, materials), well-characterized (thrust, specific impulse, efficiency) thruster while successfully avoiding significant plasma perturbation during probe measurements. The major components of the experimental investigation are listed below:

1. A laboratory-model 5 kW Hall thruster was designed and constructed. This thruster was built specifically for electrostatic probe diagnostic access. Performance was shown to correspond very closely to that of currently available commercial thrusters, thus validating the applicability of subsequent research.
2. A qualitative assessment of the effect of probe material ablation on Hall thruster operation was performed. This provided information on probe survivability necessary for accurate probe measurements inside the Hall thruster.
3. A high-speed probe positioning system was developed which enabled probe measurements without destroying the probe itself while limiting perturbation to the plasma.
4. A comprehensive set of internal plasma parameters was obtained. Measurements were made in both the axial and radial directions and included the following:
 - a. Electron temperature
 - b. Ion number density
 - c. Plasma potential
 - d. Vacuum radial magnetic field
 - e. Vacuum axial magnetic field
 - f. Hall current

The experimental data obtained were then compared to the results generated by a 2D model developed by Koo²³. This allowed for limited verification of the model, providing a tool for future optimization of the Hall thruster.

References for Chapter 1

¹ Kaufman, H.R., "Technology of Closed-Drift Thrusters," *AIAA Journal*, Vol. 23, No. 1, 1985, 78-86.

² Artsimovich, L., Andronov, I., Esipchuk, I., Morozov, A., Snarsky, R., "Development of a stationary plasma thruster (SPT) and its testing on the earth artificial satellite 'Meteor,'" *Kosmicheskie Issledovaniya* (a Soviet journal), Vol. 12, No. 3, pp. 451-468. (in Russian)

³ Brophy, J., et al., "Performance of the Stationary Plasma Thruster: SPT-100," AIAA-92-3155, 28th AIAA / SAE / ASME / ASEE Joint Propulsion Conference, Nashville, TN, July 6-8, 1992.

⁴ Sankovic, J., Hamley, J., and Haag, T., "Performance evaluation of the Russian SPT-100 thruster at NASA LeRC," IEPC-93-094, 23rd International Electric Propulsion Conference, Seattle, WA, September 13-16, 1993.

⁵ Garner, C., Polk, J., Goodfellow, K., and Brophy, J., "Performance evaluation and life testing of the SPT-100," IEPC-93-091, 23rd International Electric Propulsion Conference, Seattle, WA, September 13-16, 1993.

⁶ Garner, C., Brophy, J., Polk, J., and Pless, L., "A 5,730-hr cyclic endurance test of the SPT-100," AIAA-95-2667, 31st AIAA / ASME / SAE / ASEE Joint Propulsion Conference, San Diego, CA, July 10-12, 1995.

⁷ Spanjers, G., Birkan, M., Lawrence, T., "The USAF Electric Propulsion Research Program," AIAA-2000-3146, 36th AIAA / ASME / SAE / ASEE Joint Propulsion Conference, Huntsville, AL, July 16-19, 2000.

⁸ Dunning, J., Sankovic, J., "NASA's Electric Propulsion Program," AIAA-2000-3145, 36th AIAA / ASME / SAE / ASEE Joint Propulsion Conference, Huntsville, AL, July 16-19, 2000.

⁹ Myers, R.M., "Overview of Major U.S. Industrial Programs in Electric Propulsion," AIAA-2000-3147, 36th AIAA / ASME / SAE / ASEE Joint Propulsion Conference, Huntsville, AL, July 16-19, 2000.

¹⁰ Martinez-Sanchez, M., Pollard, J.E., "Spacecraft Electric Propulsion – an Overview," *Journal of Propulsion and Power*, Vol. 14, No. 5, Sept.-Oct. 1998, 688-689.

¹¹ Grishin, S.D., Erofeev, V.S., Zharinov, A.V., Naumkin, V.P., Safronov, I.N., "Characteristics of a Two-Stage Accelerator with an Anode Layer," *Journal of Applied Mathematics and Technical Physics*, No. 2, Mar-Apr 1978, 28-36.

¹² Byers, D.C., "An Experimental Investigation of a High-Voltage Electron Bombardment Ion Thruster," *Journal of the Electrochemical Society*, Vol. 116, No. 1, Jan.1969.

¹³ King, L.B., *Transport Property and Mass Spectral Measurements in the Plasma Exhaust Plume of a Hall-Effect Space Propulsion System*, Ph.D. Thesis, University of Michigan Department of Aerospace Engineering, University Microfilms International, 1998.

¹⁴ Kim, S.-W., *Experimental Investigations of Plasma Parameters and Species-Dependent Ion Energy Distribution in the Plasma Exhaust Plume of a Hall Thruster*, Ph.D. Thesis, University of Michigan Department of Aerospace Engineering, University Microfilms International, 1999.

¹⁵ Morozov, A., Esipchuk, Y., Tilinin, G., Trofimov, A., Sharov, Y., and Shchepkin, G., "Plasma accelerator with closed electron drift and extended acceleration zone," *Soviet Physics-Technical Physics*, Vol. 17, July 1972, pp. 38-45.

¹⁶ Askhabov, S.N., Melikov, I.V., Fishgoit, V.V., "Electric Discharge in Direct-Flow Hall Accelerator," *Soviet Physics-Technical Physics*, Vol. 22, No. 1, April 1977, pp. 453-458.

¹⁷ Bishaev, A.M., Kim, V., "Local Plasma Properties in a Hall-Current Accelerator with an Extended Acceleration Zone," *Soviet Physics-Technical Physics*, Vol. 23, No. 9, September 1978, pp. 1055-1057.

¹⁸ Barkalov, E.E., Veselovzorov, A.N., Subbotin, M.L., "Experimental Study of the Azimuthal Electron Drift Current in Hall Accelerators," *Soviet Physics-Technical Physics*, Vol. 35, No. 2, February 1990, pp. 238-239.

¹⁹ Guerrini, G., Michaut, C., Dudeck, M., Vesselovzorov, A.N., Bacal, M., "Characterization of Plasma Inside the SPT-50 Channel by Electrostatic Probes," IEPC-97-053, 25th International Electric Propulsion Conference, Cleveland, OH, August 1997.

²⁰ Hargus, W.A., Meezan, N.B., Cappelli, M.A., "A Study of a Low Power Hall Thruster Transient Behavior," IEPC-97-058, 25th International Electric Propulsion Conference, Cleveland, OH, August 1997.

²¹ Hargus, W.A., Cappelli, M.A., "Interior and Exterior Laser-Induced Fluorescence and Plasma Potential Measurements on a Laboratory Hall Thruster," AIAA-99-2721, 35th AIAA / ASME / SAE / ASEE Joint Propulsion Conference, Los Angeles, CA, June 20-24, 1999.

²² Raitses, Y., Ashkenazy, J., Appelbaum, G., "Probe Measurements of Plasma Properties inside an Experimental Hall Thruster," AIAA-98-3640, 34th AIAA / ASME / SAE / ASEE Joint Propulsion Conference, Cleveland, OH, July 13-15, 1998.

²³ Koo, J., Boyd, I., Haas, J., Gallimore, A., "Computation of the Internal Flow of a 2kW-Class Hall Thruster," to be presented at the 37th AIAA/ASME/SAE/ASEE Joint Propulsion Conference Salt Lake City, Utah, July, 2001.

CHAPTER 2

FACILITIES AND DIAGNOSTICS - AIR FORCE RESEARCH LABORATORY (AFRL)

Electrostatic (or Langmuir) probes are among the simplest and most commonly used plasma diagnostic tools. Their use dates back to Langmuir's¹ original development of the theory to describe probe behavior in a plasma. Since that time electrostatic probes have found use in a wide range of disciplines ranging from nuclear fusion² to atmospheric and space sciences³. In particular, they have been used extensively in the field of electric propulsion to provide a relatively simple means of measuring electron temperature, electron number density, plasma potential and floating potential. Electrostatic probes have been used in single, double, triple and quadruple configurations in a number of devices including arcjets, MPD thrusters, ion engines and Hall thrusters^{4,5,6,7,8,9,10,11}.

In plasmas with highly energetic charged particles, probe material is generally sputtered and/or ablated by direct particle flux on very small time scales. The local plasma temperature and density may then be modified through emission of relatively cold probe material. These perturbations may remain localized near the probe, or may propagate further into the plasma affecting the macroscopic properties of the plasma being interrogated. As time scales increase, probe survival becomes an issue. In the case of

Hall thrusters, for measurements downstream of the exit plane, probe survival is not a concern nor does the presence of the probe adversely affect thruster operation. However, within the discharge chamber, plasma temperature and density increase which leads to increased probe heating. Moreover, the presence of an intense Hall current in the acceleration region of the Hall thruster further exacerbates this problem. Probe material ablation then becomes significant and survival times are shortened drastically. Under these conditions, a high speed, reciprocating probe system can reduce the amount of ablated material, allowing for more accurate measurements of local plasma parameters and assuring probe survival.

Experiments conducted at the Air Force Research Laboratory (AFRL) aimed at quantifying the perturbative effects of electrostatic probes on the operation of a Hall thruster. The facilities and diagnostic components employed in this phase of the research are described in detail below.

2.1 Vacuum Chamber – Chamber 6

Experiments at AFRL were conducted in the electric propulsion laboratory's Chamber 6, a 2 m diameter by 3 m long vacuum chamber. Figure 2.1 shows the layout of Chamber 6. Rough vacuum was provided by a single Stokes mechanical pump and blower. High vacuum was achieved by 4 copper cryopanels maintained at 25 K by 4 APD cold heads and model HC-8C helium compressors and a 22 in. APD cryopump. Heat load to the cryopanels was minimized by a pair of shrouds coated with low emissivity paint and chilled by a Polycold refrigeration unit. This configuration yielded a total pumping speed

of 26,000 l/s of xenon with an ultimate base pressure of 9×10^{-7} Torr. Pressure was measured using a MKS Model 919 Hot Cathode Ionization Gauge and remained below 5×10^{-5} Torr during all tests. Propellant flow was maintained by an array of Unit Model 8100 mass flow controllers, calibrated specifically for xenon. Flow rates were calibrated independently by comparison with the time dependent pressure rise in a known volume.

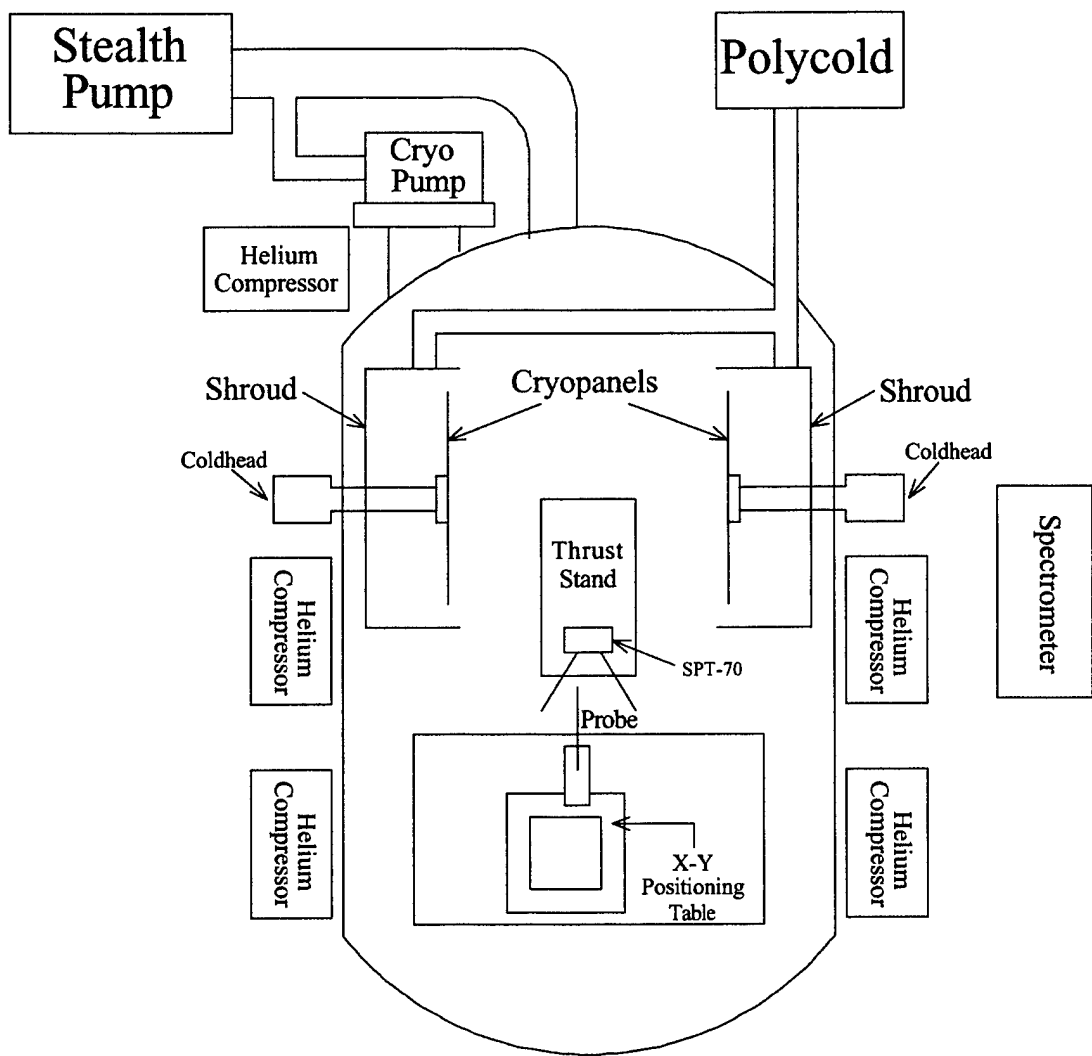


Figure 2.1 Air Force Research Laboratory (AFRL) Chamber 6 Layout. Rough vacuum was reached with a single Stokes stealth pump. Subsequent high vacuum was accomplished with two copper cryopanels and a single cryopump. The layout of the thruster, probe, and positioning system is also shown.

2.2 Thruster – SPT-70

A Fakel SPT-70 was used for all experiments at AFRL. This thruster was designed to operate at 660 W nominal discharge power yielding 40 mN of thrust and 1500 s of specific impulse at 40% efficiency¹². These performance values correspond to operating conditions of 300 V and 2.2 A with a xenon flow rate of 26 sccm, 3 sccm of which was supplied to the cathode.

Propellant flow to the thruster was controlled by an array of Unit Model 8100 mass flow controllers, calibrated for xenon. Flow system components and tubing were cleaned and electropolished and all connections welded. System leak rates were determined to be less than 1×10^{-7} sccm.

2.3 Probe

The goal of this initial set of experiments was to quantify the effects of an ablating probe on thruster operation. Since the aim was to destroy the probe, a simple “dummy” probe was constructed. It was projected that future experiments would make use of a quadruple probe for internal plasma measurements. Thus the “dummy” probe used here was built in the same configuration. It consisted of four tungsten electrodes, each with a diameter of 0.38 mm and a length of 1.88 mm, mounted in an alumina insulator; three electrodes were oriented with the axis of the probe while the fourth was bent ninety degrees. Figure 2.2 illustrates the probe configuration.

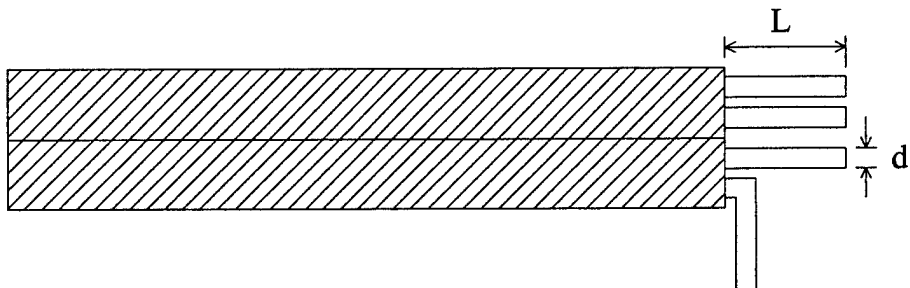


Figure 2.2 Configuration of “Dummy” probe used in AFRL experiment. The probe consisted of 4 tungsten electrodes, each with a diameter $d = 0.38$ mm and a length $L = 1.88$ mm, mounted in an alumina insulator. Three electrodes were oriented with the axis of the probe while the fourth was bent ninety degrees.

The probe was aligned with the thruster and inserted using the positioning system described in the next section. The probe and positioning system setup is shown in Figure 2.1.

2.4 Positioning System

The quadruple probe used in these experiments was mounted to a high speed reciprocating linear actuator. This actuator had a manufacturer specified maximum speed of 1.3 m/s with an acceleration time constant of approximately 8 ms. The actuator was operated at its positive and negative physical limits only, using a Stanford Research Systems Model DS535 Pulse Generator to drive the actuator to its physical limit in one direction, pause for a specified period of time, and then return to its opposite limit. The actuator had a stroke length of 50 mm and a transit time of approximately 150 ms. A minimum of 200 ms was required for the actuator to reverse direction at its positive limit. The minimum total time required to insert and remove the probe was approximately 0.5 s

and was estimated from the rate of change of probe traces recorded on a TEK TDS460 oscilloscope.

The reciprocating probe assembly was in turn mounted to a Parker 2-axis positioning table with a total travel of 0.3 m in both directions but with a much slower speed than the actuator. This table was used to move the probe from a safety position well outside the thruster plume to the centerline of the discharge chamber, at the 9 o'clock position (facing the thruster exit), and 25 – 50 mm downstream. This served as the home position for the reciprocating probe, which moved in an axial direction only, positioning the probe either at the exit plane or several millimeters upstream of the exit plane. Refer back to Figure 2.1 for the experimental setup.

2.5 Spectrometer

A SPEX 1 m spectrometer with a 1200 grooves/mm, 11 cm, first order grating was used during the testing to detect species from the ablating tungsten electrode and alumina insulator. The tip of the probe at the exit plane of the thruster was imaged onto the entrance slit of the spectrometer using a 600 mm focal length, 76 mm lens. A pair of telescoping mirrors rotated the probe image, aligning the axis of the probe along the slit. Output was collected by a Hamamatsu 921 photomultiplier tube (PMT) and recorded on a Tektronix TDS460A oscilloscope. The entrance and exit slit widths were both 50 μm providing a resolution of approximately 0.3 Å. Figure 2.3 illustrates the spectrometer setup.

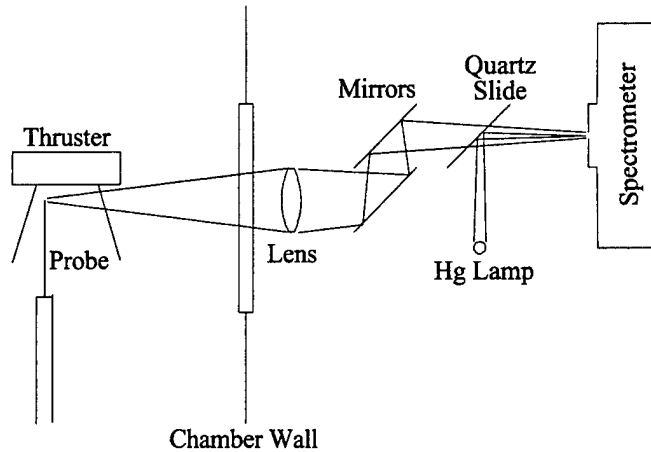


Figure 2.3 Spectrometer setup. The probe tip was imaged onto the entrance slit of the spectrometer through a quartz window on the chamber. Calibration was performed in-situ with a mercury lamp.

In-situ calibration of the spectrometer was accomplished via a mercury lamp and quartz slide having a transparency of 95%. The slide was placed at a 45° angle in front of the entrance slit, while the mercury lamp was placed 90° to the side of the entrance slit. This allowed 95% of the signal from the probe to be transmitted through the slide while 5% of the signal from the mercury lamp was reflected into the slit for calibration.

References for Chapter 2

- ¹ Mott-Smith, H.M., Langmuir, I., "The theory of collectors in gaseous discharges," *Physics Review*, Vol. 28, 1926, p. 727.
- ² Rhodes T.L., Ritz, C.P., Bengtson, R.D., Carter, K.R "Fast Reciprocating Probe System Used to Study Edge Turbulence on TEXT", *Review of Scientific Instruments*, Vol. 61, No. 10, October 1990, pp. 3001-3003.
- ³ Seifert, W., Johannig, D., Lehmann, H., Bankov, N., "Methods for the Numerical Calculation of the Plasma Potential from Measured Langmuir Probe Characteristics", *Contributions to Plasma Physics*, Vol. 26, No. 4, 1986, pp. 237-254.
- ⁴ Marrese, C.M., Haas, J.M., Domonkos, M.T., Gallimore, A.D., Tverdoklebov, S., Garner, C., "D-100 Performance and Plume Characterization on Krypton," AIAA 96-2969, 32nd AIAA / ASME / SAE / ASEE Joint Propulsion Conference, July 1996.
- ⁵ Gallimore, A.D., Reichenbacher, M.L., Marrese, C.M., Kim, S-W, Foster, J.E., "Near and Far-field Plume Studies of a 1 kW Arcjet," AIAA 94-3137, 30th AIAA / ASME / SAE / ASEE Joint Propulsion Conference, June 1994.
- ⁶ Kim, S-W., Foster, J.E., Gallimore, A.D., "Very-Near-Field Plume Study of a 1.35 kW SPT-100," AIAA 96-2972, 32nd AIAA / ASME / SAE / ASEE Joint Propulsion Conference, July 1996.
- ⁷ De Boer, P.T.C., "Electric Probe Measurements in the Plume of an Ion Thruster," *Journal of Propulsion and Power*, Vol. 12, No. 1, Jan.-Feb. 1996.
- ⁸ Burton, R.L., DelMedico, S.G., Andrews, J.C., "Application of a Quadruple Probe Technique to MPD Thruster Plume Measurements," *Journal of Propulsion and Power*, Vol. 9, No. 5, Sept.-Oct. 1993.
- ⁹ Guerrini, G., Michaut, C., Dudeck, M., Vesselovzorov, A.N., Bacal, M., "Characterization of Plasma Inside the SPT-50 Channel by Electrostatic Probes," IEPC-97-053, 25th International Electric Propulsion Conference, Cleveland, OH, August 1997.
- ¹⁰ Tilley, D.L., Kelly, A.J., Jahn, R.G., "The Application of the Triple Probe Method to MPD Thruster Plumes," AIAA 90-2667, 26th AIAA / ASME / SAE / ASEE Joint Propulsion Conference, July 1990.
- ¹¹ Burton, R.L., Bufton, S.A., "Exit-Plane Electrostatic Probe Measurements of a Low-Power Arcjet," *Journal of Propulsion and Power*, Vol. 12, No. 6, Nov-Dec 1996, pp. 1099-1106.

¹² Haas, J.M., Spanjers, G., McFall, K., Spores R., "An Investigation of Electrostatic Probe Perturbations on the Operational Characteristics of a Hall Thruster and on the Measurement of Local Plasma Parameters," AIAA-98-3656, 34th AIAA / ASME / SAE / ASEE Joint Propulsion Conference, July 1998.

CHAPTER 3

EXPERIMENTAL RESULTS – AFRL

Using the experimental setup outlined in the previous chapter, thruster operating conditions were monitored with the probe ablating at the exit plane of the thruster. A simple thermal model was developed to predict the ablation time for the tungsten and alumina probe in the high temperature, high density Hall thruster discharge channel. Implications for probe residence time, material, and size are discussed.

3.1 Electrostatic Probe – CDT Interaction

Figure 3.1 illustrates the effect of probe material ablation on the operational characteristics of the thruster. No attempt was made to avoid material ablation since the purpose of this experiment was to determine the effect probe ablation has on thruster operation. The probe was positioned at the exit plane for an extended period of time to study both the transient and steady-state effects. The spectrometer grating was set at zero wavelength and broadband emission from the probe monitored. Recall that positioning of the probe consisted of two steps: moving the probe to its home position 25-50 mm downstream of the exit plane with the low-speed table and inserting the probe with the

high-speed actuator. At time $t = 0$ (not shown on the plot), the probe began moving to its home position. At time $t = 30$ s, the probe was positioned at the thruster exit plane where it remained for approximately 10 s and was then removed.

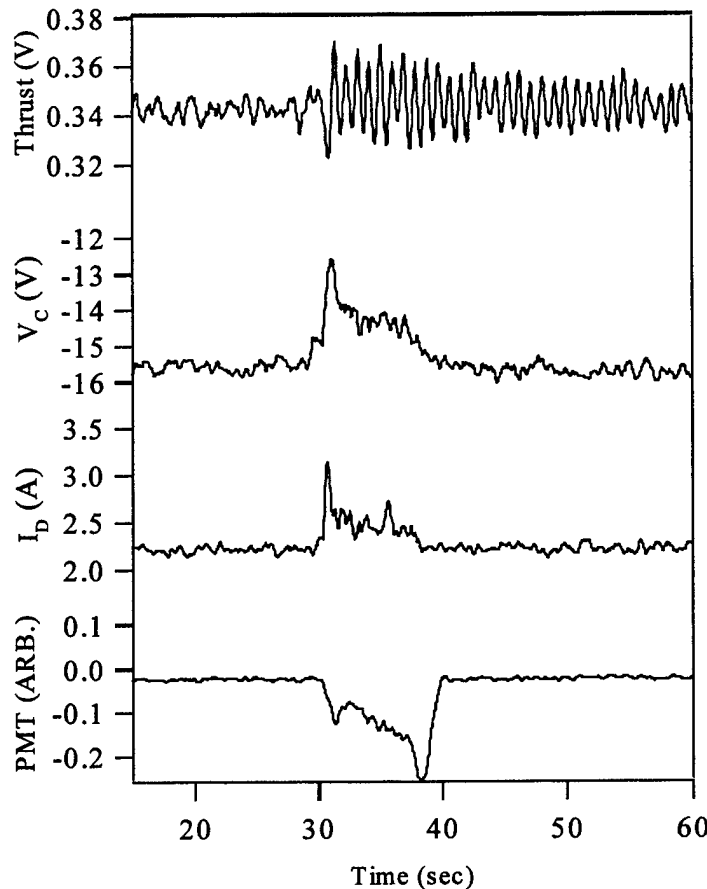


Figure 3.1 Thruster operational parameter variations with probe ablation. Discharge current, cathode potential, and thrust all varied significantly with the onset of probe ablation, indicated by the output from the PMT. The spectrometer grating was set at zero wavelength.

The bottom plot is the output from the spectrometer and shows clearly when the probe began to ablate. Discharge current initially increased by fifty percent then dropped to a value approximately twenty percent above the nominal level. Cathode potential behaved similarly, increasing initially by twenty percent then leveling off approximately ten percent above nominal. Both discharge current and cathode potential remained

artificially high as long as the probe remained at the exit plane. The top plot in Figure 3.1 shows the unconverted output from the thrust stand and illustrates the oscillation induced by the ablating probe. This output voltage is linearly proportional to the thrust. The continuing oscillation after the probe was removed and ceased ablating material was a result of the thrust stand being under-damped.

With the above results as a baseline, the high-speed actuator was operated at its maximum speed and the probe was inserted into the thruster 3 – 5 mm upstream of the exit plane. This was done to determine if the probe could be inserted and removed from the thruster while avoiding the observed perturbations. The actuator proved to be too slow to avoid ablating probe material and perturbing the thruster. This was due, in part, to the short actuator stroke length, which was only 50 mm; the necessity of moving the probe into position 25 – 50 mm downstream of the exit plane with the low-speed table resulted in the probe being heated considerably before it was inserted, at high speed, into the thruster. It was concluded that a high-speed positioning system with longer travel and possibly increased speed and acceleration was needed. In order to determine the necessary speed and acceleration, a simple thermal model was developed to predict resident times necessary to avoid probe material ablation. This is discussed in the following section.

These experiments also yielded an unexpected result. Upon examination of the “dummy” probe after it had been inserted into the thruster, it appeared that the probe had

experienced very localized ablation several millimeters upstream of the tip, as illustrated in Figure 3.2.

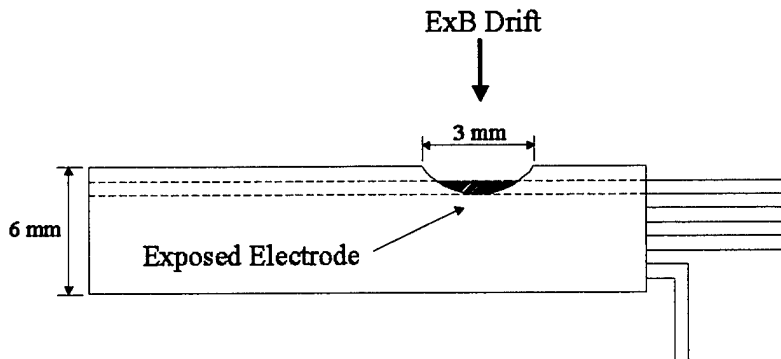


Figure 3.2 Illustration of probe ablation from AFRL experiment. The portion of exposed electrode occurs on the upper side of the probe; as indicated, this is the side oriented toward the high-energy, drifting electrons. The probe position with respect to the exit plane, in conjunction with the localized ablation, strongly supports the conclusion that the Hall current is a dominant heating mechanism for probes inside the thruster.

The ablation pattern in Figure 3.2 implied that the heating mechanism varied along the axis of the discharge chamber, with greater heating occurring at a location several millimeters upstream of the exit plane. This is the general location of the peak electric field in Hall thrusters of this type¹ (i.e., thrusters with a ceramic discharge chamber) and it follows that this would be the location of maximum Hall current. This apparent dominance of the Hall current as a probe heating mechanism is supported by the results of the thermal model presented in the next section.

3.2 Electrostatic Probe Thermal Model

Once the effects of ablating probe material were better understood, a simple model was used to predict the maximum residence time of an electrostatic probe inside the Hall

thruster before the onset of ablation². While the initial experiments of the previous section were conducted using an SPT-70 operating at 660 W, the ultimate goal was to make measurements inside a 5 kW laboratory-model Hall thruster. Thus the parameters in the model presented below reflect conditions expected in a 5 kW thruster. Initially, the probe was modeled as a cylinder with radius r and length l with heat conduction along the length of the probe taken into account. However, because of the short time scales involved, it was determined that heat conduction was negligible and so a simplified, “bulk” heating approach was used. The model assumed that all probe heating resulted from particle flux to the surface and consisted of both a directed component dictated by the thruster parameters and a random component dictated by the dynamics of the sheath surrounding the probe. The total particle flux was further subdivided into the contribution from the electrons and ions. Equation 3-1 is the power density to the probe, which is expressed as the sum of the products of the flux of each particle species, j , and its kinetic energy.

$$\frac{P}{A_{total}} = \sum_j K_j f_j = \frac{1}{2} m_j V_j^2 f_j \quad \text{Eq. 3-1}$$

The four components of the total power density seen by the probe are estimated based on standard Langmuir probe theory and consist of the following²:

Directed ion flux to the probe tip where

$$f = n_i V \quad \text{Eq. 3-2}$$

$$V = \sqrt{\frac{2\phi q}{M}}$$

Eq. 3-3

Random ion flux through the sheath where

$$f = n_i V$$

Eq. 3-4

$$V = \sqrt{\frac{\kappa T_e}{M}}$$

Eq. 3-5

Random electron flux through the sheath where

$$f = \frac{1}{4} n V$$

Eq. 3-6

$$n = n_e \exp \left[\frac{q(\phi_f - \phi_p + \Delta\phi)}{\kappa T_e} \right]$$

Eq. 3-7

$$V = \sqrt{\frac{8\kappa T_e}{\pi m}}$$

Eq. 3-8

Directed electron flux from the Hall current where

$$V_{ExB} = \frac{E_y}{B_z} \quad \text{Eq. 3-9}$$

$$f = n_0 V_{ExB} \quad \text{Eq. 3-10}$$

The bulk melting time is given by Equation 3-11³:

$$t_{bulk} = \frac{r\rho C_p T_{max}}{2[P/A]_{total}} \quad \text{Eq. 3-11}$$

It was assumed that the plasma was quasineutral ($n_i = n_e$) and a conservative estimate of $5 \times 10^{18} \text{ m}^{-3}$ for number density was used⁴. The results of the thermal model indicated that the contribution of the Hall current to the total power density was at least an order of magnitude larger than each of the other components. As stated previously, this supports experimental data, which indicated the dominant heating mechanism was the Hall current (see Figure 3.2). Figure 3.3 shows the dependence of alumina ablation time on the axial electric field for several values of the radial magnetic field. Ablation times for tungsten, both predicted and observed, were much longer

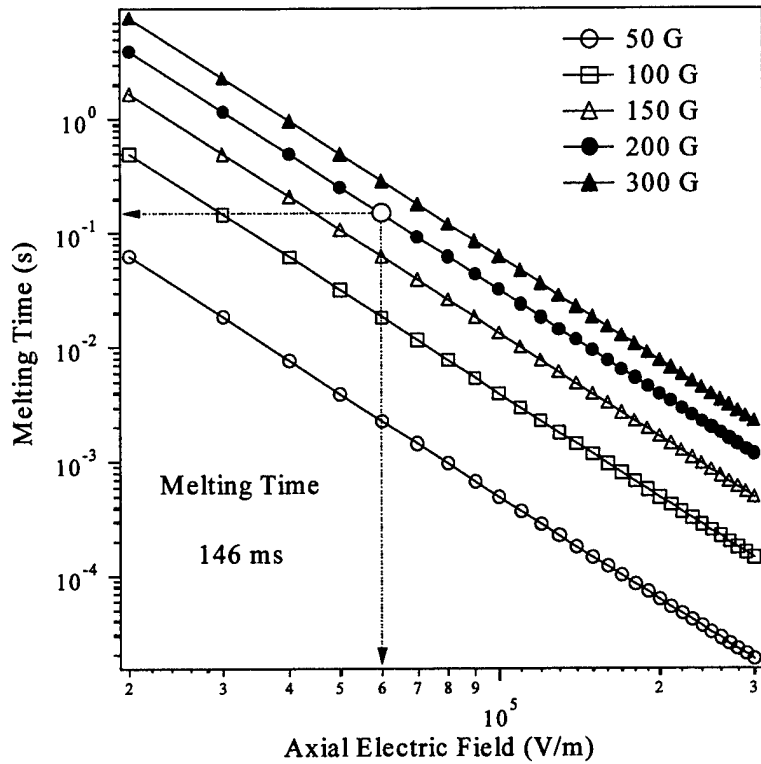


Figure 3.3 Probe melting time versus axial electric field strength for several magnetic field values. Representative values for electric field, 6×10^5 V/m, and magnetic field, 200 G, yield an ablation time of approximately 150 ms for the alumina insulator.

Using representative values for a 5 kW Hall thruster, $E = 6 \times 10^4$ V/m and $B = 200$ G, the power density to the probe resulting from the Hall current was estimated to be 1.2×10^7 W/m². This yielded a predicted alumina ablation time of approximately 150 ms, as shown in Figure 3.3, and an ablation threshold for alumina of 1.8×10^6 J/m². The 150 ms ablation time is considerably less than the 0.5 s it took the actuator to move from 50 mm downstream, into the thruster, and back. The 150 ms time became the figure of merit (tungsten ablation times were much longer) for the development of the high-speed electrostatic probe system to be discussed in the next chapter. It should be noted that, far downstream of the exit plane, where the probe would reside between “sweeps” inside the thruster (assuming an improved positioning system with a much larger stroke length),

plasma density and temperature were sufficiently small that probe heating was considered to be negligible.

3.3 Probe Construction Considerations

Several factors were taken into consideration in the design of the electrostatic probe. While the thermal model indicated that the ablation time was effectively independent of the probe size, it was highly dependent on the material properties, particularly density and specific heat. The results presented in Figure 3.3 are for standard probe insulator material, alumina. No other refractory metal surpassed the thermal characteristics of tungsten. Several materials, on the other hand, were considered as a replacement for alumina as an insulator. Beryllia (BeO) had a density and melting temperature comparable to alumina while possessing a higher value of specific heat, which, referring back to Equation 3-11, would result in longer ablation times. However, beryllia has a high pulmonary toxicity that makes it unsuitable for general laboratory use. Diamond was also considered because of its high specific heat but was eliminated based on its large secondary electron emission coefficient that would create significant problems in a diagnostic that depends on the collection of charged particles to measure plasma parameters. Silicon nitride possessed a high working temperature and large specific heat. However, its thermal properties offered no advantages over alumina and it was not nearly as inexpensive and easily acquired in tube form. As such, it was determined that alumina was the best choice for the probe insulator.

Although the thermal model indicated probe size was negligible from a heating/material ablation standpoint, size was still an important consideration in probe design. The

dimensions of the thruster dictated that the probe size should be minimized as much as possible in order to improve the spatial resolution of the measurements. A smaller electrode size would also minimize the current collected by the probe thus reducing perturbation from a localized depletion of charged particles. Conversely, the characteristics of the high-speed actuator necessitated a probe large enough that it could withstand the mechanical stress of a large acceleration. Through trial and error, it was determined that a probe constructed of an alumina insulator 1.5 mm in diameter would meet the size and strength requirements.

References for Chapter 3

-
- ¹ Hargus, W.A., Cappelli, M.A., "Interior and Exterior Laser-Induced Fluorescence and Plasma Potential Measurements on a Laboratory Hall Thruster," AIAA-99-2721, 35th AIAA / ASME / SAE / ASEE Joint Propulsion Conference, Los Angeles, CA, June 20-24, 1999.
- ² Haas, J.M., Spanjers, G., McFall, K., Spores R., "An Investigation of Electrostatic Probe Perturbations on the Operational Characteristics of a Hall Thruster and on the Measurement of Local Plasma Parameters," AIAA-98-3656, 34th AIAA / ASME / SAE / ASEE Joint Propulsion Conference, July 1998.
- ³ Lochte-Holtgreven, W., Plasma Diagnostics, AIP Press, New York, 1995.
- ⁴ Bishaev, A.M., Kim, V., "Local Plasma Properties in a Hall-Current Accelerator with an Extended Acceleration Zone," *Soviet Physics-Technical Physics*, Vol. 23, No. 9, September 1978, pp. 1055-1057.

CHAPTER 4

FACILITIES AND DIAGNOSTICS - PLASMADYNAMICS AND ELECTRIC PROPULSION LABORATORY (PEPL)

Using the information from the AFRL experiment results, the High-speed Axial Reciprocating Probe (HARP) positioning system was constructed. Concurrently, a 5 kW laboratory model Hall thruster, designated the P5, was designed and built. Both the HARP and P5 thruster were thoroughly tested and their performance validated at the University of Michigan Plasmadynamics and Electric Propulsion Laboratory (PEPL). This chapter describes the vacuum facilities, thruster, positioning system, and various probes which were used to generate the internal plasma measurements to be presented in Chapter 5.

4.1 Vacuum Chamber – Large Vacuum Test Facility (LVTF)

Experiments at PEPL were conducted in the 6 m by 9 m Large Vacuum Test Facility (LVTF), illustrated in Figure 4.1. High vacuum in the LVTF was achieved by four CVI Model TM-1200 Re-Entrant Cryopumps, each of which was surrounded by a LN₂ baffle. This configuration yielded a total xenon pumping speed of 140,000 l/s with a base pressure of less than 3×10^{-7} Torr. This facility has since (August 2000) been upgraded to

seven cryopumps for a total xenon pumping speed close to 250,000 l/s. Propellant flow was maintained by two MKS Model 1100 Mass Flow Controllers. The controllers were calibrated using the ideal gas law and the time rate of change of the pressure in a known volume. The data were further corrected for the compressibility of xenon. This yielded a total mass flow uncertainty of less than 1%. Chamber pressure was monitored using two gauges: a Varian model 571 gauge with a HPS model 919 Hot Cathode Controller and a Varian model UHV-24 nude gauge with a Varian UHV senTorr Vacuum Gauge Controller. The nude gauge, controller, and cable were calibrated as one unit on nitrogen by the manufacturer. Pressure measurements from both gauges were corrected for xenon using a calibration factor of 2.87¹.

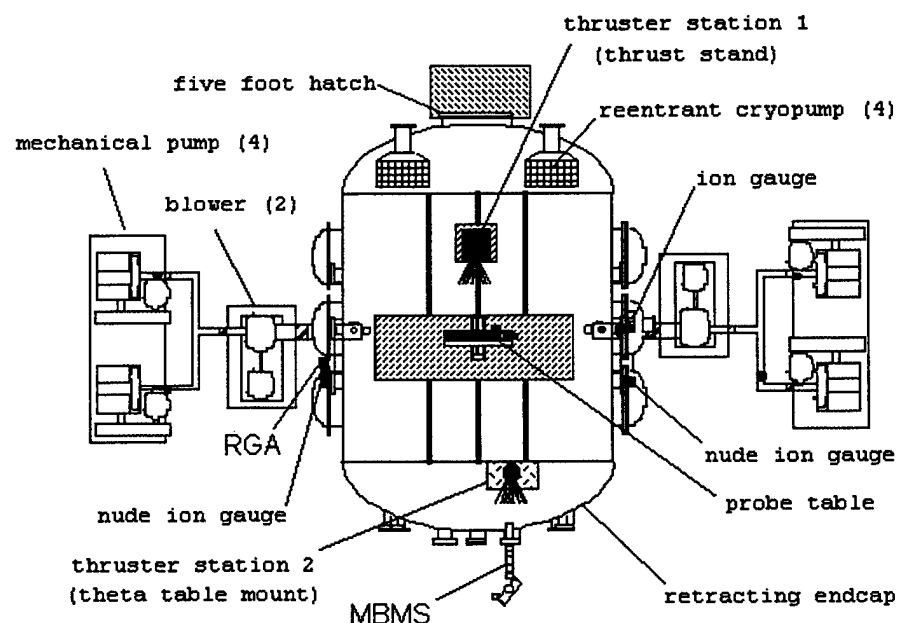


Figure 4.1 Shown is the Large Vacuum Test Facility (LVTF) at the University of Michigan. The LVTF is a stainless-steel clad chamber, 6 m in diameter and 9 m long. It has two pairs of mechanical pumps each backed by a single blower, providing a rough vacuum of better than 10 mTorr. High vacuum is achieved with four reentrant cryopumps provided a pumping speed of 140,000 l/s of xenon. The ultimate base pressure of this configuration is 1×10^{-7} Torr.

4.2 Thruster – P5

In the past, Hall thruster research concentrated primarily on the 1.35 kW class of thrusters and their applicability to military and commercial satellite missions. Recent trends in industry and government have shifted the focus to higher power thrusters. Of particular interest is the 5 kW class of thrusters, as engineers seek to expand the role of Hall thrusters to include orbit topping and orbit transfer missions. The SPT-140², T-160³, and D-100⁴ are all currently undergoing evaluation and testing; unfortunately, they are few in number and thus generally unavailable for research purposes.

It is with the aforementioned issues in mind that the University of Michigan initiated a joint program with the Air Force Research Laboratory to develop a 5 kW Hall thruster to be used for basic thruster physics research. This thruster was designated the P5 and is described in more detail below.

4.2.1 P5 Design Considerations

The goals of this joint program were threefold: design and build a Hall thruster with performance characteristics comparable to current state-of-the-art thrusters, provide for extensive diagnostic capabilities, particularly internal diagnostics, and provide for easy modifications to enable changes in thruster configuration. As pointed out earlier, both government and industry are interested in 5 kW thrusters for orbit topping and orbit transfer missions in addition to stationkeeping. From a research standpoint, a 5 kW thruster is large enough to allow for good spatial resolution of electrostatic probe

measurements while, at the same time, not exceeding the pumping capacity of the available vacuum facilities.

Having determined the desired thruster power level, it was necessary to choose a thruster type; one with ceramic discharge channel walls (SPT) or one with conducting channel walls (TAL). In general, the discharge channel in a TAL is more narrow and shallow than in an SPT, with sharper axial plasma parameter gradients. This makes it more difficult to resolve the axial profiles of a given plasma parameter. In addition, the available design equations from the MIT summer workshop⁵, which were relied upon to determine many thruster dimensions, were applicable only to thrusters with ceramic walls. Thus the ceramic channel was chosen.

With the power level and thruster type determined, a survey of existing commercial thrusters was used to establish a relationship between thruster power, thruster size, and observed performance. This activity consisted of several steps, which have been conveniently compiled by Gulczinski⁶ and are summarized below. Figure 4.2 illustrates thruster power as a function of specific impulse, from which a target specific impulse of 2200 s was obtained.

Figure 4.3 shows the relationship between thruster efficiency and specific impulse. From this graph, a 5 kW thruster operating at 2200 s specific impulse was projected to achieve an efficiency of 61%.

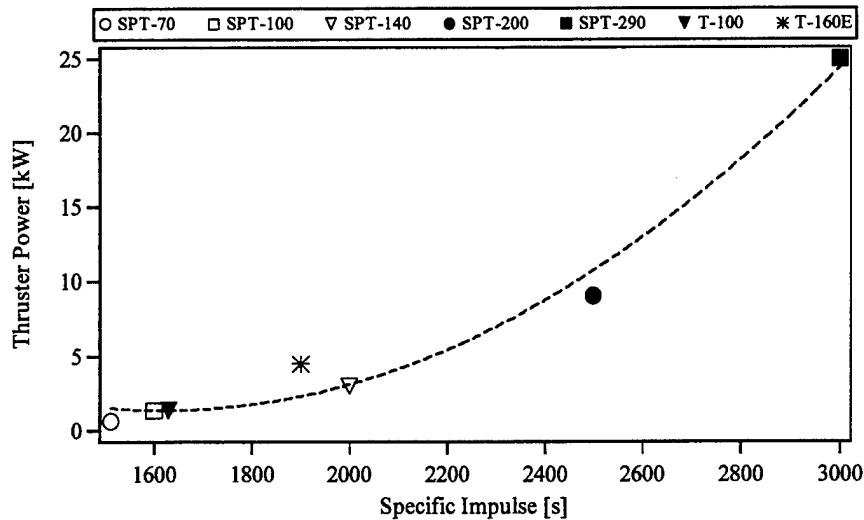


Figure 4.2 Thruster power versus specific impulse for several commercial thrusters.

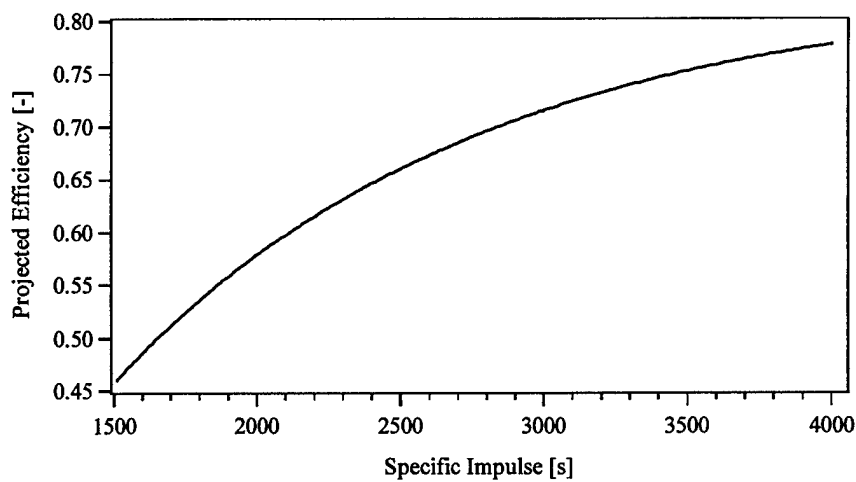


Figure 4.3 Thruster efficiency versus specific impulse.

The next step was to relate the efficiency to the mass flow rate as shown in Equation 4-1.

$$\dot{m}_a = \frac{2\eta P_D}{(I_{sp}g)^2} \quad \text{Eq. 4-1}$$

Equation 4-1 yielded a mass flow rate of 13 mg/s. Figure 4.4 relates thruster diameter to mass flow rate and enabled the determination of the thruster diameter, 170 mm, when used in conjunction with the results of Equation 4-1.

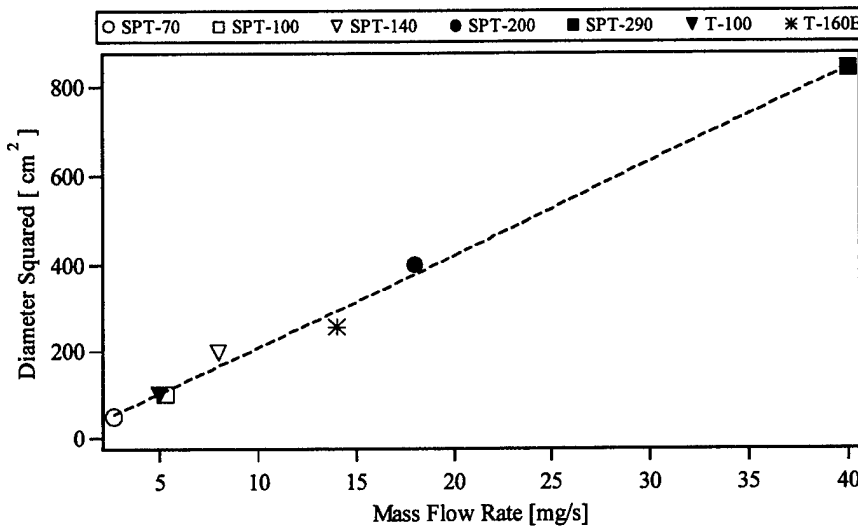


Figure 4.4 Thruster diameter versus mass flow rate.

Having determined the diameter and projected performance levels, Russian empirical design equations presented in a workshop held at MIT in the summer of 1990 were used to calculate the remaining dimensions of the thruster. These dimensions included the discharge channel width and depth, and the front inner and outer pole separation distance. These design equations also provided an estimate of the peak radial magnetic field along the channel centerline. The target performance, thruster dimensions, and magnetic field for the P5 are summarized in Table 4-1.

Specific Impulse	[s]	2200
Thrust	[mN]	283
Efficiency	[%]	61
Mass flow Rate	[mg/s]	13
Diameter	[mm]	170
Channel Width	[mm]	25.4
Channel Depth	[mm]	38.1
Front Pole Separation	[mm]	38.1
Peak Radial Magnetic Field	[G]	280

Table 4-1 Target performance and size characteristics of the P5.

The final step in the design process was to optimize the magnetic circuit using QuickField™ 3.4, a 2.5 dimensional magnetostatic code. Using the dimensions in Table 4-1 and estimating a pole piece thickness of 6.35 mm, a baseline thruster design was generated. The initial pole piece thickness was chosen such that they did not saturate for the flux density needed to produce a 350 G radial magnetic field on channel centerline. A value of 350 G was used to allow for the uncertainty in the flux density calculation. The resulting magnetic field structure for this baseline design is shown in Figure 4.5. The axial profiles of the radial and axial magnetic fields on the discharge chamber centerline are shown in Figure 4.6.

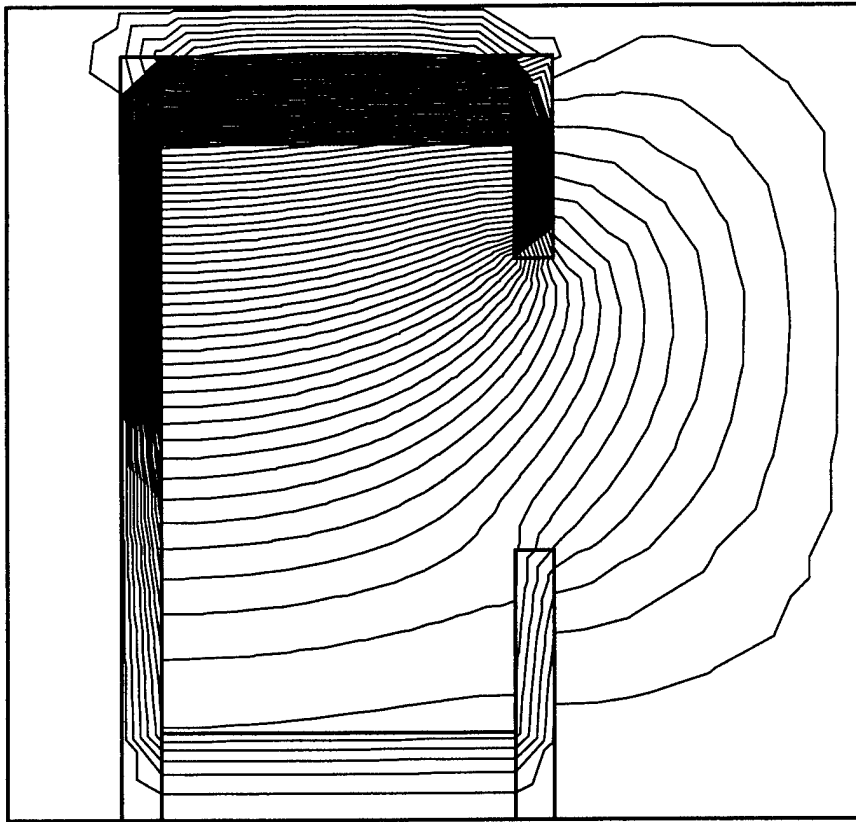


Figure 4.5 Magnetic field structure for baseline P5 design.

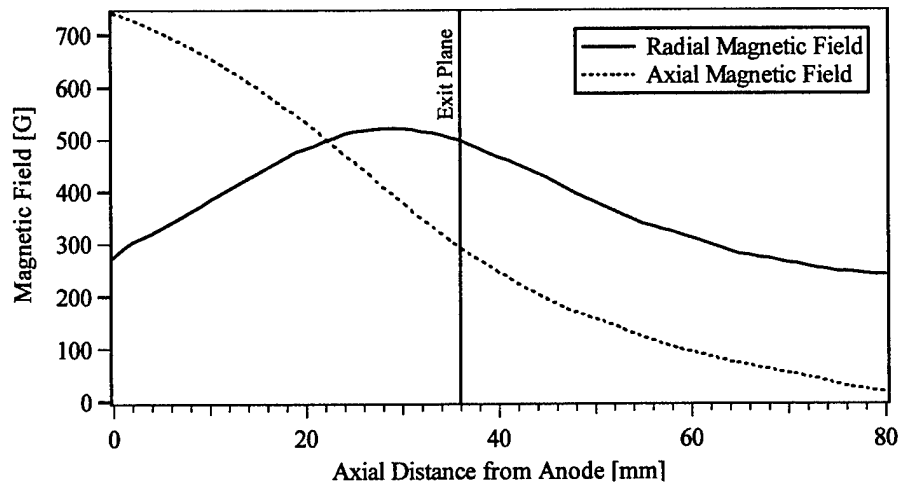


Figure 4.6 Axial profiles of axial and radial magnetic fields on channel centerline for the baseline P5 design.

Recall from the discussion of Hall thruster physics in Chapter 1 that the magnetic field in the discharge channel should be essentially radial in order to trap electrons and retard their motion toward the anode. An equally important criterion, from a plasma stability point-of-view, is that the axial gradient of the radial magnetic field be positive in the channel where ion acceleration occurs. Figure 4.6 shows that this second criterion is met; however, the magnetic field has a substantial axial component, particularly near the anode. This enhances axial electron transport to the anode and lowers the efficiency of the thruster. This large axial field was reduced through the use of magnetic screens. The screens extended axially from the back pole piece to within several millimeters of the front pole pieces, along the outside of the walls of the discharge channel. The screens provided an alternate path for the magnetic field, preferentially reducing the axial component of the field due to their placement and orientation. Many simulations were run, varying the screen position and size, in order to reduce the axial magnetic field component while maintaining the radial component. The final iteration of the magnetic circuit and the resulting field structure is shown in Figure 4.7. The axial profiles of the axial and radial magnetic field on channel centerline are shown in Figure 4.8. These figures show that the screens were very effective in reducing the axial magnetic field component while maintaining a sufficiently large radial component with a positive axial gradient in the channel.

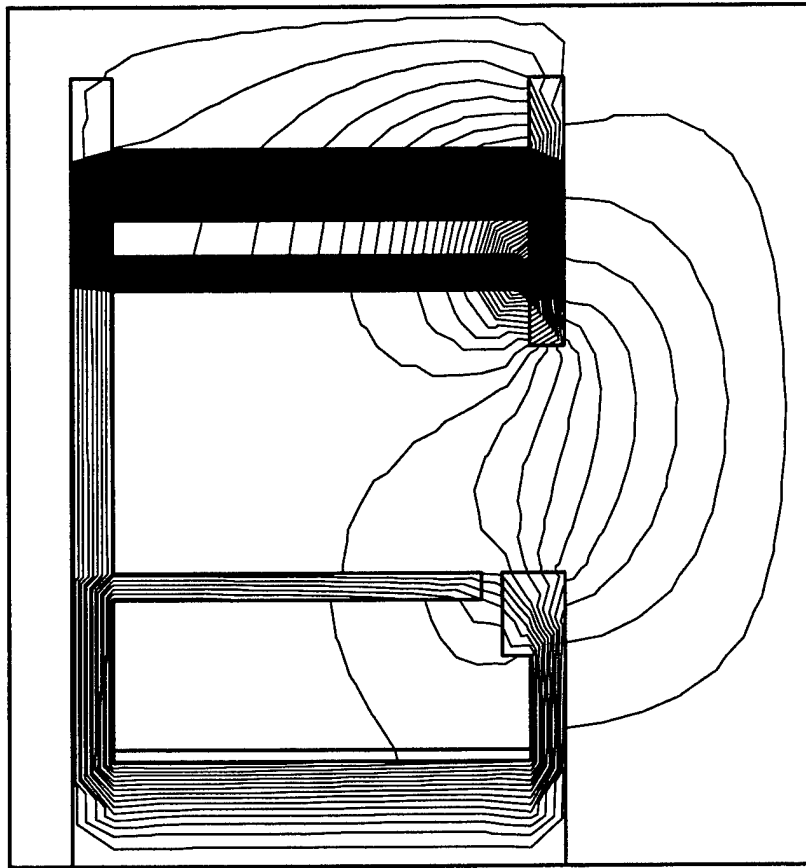


Figure 4.7 Magnetic field structure for the final design of the P5.

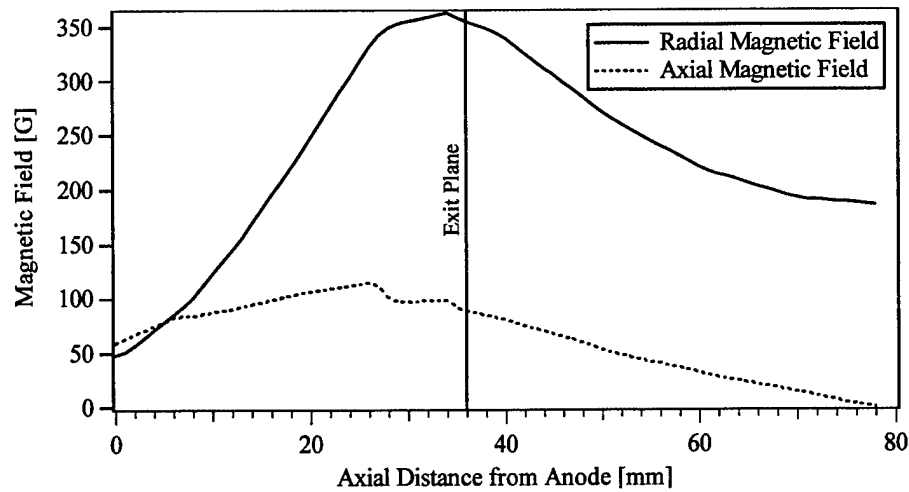


Figure 4.8 Axial profiles of axial and radial magnetic fields on channel centerline for the final design of the P5.

Figure 4.9 is a picture of the fully assembled P5 just prior to its first firing. Figure 4.10 is a cross-section of the P5 showing all the major dimensions. The full set of engineering drawings has been published previously⁶.



Figure 4.9 University of Michigan/AFRL P5 5 kW Hall Thruster. The P5 is an SPT-type thruster incorporating a ceramic discharge channel. The radial magnetic field is provided by eight outer electromagnets in parallel with each other and in series with a single inner electromagnet. Propellant is injected at the rear of the channel through the anode, which also serves as the propellant feed system. Not shown is the LaB₆ cathode used for beam neutralization.

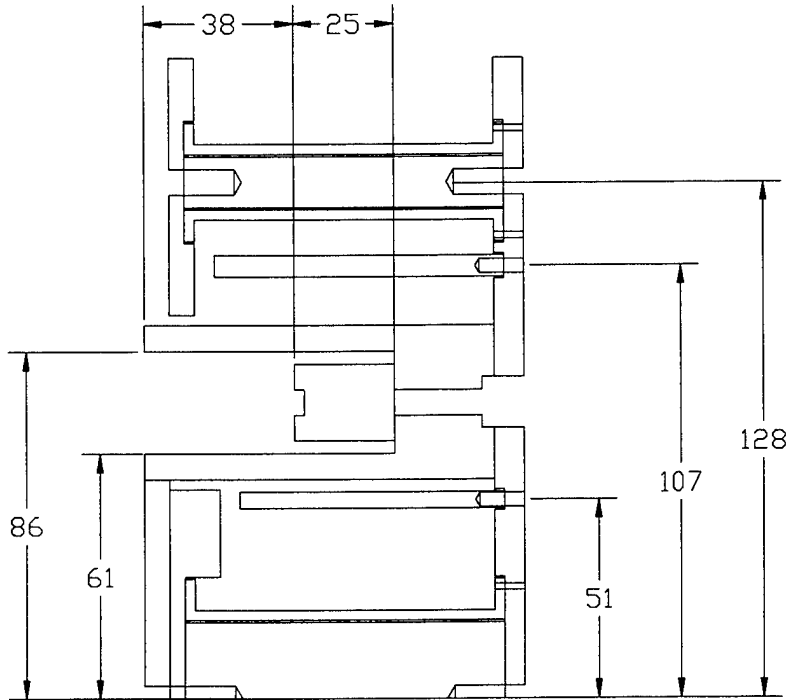


Figure 4.10 Cross section of P5 thruster showing major dimensions. The inner and outer walls of the discharge channel are 61 and 86 mm from centerline, respectively. The channel is 25.4 mm wide and 38.1 mm deep. The inner and outer screens are centered 51 and 107 mm from centerline, respectively.

Several magnetic materials were considered for the magnetic circuit of the P5, each offering slightly different magnetic properties. Of the materials considered, simple cast iron was by far the most cost effective and readily available. It had a large saturation threshold, was easy to machine, was available in plate, bar, and rod form in dimensions sufficiently large for the P5, had a moderately large permeability, and was very inexpensive. All of the pole pieces as well as the electromagnet cores were machined from stock, cast gray iron. The anode/gas distribution system was constructed from non-magnetic 324 stainless steel. Bobbins for the electromagnets were machined from magnetic 430F stainless steel. This allowed the electromagnets to be wound separate from the cores, which were then inserted during final construction of the thruster. The

magnet wire was 18 AWG nickel coated copper with a double layer of fiberglass insulation. The binder used in the fiberglass had a relatively low working temperature, however, the fiberglass had a manufacturer specified temperature limit in excess of 600 °C. The P5 had a single inner coil with 240 windings and eight outer coils each with 120 windings. The discharge chamber was made of an M26 grade boron nitride ceramic manufactured by Carborundum. This particular ceramic was a mixture of 50% boron nitride (BN) and 50% silica (SiO₂). It was chosen for its similarity to commercial thruster discharge channel material and for its excellent resistance to thermal shock.

4.2.2 P5 Performance Validation

Once the P5 was constructed, it was necessary to thoroughly characterize its performance in order to ensure that subsequent research would be relevant to the understanding of commercial thrusters. Toward that end, the thruster was mounted on a NASA Glenn Research Center (GRC) type inverted ballistic pendulum thrust stand. Performance was measured at discharge voltages ranging from 200 V to 500 V, and at discharge currents of 5.5 A, 7.6 A, and 10 A. Anode mass flow rates for these three current values were 58 sccm, 79 sccm, and 105 sccm, respectively. The cathode mass flow rate was kept constant at 6 sccm for all cases. Note that 1 sccm of xenon is equal to 9.76×10^{-2} mg/s.

Figures 4.11 – 4.13 show P5 performance measurements and compare them to various commercial thrusters. Thrust uncertainty was estimated to be +1.2/-8 mN, specific impulse +20/-131 s, and efficiency +1/-8.3%. Specific impulse and efficiency were calculated using both anode and cathode mass flow.

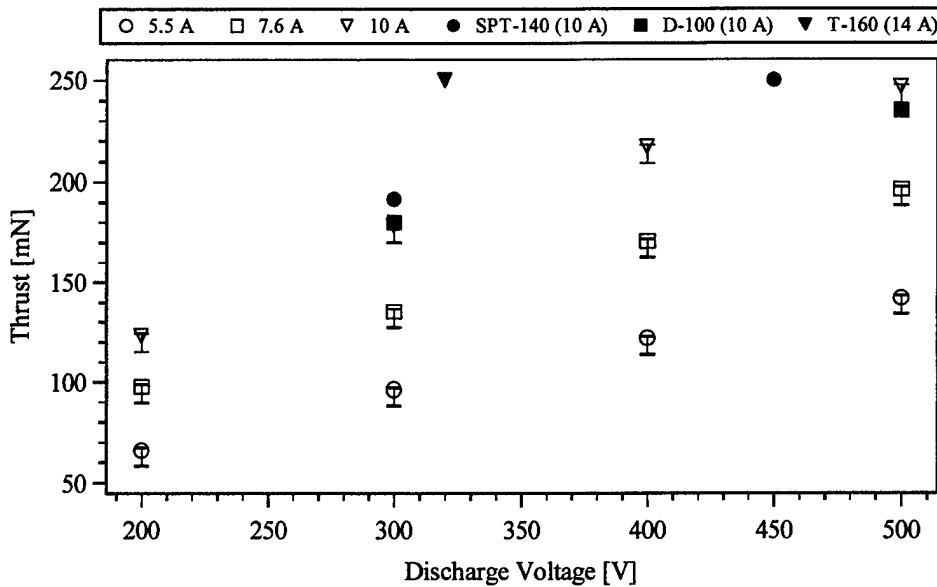


Figure 4.11 Thrust versus discharge voltage. Thrust was measured at 200, 300, 400, and 500 V for current settings: 5.5, 7.6, and 10 A. Thrust measurements from three commercial thrusters of similar power are included for comparison. No pressure corrections were made for any of the data.

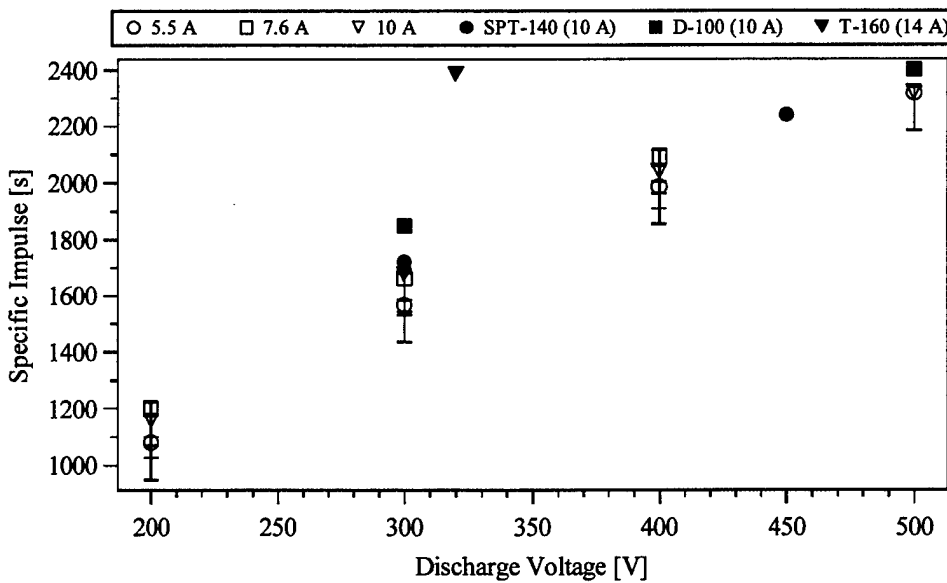


Figure 4.12 Specific impulse versus discharge voltage. Specific impulse was calculated from the thrust measurements of Figure 2.10. Total xenon mass flow rates (anode + cathode) were used. Specific impulse values for three commercial thrusters of similar power are included for comparison. No pressure corrections were made for any of the data.

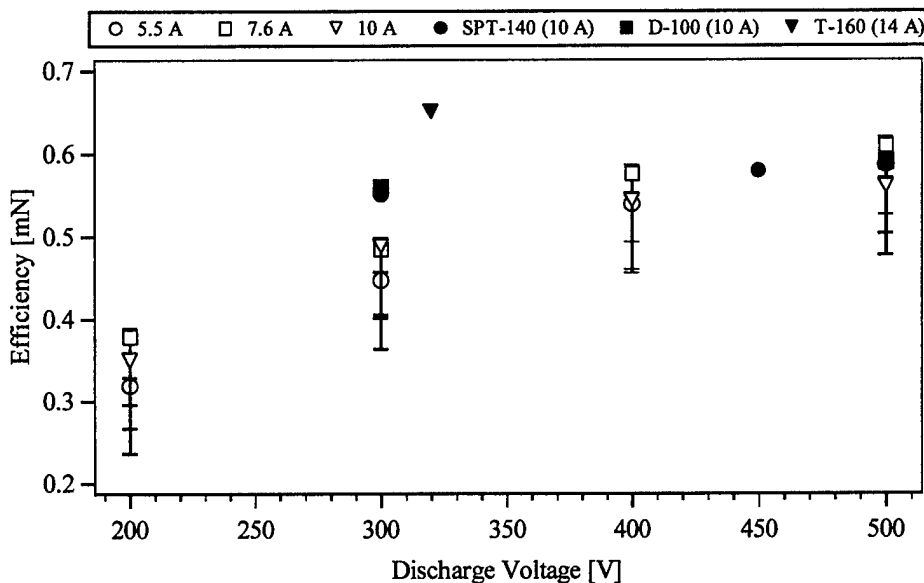


Figure 4.13 Efficiency versus discharge voltage. Efficiency was calculated from the thrust measurements of Figure 2.10. Total xenon mass flow rates (anode + cathode) were used. Efficiency values for three commercial thrusters of similar power are included for comparison. No pressure corrections were made for any of the data.

For each performance parameter, the data for the three current levels are presented as a function of discharge voltage. During testing, tank pressure was 7.3×10^{-6} Torr for a discharge current of 5.5 A (anode mass flow rate of 58 sccm), 9.3×10^{-6} Torr for a discharge current of 7.6 A (79 sccm), and 1.1×10^{-5} Torr for a discharge current of 10 A (105 sccm). These pressures have been corrected for xenon and are an average of readings from two separate ion gauges.

As can be seen from Figures 4.11 – 4.13, performance values for the P5 compare favorably to those of commercial thrusters^{7,8,9}. It should be noted that the SPT-140 was tested at Fakel at pressures ranging from 2.5×10^{-4} to 3.6×10^{-4} Torr, the D-100 was tested at JPL at a pressure of 3×10^{-5} Torr, and the T-160 was tested at NIITP, in Russia, at an unknown pressure. No correction for elevated chamber pressure, which artificially

boosts engine performance due to the backflow of residual vacuum chamber gases, were made for any of these data.

In addition to thrust measurements, ion current density measurements were made in order to determine the amount of plume divergence. Faraday probe measurements were made in a radial sweep, 0.5 m from the thruster exit plane. The Faraday probe had a tungsten coated, stainless steel collector with an area of $4.34 \times 10^{-4} \text{ m}^2$ and a stainless steel guard ring. Both the collector and guard ring were biased at -50 V. Several preliminary measurements were taken at different bias voltages to determine a voltage at which all electrons were repelled. The ion current failed to saturate even at -50 V but the voltage could not be reduced any further without causing arcing between the collector and shield. Faraday probe measurements were taken on a continuous sweep from +70° to -70°, relative to the thruster centerline, at each performance operating condition. The cathode was mounted in the 12 o'clock position on the thruster. Ion current density data are shown in Figures 4.14, 4.15, and 4.16 at discharge currents of 5.5 A, 7.6 A, and 10 A, corresponding to anode mass flow rates of 58 sccm, 79 sccm, and 105 sccm, respectively. Ion current was measured as a voltage drop across a resistor with a Tektronix AM501 op-amp, the output of which went to a Tektronix TDS540 oscilloscope. The estimated uncertainty in the ion current density was $\pm 5\%$. The uncertainty in radial position was $\pm 3^\circ$.

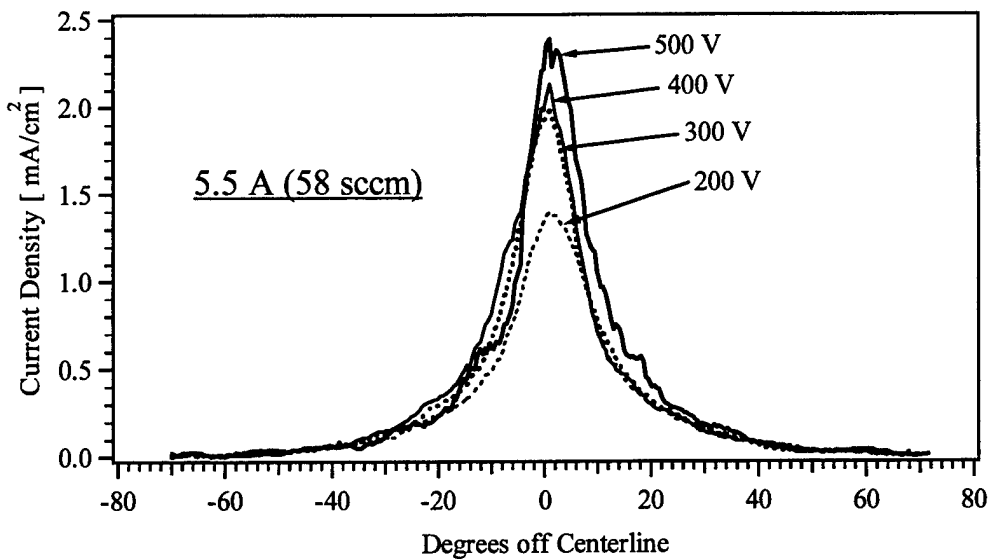


Figure 4.14 P5 ion current density at 58 sccm. The current density on centerline increased with increasing discharge voltage.

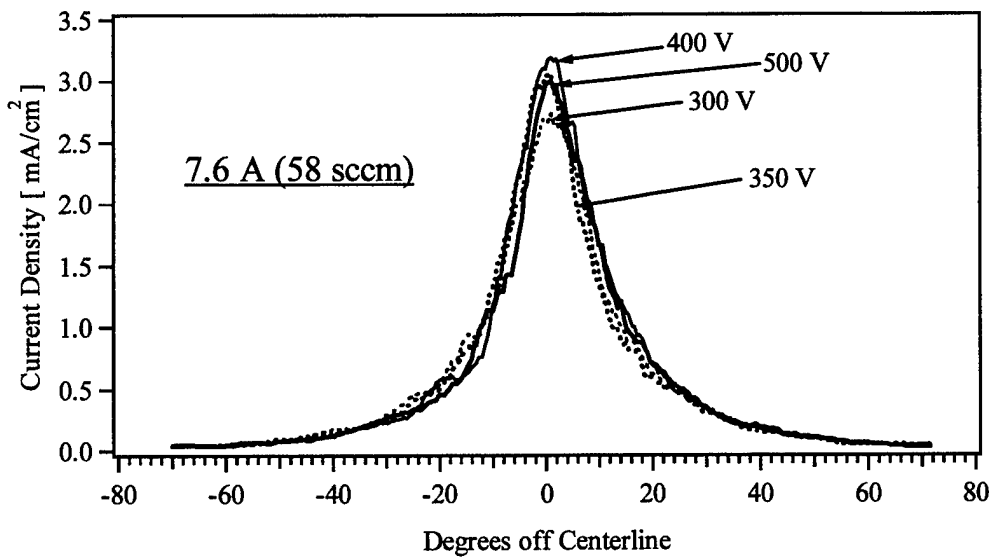


Figure 4.15 P5 ion current density at 79 sccm. Current density on centerline increased with increasing voltage with the exception of the 500 V case, where current density dropped slightly.

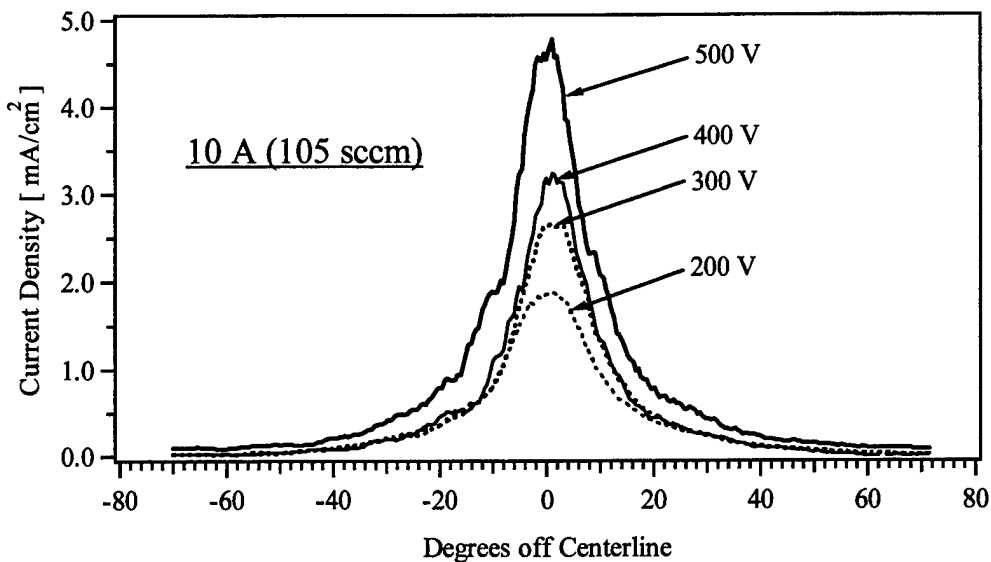


Figure 4.16 P5 ion current density at 105 sccm. As at the lower discharge current settings, current density on centerline increased with increasing discharge voltage. As expected the current density, in general, increased with increasing discharge current.

For all cases, approximately 80% of the total integrated ion current was between $\pm 20^\circ$.

For the SPT-140 at 300 V and 10 A, considering only data between $\pm 70^\circ$, 80% of the total current is contained in a half-angle of $19^\circ 10'$.

Current-Voltage characteristics were determined for the three anode mass flow rates. Voltage was measured using a Tektronix 1000x voltage probe connected to a Tektronix TDS540 oscilloscope. Current was measured using a Hall current sensor connected to the same oscilloscope. The uncertainty of both measurements was dictated by the resolution of the scope and was estimated to be $\pm 4\%$. The results are presented in Figure 4.17. Note that the current peaks at a discharge voltage of approximately 100 V before decreasing and leveling off at a constant value at voltages above 200 V.

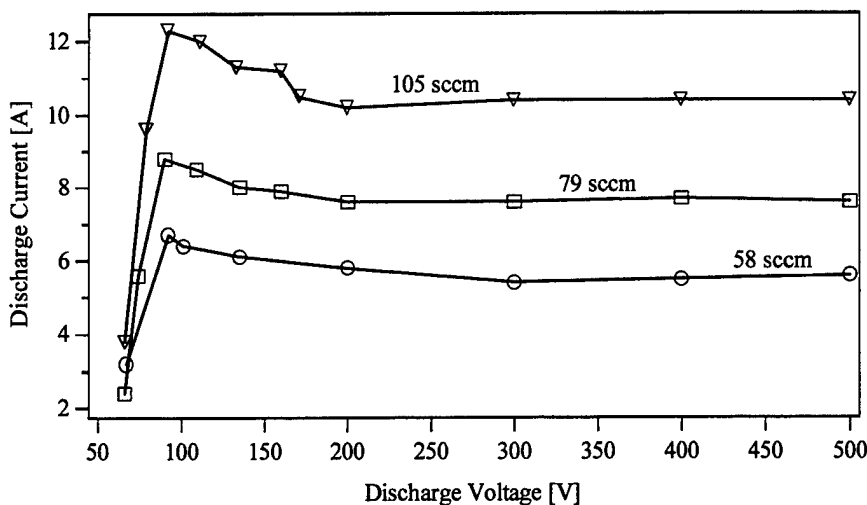


Figure 4.17 P5 current-voltage characteristics. Thruster ignition occurred at approximately 65 V at each flow rate; discharge current increased from its initial condition, reaching a peak at 100 V. Constant current was achieved beyond 200 V.

Time resolved current and voltage traces were recorded with the same set-up described above to show the thruster oscillations. Figure 4.18 shows traces at an operating condition of 487 V and 10.3 A (~ 5 kW).

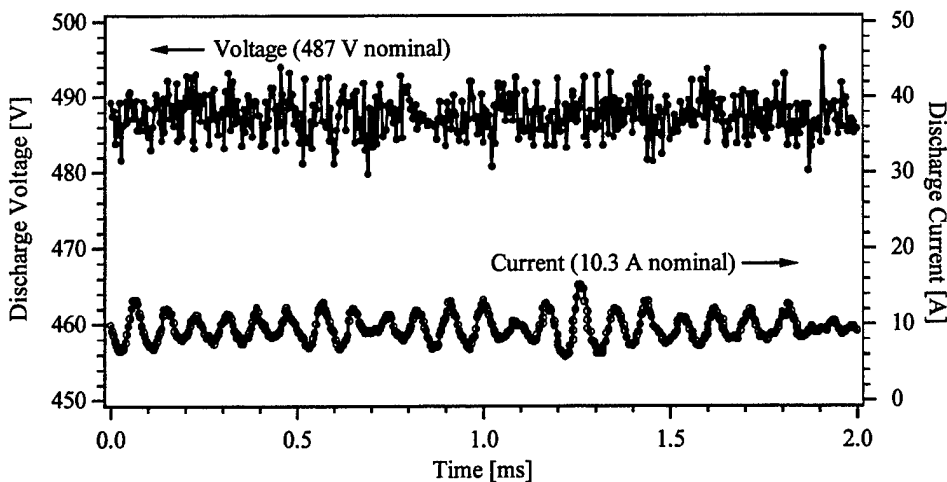


Figure 4.18 P5 current and voltage traces. The thruster operating condition was approximately 5 kW (487 V, 10.3 A). Sampling frequency was 4 μ s. Note the well defined discharge current oscillation characteristic of Hall thrusters; for the P5 the oscillation frequency was 11 kHz.

The thruster shows a very well defined current oscillation with a frequency of 11 kHz. This corresponds to the cycle of ion formation and subsequent depletion, often referred to as the Hall thruster “breathing” mode¹¹. This oscillation frequency agrees well with the characteristic 10–20 kHz oscillations observed in most commercial thrusters.

4.3 High-speed Axial Reciprocating Probe System – (HARP)

In plasmas with highly energetic charged particles, probe material is generally sputtered and/or ablated on very small time scales by the direct flux of these particles. The local plasma temperature and density may then be modified through emission of relatively cool probe material. These perturbations may remain localized near the probe, or may propagate further into the plasma affecting the macroscopic properties of the plasma being interrogated. As time scales increase, probe survival becomes an issue. In the case of Hall thrusters, for measurements downstream of the exit plane, probe survival is not a concern nor does the presence of the probe adversely affect thruster operation. However, within the discharge chamber, plasma temperature and density increase which leads to increased probe heating. Moreover, the presence of an intense Hall current in the acceleration region of the Hall thruster further exacerbates this problem. Probe material ablation then becomes significant and survival times are shortened drastically. Under these conditions, a high speed, reciprocating probe system can reduce the amount of ablated material, allowing for more accurate measurements of local plasma parameters and assuring probe survival.

The need for high-speed probe positioners has existed in other fields for many years. External, pneumatic systems are commonly used, for example, to study edge effects in Tokamaks¹². This type of actuator proved to be infeasible for studying Hall thrusters due to the necessity of positioning the thruster as far from the walls of the vacuum chamber as possible in order to minimize contamination from sputtered material and background gases. This limitation on thruster position required that the actuator be placed inside the chamber thus ruling out pneumatic systems. A second alternative was a conventional belt/pulley or leadscrew-type assembly. These were also ruled out because they were incapable of providing the high acceleration and velocity necessary. It was determined that the best choice was a linear motor assembly providing direct linear motion at very high speed and acceleration. The linear motor selected was an LM210 manufactured by Trilogy. It was a three-phase brushless DC servo motor consisting of a linear, "U"-shaped magnet track and a "T"-shaped coil moving on a set of linear tracks. The only contact between moving parts was through the guide rails, providing very little resistance. The motor employed Sine commutation, using a linear encoder built into the magnet track to provide position feedback for very smooth motion. The linear encoder provided positioning resolution to 5 microns. A Pacific Scientific SC950 digital, brushless servo drive was used to control the motor, which in turn was controlled through a PC via a serial cable. The table was covered by a stainless steel and graphite shroud to protect it from direct impact of high-energy ions and to prevent the motor from being excessively heated, which would lead to performance degradation. One side had a thin slit running the length of the table through which a probe boom extended. Figure 4.19 shows the High-speed Axial Reciprocating Probe (HARP) assembly, protective shroud and the

boom to which an electrostatic probe is attached. Figure 4.20 shows the HARP alignment with respect to the thruster.

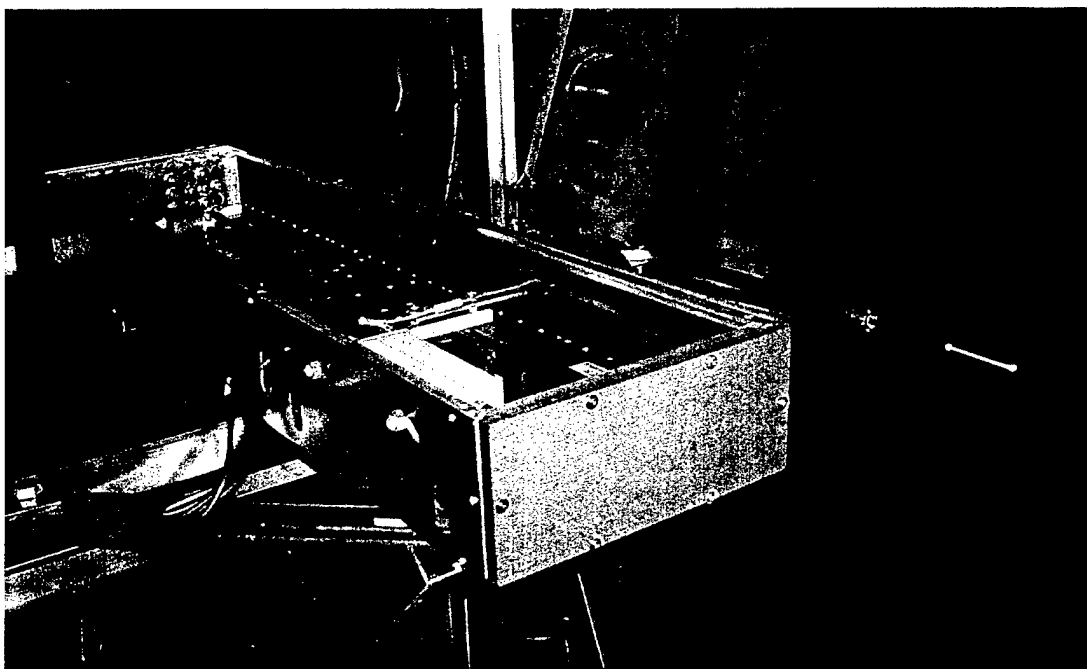
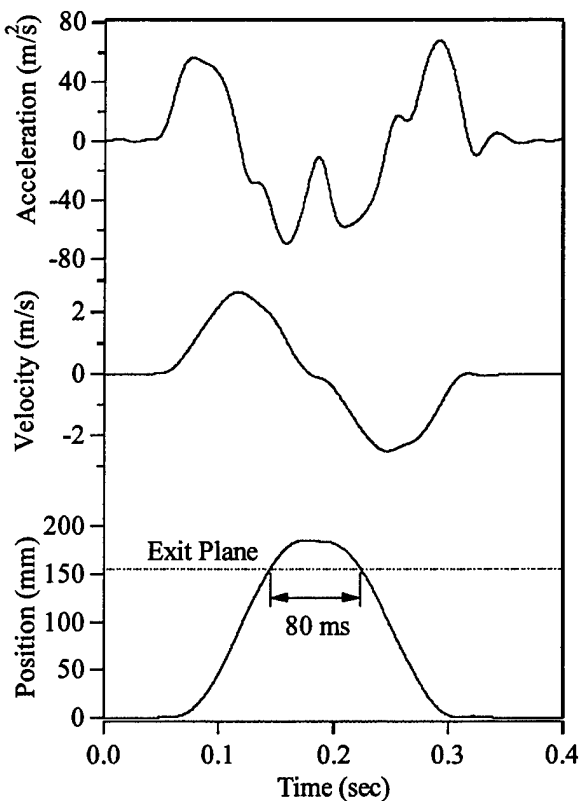


Figure 4.19 High -speed Axial Positioning (HARP) system showing actuator, stainless steel and graphite shroud, and probe boom. The top cover has been removed to show the actuator. The assembly was mounted on the chamber centerline with the probe boom directly downstream of the thruster.

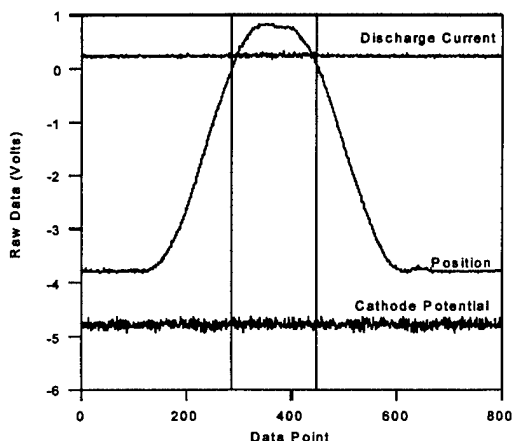


Figure 4.20 HARP system alignment with respect to thruster. The HARP assembly was mounted such that the probe height was coincident with the thruster centerline and its axis was aligned with the thruster axis. The probe started from rest approximately 150 mm downstream of the thruster exit plane, accelerated to a position 10 mm downstream of the anode face, and returned. Data were collected during the entire inward and outward "sweep" of the probe.

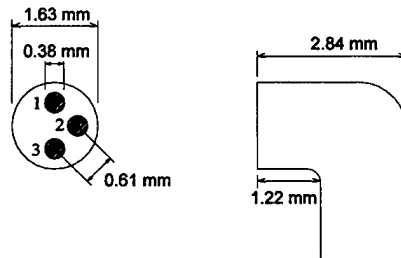
Once assembled, the HARP system's performance was thoroughly characterized to verify its projected performance. Figure 4.21 shows HARP performance, thruster perturbation, and the planar triple probe used to determine perturbation levels. Figure 4.21a is a representative plot of position, velocity and acceleration versus time. From the plot, it can be determined that the total residence time inside the chamber is approximately 80 ms. This time varied slightly from stroke to stroke but always remained under 100 ms, well below the predicted 150 ms ablation time. The plot also shows the maximum velocity, 3 m/s, and acceleration, 6 g's, that the system achieved.



a) Thruster performance



b) Thruster perturbation



c) Planar triple probe

Figure 4.21 Representative HARP system performance and thruster perturbation. The system achieved a maximum speed and acceleration of 3 m/s and 6 g, respectively. Residence time in the discharge channel was less than 100 ms and resulted in no observable perturbation to the discharge current.

Figure 4.21b shows the triple probe (Figure 4.21c) position, discharge current, and cathode potential. From this plot it can be seen that, while the probe was inside the thruster, no observable perturbation to the thruster occurred.

The HARP system provided only the axial positioning of the probes. In order to generate the two-dimensional (2D) mapping inside the discharge channel, the thruster was mounted to a custom built, two-axis positioning stage developed by New England Affiliated Technologies (NEAT). This allowed the thruster to be moved radially between each axial probe sweep. The 2D data collection domain is shown in Figure 4.22.

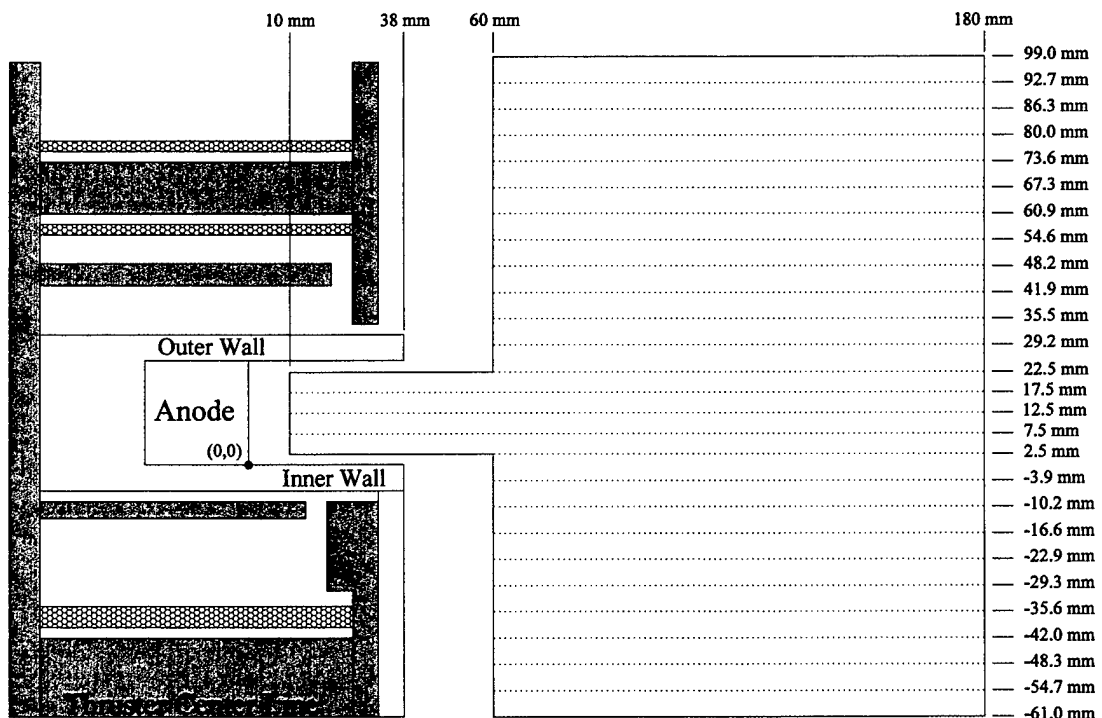


Figure 4.22 Data collection domain. The internal area mapped begins 10 mm downstream of the anode face and extends to 60 mm. Radial, data is collected starting 2.5 mm from the inner wall and ending 2.5 mm from the outer wall. The large external domain extends radially from the thruster centerline to the outer pole piece and 180 mm downstream.

The internal area mapped begins approximately 10 mm from the anode face, extends 2 cm downstream of the exit plane, and comes to within 2.5 mm of the inner and outer walls of the discharge chamber. Data obtained in this internal area will be the main focus of subsequent chapters. The larger area extends axially from 2 to 14 cm downstream of the exit plane and radially from the thruster centerline to the outer edge of the outer front pole piece. The large gap in front of the anode and the face of the thruster is due to limitations of the HARP. The HARP experienced occasional overshooting of its target position and as a result a large safety margin was required to avoid hitting the thruster and destroying the probe.

4.4 Probes

The preceding chapters have described efforts to understand and avoid thruster perturbations while using electrostatic probes inside the Hall thruster. This section describes in detail the probes that were used to measure internal plasma parameters in the P5. In addition, the Hall probe used to map vacuum radial and magnetic fields will be discussed.

4.4.1 Emissive Probe

Inside the Hall thruster, the flux of high-energy particles sputters and/or heats electrostatic probe material causing it to ablate. Local plasma characteristics are then affected through emission of relatively cool probe material. These local variations propagate through the plasma, perturbing thruster operation, making it imperative that the

residence time of any diagnostic inside the Hall thruster be minimized. It is for this reason that the floating emissive probe was chosen to make plasma potential measurements inside the P5. The floating emissive probe provides a direct measure of plasma potential without the requirement of a voltage sweep or data reduction operations, as is the case for both the standard emissive probe and the Langmuir (electron-collection) probe.

Figure 4.23 shows a schematic of the emissive probe construction. The emitting portion of the probe was a filament made from 0.127 mm diameter tungsten wire. The ends of this filament were inserted approximately 76 mm down a 152 mm length of double bore alumina tubing along with 30 AWG copper wire leads. The alumina insulator had an outer diameter of 1.5 mm.

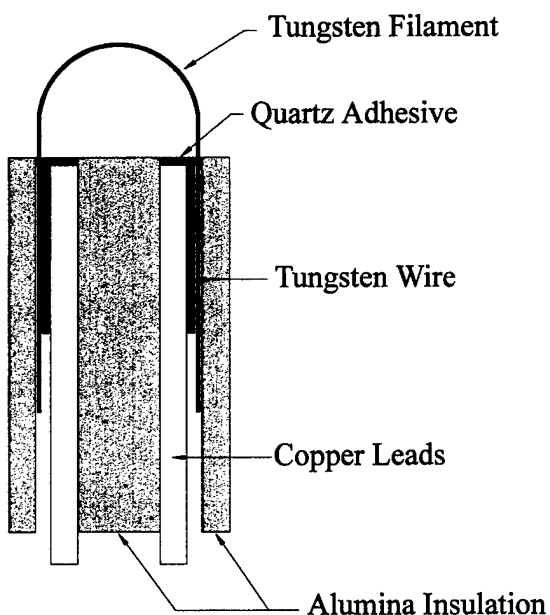


Figure 4.23 Schematic of the emissive probe. The probe was constructed using 0.127 mm diameter tungsten wire for the emitting filament, insulated by 1.5 mm diameter alumina tubing.

Once the tungsten filament and copper leads were in place additional, shorter lengths of tungsten wire were inserted into the alumina tubing to provide a tight fit and guarantee good contact between the tungsten and copper wires. The width and height of the filament when mounted in the alumina insulator was approximately 1 mm. The probe was oriented such that the alumina insulator was aligned with the axis of the thruster and the plane of the loop of the probe filament was perpendicular to the thruster radial direction.

While the floating emissive probe offers many advantages, there are limitations that must be taken into account. Specifically, the presence of a magnetic field and large density gradients may result in space-charge effects, causing significant variation between the potential of the emitting probe and the actual plasma potential. In the case of the P5, the magnetic field is sufficiently weak that space-charge effects can be avoided by sizing the probe such that the probe wire diameter is much less than the electron gyroradius. Hershkowitz¹³ indicated this condition as shown in Equation 4-2

$$B \ll \frac{4.8(T_{eV})^{1/2}}{d} \quad \text{Eq. 4-2}$$

where T_{eV} is the electron temperature in eV, d is the emitting filament diameter in cm and B is the magnetic field in Gauss. The emissive probe used in the P5 had a diameter of 0.0127 cm. The electron temperature varied between 10 and 40 eV in the channel

(based on double Langmuir probe measurements made in the P5), with higher values generally corresponding to areas of large magnetic fields. Using the minimum electron temperature, the worst case condition is $B \ll 1200$ G. The magnetic field in the P5 peaked at 200 G, indicating that space-charge effects were negligible.

Figure 4.24 shows a schematic of the probe circuit.

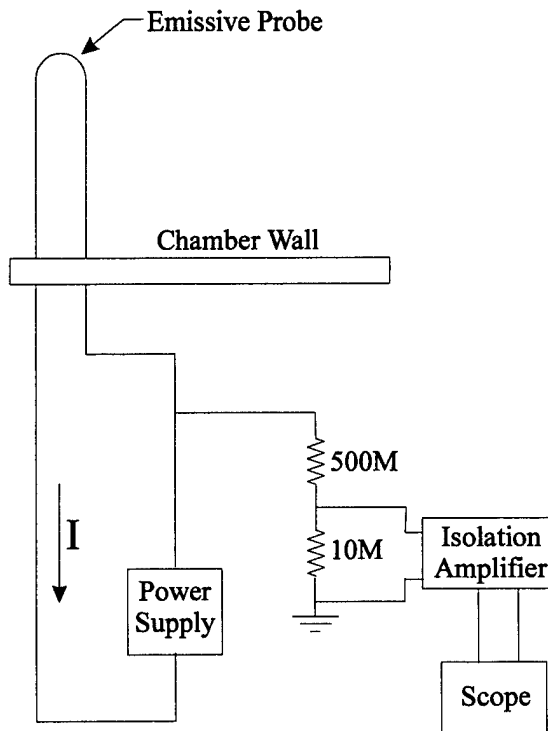


Figure 4.24 Floating emissive probe circuit. Current is applied to the electrode (generally small gauge tungsten wire), heating it to the point where electrons are thermionically emitted. When heated sufficiently, the emitted electrons essentially neutralize the sheath. At this point, the probe will float at the local plasma potential.

The theory of the floating emissive probe is well established and relatively straight forward to implement¹⁴. Current is applied to the electrode (generally small gauge tungsten wire), heating it to the point where electrons are thermionically emitted. When

heated sufficiently, the emitted electrons essentially neutralize the sheath. At this point, the probe will float at the local plasma potential. The circuit consisted of the emissive probe, a floating power supply capable of supplying enough current to heat the filament (4 – 7 A), and a voltage meter. The sampling rate of the oscilloscope was dictated by the total transit time of the probe and was set at 1 ms. This resulted in aliasing of the signal so that high frequency oscillations in the 10–30 kHz range, typical of the Hall thruster, could not be resolved. Therefore, the data presented constitutes a “time-averaged” plasma potential. The correct heater current was determined by taking several preliminary sweeps and observing when the probe potential saturated. Figure 4.25 shows the difference between sufficient and insufficient heater current.

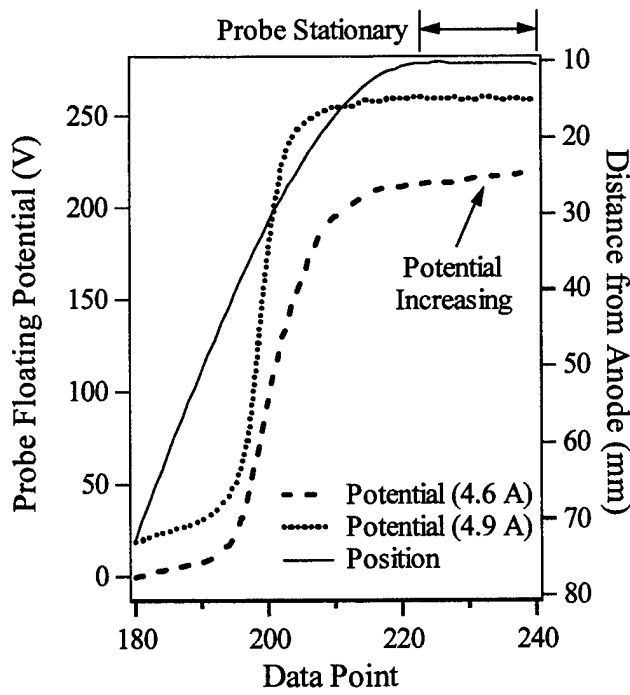


Figure 4.25 Illustration of potential change with and without sufficient heater current applied to filament.

As stated previously, electrostatic probes are heated considerably by the flux of high-energy particles in the discharge channel of the Hall thruster. One consequence of this effect is that when the emissive probe is inserted into the thruster with insufficient power to reach the saturation emissive current, the plasma provides additional filament heating and the probe potential continues to increase when the probe is stationary. By increasing the heater current on each subsequent sweep and observing when the potential remained constant while probe position was fixed inside the thruster, a sufficient heater current was determined.

A floating power supply provided current to heat the filament to the point where it was thermionically emitting sufficient electrons to neutralize the sheath. At this point, the probe was theoretically floating at the local plasma potential. The power supply was not perfectly isolated from ground, however, which introduced the possibility of significant leakage current when the circuit floated at high potential. This could result in the circuit floating at a potential less than the true potential. To determine the effect of this leakage current, the measured plasma potential near the anode was compared to the true anode potential. The excellent agreement between the two (< 2 V difference) indicated that the effect of leakage current was negligible. The heater current varied between tests due to slight variations in individual probe designs, ranging between 4.5 A and 6.0 A. The probe potential was divided and sent through an isolation amplifier capable of floating its input as high as 2500 V. Because the heater current remained on during the duration of the measurement, a voltage drop existed across the tungsten filament. This value remained below 5 V for each data sweep, and contributed an estimated uncertainty of

approximately ± 2.5 V. The fragility of the emissive probe when swept at high speed made it very difficult to perform multiple measurements. However, two sets of data were collected for each axial sweep (during insertion and removal of the probe) providing an estimate of the reproducibility of the data. Analysis of both sets of data indicated an average standard deviation of less than 4%. An analysis by Hargus¹⁵ of the change in apparent potential due to the presence of the heater current indicated an uncertainty of approximately $-3/+6$ V. Coaxial cables were used for the entire circuit, both inside and outside the chamber, to reduce noise. In addition, isolated feedthroughs allowed every component of the circuit to be grounded at a single point to minimize noise pick-up through ground loops.

4.4.2 Double Langmuir Probe

Langmuir probes provide one of the best means for making spatially resolved measurements of electron temperature and number density in plasmas. While the basic probe theory in an ideal plasma is quite simple to implement, the plasma characteristics in the discharge channel of the Hall thruster create significant difficulties in collecting and interpreting probe data. Therefore, great care must be taken in choosing the shape, size, and orientation of the probe due to the presence of streaming ions, high plasma potentials and potential gradients, and large radial magnetic fields. Fortunately, many of these effects can be made negligible with proper consideration.

Langmuir probes are generally classified according to two parameters: the number and the shape of the electrodes. Planar, cylindrical, and spherical probes with one to four

electrodes have been used in a wide range of plasmas and the theory of their operation is extensive. Spherical probes were immediately rejected for this experiment because of the difficulty in their construction, particularly of sizes small enough to provide good spatial resolution inside the thruster. Both planar and cylindrical probes are easily constructed at very small sizes and can be configured as single, double or triple probes.

Recalling that the probe is inserted and removed from the thruster in approximately 100 ms, the triple probe is very attractive because it does not require a voltage sweep¹⁶. It needs only a fixed voltage between two electrodes while the third floats. However, in this case size again becomes an issue. Because of the wide range of parameters in the thruster, the Debye length can grow considerably, necessitating a large separation between electrodes. This leads to a large overall probe size that can severely perturb the thruster and reduces the resolution of the measurement.

Of the single and double probe configurations, the double probe provides several advantages in the Hall thruster. The single probe potential is biased with respect to some fixed reference; generally electrical or chamber ground. The bias range starts highly negative (ion saturation) and extends to the plasma potential (electron saturation). In the Hall thruster, plasma potential ranges from tens of volts in the near-field region to several hundreds of volts (discharge voltage) near the anode¹⁷. This greatly complicates the experimental setup as the sweep voltage range is quite large and changes dramatically throughout the discharge chamber. This need to bias the probe at or beyond the plasma potential also creates serious perturbation problems. The electron saturation current can

be several orders of magnitude larger than the ion saturation current and drawing this much current from the plasma can cause serious perturbations to thruster operation.

The double probe eliminates most of the problems associated with the single probe. A voltage sweep is still required but it is between two electrodes which float as a whole, one above the floating potential and one below. The electron current to a given electrode is limited by the ion saturation current of the other electrode and, because the probe is floating, the net current to the probe is zero. This results in very little perturbation to the plasma. Also, because the current is limited to the ion saturation current, a much smaller voltage sweep range is required.

The decision to use a double probe dictated the final choice of a cylindrical geometry. As stated above, the current collected by a double probe electrode is limited to the ion saturation current. For the temperatures and number densities expected (\sim 10-50 eV, $1-5 \times 10^{18} \text{ m}^{-3}$), this is on the order of several 10-100 microamps, which can be quite difficult to measure accurately. This is particularly difficult in chambers as large as the LVTF because the large line lengths between the probe and external data acquisition system introduce a large amount of capacitance¹⁸. The current magnitude, of course, depends on the probe size as well. Therefore, the cylindrical probe was chosen to maximize the ion saturation current.

The magnetic field in the thruster influences probe measurements because it constrains the motion of the charged particles. For the conditions in the P5, the ions are essentially

unmagnetized based on their gyroradii being much larger than the probe dimensions. The electrons, on the other hand, have much smaller gyroradii owing to their much smaller mass. The magnetic field effect manifests itself in two ways; it reduces the electron saturation current¹⁹ and causes anisotropy of the electron energy distribution function (EEDF)²⁰. Reduction of the electron saturation current causes the electron number density to be substantially underpredicted. This is not an issue with the double probe as number density is inferred from the ion saturation current. Electron temperature can still be determined by standard theory from the slope of the I-V characteristic.

The question of EEDF anisotropy has been investigated by Passoth¹⁹ and was shown to depend not on the magnetic field (B) itself but on the ratio B/p_o , where p_o is the pressure in the containment vessel. Higher pressure effectively increases the number of electron-neutral collisions, randomizing electron motion and reducing any anisotropy induced by the presence of a magnetic field. It has been shown experimentally by Aikawa²⁰ that, at a vessel pressure of 1.2×10^{-4} Torr, anisotropy of the EEDF was negligible for $B \leq 300$ G, or $B/p_o \leq 2.5 \times 10^6$ G/Torr. In the P5, B has a maximum of 200 G and the pressure in the discharge chamber is estimated to be approximately 1×10^{-3} Torr. This yields a value of $B/p_o \leq 2 \times 10^5$ G/Torr for these experiments, an order of magnitude less than the threshold established by Aikawa. Therefore, there was expected to be no substantial anisotropy in the EEDF in this experiment.

The final consideration in probe design was the orientation of the electrode axis. If the probe axis is aligned with the thruster axis, the electrode could see a potential gradient

along its length where the electric field is large. This distorts the probe characteristic, introducing a rounding of the “knee” at the space potential¹⁹. However, as previously noted, the double probe does not rely on measuring the electron saturation current so this effect is negligible. Alignment with the thruster axis also aligns the axis of the probe with the flowing ions and introduces the problem of “end effects”²¹. “End effects” can be minimized by making the probe length to diameter ratio sufficiently large. This alignment has the added benefit of orienting the probe perpendicular to the radial magnetic field, which further minimizes the effect of the magnetic field on electron collection¹⁹. Conversely, by orienting the probe axis perpendicular to the flow, the high-speed ions distort the electron sheath and the electron temperature can no longer be determined by standard theory²¹.

In summary, it was determined that a double cylindrical probe aligned with the axis of the thruster essentially eliminates the problem of the magnetic field effect on electron collection. Several probes were built and tested and the various parameters adjusted as more experience was gained. The final iteration is presented in Figure 4.26.

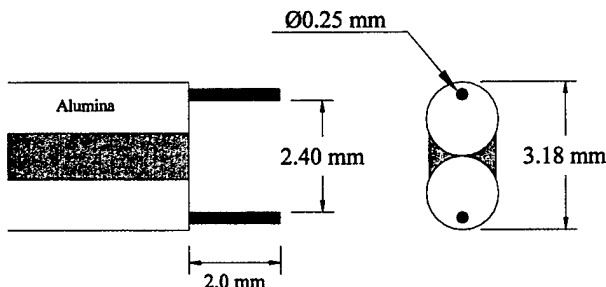


Figure 4.26 The double cylindrical floating probe consisted of two tungsten electrodes 0.25 mm in diameter, 2 mm long, and separated by a distance of 2.4 mm. The alumina insulator had a width of 3.18 mm.

Each tungsten electrode had a diameter of 0.25 mm and a length of 2.0 mm. The electrodes were insulated from each other and the plasma by alumina tubing and cemented in place with an alumina adhesive. The dimensions were chosen to balance the need for sufficiently large collected currents and length to diameter ratios (larger electrodes), with the need for sufficient resolution and minimal thruster perturbation (smaller electrodes).

As mentioned earlier, one difficulty with the double probe is that it requires a voltage sweep to determine the I-V characteristic. Under less demanding circumstances, this can be accomplished with a bi-polar power supply and function generator. The difficulty with this type of setup is that the probe, and hence any required circuitry, is required to float. The floating potential can swing several hundred volts, in a matter of milliseconds, as the probe is moved into the channel. This creates a problem for all of the electronics and can result in significant errors in the measured current if there is any appreciable stray capacitance in the circuit. This problem was minimized by careful attention to the circuit construction to minimize stray capacitance and by using batteries to supply the bias voltage. A potentiometer was attached to the battery output so that the bias could be adjusted. The probe and circuit were isolated from the data collection equipment by two AD210 isolation amplifiers. Figure 4.27 shows the probe circuit.

For each fixed bias point, the probe current and voltage were measured at each spatial location in the 2D domain of Figure 4.22. The resulting data were then reassembled to get a single current-voltage trace at each point in the domain. Figure 4.28 shows a

representative double probe trace 32 mm from the anode (6 mm inside the discharge channel) at the center of the channel for a thruster operating condition of 300 V and 10 A.

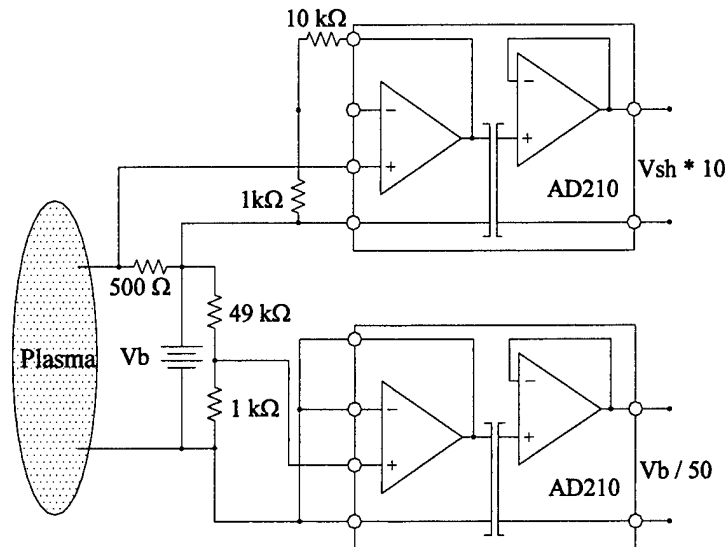


Figure 4.27 Floating double probe circuit. Batteries supplied the bias between the electrodes and a pair of high common mode voltage, isolation amplifiers isolated the circuit from the data acquisition hardware.

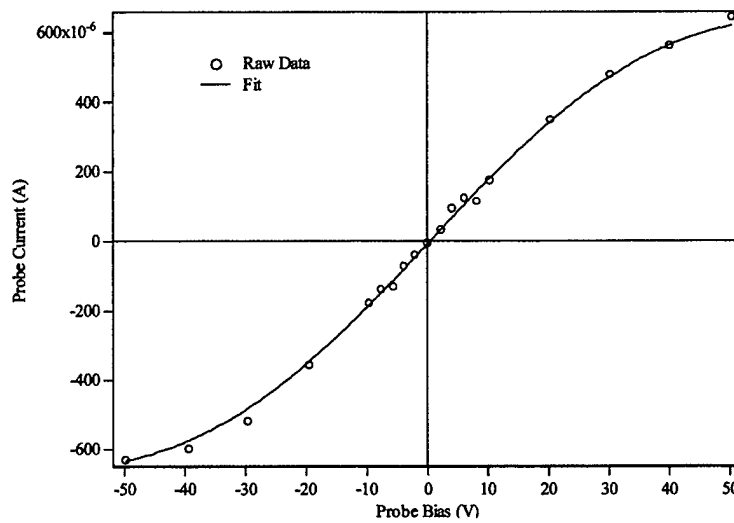


Figure 4.28 Representative probe characteristic at an axial location of 32 mm and a radial position of 12.5 mm (discharge chamber centerline).

In order to obtain the electron temperature and ion number density, the data were fit to the theoretical current-voltage expression for a symmetric double probe¹⁸.

$$I = I_{sat} \cdot \tanh\left(\frac{\phi}{2T_{ev}}\right) + A_1 \cdot \phi + A_2 \quad \text{Eq. 4-3}$$

In Equation 4-3, T_{ev} is the electron temperature in eV, I_{sat} is the ion saturation current to either probe, the parameter A_1 accounts for sheath expansion in the ion saturation region, and the parameter A_2 reflects any offset current due to stray capacitance¹⁸. The scientific graphing package Igor was used to fit this equation to the experimental data using a Levenberg-Marquardt method. Ion number density was then calculated from Equation 4-4, using the Bohm²¹ approximation for ion velocity.

$$n_i = \frac{I_{sat}}{A_s (qZ_i)^{3/2}} \left(\frac{M_i}{T_{ev}} \right)^{1/2} \quad \text{Eq. 4-4}$$

Here, A_s is the ion collection area and is initially considered to be equal to the probe surface area. In reality, the true collection area depends on the thickness of the sheath surrounding the probe, which is determined through an iterative process. Having calculated the temperature and initial number density, the sheath thickness is calculated according to Equation 4-5²²:

$$\delta = 1.02 \lambda_D \left[\left(\frac{1}{2} \ln \left(\frac{m}{M} \right) \right)^{1/2} - \frac{1}{\sqrt{2}} \right]^{1/2} \left[\left(\frac{1}{2} \ln \left(\frac{m}{M} \right) \right)^{1/2} + \sqrt{2} \right] \quad \text{Eq. 4-5}$$

where λ_D is the Debye shielding length for electrons. It follows that the sheath area is then

$$A_s = A_p \left(1 + \frac{\delta}{r} \right) \quad \text{Eq. 4-6}$$

where A_s is the area of the sheath, A_p is the area of the probe, and r is the radius of the probe. With the corrected area for the sheath, the number density is re-calculated. This process is repeated until the number density converges to a final solution.

The above analysis assumes that the “end effects” are negligible based on the dimensions and orientation of the probe electrodes. Using the plasma potential measurements from the emissive probe, the axial ion velocity can be estimated and the effect of the directed ion flux to the tip of the probe included. This is accomplished by assuming quasi-neutral ($n_i = n_e$), steady, one-dimensional flow in the discharge channel. Thus the continuity equations for ions and neutrals can be written as:

$$\nabla \cdot (n_i \vec{V}_i) = \kappa(T_{ev}) n_i n_n \quad \text{Eq. 4-7}$$

$$\nabla \cdot (n_n \vec{V}_n) = -\kappa(T_{ev}) n_i n_n \quad \text{Eq. 4-8}$$

and the momentum equations as:

$$\nabla \cdot (n_i \vec{V}_i \vec{V}_i) = \frac{qE_y n_i}{M} + \kappa(T_{ev}) n_i n_n \vec{V}_i \quad \text{Eq. 4-9}$$

$$\nabla \cdot (n_n \vec{V}_n \vec{V}_n) = -\kappa(T_{ev}) n_i n_n \vec{V}_n \quad \text{Eq. 4-10}$$

Combining the above equations, and using a forward differencing discretization, the set is reduced to two equations:

$$n_i V_i|_k + n_n V_n|_k = n_i V_i|_{k+1} + n_n V_n|_{k+1} \quad \text{Eq. 4-11}$$

$$\frac{n_i V_i^2|_{k+1} - n_i V_i^2|_k}{\Delta y} + \frac{n_n V_n^2|_{k+1} + n_n V_n^2|_k}{\Delta y} = \frac{qE_y}{M} \frac{1}{2} (n_i|_{k+1} + n_i|_k) \quad \text{Eq. 4-12}$$

In Equations 4-11 and 4-12, n_i and E_y are known quantities, as are the initial conditions at the rear of the channel. V_i and n_n are calculated by stepping sequentially through each axial position.

Once the ion velocity has been estimated, the ion number density can be re-calculated taking into account the flux of ions to the probe tip. The area used for this portion of the

collected ion current, A_d , includes the probe tip area as well as the portion of the sheath in which entering ions are collected before they bypass the electrode:

$$A_d = \pi \left(r + \frac{Z^{1/2} l}{V_i} \left(\frac{T_{ev}}{M} \right)^{1/2} \right)^2 \quad \text{Eq. 4-13}$$

$$n_i = \frac{I_{sat}}{A_s (qZ)^{3/2} \left(\frac{T_{ev}}{M} \right)^{1/2} + qZV_i A_d} \quad \text{Eq. 4-14}$$

Combining this with the sheath calculation, the ion number density calculation can be iterated until it converges to a final solution.

4.4.3 Hall Current Probe

The Hall current is an important feature of the Hall thruster, although its role in thruster operation is far from understood. This current was measured using a floating double probe with a planar electrode oriented in the azimuthal direction. The second electrode was a large cylinder with its axis aligned with the thruster radius. This enabled the collection of a large ion saturation current (by the cylindrical probe) causing the planar electrode to be biased well into the electron collection region. By reversing the magnetic field, and hence the electron drift direction, the electron current was measured with and without the azimuthal component, the difference being the Hall current. Figure 4.29 shows the Hall current probe configuration and electrode orientation.

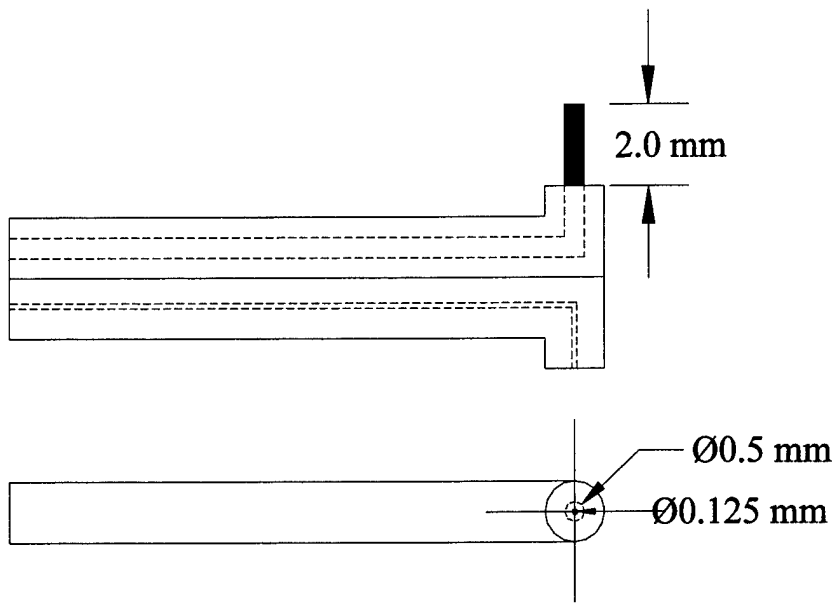


Figure 4.29 Hall current probe. The planar electrode was 0.125 mm in diameter while the cylindrical electrode had a diameter of 0.5 mm and a length of 2 mm.

4.4.4 Magnetic Field Probe

The magnetic field structure inside the P5 was measured using a Hall sensor. Benchtop magnetic field measurements were made using a commercial system manufactured by F. W. Bell. The system consisted of a Hall sensor connected to a Gaussmeter, which provided a fixed current signal and measured the resulting voltage drop across the output terminals of the sensor in the presence of a magnetic field. The measured voltage was then converted to its corresponding magnetic field magnitude using the manufacturer supplied, NIST traceable, calibration factor. The sensor itself was mounted to a two-axis positioning system to allow two-dimensional mapping of the radial and axial magnetic field magnitude in the discharge channel of the P5.

References for Chapter 4

- ¹ Dushman, S., *Scientific Foundations of Vacuum Technique*, Vol. 4, John Wiley & Sons, Inc., New York, 1958.
- ² Manzella, D.H., et al., "Performance Evaluation of the SPT-140," IEPC 97-059, 25th International Electric Propulsion Conference, Cleveland, OH, August 1997.
- ³ Sankovic, J.M., Haag, T.W., Manzella, D.H., "Performance Evaluation of a 4.5 kW SPT Thruster," IEPC 95-030, 24th International Electric Propulsion Conference, Moscow, Russia, September 1995.
- ⁴ Tverdokhlebov, S.O., and Garkusha, V.I., "High-Voltage Mode of a TAL Thruster Operation," IEPC 97-023, 25th International Electric Propulsion Conference, Cleveland, OH, August 1997.
- ⁵ Maslenikov, N.A., Russian Electric Propulsion Seminar, Massachusetts Institute of Technology, 1991.
- ⁶ Gulczinski, F.S., *Examination of the Structure and Evolution of Ion Energy Properties of a 5 kW Class Laboratory Hall Effect Thruster at Various Operational Conditions*, Ph.D. Thesis, University of Michigan Department of Aerospace Engineering, University Microfilms International, 1999.
- ⁷ Arkhipov, B., et al., "Extending the Range of SPT Operation: Development status of 300 and 4500 W Thrusters," AIAA 96-2708, 32nd Joint Propulsion Conference, July 1996.
- ⁸ Garner, C.E., et al., "Evaluation of a 4.5 kW D-100 Thruster with Anode Layer," AIAA 96-2967, 32nd Joint Propulsion Conference, July 1996.
- ⁹ Petrosov, V.A., et al., "Investigation 4.5 kW High Efficiency Hall type t-160 Electric Thruster," IEPC 95-03, 24th International Electric Propulsion Conference, September 1995.
- ¹⁰ Fife, J.M., Hargus, W.A., Jaworske, D.A., Sarmiento, C., Mason, L., Jankovsky, R., Snyder, J.S., Malone, S., Haas, J.M., Gallimore, A.D., "Spacecraft Interaction Test results of the High Performance Hall System SPT-140," AIAA-2000-3521, 36th AIAA / ASME / SAE / ASEE Joint Propulsion Conference, Huntsville, AL, July 16-19, 2000.
- ¹¹ Koo, J., Boyd, I., Haas, J., Gallimore, A., "Computation of the Internal Flow of a 2kW-Class Hall Thruster," to be presented at the 37th AIAA/ASME/SAE/ASEE Joint Propulsion Conference Salt Lake City, Utah, July, 2001.

¹² Boedo, J., Gray, D., Chousal, L., Conn, R., "Fast Scanning Probe for Tokamak Plasmas," *Review of Scientific Instruments*, Vol. 69, No. 9, July 1998, p. 2663.

¹³ Hershkowitz, N., Cho, M., "Measurement of Plasma Potential Using Collecting and Emitting Probes," *Journal of Vacuum Science & Technology A*, Vol. 6, No. 3, May 1988, p.2054.

¹⁴ Kemp R.F., Sellen J.M. Jr., "Plasma Potential Measurements by Electron Emissive Probes," *Review of Scientific Instruments*, Vol. 37, No. 4, April 1966, p. 455.

¹⁵ Hargus, W.A., Cappelli, M.A., "Interior and Exterior Laser-Induced Fluorescence and Plasma Potential Measurements on a Laboratory Hall Thruster," AIAA-99-2721, 35th AIAA / ASME / SAE / ASEE Joint Propulsion Conference, Los Angeles, CA, June 20-24, 1999.

¹⁶ Tilley, D.L., et. al., "The Application of the Triple Probe Method to MPD Thruster Plumes," AIAA 90-2667, 26th Joint Propulsion Conference, July 1990.

¹⁷ Haas, J.M., Gallimore, A.D., "Characterization of the Internal Plasma Structure of a 5 kW Hall Thruster," IEPC-99-078, 26th International Electric Propulsion Conference, Kitakyushu, Japan, October 1999.

¹⁸ Smith, B.A., Overzet, L.J., "Improvements to the floating double probe for time-resolved measurements in pulsed rf plasmas," *Review of Scientific Instruments*, Vol. 69, No. 3, p. 1372, March 1998.

¹⁹ Passoth, E., et. al., "An experimental study of plasma density determination by a cylindrical Langmuir probe at different pressures and magnetic fields in a cylindrical magnetron discharge in heavy rare gases," *Journal of Physics D.*, Vol.30, No.12, June 1997, p.1763-77.

²⁰ Aikawa, H., "The Measurement of the Anisotropy of Electron Distribution Function of a Magnetized Plasma," *Journal of the Physical Society of Japan*, Vol. 40, No. 6, June 1976.

²¹ Chung, P.M., et. al., "Electrostatic Probes in Stationary and Flowing Plasmas: Part 1. Collisionless and Transitional Probes," *AIAA Journal*, Vol. 12, No. 2, February 1974.

²² Peterson, P.Y., *Initial Scoping Studies on Applied Magnetically Distributed Arcs for Plasma Torches*, M.S. Thesis, Raleigh, North Carolina: Department of Nuclear Engineering, North Carolina State university, 1996.

CHAPTER 5

INTERNAL AND NEAR FIELD PLASMA – PEPL

This chapter presents the data obtained with the electrostatic probes described in Chapter

4. Section 5.1 contains individual plots of all the internal and near field probe data, followed by Section 5.2, which discusses the probe results.

5.1 Probe Data

Internal plasma parameter measurements were made at two operating conditions: 1.6 kW and 3 kW. The discharge voltage was held constant at 300 V during all measurements. At 1.6 kW, the discharge current was 5.4 A, which corresponded to an anode mass flow rate of 63 sccm and a tank pressure of 2.1×10^{-5} Torr. The inner magnet current was set at 2 A and the outer magnet current was set at 1 A with the exception of the plasma potential measurements which had inner and outer magnet current settings of 3 A and 2 A, respectively. This was unavoidable as the thruster became unstable at the lower magnet settings during temperature and density measurements. It was considered more important to maintain the same mass flow rate, discharge current, and discharge voltage between tests, therefore the magnets were adjusted to accomplish stable operation. The profile shapes for the two magnet settings remained essentially the same while the

magnitude differed by no more than approximately 10%. This difference was considered to have very little effect on the final measurements. At 3 kW, the discharge current was 10 A, which corresponded to an anode mass flow rate of 110 sccm and a tank pressure of 3.2×10^{-5} Torr. Inner and outer magnet current was 3 A and 2 A, respectively. Probes were aligned by hand before being actuated at high speed by the HARP system; this introduced an uncertainty in the indicated axial position of ± 1.5 mm.

5.1.1 Plasma and Floating Potential

Plasma potential was measured using the emissive probe described in section 4.4.1. Data were collected during both insertion and removal of the probe from the discharge channel and averaged. Figures 5.1 – 5.10 show the plasma potential axial profiles for the 1.6 kW case. All plasma potential measurements are made with respect to electrical ground. Measurement uncertainty was estimated to be $-3/+6$ V (see discussion of emissive probe, Section 4.4.1).

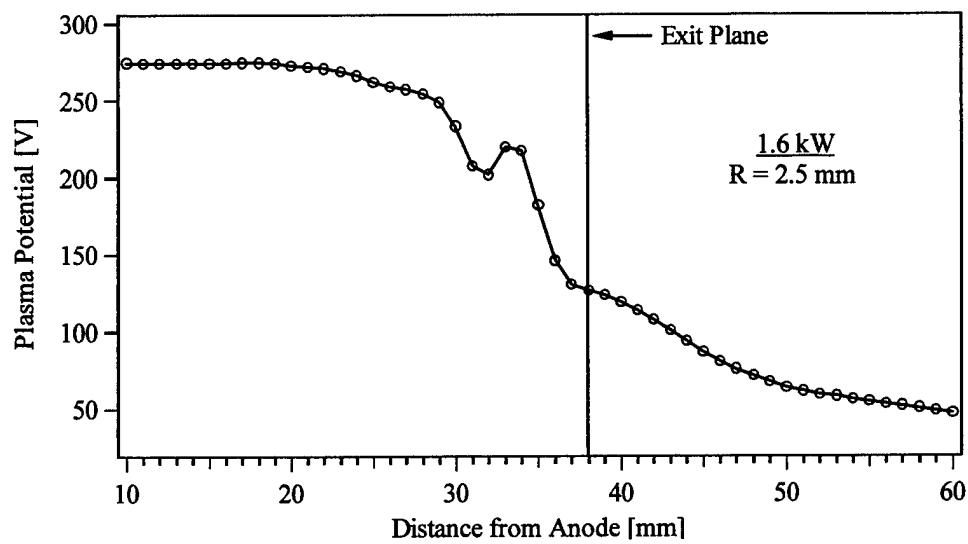


Figure 5.1 Plasma potential, 1.6 kW, R = 2.5 mm.

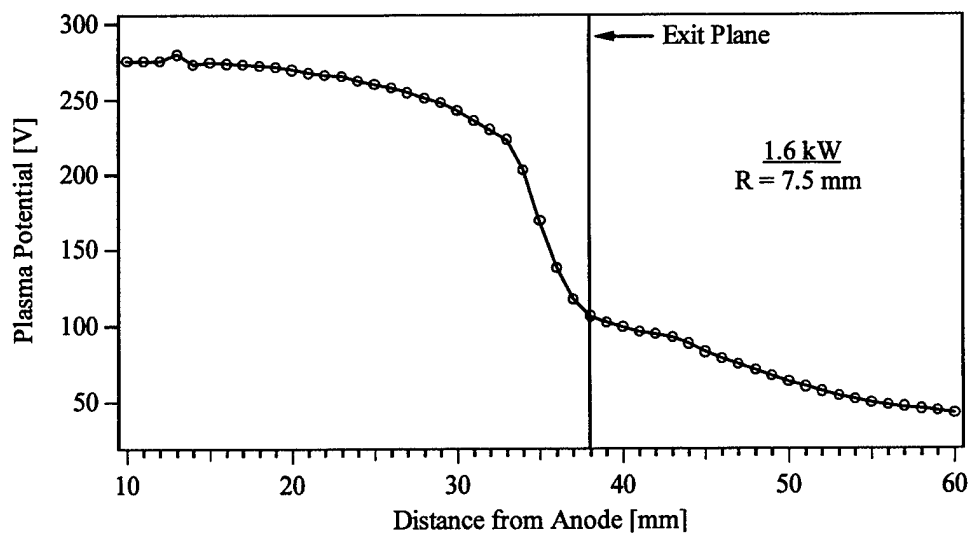


Figure 5.2 Plasma potential, 1.6 kW, R = 7.5 mm.

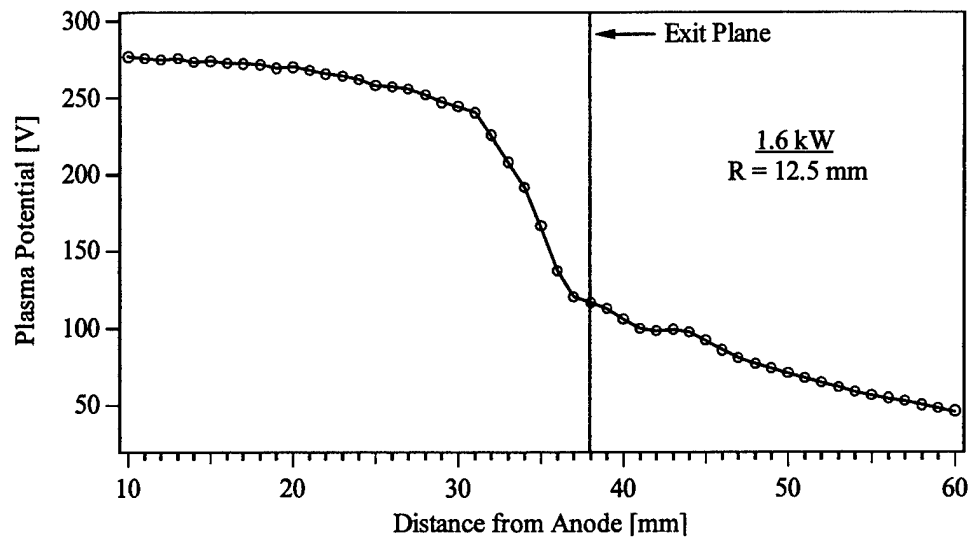


Figure 5.3 Plasma potential, 1.6 kW, R = 12.5 mm.

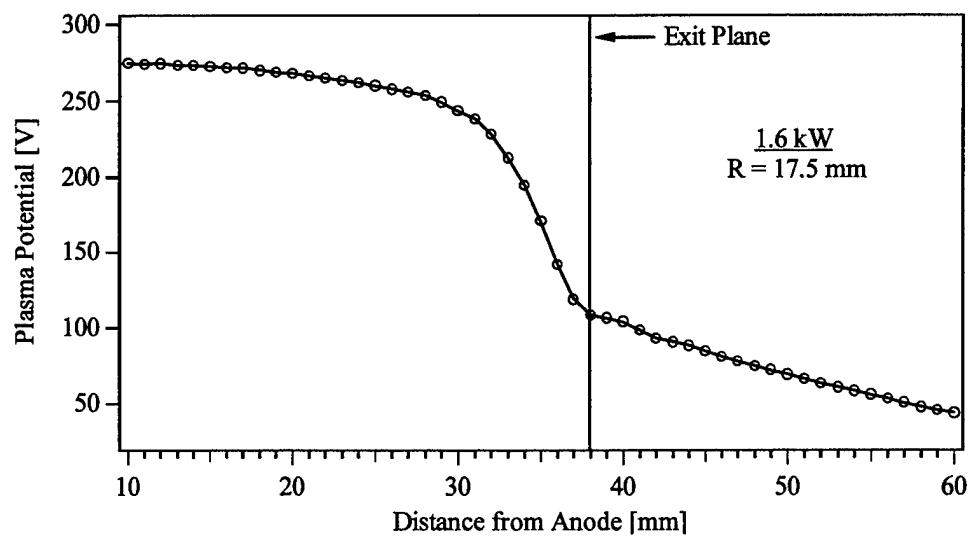


Figure 5.4 Plasma potential, 1.6 kW, R = 17.5 mm.

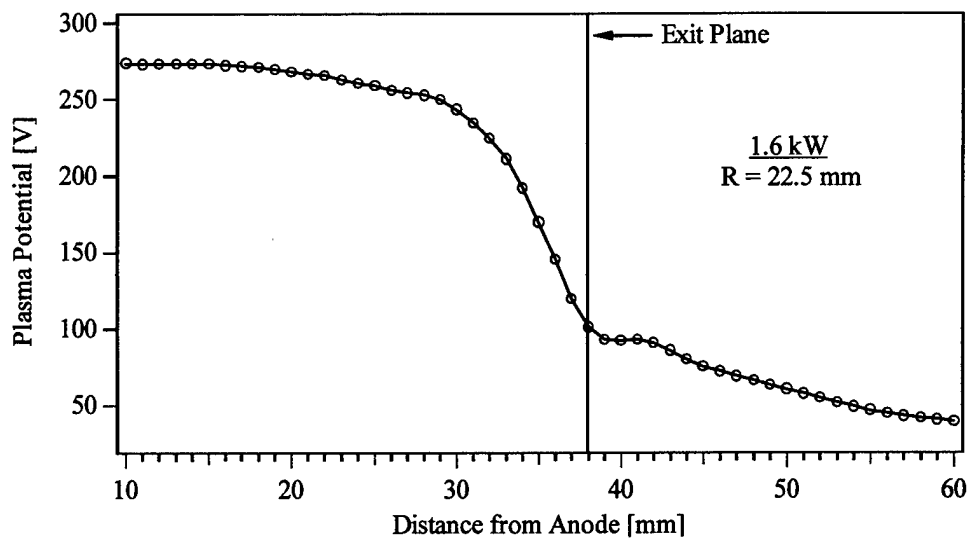


Figure 5.5 Plasma potential, 1.6 kW, $R = 22.5$ mm.

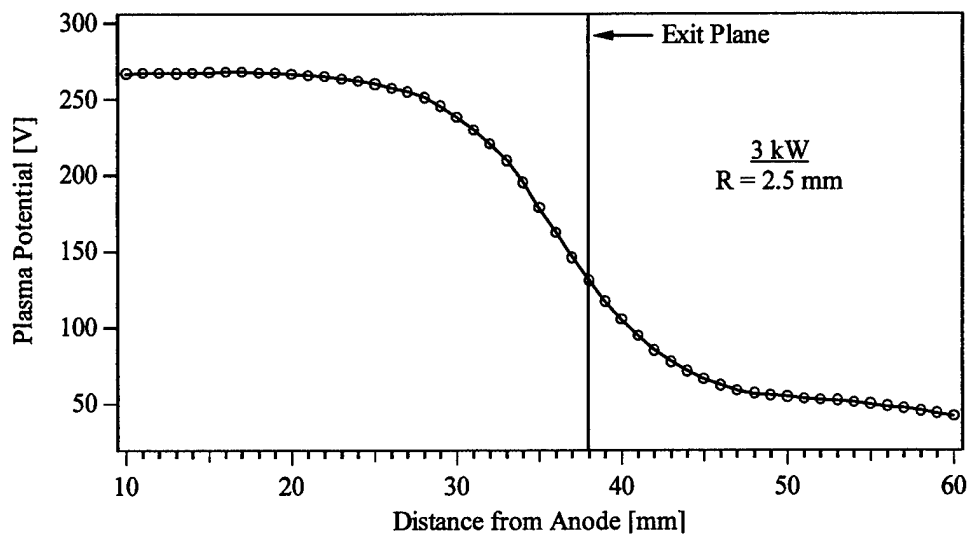


Figure 5.6 Plasma potential, 3 kW, $R = 2.5$ mm.

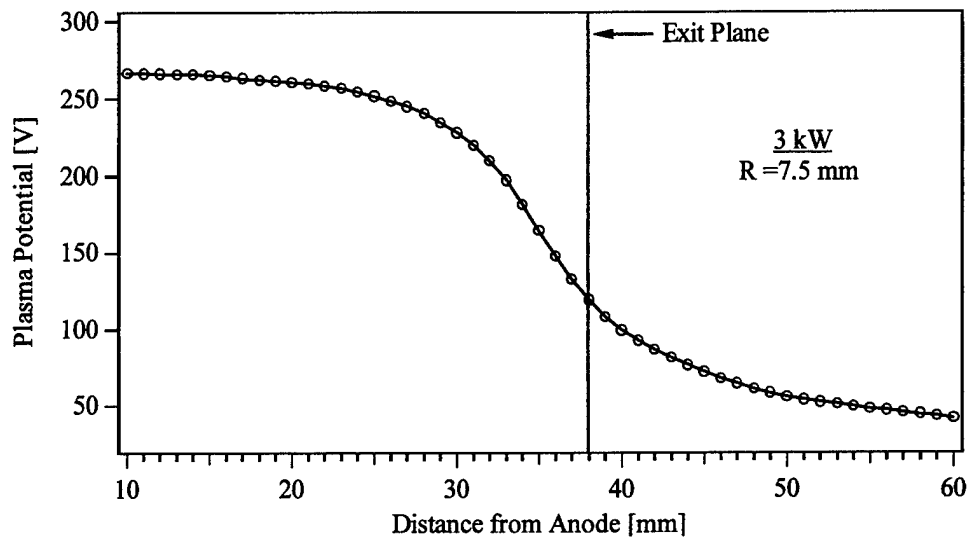


Figure 5.7 Plasma potential, 3 kW, $R = 7.5$ mm.

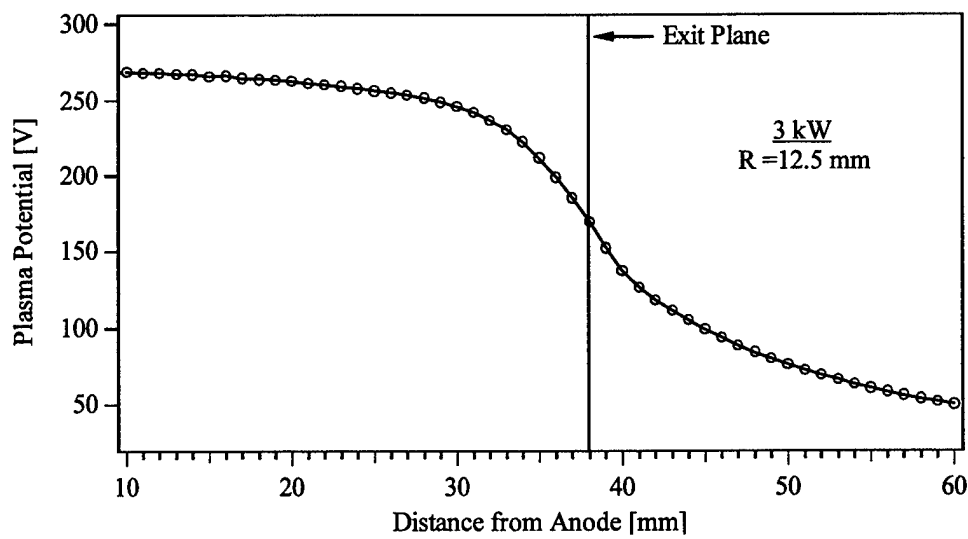


Figure 5.8 Plasma potential, 3 kW, $R = 12.5$ mm.

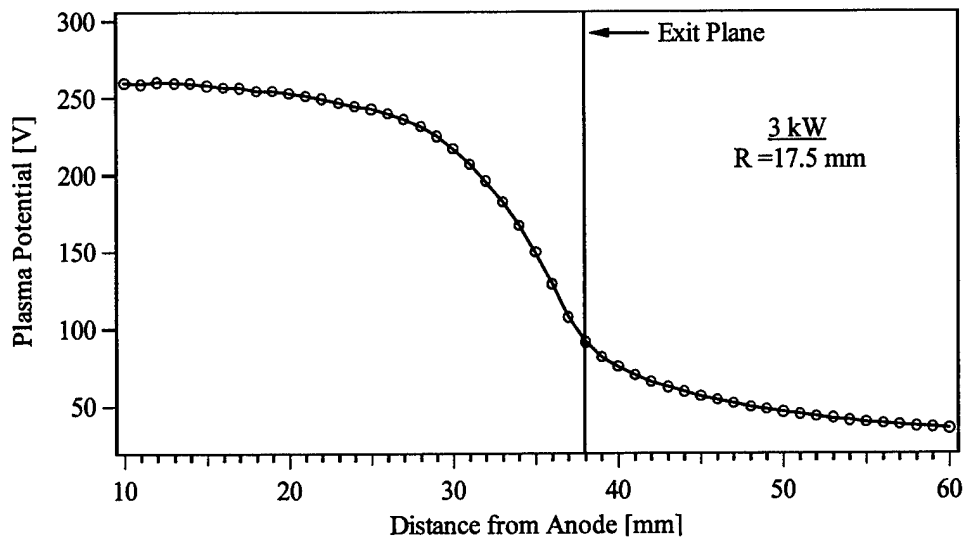


Figure 5.9 Plasma potential, 3 kW, $R = 17.5$ mm.

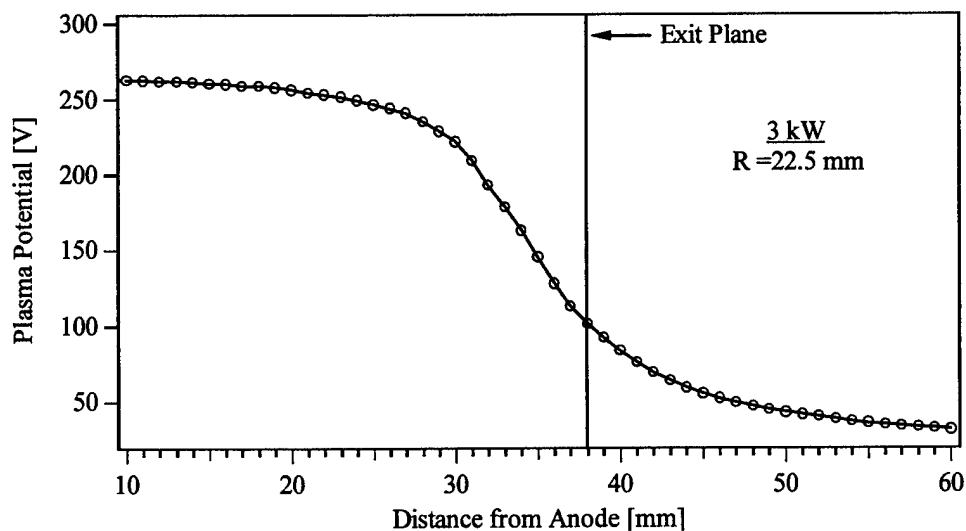


Figure 5.10 Plasma potential, 3 kW, $R = 22.5$ mm.

Floating potential was measured using one electrode of the double Langmuir probe illustrated in Figure 4.26. Measurements, shown in Figures 5.11 – 5.20, were made at the same thruster operating conditions as for the plasma potential. Uncertainty of the floating potential was estimated to be ± 2 V, based on the resolution of the oscilloscope used for

data acquisition. All floating potential measurements were made with respect to electrical ground.

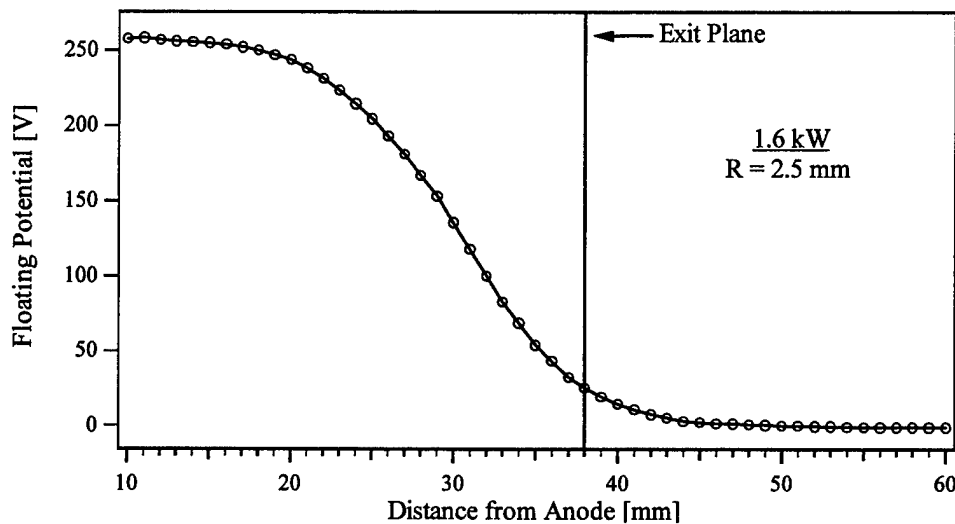


Figure 5.11 Floating potential, 1.6 kW, $R = 2.5$ mm.

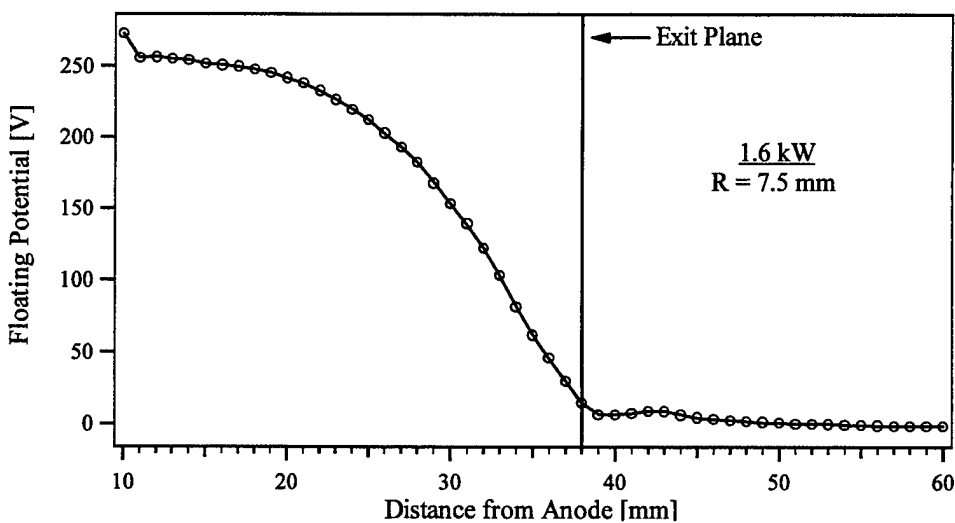


Figure 5.12 Floating potential, 1.6 kW, $R = 7.5$ mm.

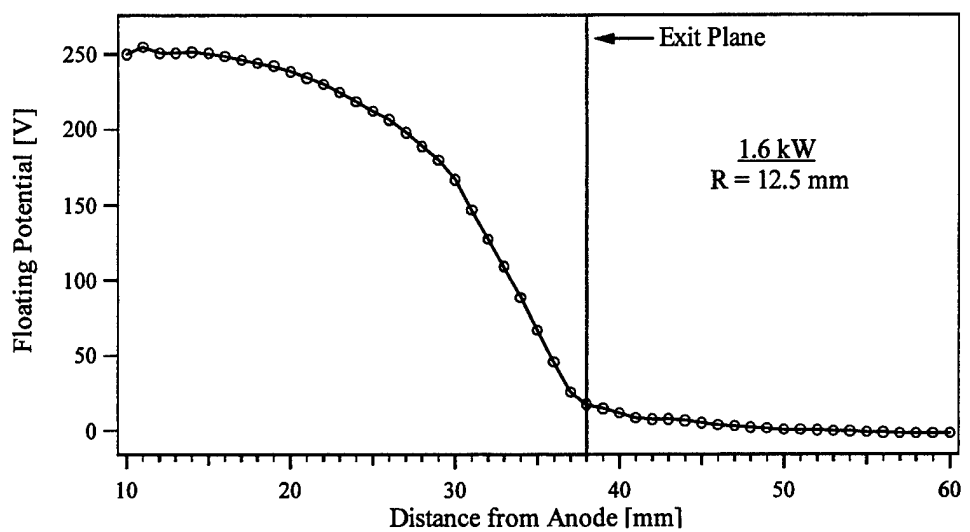


Figure 5.13 Floating potential, 1.6 kW, $R = 12.5$ mm.

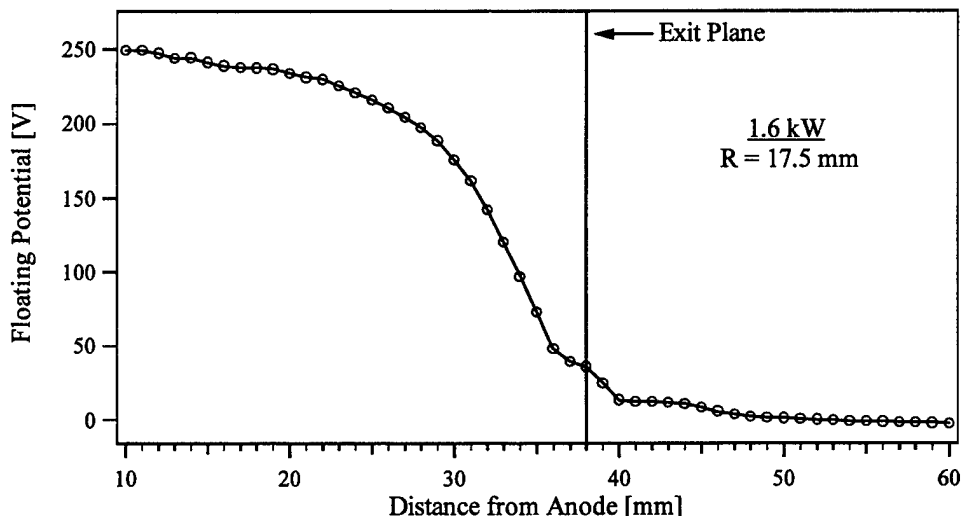


Figure 5.14 Floating potential, 1.6 kW, $R = 17.5$ mm.

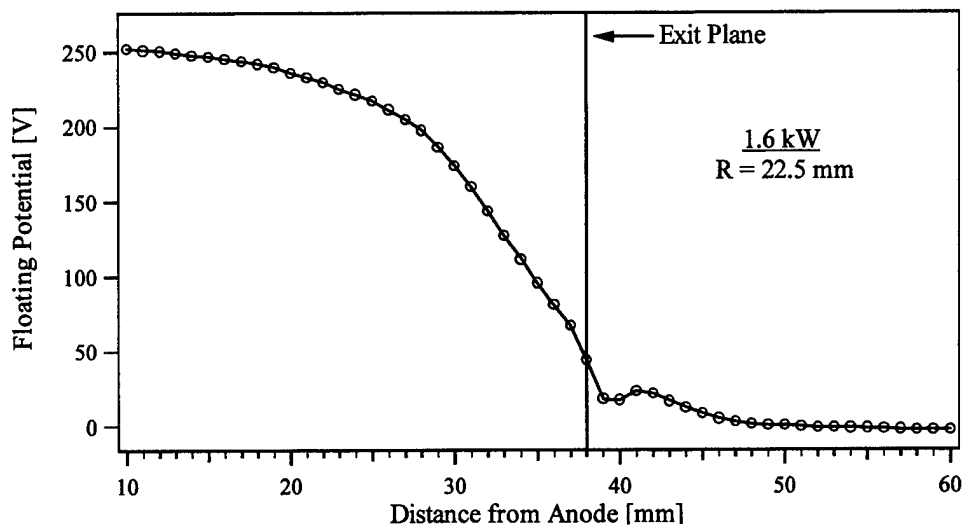


Figure 5.15 Floating potential, 1.6 kW, $R = 22.5$ mm.

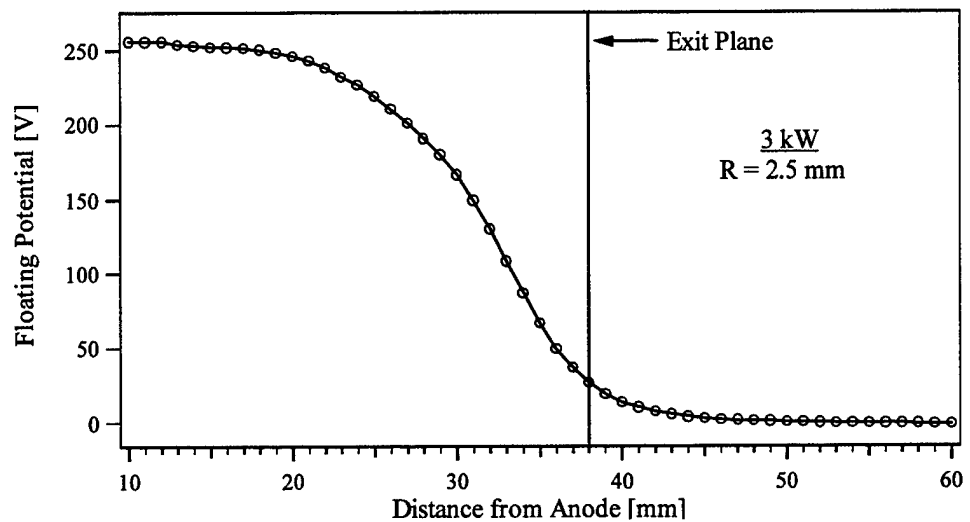


Figure 5.16 Floating potential, 3 kW, $R = 2.5$ mm.

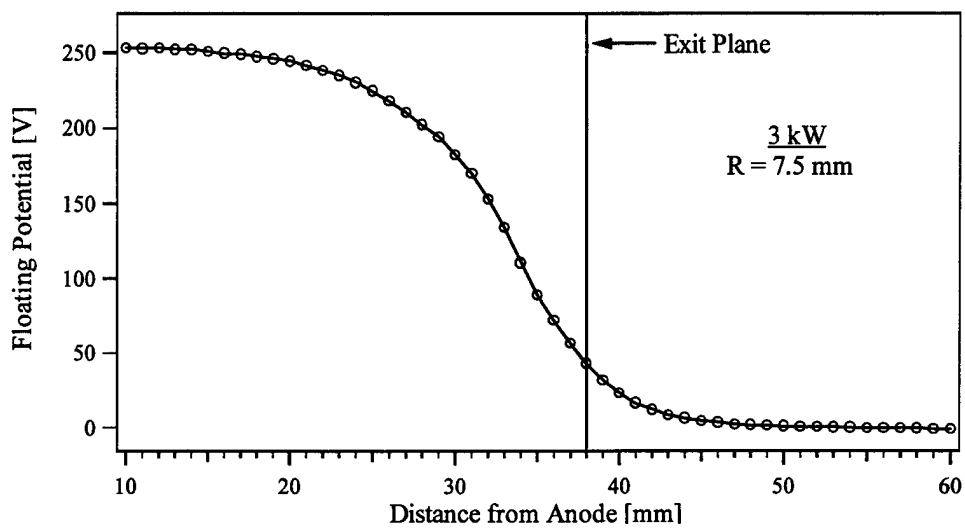


Figure 5.17 Floating potential, 3 kW, $R = 7.5$ mm.

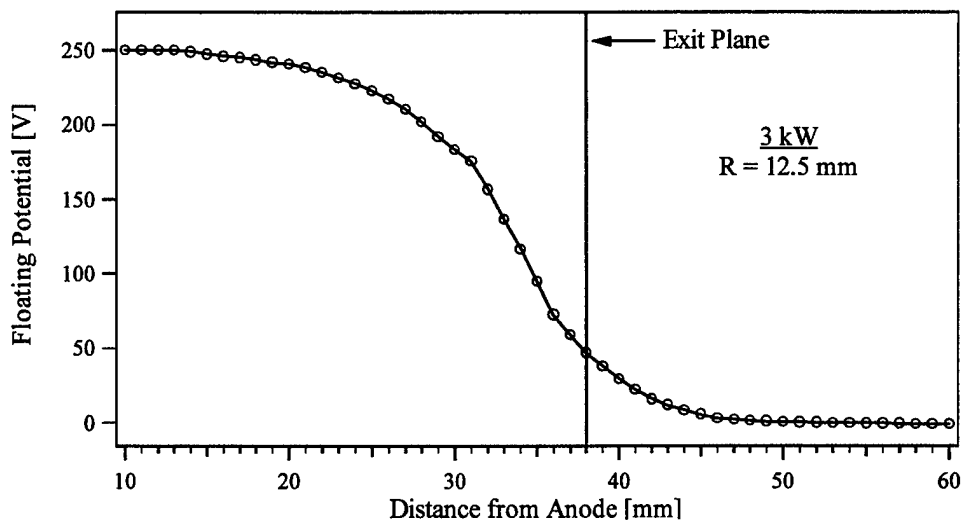


Figure 5.18 Floating potential, 3 kW, $R = 12.5$ mm.

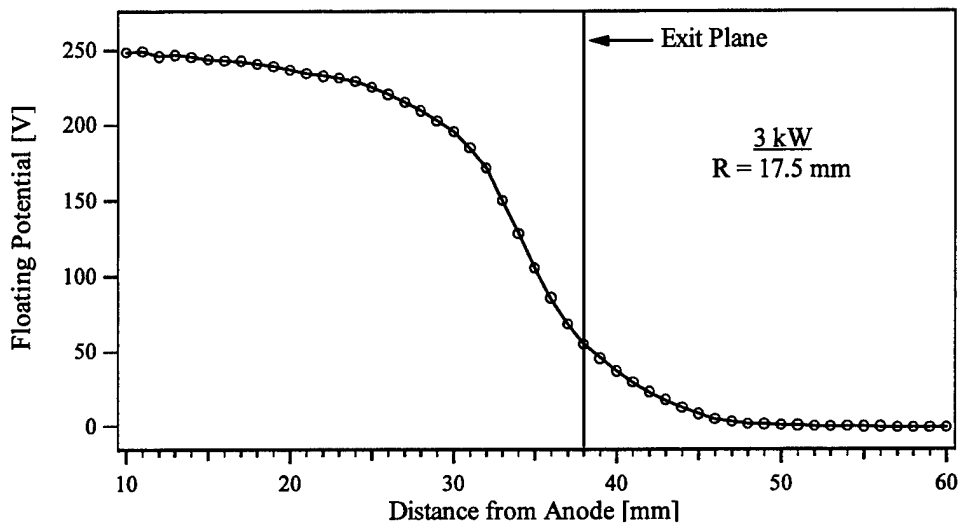


Figure 5.19 Floating potential, 3 kW, $R = 17.5$ mm.

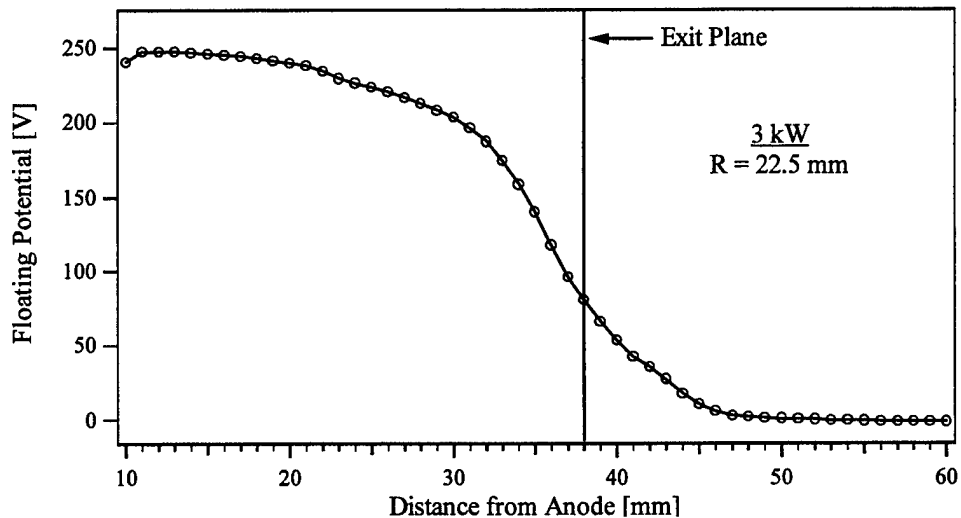


Figure 5.20 Floating potential, 3 kW, $R = 22.5$ mm.

5.1.2 Ion Number Density and Electron Temperature

Ion number density, Figures 5.21 – 5.30, and electron temperature, Figures 5.31 – 5.40 were measured in the discharge channel and the near field region of the P5 using the double Langmuir probe described in Section 4.4.2. Data were taken at the same operating conditions as with the emissive probe, 1.6 kW and 3 kW. The magnetic settings for the 1.6 kW case were 2 A and 1 A on the inner and outer magnet coils, respectively. Based on the use of standard Langmuir probe theory (see Equation 4-3), ion number density and electron temperature measurements had an uncertainty of 50% and 20%, respectively¹.

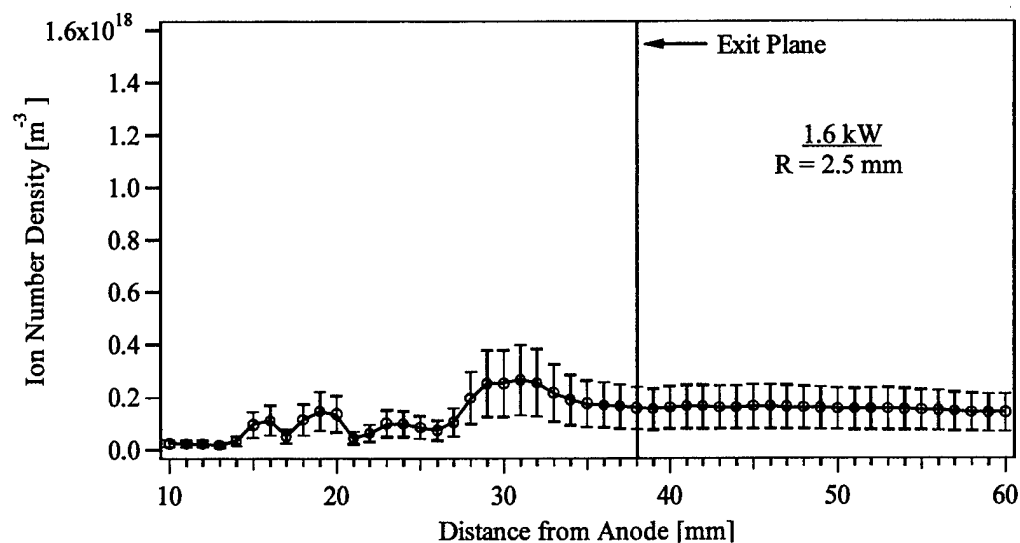


Figure 5.21 Ion number density, 1.6 kW, R = 2.5 mm.

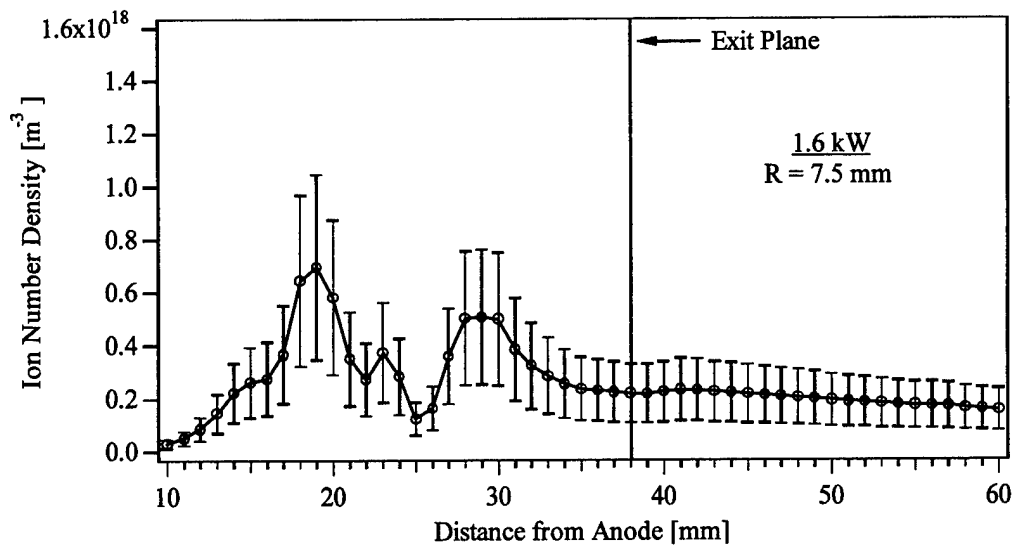


Figure 5.22 Ion number density, 1.6 kW, R = 7.5 mm.

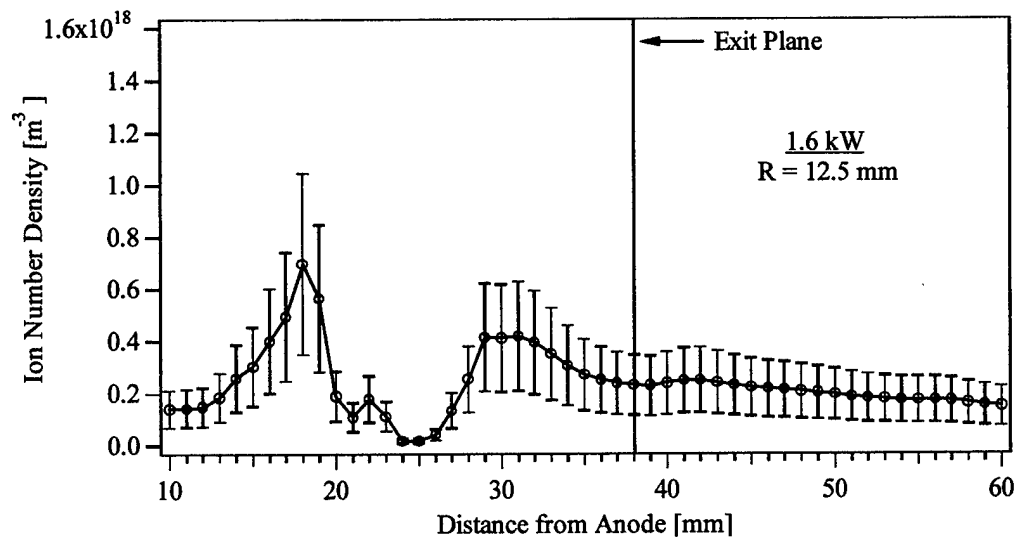


Figure 5.23 Ion number density, 1.6 kW, R = 12.5 mm.

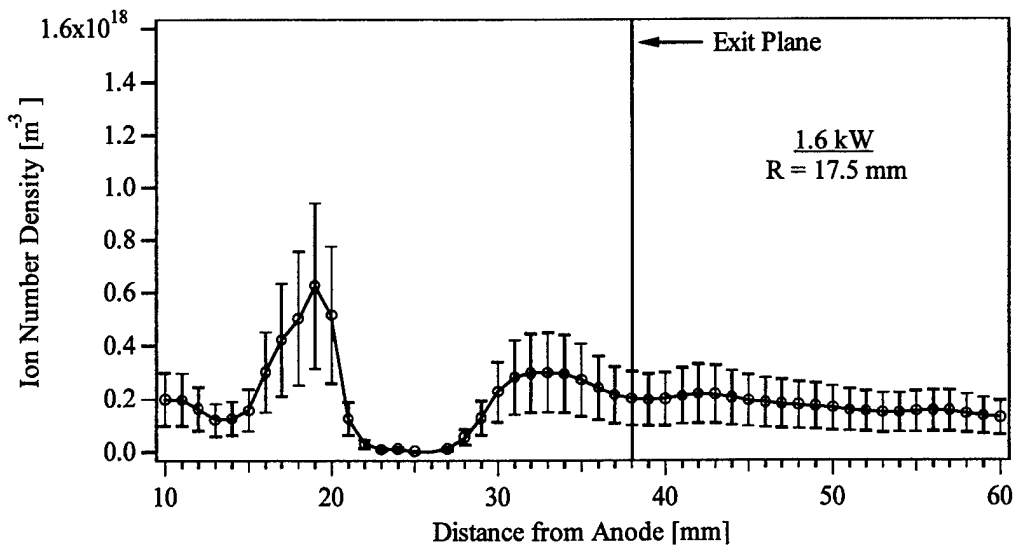


Figure 5.24 Ion number density, 1.6 kW , $R = 17.5 \text{ mm}$.

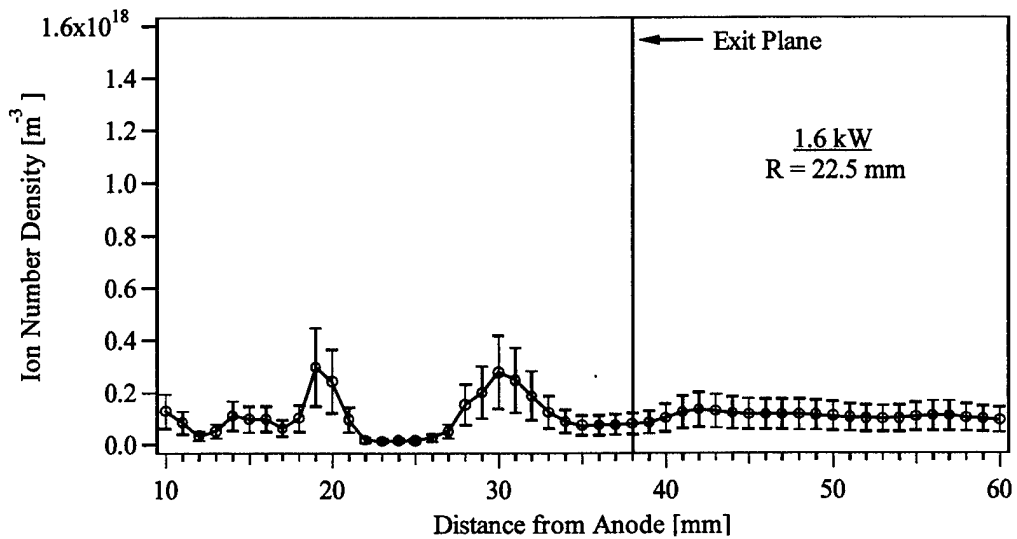


Figure 5.25 Ion number density, 1.6 kW , $R = 22.5 \text{ mm}$.

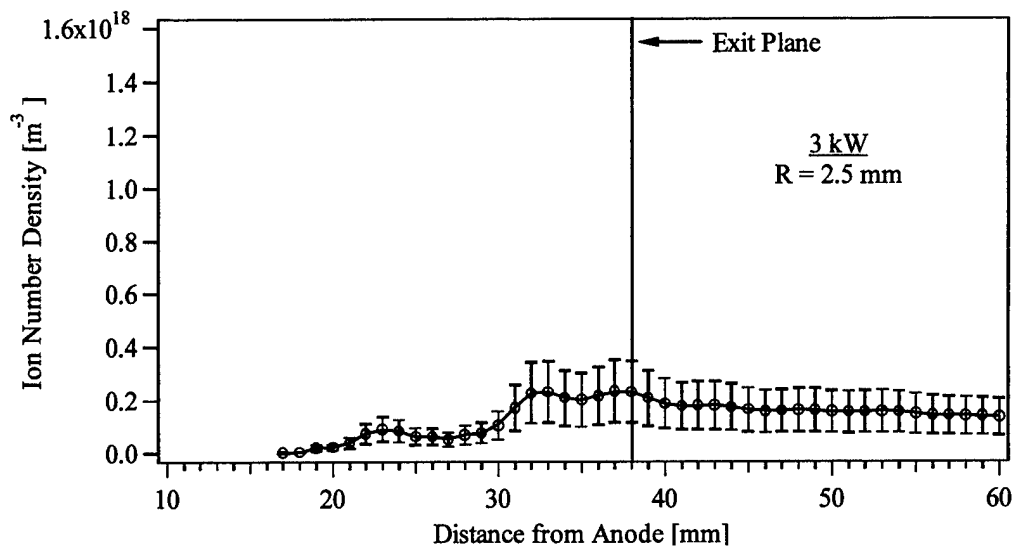


Figure 5.26 Ion number density, 3 kW, R = 2.5 mm.

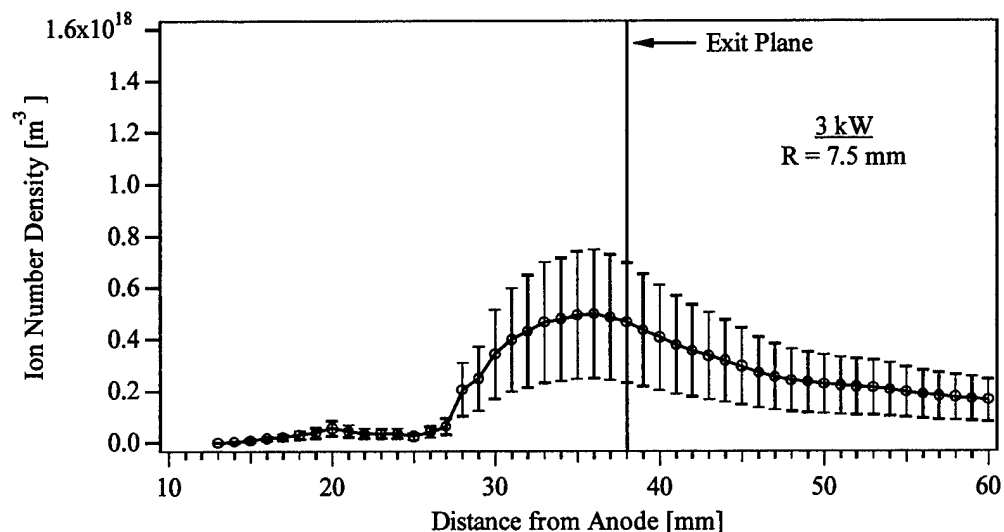


Figure 5.27 Ion number density, 3 kW, R = 7.5 mm.

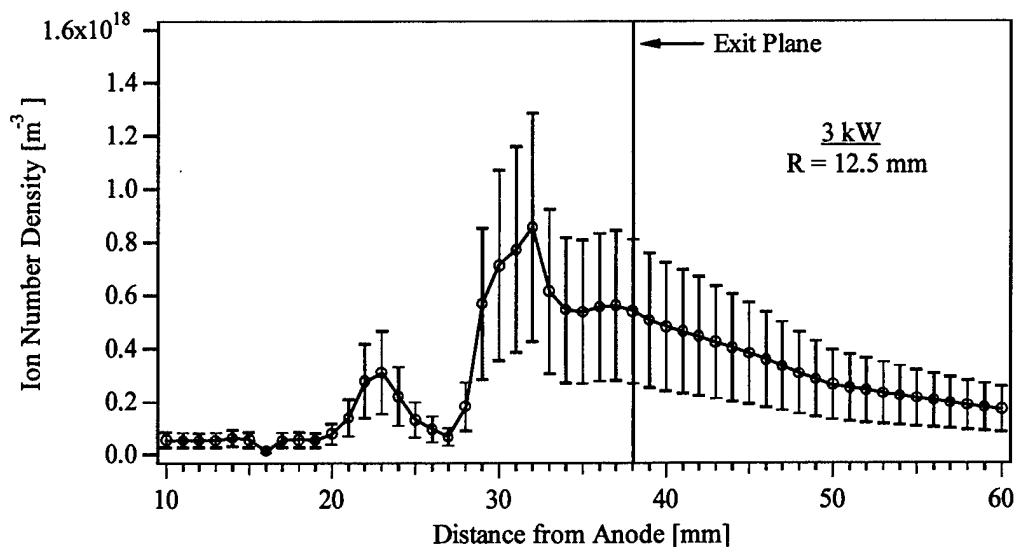


Figure 5.28 Ion number density, 3 kW, R = 12.5 mm.

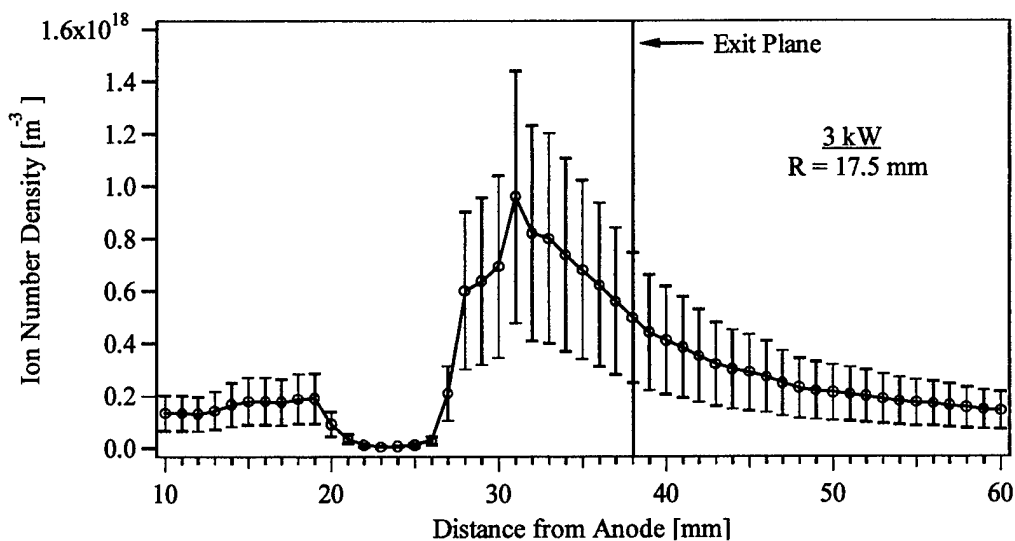


Figure 5.29 Ion number density, 3 kW, R = 17.5 mm.

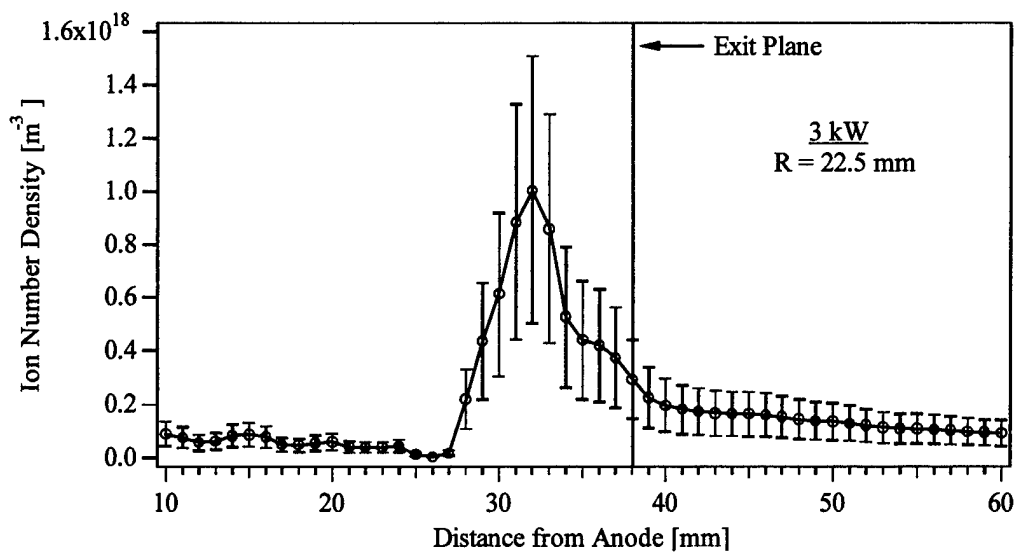


Figure 5.30 Ion number density, 3 kW , $R = 22.5 \text{ mm}$.

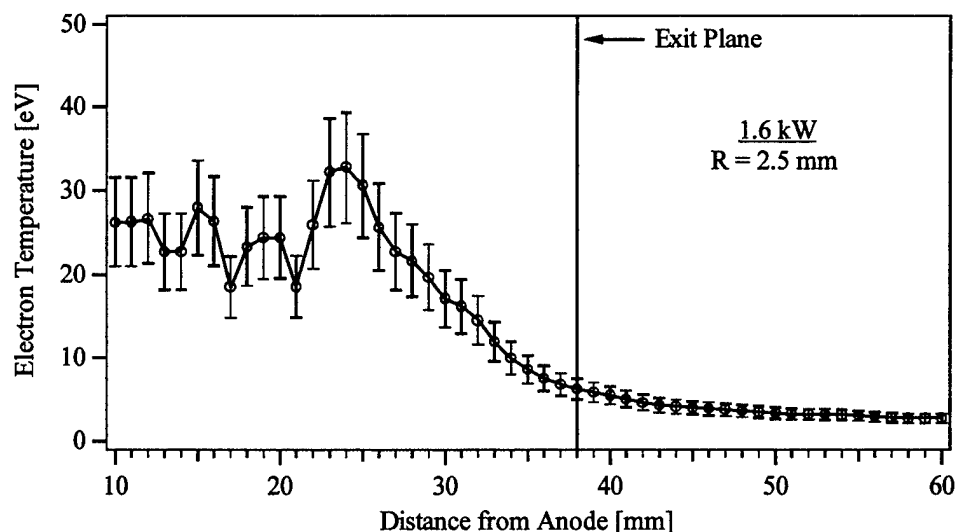


Figure 5.31 Electron Temperature, 1.6 kW , $R = 2.5 \text{ mm}$.

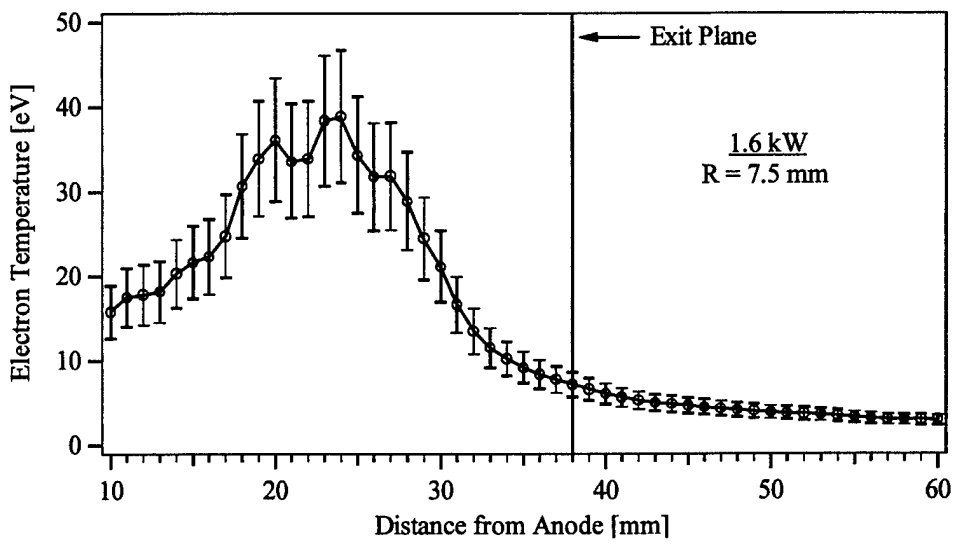


Figure 5.32 Electron Temperature, 1.6 kW, R = 7.5 mm.

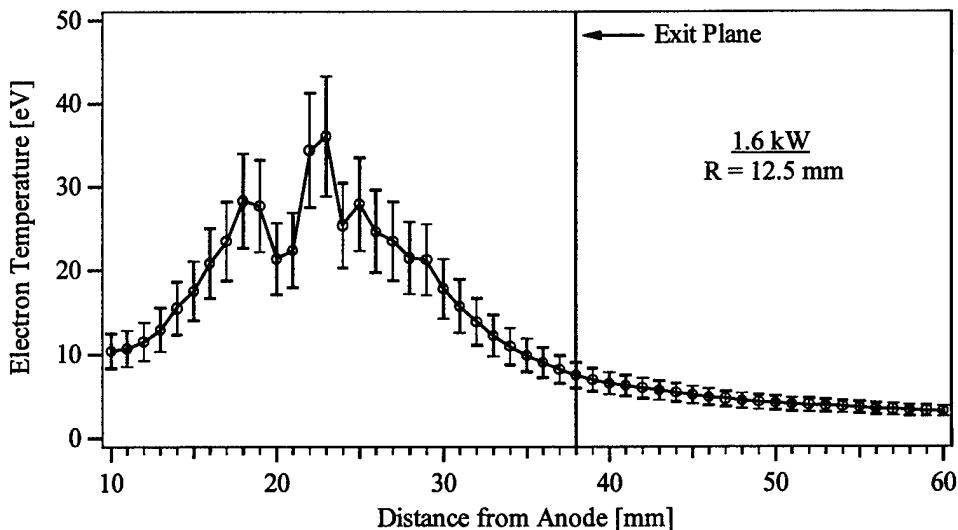


Figure 5.33 Electron Temperature, 1.6 kW, R = 12.5 mm.

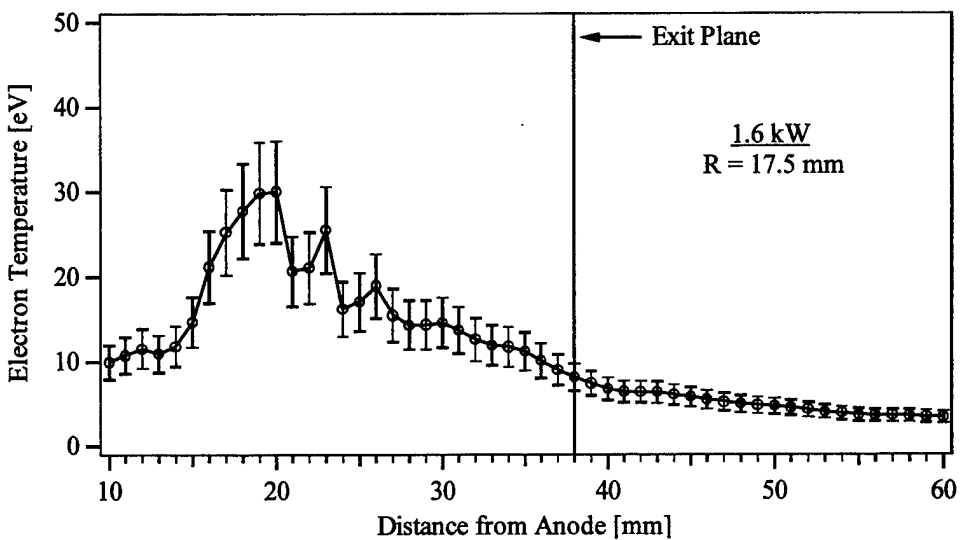


Figure 5.34 Electron Temperature, 1.6 kW, R = 17.5 mm.

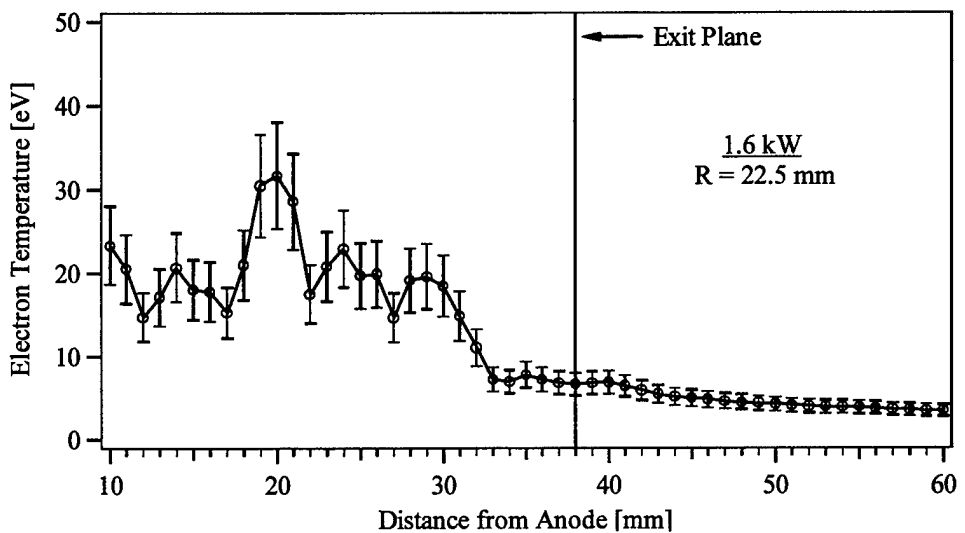


Figure 5.35 Electron Temperature, 1.6 kW, R = 22.5 mm.

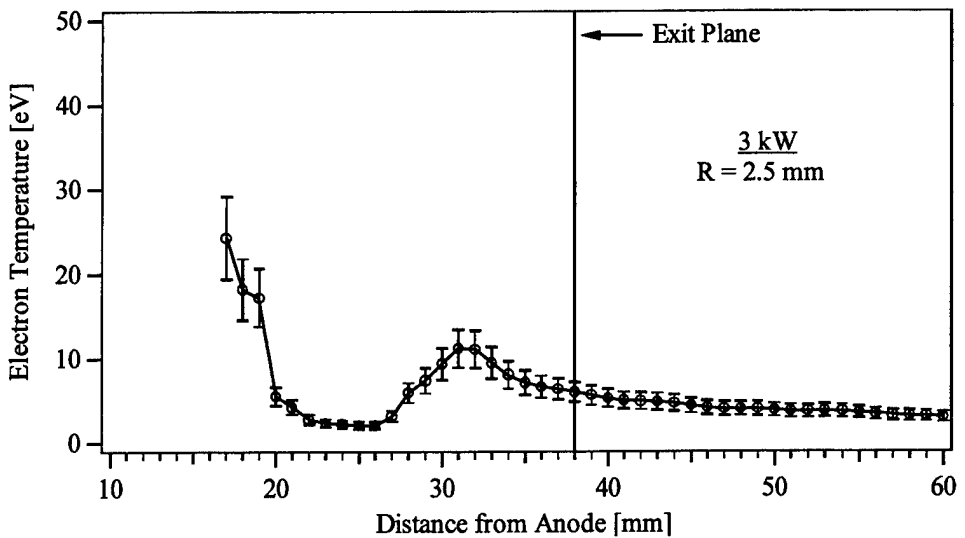


Figure 5.36 Electron Temperature, 3 kW , $R = 2.5 \text{ mm}$.

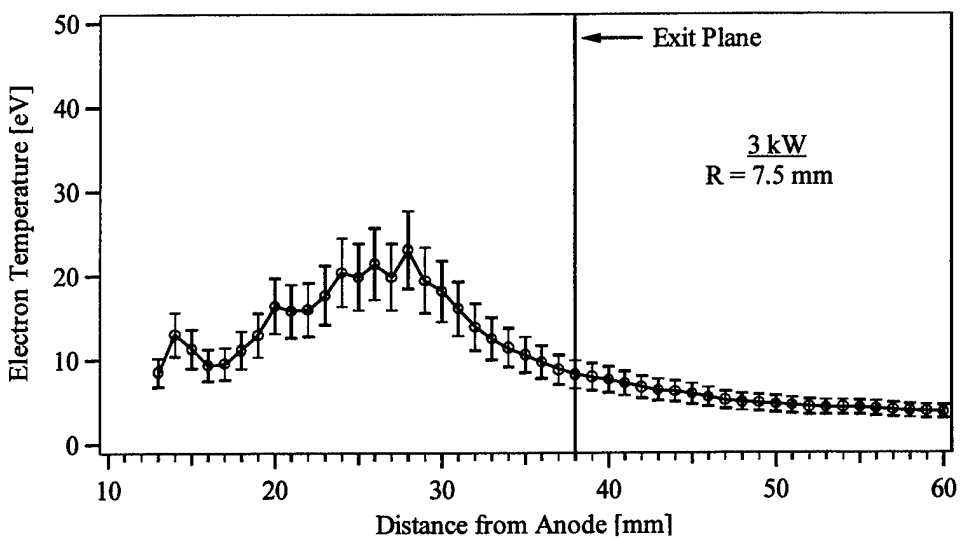


Figure 5.37 Electron Temperature, 3 kW , $R = 7.5 \text{ mm}$.

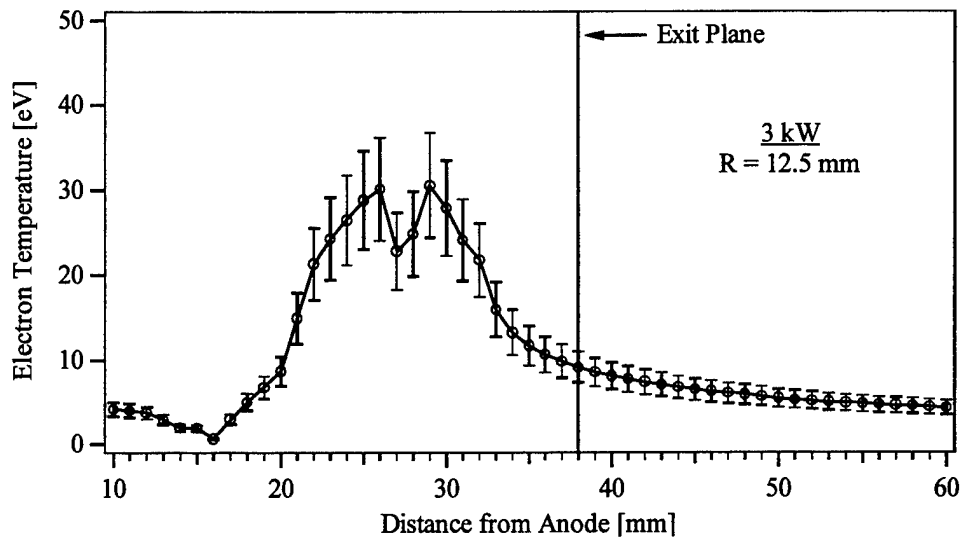


Figure 5.38 Electron Temperature, 3 kW, R = 12.5 mm.

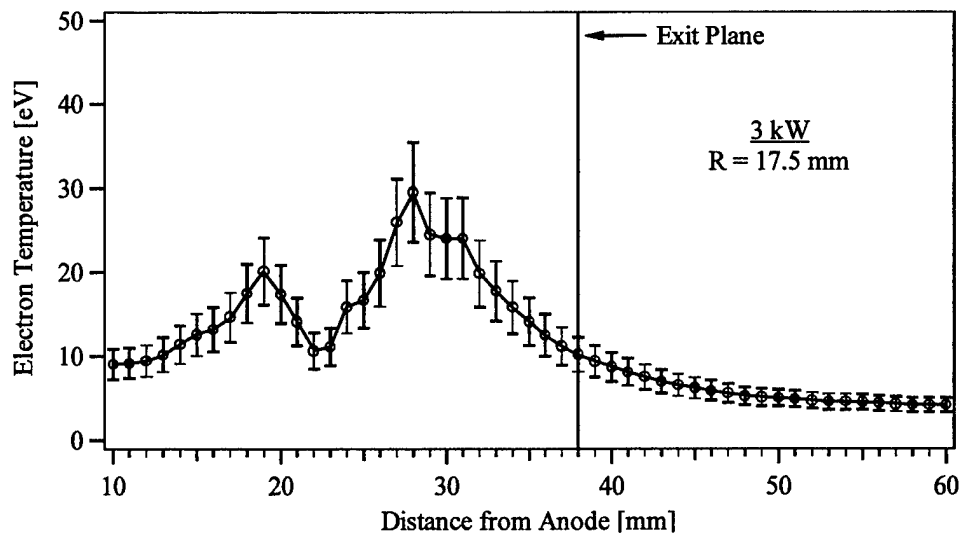


Figure 5.39 Electron Temperature, 3 kW, R = 17.5 mm.

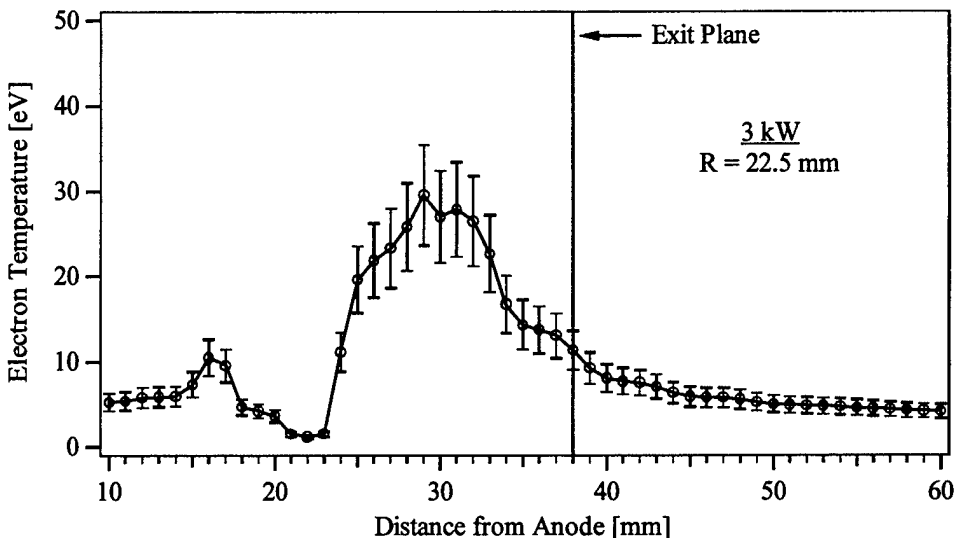


Figure 5.40 Electron Temperature, 3 kW, R = 22.5 mm.

5.1.3 Radial and Axial Magnetic Field – Vacuum

Vacuum field data were obtained with the commercial Gaussmeter described in Section 4.4.4. Magnetic field uncertainty was specified by the manufacturer to be less than 1%.

Based on the size of the Hall sensor, there was an uncertainty in the probe axial position of ± 1 mm and the radial position of less than 1 mm, for the radial magnetic field measurements, shown in Figures 5.41 – 5.50. Vacuum axial magnetic field values, shown in Figures 5.51 – 5.60, were obtained with a Hall sensor similar in size to that used for the radial measurements but rotated 90 degrees such that its face was normal to the thruster axis. For the axial field measurements, the axial uncertainty was less than 1 mm while the radial uncertainty was approximately ± 1 mm.

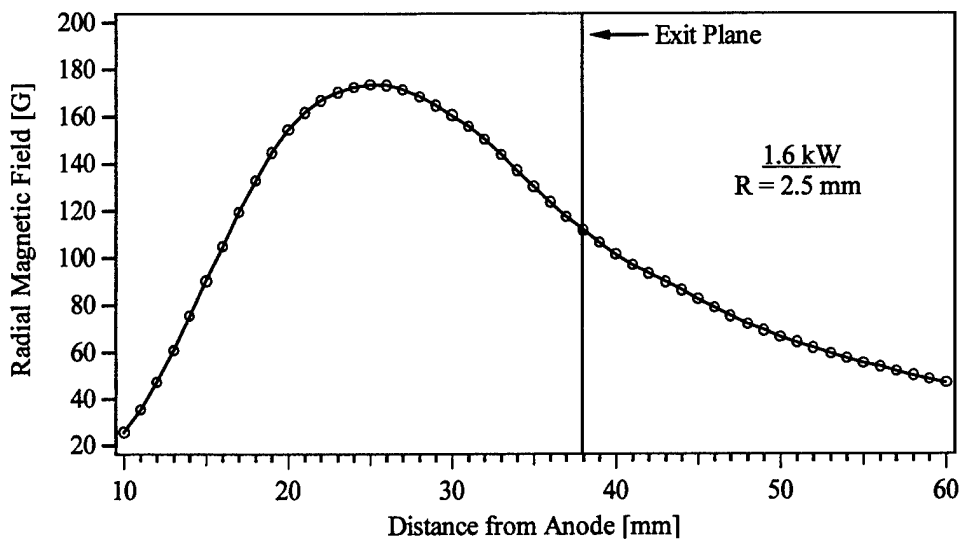


Figure 5.41 Vacuum radial magnetic field, Hall probe, 1.6 kW, R = 2.5 mm.

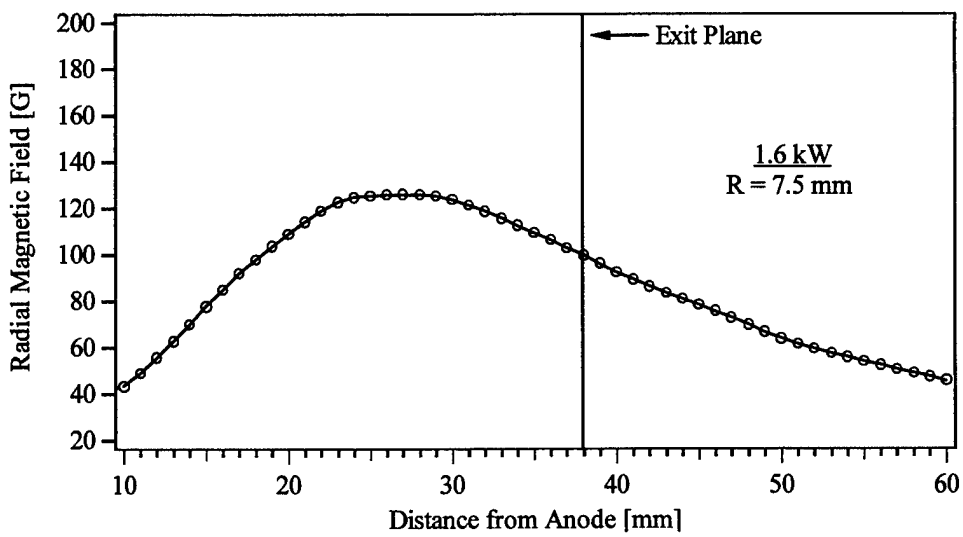


Figure 5.42 Vacuum radial magnetic field, Hall probe, 1.6 kW, R = 7.5 mm.

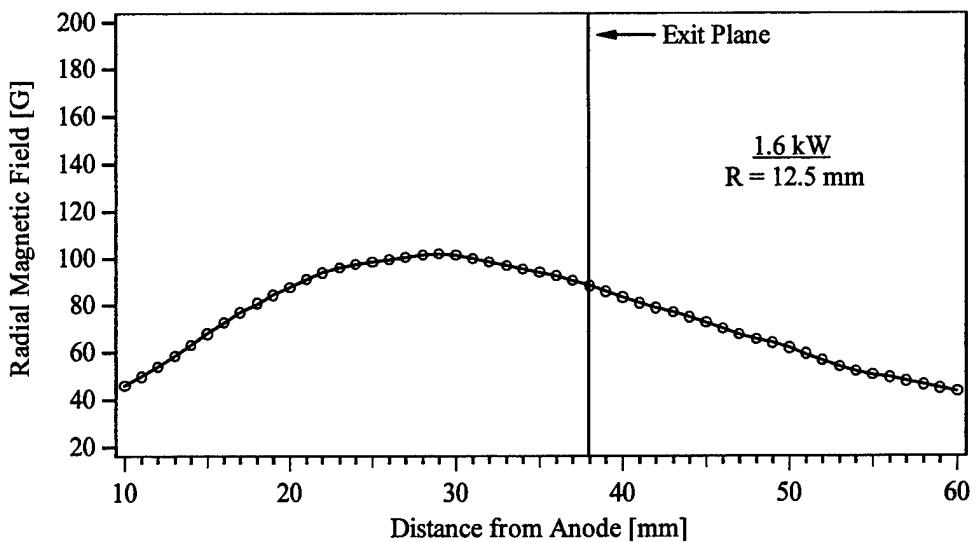


Figure 5.43 Vacuum radial magnetic field, Hall probe, 1.6 kW, $R = 12.5 \text{ mm}$.

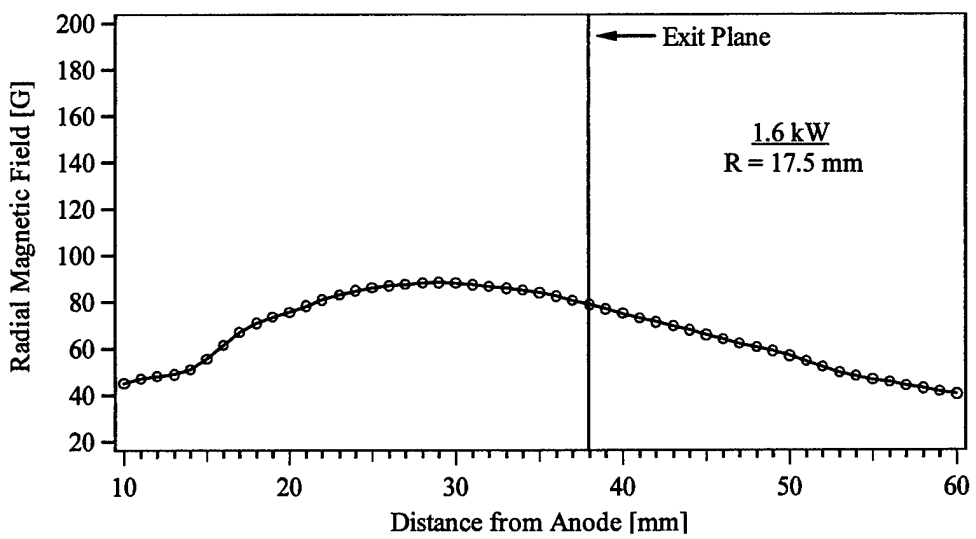


Figure 5.44 Vacuum radial magnetic field, Hall probe, 1.6 kW, $R = 17.5 \text{ mm}$.

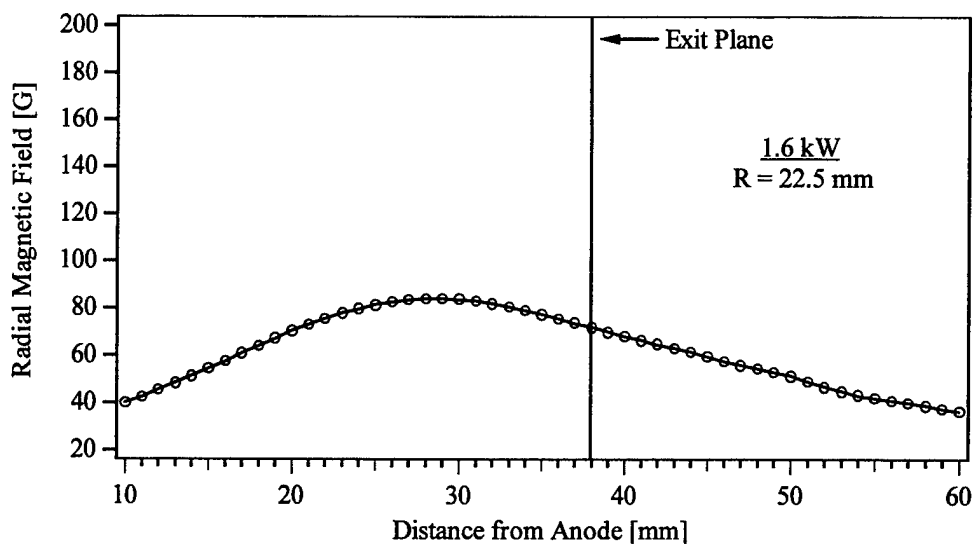


Figure 5.45 Vacuum radial magnetic field, Hall probe, 1.6 kW, $R = 22.5$ mm.

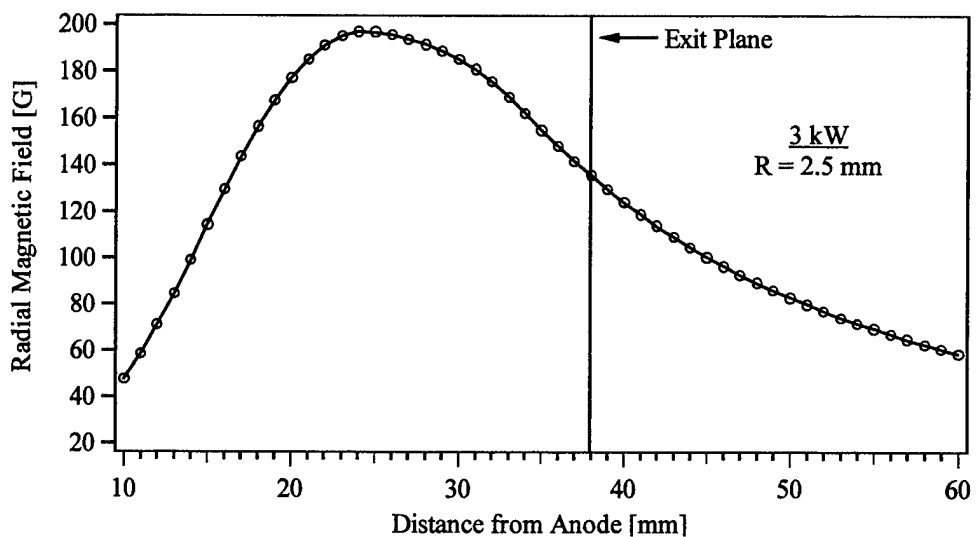


Figure 5.46 Vacuum radial magnetic field, Hall probe, 3 kW, $R = 2.5$ mm.

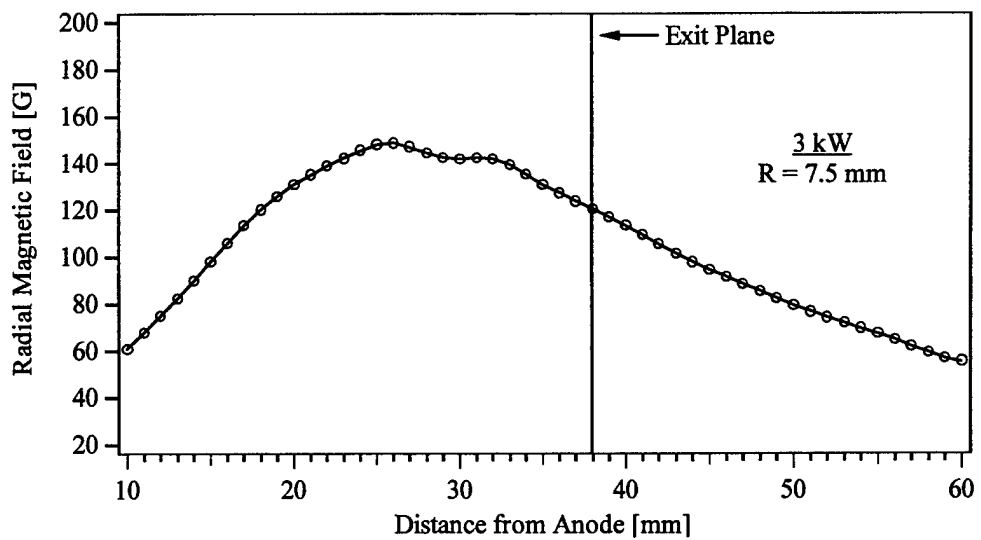


Figure 5.47 Vacuum radial magnetic field, Hall probe, 3 kW, R = 7.5 mm.

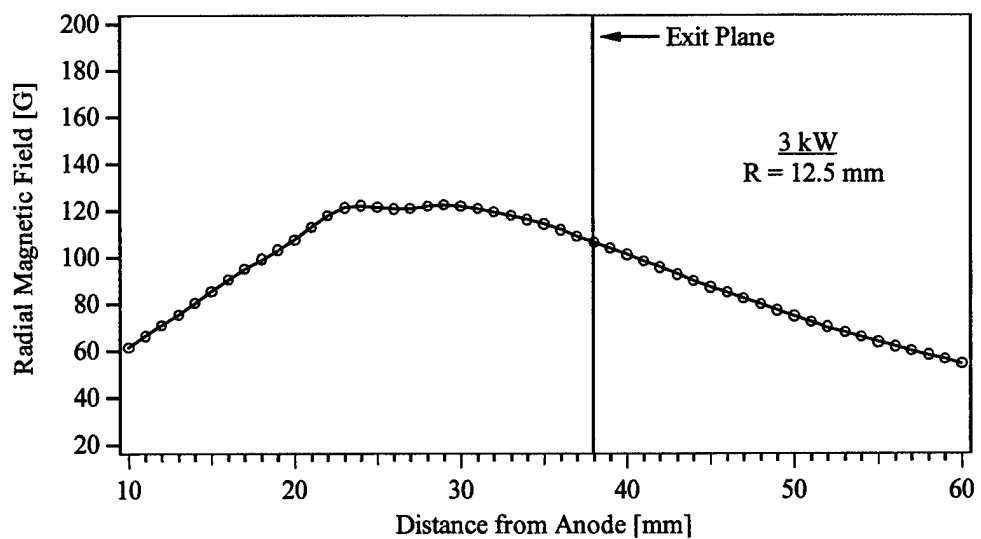


Figure 5.48 Vacuum radial magnetic field, Hall probe, 3 kW, R = 12.5 mm.

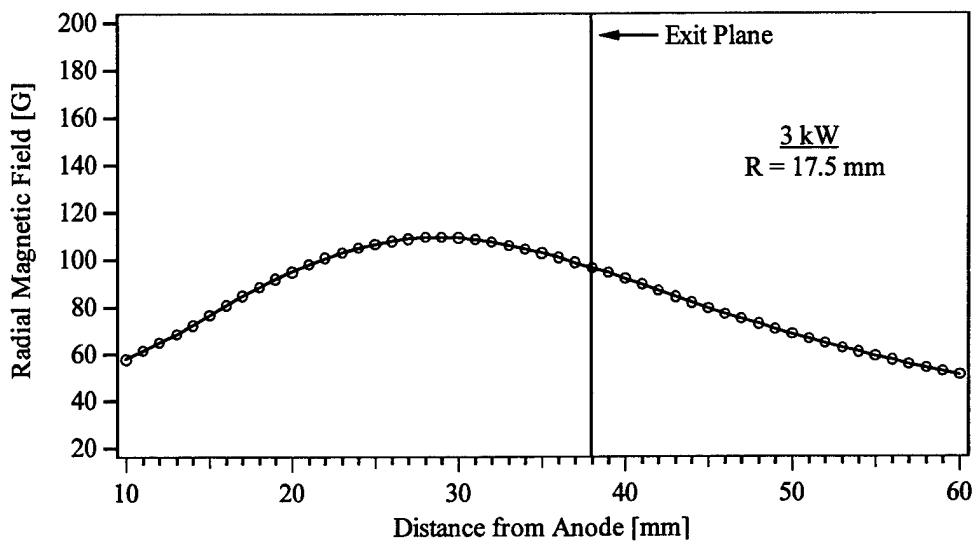


Figure 5.49 Vacuum radial magnetic field, Hall probe, 3 kW, $R = 17.5$ mm.

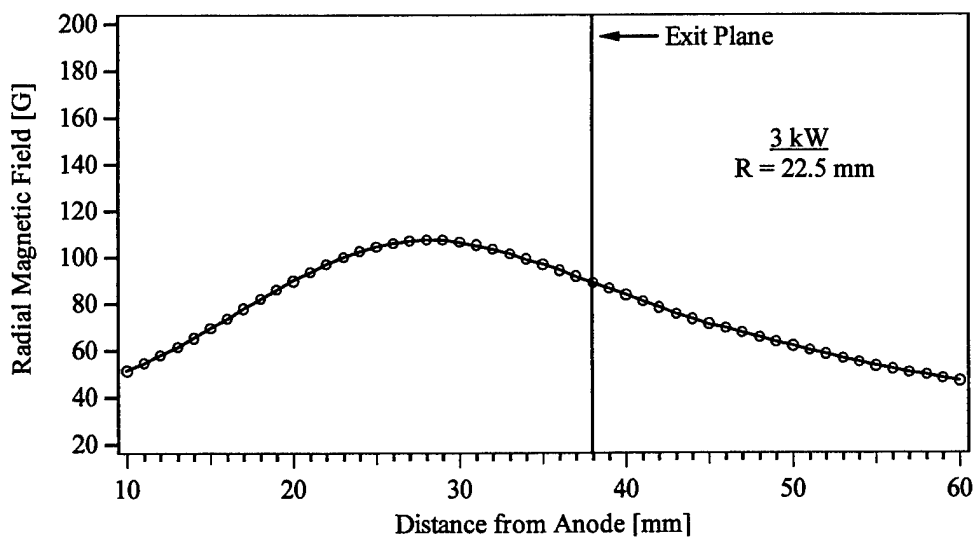


Figure 5.50 Vacuum radial magnetic field, Hall probe, 3 kW, $R = 22.5$ mm.

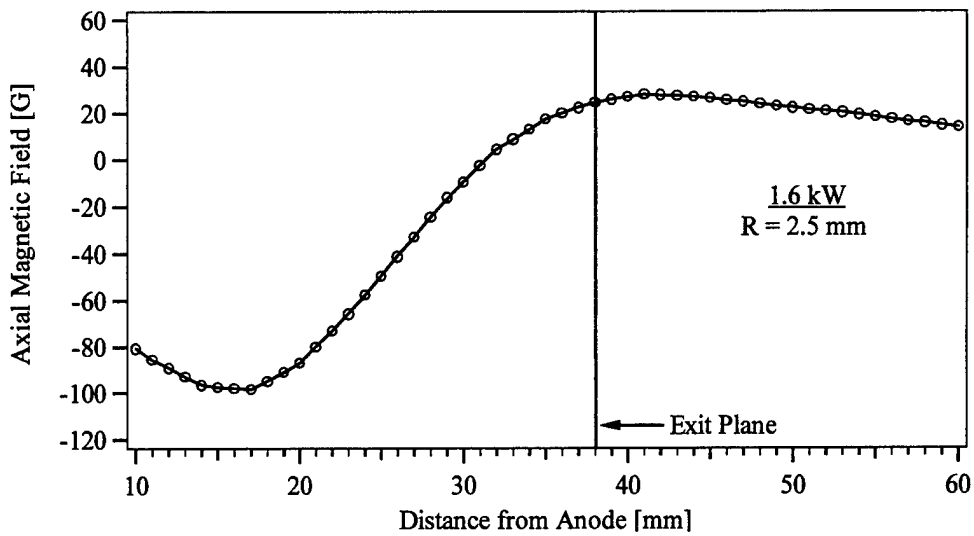


Figure 5.51 Vacuum axial magnetic field, Hall probe, 1.6 kW, $R = 2.5$ mm.

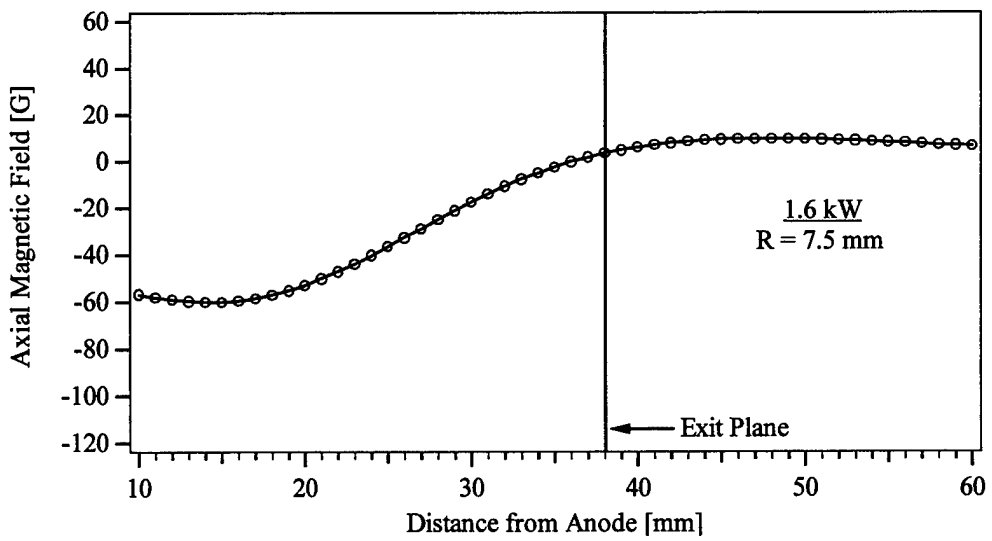


Figure 5.52 Vacuum axial magnetic field, Hall probe, 1.6 kW, $R = 7.5$ mm.

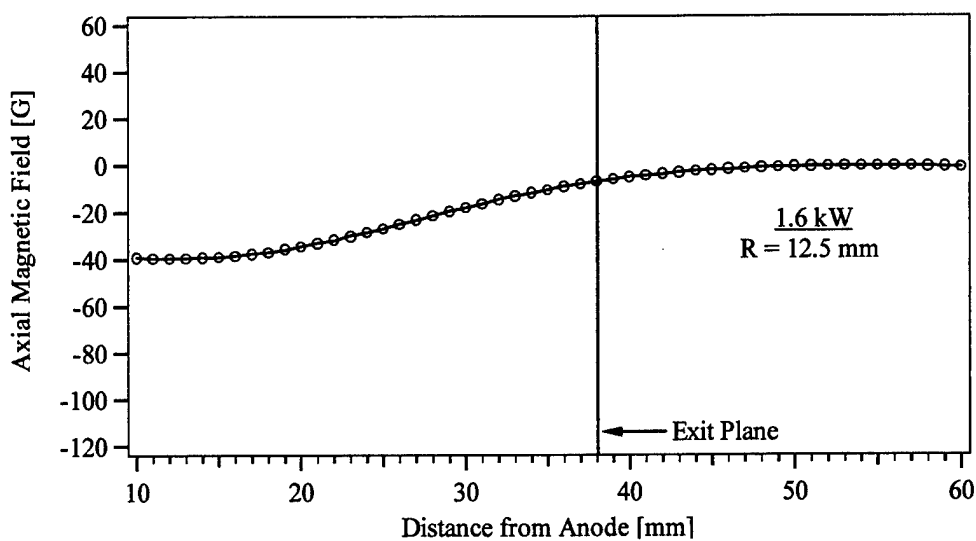


Figure 5.53 Vacuum axial magnetic field, Hall probe, 1.6 kW, R = 12.5 mm.

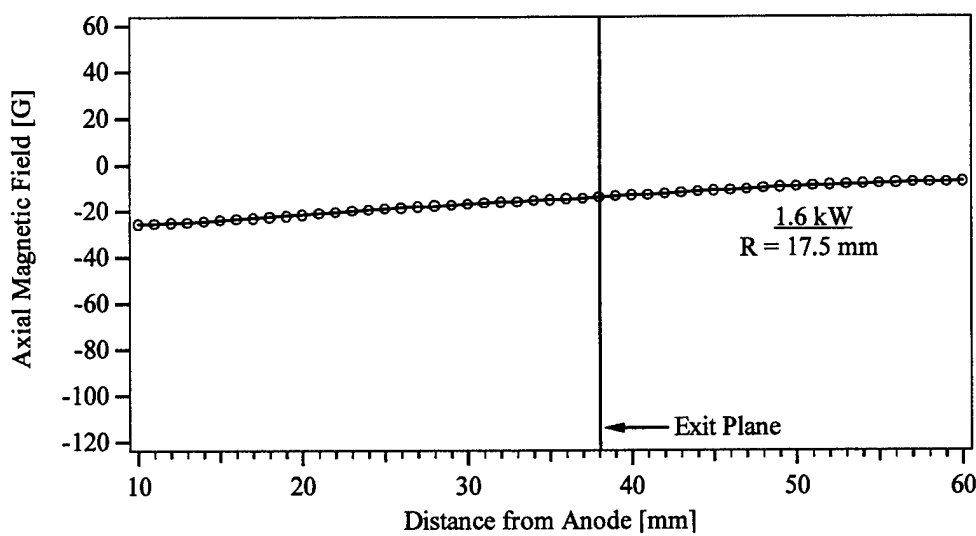


Figure 5.54 Vacuum axial magnetic field, Hall probe, 1.6 kW, R = 17.5 mm.

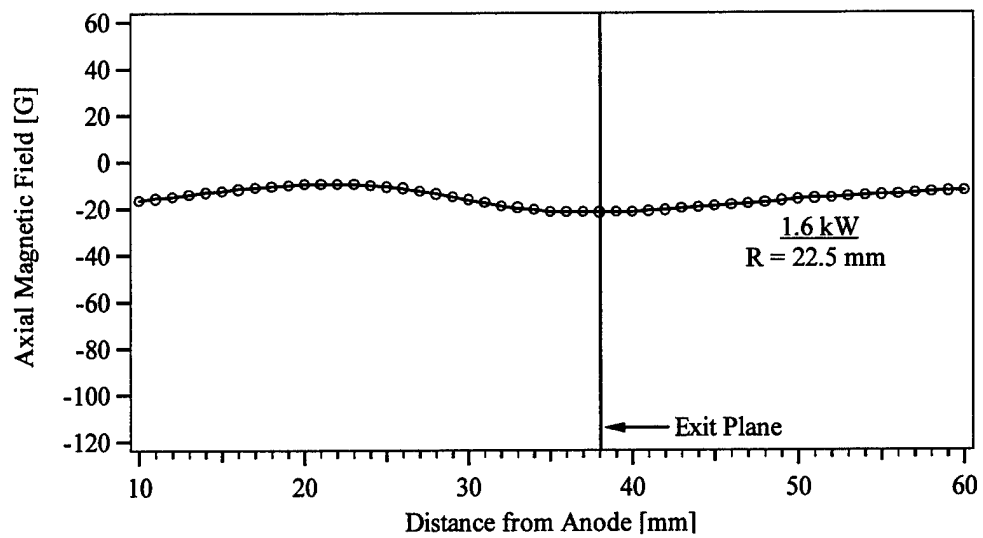


Figure 5.55 Vacuum axial magnetic field, Hall probe, 1.6 kW, $R = 22.5$ mm.

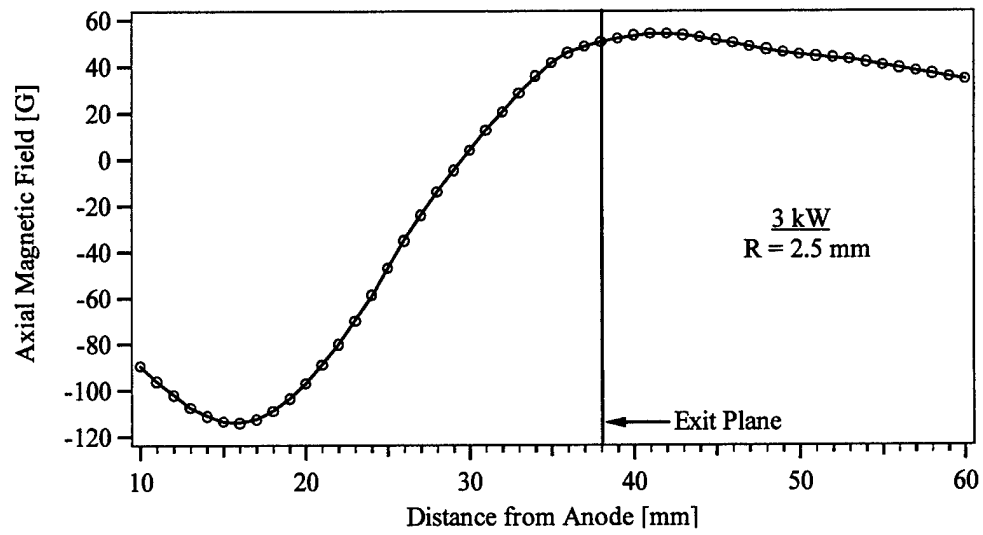


Figure 5.56 Vacuum axial magnetic field, Hall probe, 3 kW, $R = 2.5$ mm.

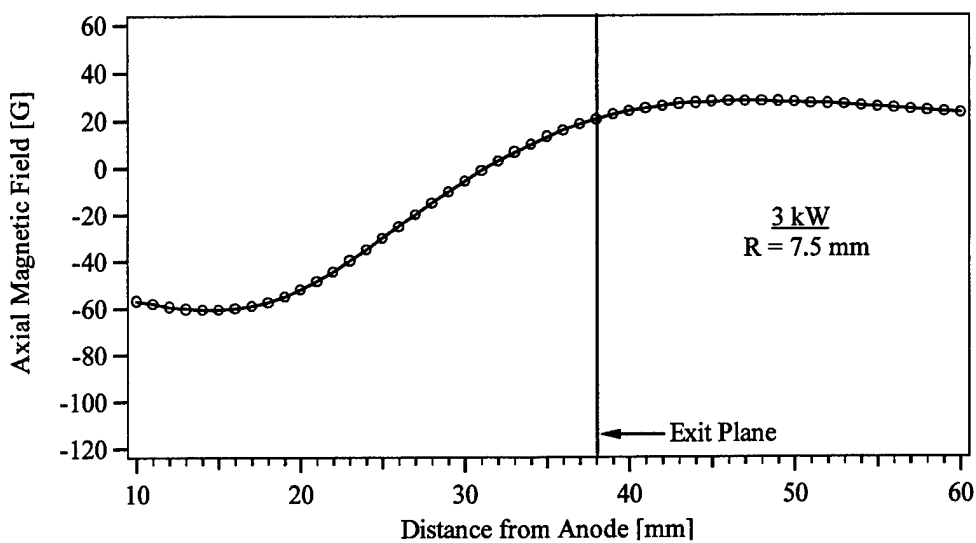


Figure 5.57 Vacuum axial magnetic field, Hall probe, 3 kW, R = 7.5 mm.

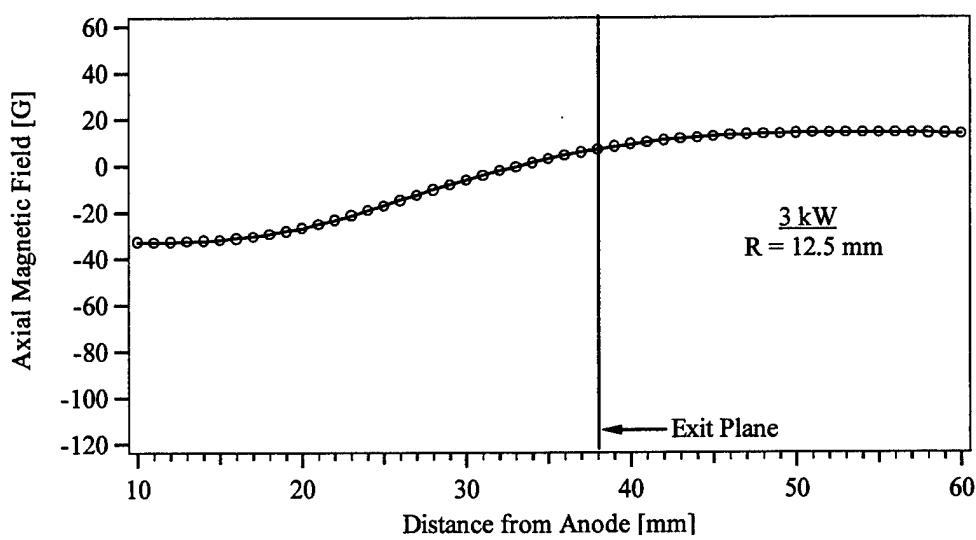


Figure 5.58 Vacuum axial magnetic field, Hall probe, 3 kW, R = 12.5 mm.

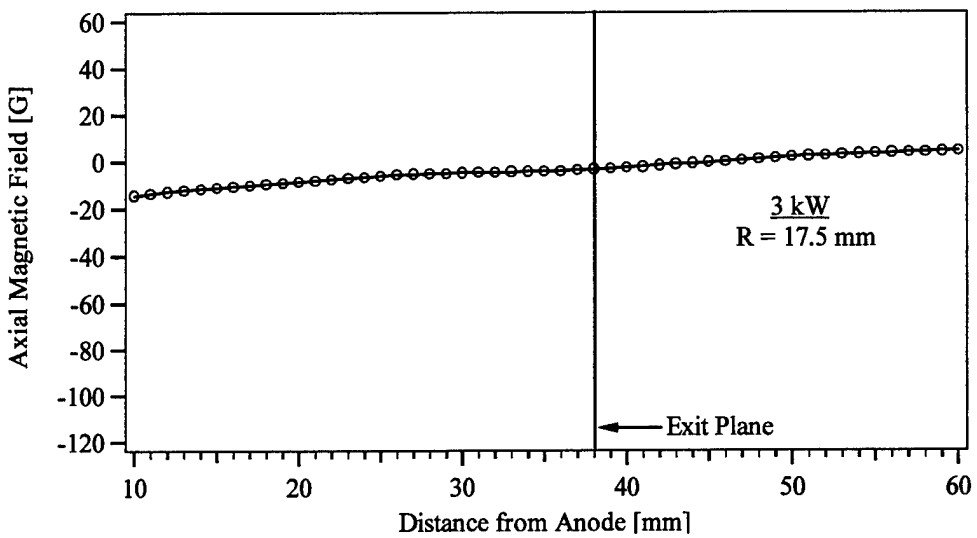


Figure 5.59 Vacuum axial magnetic field, Hall probe, 3 kW, $R = 17.5$ mm.

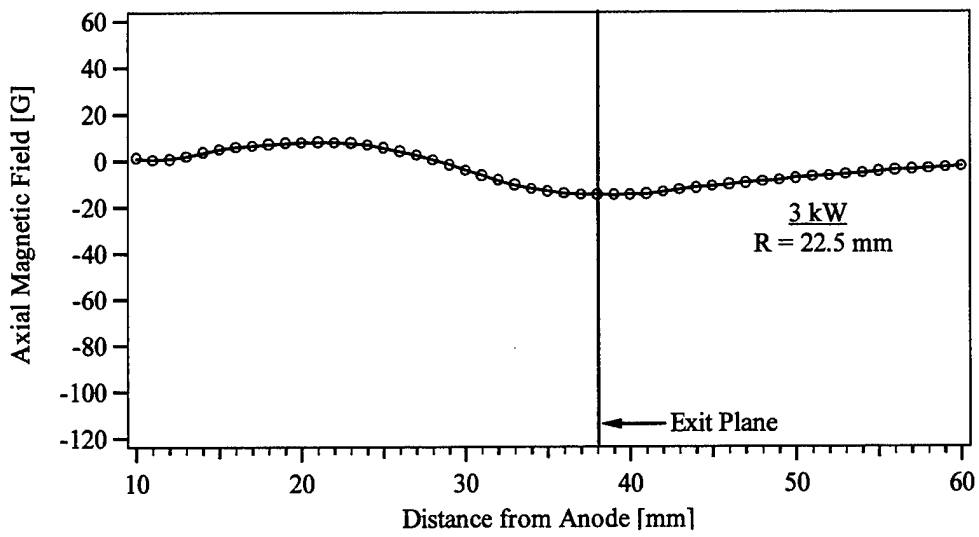


Figure 5.60 Vacuum axial magnetic field, Hall probe, 3 kW, $R = 22.5$ mm.

5.1.4 Hall Current

Hall current was measured directly using the probe described in Section 4.4.3 and is shown in Figures 5.61 – 5.70. Measurement uncertainty will be discussed in Chapter 6.

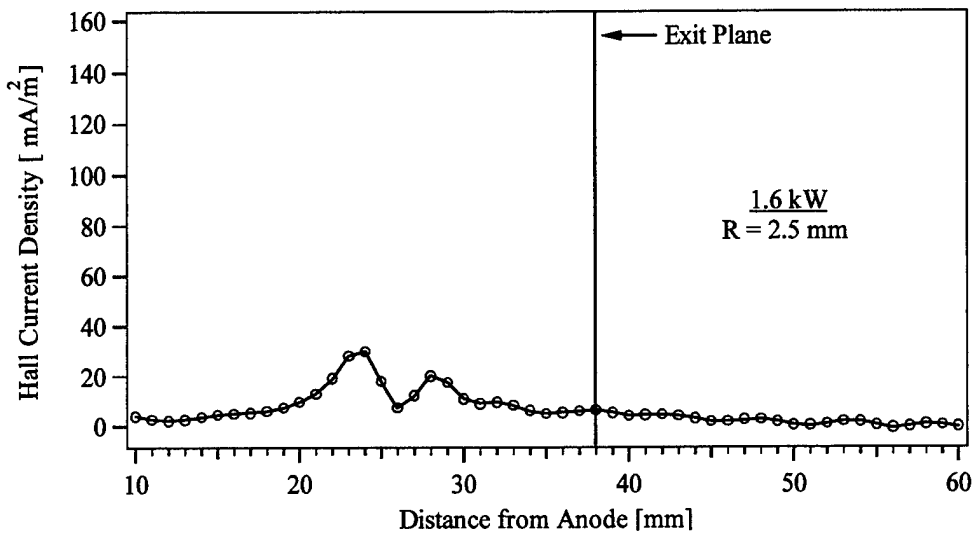


Figure 5.61 Hall current density, 1.6 kW, R = 2.5 mm.

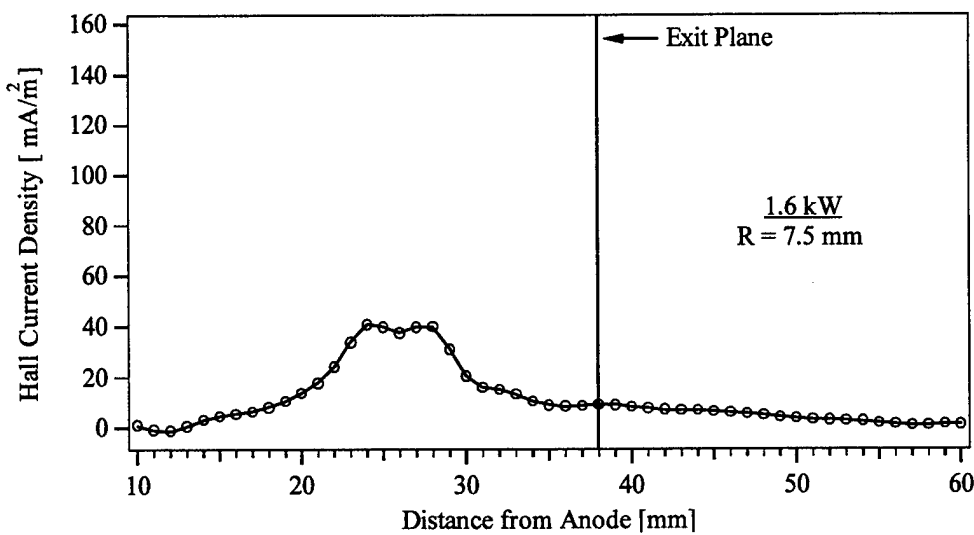


Figure 5.62 Hall current density, 1.6 kW, R = 7.5 mm.

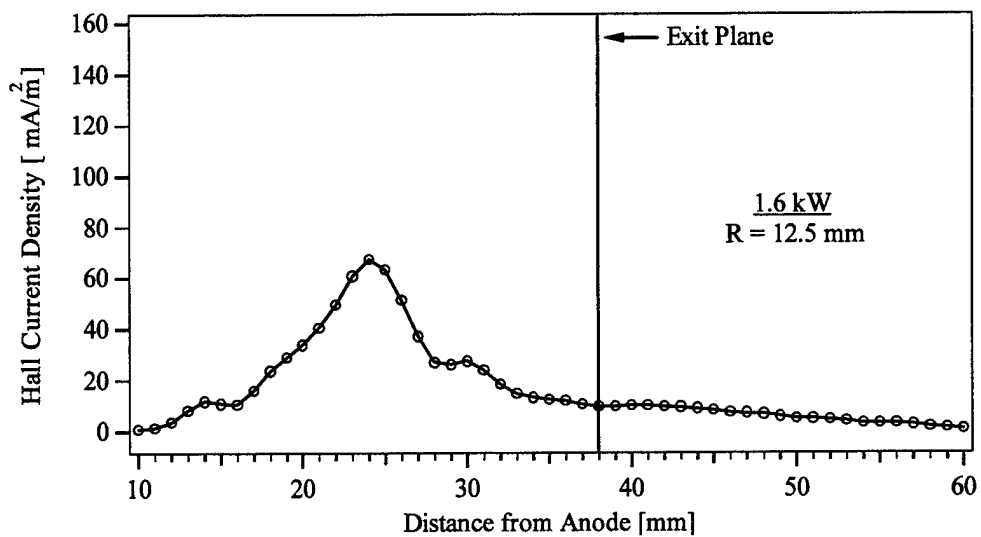


Figure 5.63 Hall current density, 1.6 kW, R = 12.5 mm.

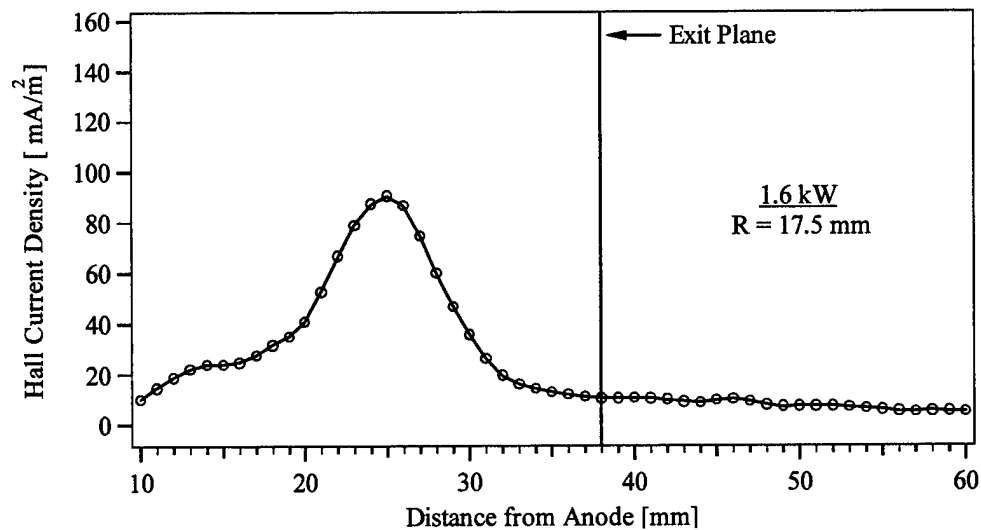


Figure 5.64 Hall current density, 1.6 kW, R = 17.5 mm.

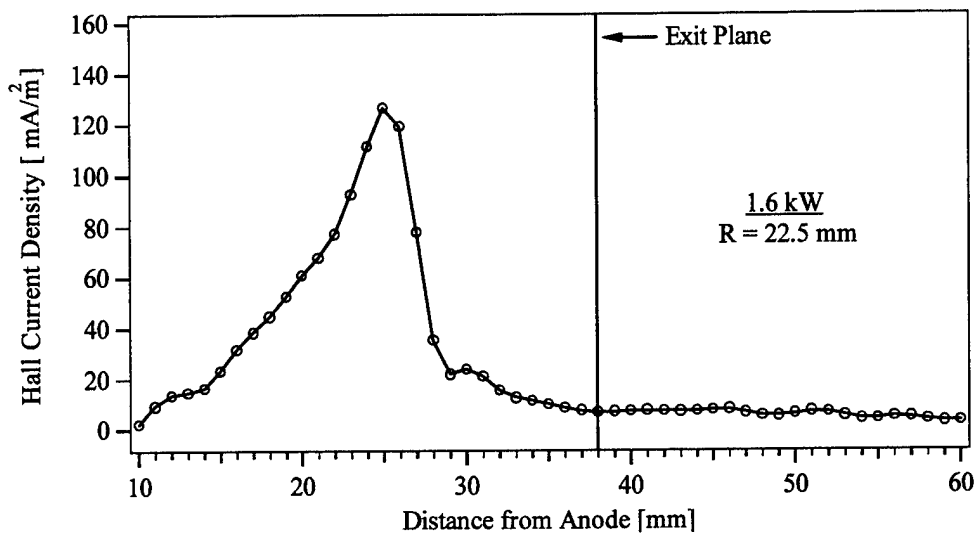


Figure 5.65 Hall current density, 1.6 kW, R = 22.5 mm.

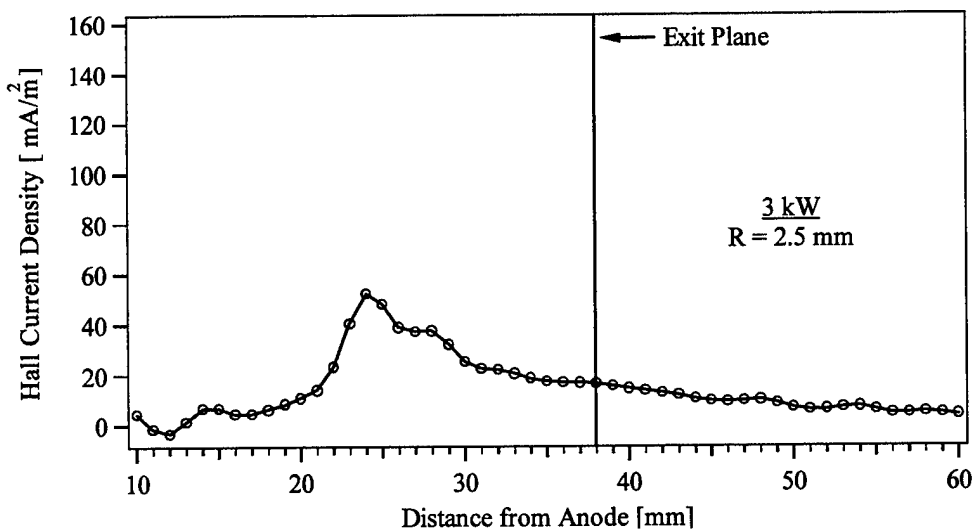


Figure 5.66 Hall current density, 3 kW, R = 2.5 mm.

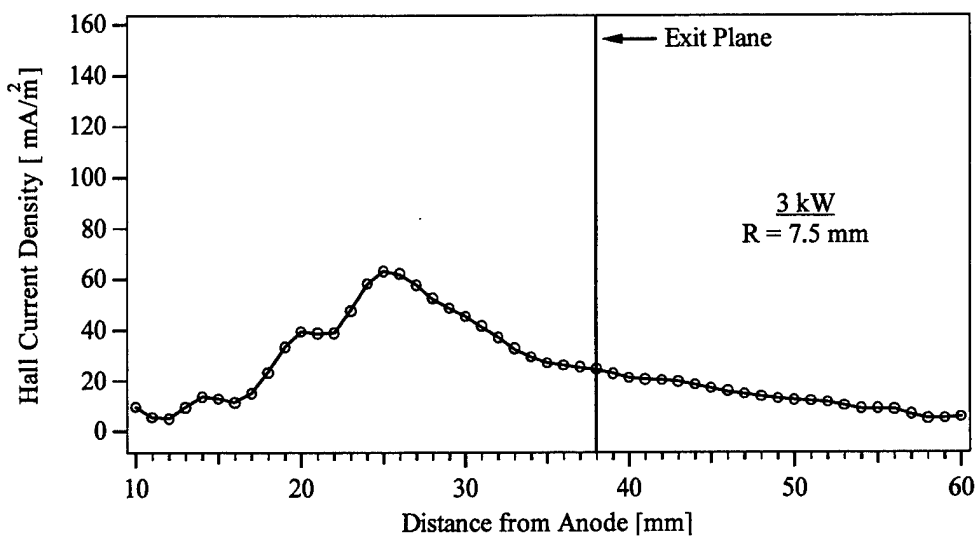


Figure 5.67 Hall current density, 3 kW, R = 7.5 mm.

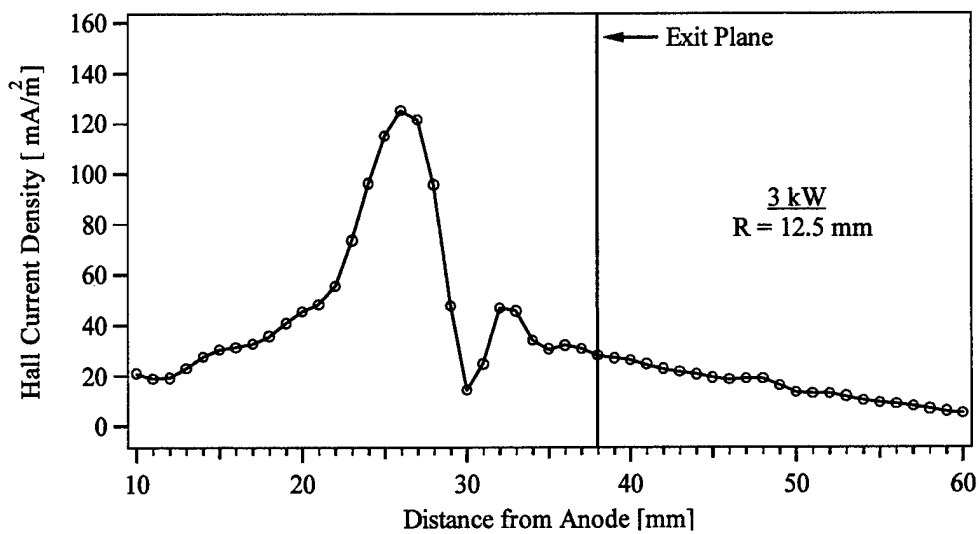


Figure 5.68 Hall current density, 3 kW, R = 12.5 mm.

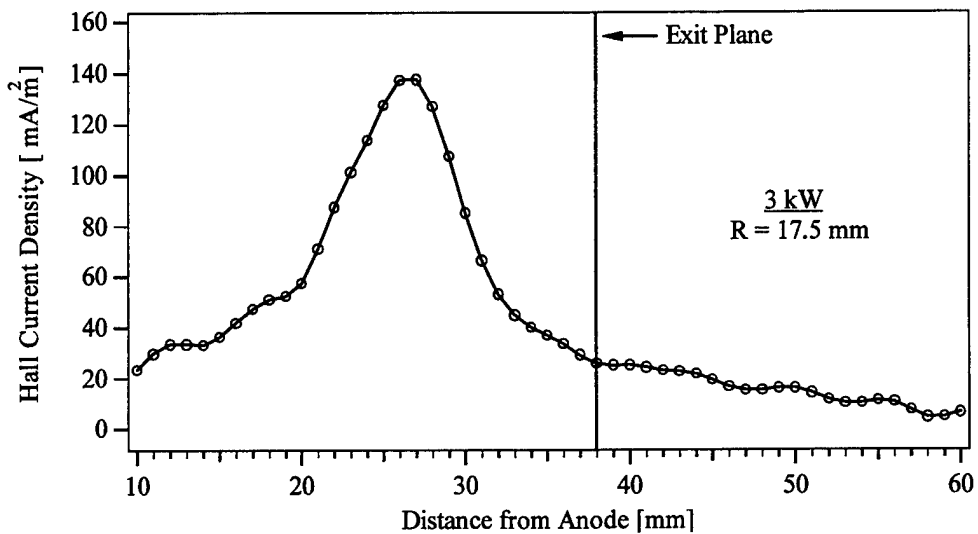


Figure 5.69 Hall current density, 3 kW, R = 17.5 mm.

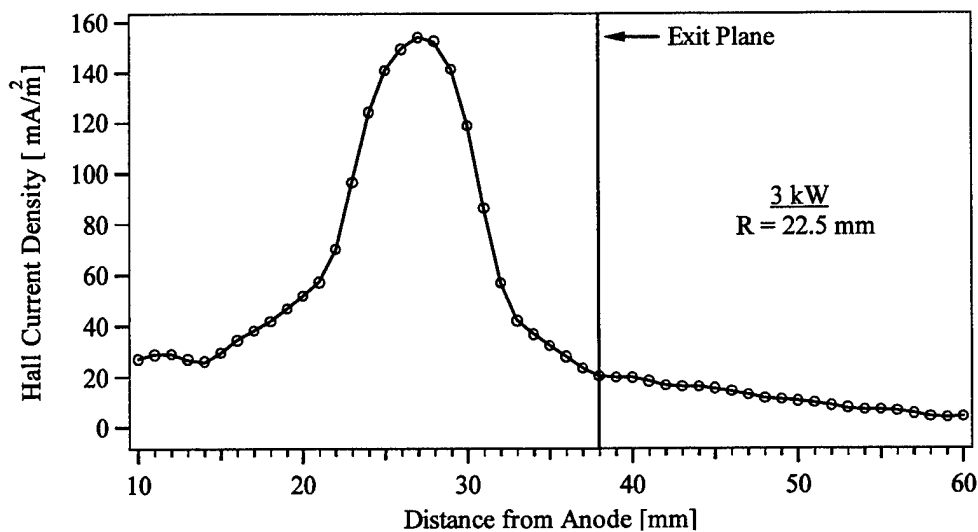


Figure 5.70 Hall current density, 3 kW, R = 22.5 mm.

5.2 Discussion of Probe Data

With the data provided in Section 5.1, it is now possible to begin examining the structure of the ionization and acceleration zones in the discharge channel of the Hall thruster. It is much more convenient to have the various plasma parameters overlaid on a single plot so that their profiles can be compared directly. Figures 5.71 – 5.80 contain the discharge channel data profiles at each thruster operating condition, at each radial position, and will be referred back to throughout the text of Section 5.2.

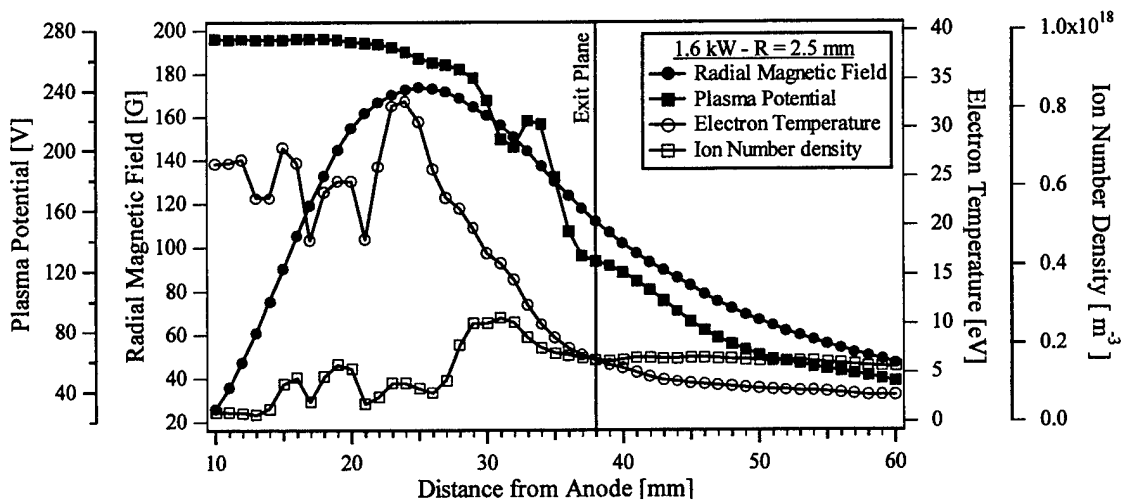


Figure 5.71 Plasma potential, radial magnetic field, electron temperature, and ion number density, 1.6 kW, R = 2.5 mm.

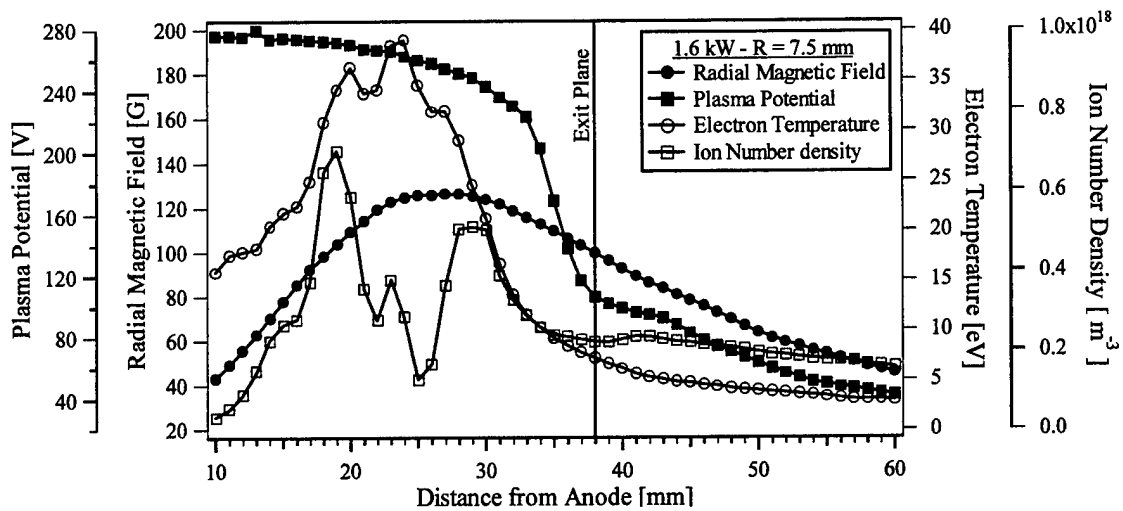


Figure 5.72 Plasma potential, radial magnetic field, electron temperature, and ion number density, 1.6 kW, $R = 7.5$ mm.

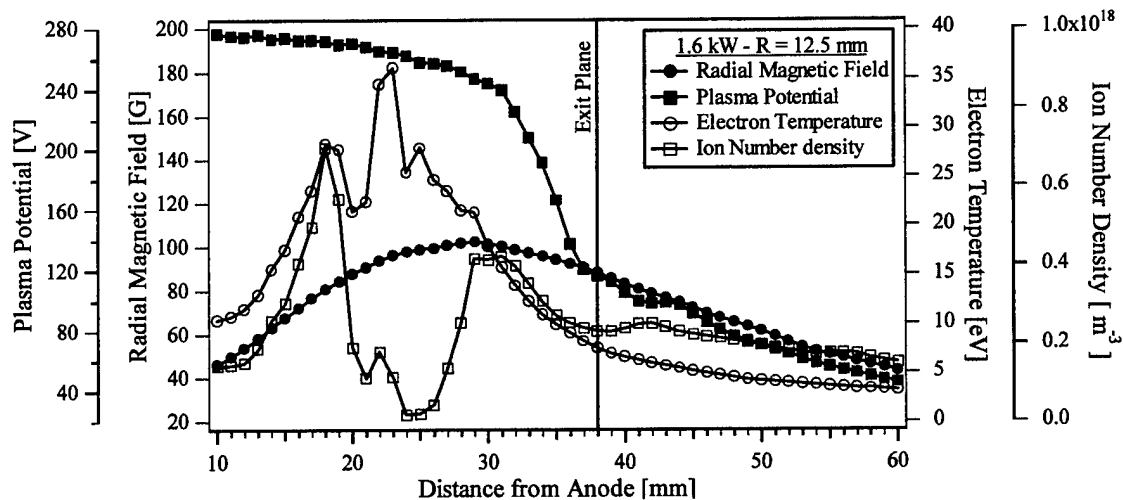


Figure 5.73 Plasma potential, radial magnetic field, electron temperature, and ion number density, 1.6 kW, $R = 12.5$ mm.

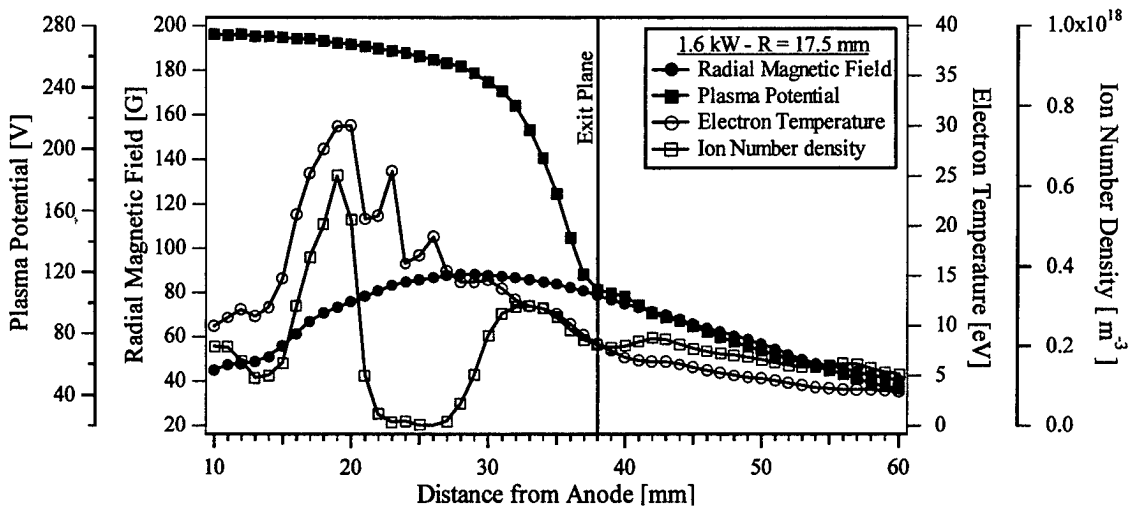


Figure 5.74 Plasma potential, radial magnetic field, electron temperature, and ion number density, 1.6 kW, $R = 17.5$ mm.

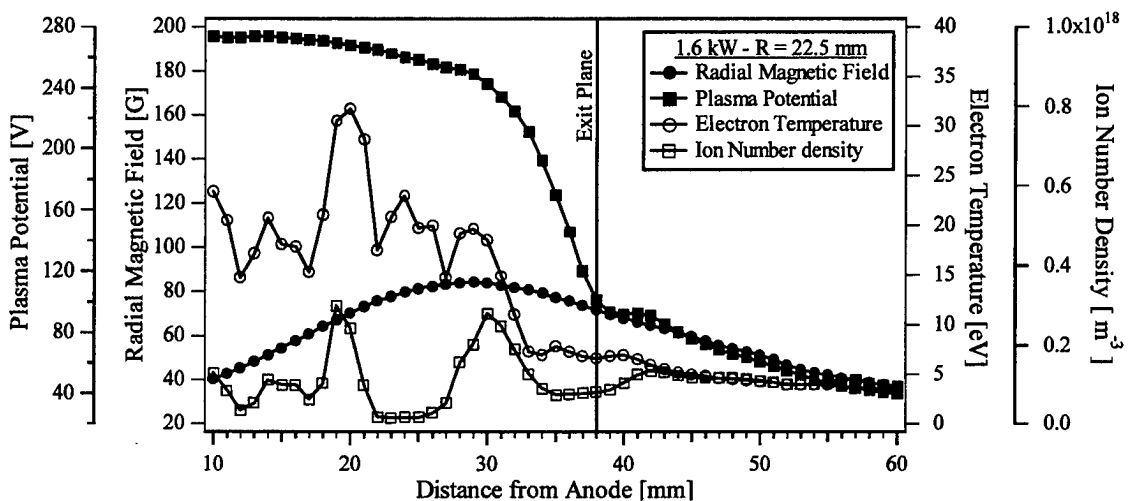


Figure 5.75 Plasma potential, radial magnetic field, electron temperature, and ion number density, 1.6 kW, $R = 22.5$ mm.

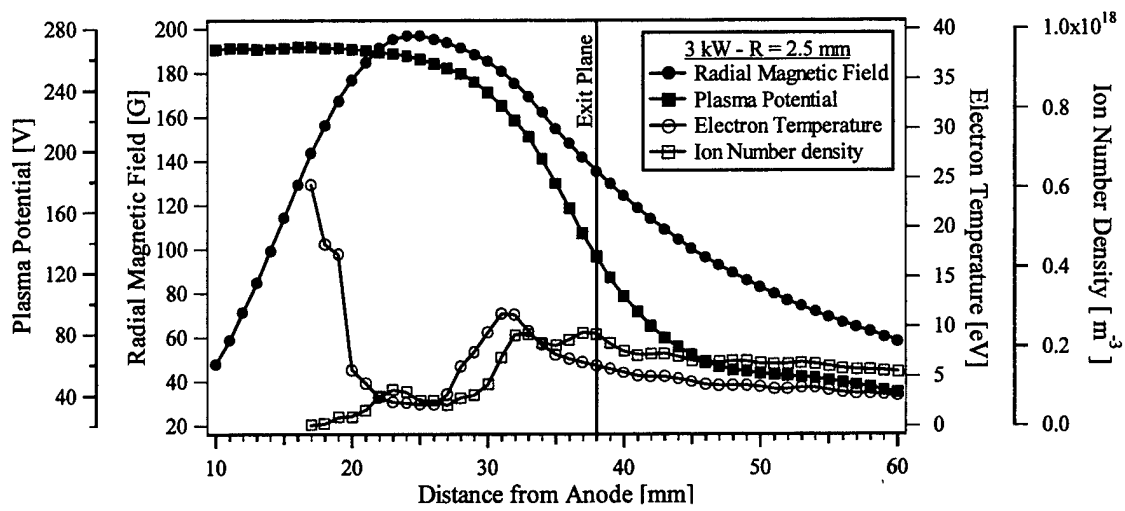


Figure 5.76 Plasma potential, radial magnetic field, electron temperature, and ion number density, 3 kW, $R = 2.5$ mm.

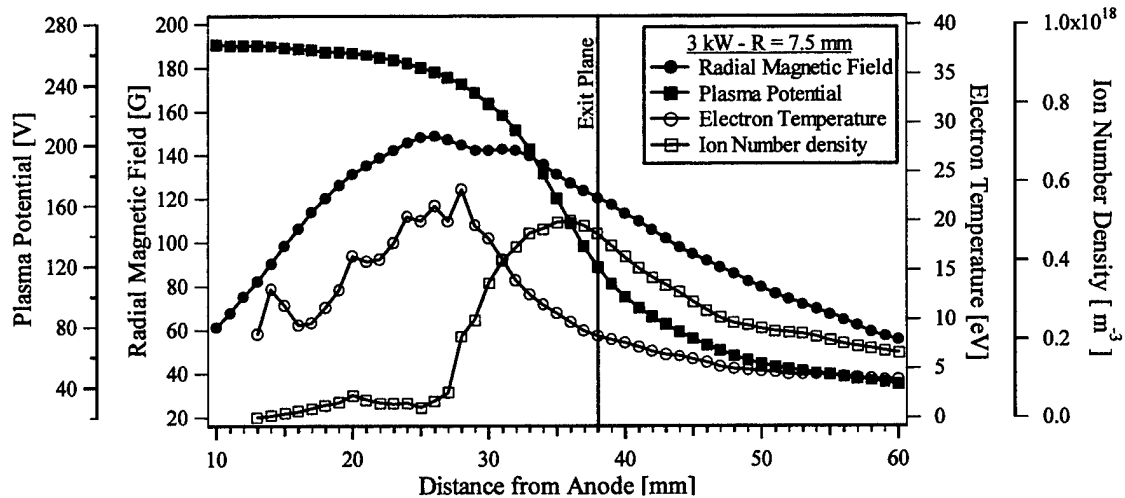


Figure 5.77 Plasma potential, radial magnetic field, electron temperature, and ion number density, 3 kW, $R = 7.5$ mm.

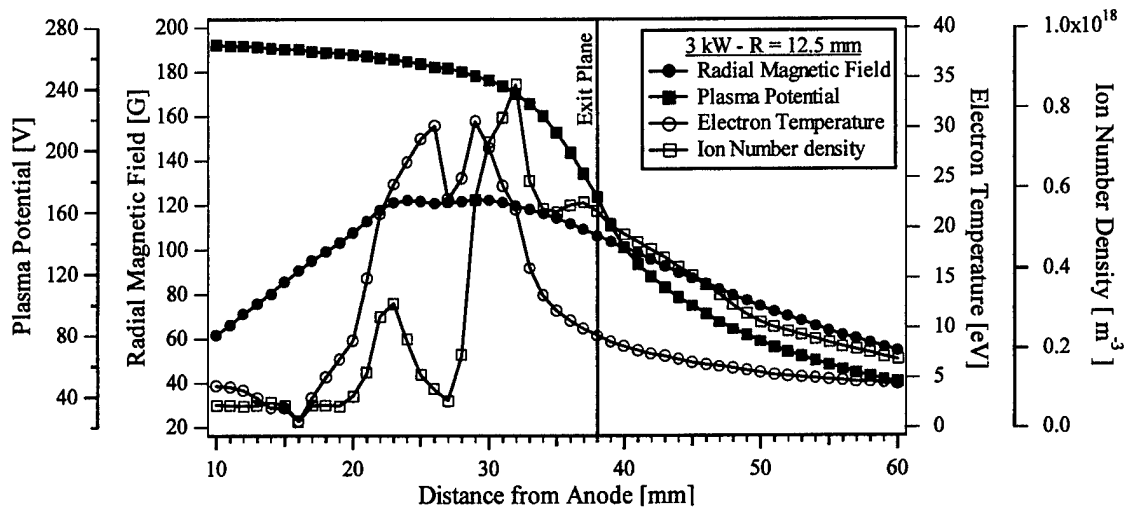


Figure 5.78 Plasma potential, radial magnetic field, electron temperature, and ion number density, 3 kW, R = 12.5 mm.

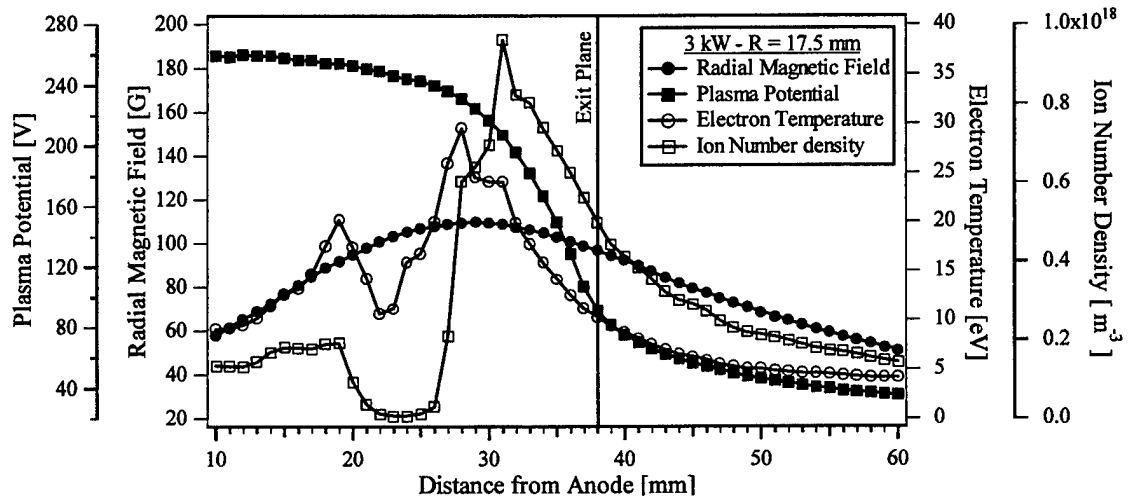


Figure 5.79 Plasma potential, radial magnetic field, electron temperature, and ion number density, 3 kW, R = 17.5 mm.

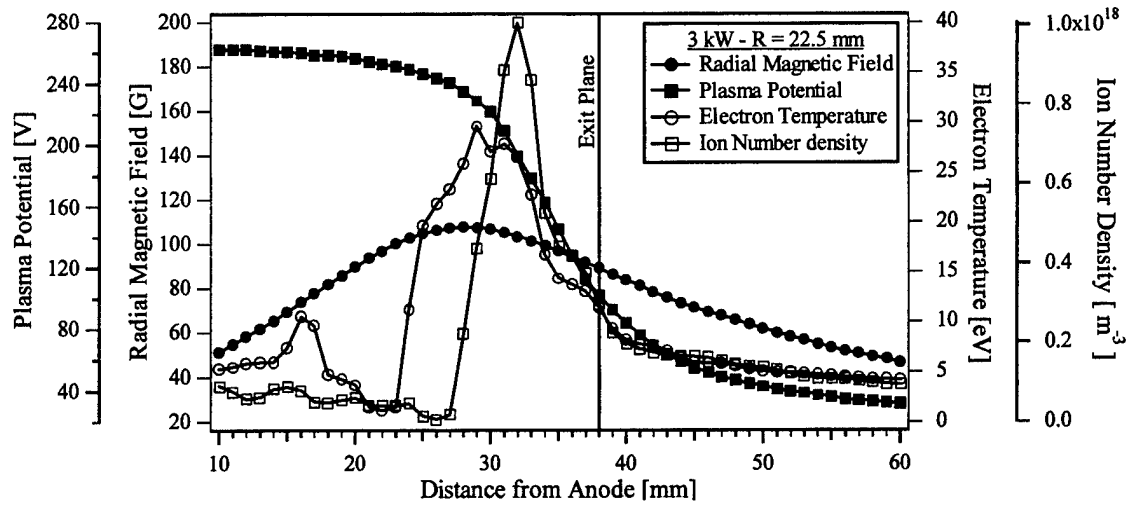


Figure 5.80 Plasma potential, radial magnetic field, electron temperature, and ion number density, 3 kW, R = 22.5 mm.

5.2.1 Plasma and Floating Potential

Plasma potential measurements with respect to electrical ground were made at a constant voltage, 300 V, at discharge current settings of 5.4 A (1.6 kW) and 10 A (3 kW). For the two cases considered here, the magnetic field profile (both magnitude and shape) was kept constant and only the mass flow rate was adjusted. The magnet settings were 3 A and 2 A on the inner and outer coils, respectively. This corresponds to the magnetic field profiles shown for the 3 kW case in Figures 5.76 – 5.80. Figures 5.71 – 5.75 show the plasma potential profiles at 1.6 kW. For the 1.6 kW case, the cathode potential with respect to ground was -21 V, therefore the anode potential was 279 V with respect to electrical ground. Figure 5.81a shows the plasma potential and axial electric field profiles at 1.6 kW.

Plasma potential profiles for the 1.6 kW case show that the potential remains nearly constant over the first 75% of the channel. As expected, a sharp drop occurs between 30 mm and 40 mm, indicative of the location of the main acceleration region. The axial electric field profiles show clearly the location of maximum acceleration at 35.5 mm, 2.5 mm upstream of the exit plane. The data indicate that the acceleration region extends 2 – 3 cm downstream of the exit plane, which agrees quite well with independent Laser-Induced Fluorescence (LIF) data taken by Williams² on the same thruster at the same conditions. These LIF measurements were made at axial positions 1 mm and 100 mm downstream of the exit plane and indicate ion speeds of 11,000 m/s and 16,000 m/s, respectively. This speed increase corresponds to an accelerating potential of approximately 90 V. Referring to Figures 5.71 – 5.75, plasma potential at the exit plane is 100 V and 10 cm downstream (not shown in the figure) decreases to approximately 15 V. Thus the accelerating potential as measured by LIF (90 V) agrees with that measured by the emissive probe (85 V) within 5%. This large potential drop outside the thruster has also been observed with the Stanford, low-power Hall thruster³. Note that the potential profile remains uniform across the width of the discharge chamber, which can be seen clearly in Figure 5.81a. LIF data from the P5² show the same uniformity.

One additional feature of the potential data that bears further scrutiny is the plateau that occurs a few millimeters downstream of the exit plane, most prominently seen on the inner wall profile, $R = 2.5$ mm. This will be discussed further below.

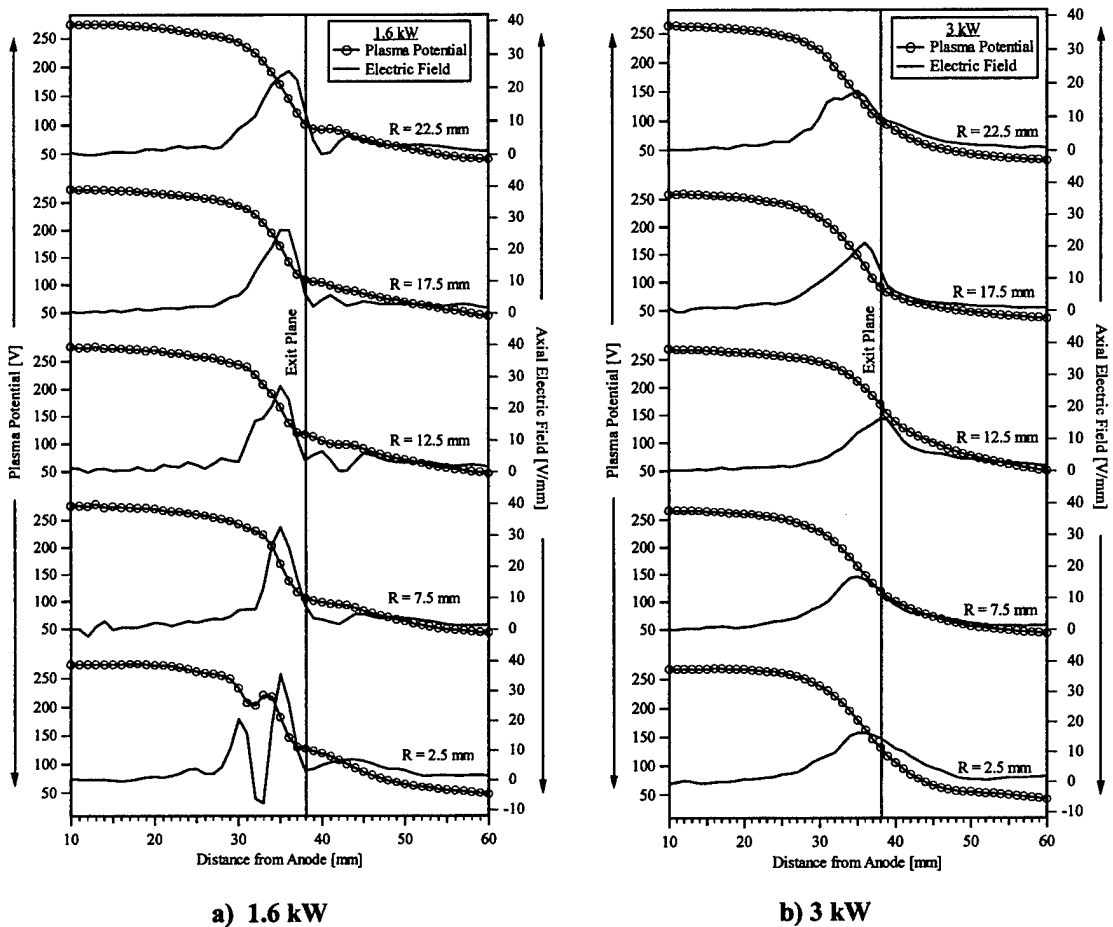


Figure 5.81 Plasma potential and electric field data. a) 1.6 kW, b) 3 kW.

Potential data were also taken at a higher power level to study the evolution of the potential structure. Figures 5.76 – 5.80 show plasma potential profiles at 300 V, 10 A at the same radial positions as in the 1.6 kW case. Cathode and anode potentials with respect to electrical ground were -23 V and 277 V, respectively. These data are very similar to the 1.6 kW case. The potential remains approximately constant, near anode potential, over the first 75% of the discharge channel. The acceleration region begins near the exit plane and extends several centimeters downstream. LIF² data at these conditions again show a significant acceleration downstream of the exit plane (~ 100 V),

however, they fail to reflect the lack of radial uniformity in the downstream accelerating potential which varies from approximately 75 V along the outer wall, to 150 V along the inner wall, to 180 V on the channel center-line. Referring to 5.81b, a significant feature of the 3 kW data is that the axial electric field magnitude is nearly 25% percent lower than that at 1.6 kW, indicating a longer acceleration region. Baranov⁴ has shown that the length of the acceleration layer depends on both the radial magnetic field profile and electron temperature. The increase in mass flow rate effectively increases the ionization collision frequency, lowering the energy of the electrons since the ionization process is a loss mechanism. The result is a lower temperature gradient, therefore, lower electric field. The reduction of temperature gradients with increasing discharge current is predicted by the one-dimensional code of Ahedo⁵. Referring to Figures 5.71 – 5.80, the peak electron temperature at 3 kW (~ 30 eV) is approximately 25% lower than at 1.6 kW (~ 40 eV).

Returning to the radial non-uniformity of the 3 kW potential profiles, note that the axial electric field peak along the outer wall (Figure 5.80) occurs 2 mm – 3 mm upstream of the exit plane as in the 5.4 A case. Along the inner wall (Figure 5.76), the peak is shifted forward but still occurs upstream of the exit plane. The most significant difference between the two cases is seen in the centerline data (Figure 5.78) where the peak axial electric field is shifted to a position downstream of the exit plane. As with the axial electric field magnitude, since the magnetic field is unchanged, this implies a shift in the electron temperature gradient. This may occur due to the higher density of ions on centerline retarding the flow of high-energy electrons toward the anode. It follows that

this effect would be less pronounced along the walls because of increased ion losses resulting from a longer acceleration region and because of wall current effects.⁶ There is also the possibility that the neutral population may not be completely uniform radially, retaining a jet-like structure by the time neutral particles transit the length of the discharge channel. Thus it may be more accurate to describe the temperature shift as the result of a high concentration of neutrals on centerline, the consequence of which is a concomitant concentration of ions.

One prominent feature that is virtually nonexistent at 3 kW is the plateau in the potential profile just downstream of the exit plane seen at 1.6 kW. This plateau is most prominent along the inner wall where the potential exhibits a local increase in the acceleration region near the exit plane. The magnitude of this perturbation decreases from the inner wall, where the radial magnetic field is strongest, to the outer wall, where the radial magnetic field is lower. Measurements of floating potential, referring back to Figures 5.11 – 5.20, with a cold probe showed similar results. At 1.6 kW, the cold probe floating potential exhibited a local plateau downstream (however, the cold probe showed the greatest perturbation along the outer wall as opposed to the inner wall for the emissive probe) of the exit plane while at 3 kW no such increase was observed. This implies that the observed plateau is an inherent feature of the plasma and not an artifact of the emitted electrons from the emissive probe. It is believed that this perturbation may be the result of turbulence in the plasma flow as it expands out of the channel. However, a satisfactory explanation for this effect is not available at this time. It is worth noting that this feature has been observed in other laboratory Hall thrusters as well².

All of the axial sweeps were combined to generate a two-dimensional contour of the plasma potential. Figure 5.82 shows the plasma potential contours for the 1.6 kW case. It is not as obvious from Figure 5.82 that a local plateau occurs just downstream of the exit plane but the radial uniformity is clear. Figure 5.83 shows the plasma potential contours for the 3 kW case. As mentioned previously, one way in which the plasma potentials of the 3 kW case differ from those of the 1.6 kW case is that the peak electric field on center line at 3 kW is shifted downstream of the exit plane. This is readily apparent in Figure 5.83 where a potential “jet” occurs on the centerline of the discharge channel.

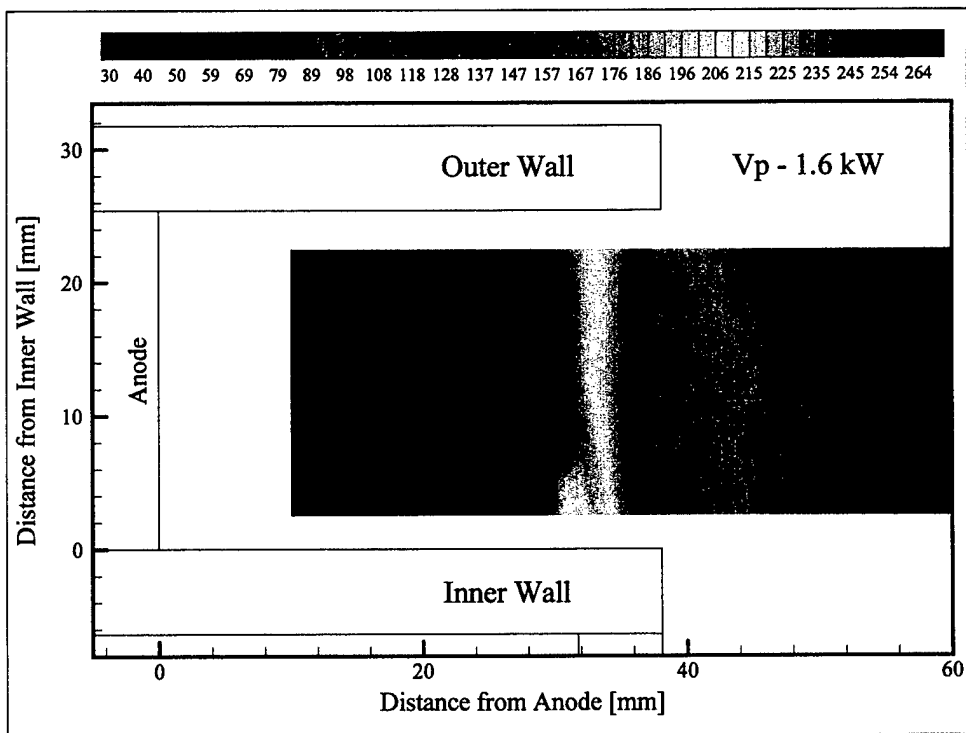


Figure 5.82 Plasma potential contours at 1.6 kW. Units are in volts.

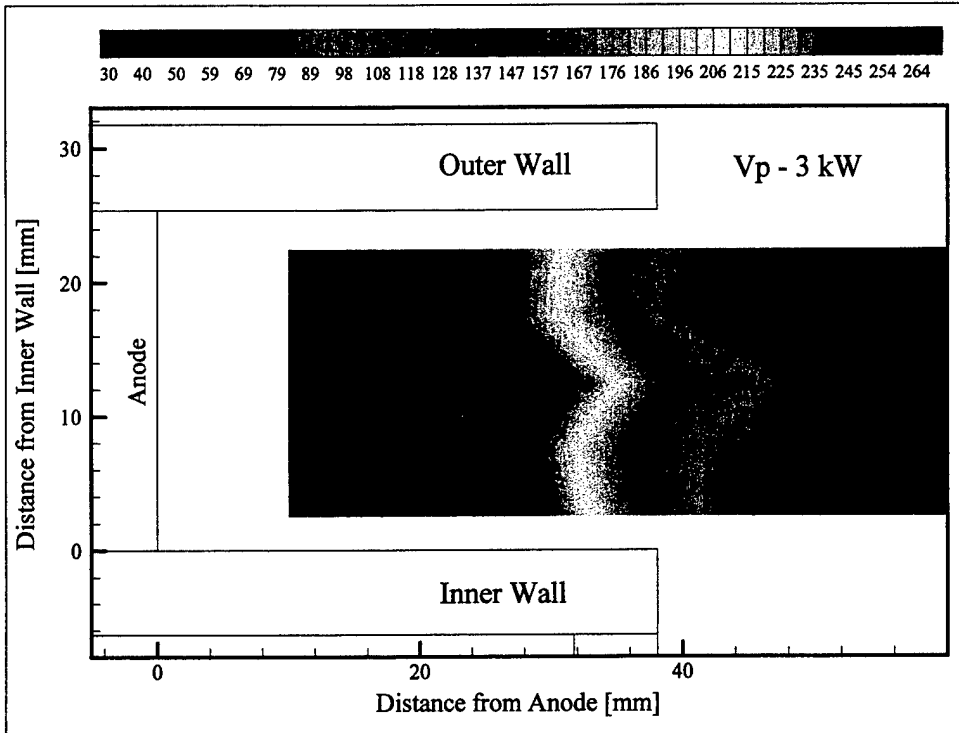


Figure 5.83 Plasma potential contours at 3 kW. Units are in volts.

Additional data at 3 kW and 2.4 kW, not included here, show this structure to be repeatable and evolving, becoming more pronounced as the discharge current is increased. This structure results in significant divergence of the ions as they are accelerated out of the thruster. LIF² data at this condition reflect the increased divergence with a 50% increase in radial ion velocity (both inward and outward) compared to the 1.6 kW case.

The discharge current was not recorded during emissive probe measurements at 1.6 kW. However, at 3 kW, the discharge current was recorded for each axial probe sweep and a 5 – 15% variation in magnitude was observed. While zero perturbation would have been preferred, the current perturbations, when combined with the plasma potential profiles,

yielded some unexpected insights. Figure 5.84 shows three representative traces of the discharge current and the computed axial electric field along the inner wall, outer wall, and on centerline.

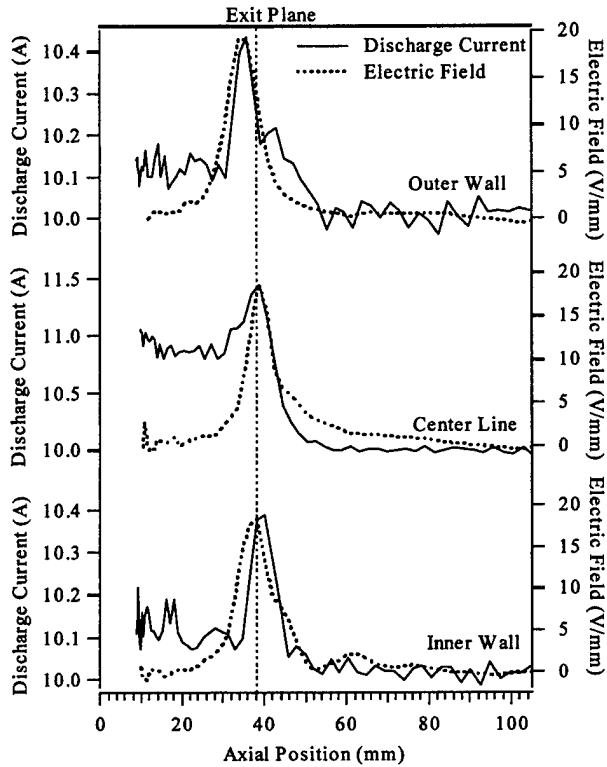


Figure 5.84 Perturbations in the discharge current as a function of probe position compared to the axial electric field profiles for the 10 A case. Profiles for the 5.4 A case showed the same correspondence.

Only three data sets are shown here, however, the axial sweep at each radial location across the discharge chamber showed the same results. From Figure 5.84, perturbations to the discharge current are seen to correspond very well to the spatial location of the peak axial electric field. Power deposition to the probe is proportional to the third power of the **ExB** drift velocity, while the **ExB** drift velocity is proportional to the magnitude of the electric field. Therefore, it is expected that the probe would experience the greatest heat load where the electric field has its largest magnitude. It follows immediately that

this would be the point of greatest probe material ablation and hence discharge current perturbation. However, if this were the only mechanism disturbing thruster operation, once the probe was inserted into the discharge chamber, a portion of the probe would always receive this heat load, and probe material would continue to ablate. In this case, the discharge current would remain artificially high while the probe was present inside the discharge chamber. This would also be the case if the probe were simply acting as a physical barrier, impeding the motion of the electrons as they drifted azimuthally inside the thruster.

Figure 5.85 shows a representative profile of the discharge current including both the insertion and removal of the probe.

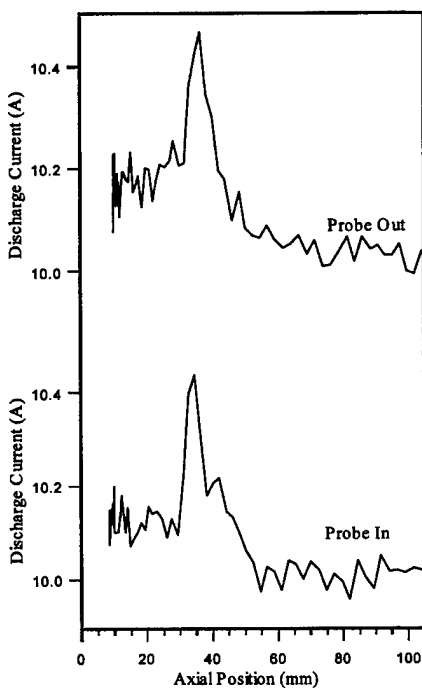


Figure 5.85 Discharge current as a function of probe position inside the discharge chamber. Data are for the 3 kW case at a radial location of $R = 22.5$ mm.

Recall that the probe assembly is 152 mm long with the emitting tungsten filament loop extending approximately 1 mm outside the alumina insulator. The axial position in Figure 5.85 corresponds to the tip of the filament. Therefore, the greatest perturbation of the discharge current occurs when the tungsten filament is coincident with the peak axial electric field. This is consistent with the initial HARP results using the planar triple probe, as shown in Figure 4.21b, where the electrode surface area exposed to the plasma was much smaller. These results suggest two possible mechanisms for thruster perturbation; either the electrode is shorting the electric field by providing a conduction path for the electrons or the emitted electrons are somehow coupling with the plasma. In order to clarify this issue, the discharge current was also monitored during measurements using a floating double Langmuir probe. The electrodes were approximately 2 mm long and remained “cold”, i.e. the probe emitted no electrons. Figure 5.86 shows the discharge current at 3 kW, comparing the perturbation from both the emissive and cold probe.

The data do not allow for a definitive conclusion, however, it is obvious from Figure 5.86 that the cold probe does perturb the thruster when coincident with the peak electric field but significantly less than for the emissive probe. Thus both mechanisms appear to contribute to thruster perturbation with the emitted electrons causing the bulk of the perturbation during plasma parameter measurements. Further, visual inspection of the probes used throughout these experiments showed no observable material ablation.

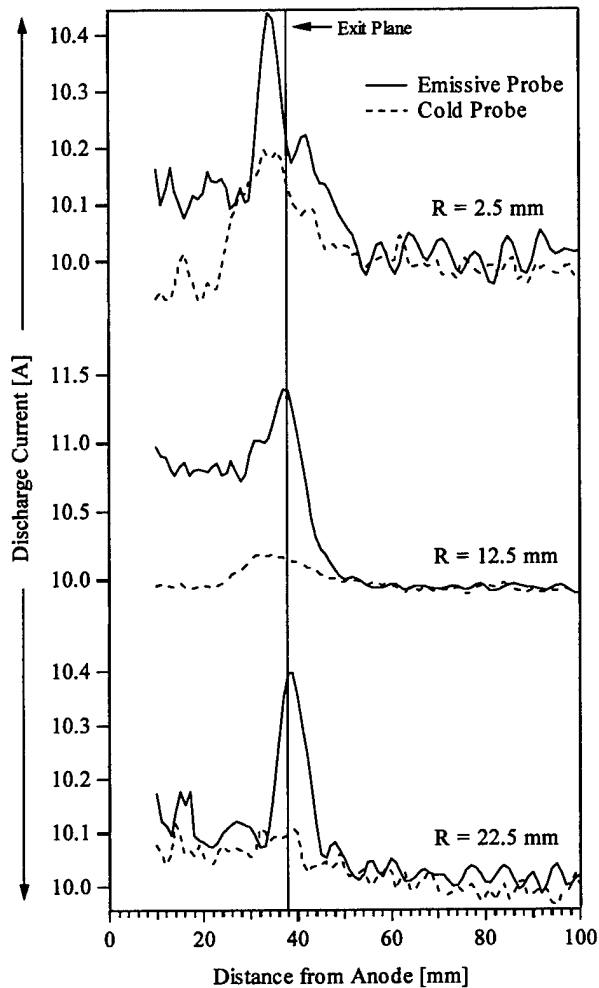


Figure 5.86 Discharge current perturbation for emissive and cold probes. Data are for the 3 kW case.

5.2.2 Electron Temperature – Ion Number Density

Electron temperature and ion number density measurements were made at a constant voltage, 300 V, at discharge current settings of 5.4 A (1.6 kW) and 10 A (3 kW). The magnet settings at 1.6 kW were 2 A and 1 A on the inner and outer coils, respectively. This corresponded to the magnetic field profiles in Figures 5.70 – 5.75. The magnet settings at 3 kW were 3 A and 2 A on the inner and outer coils, respectively. This setting corresponded to the magnetic field profiles in Figures 5.76 – 5.80. Note that in this case

the magnet settings at 1.6 kW were different from the magnet settings for the plasma potential measurements at 1.6 kW. This was unavoidable as the thruster became unstable at the lower magnet settings during temperature and density measurements. It was considered more important to maintain the same mass flow rate, discharge current, and discharge voltage between tests, therefore the magnets were adjusted to accomplish stable operation. Referring back to the magnetic field profiles, the profile shapes for the two magnet settings remained essentially the same while the magnitude differed by no more than approximately 10%. This difference was considered to have very little effect on the final measurements. The following discussion will concentrate on the internal and very-near-field channel data, the contours of which are shown in Figure 5.87 and 5.88.

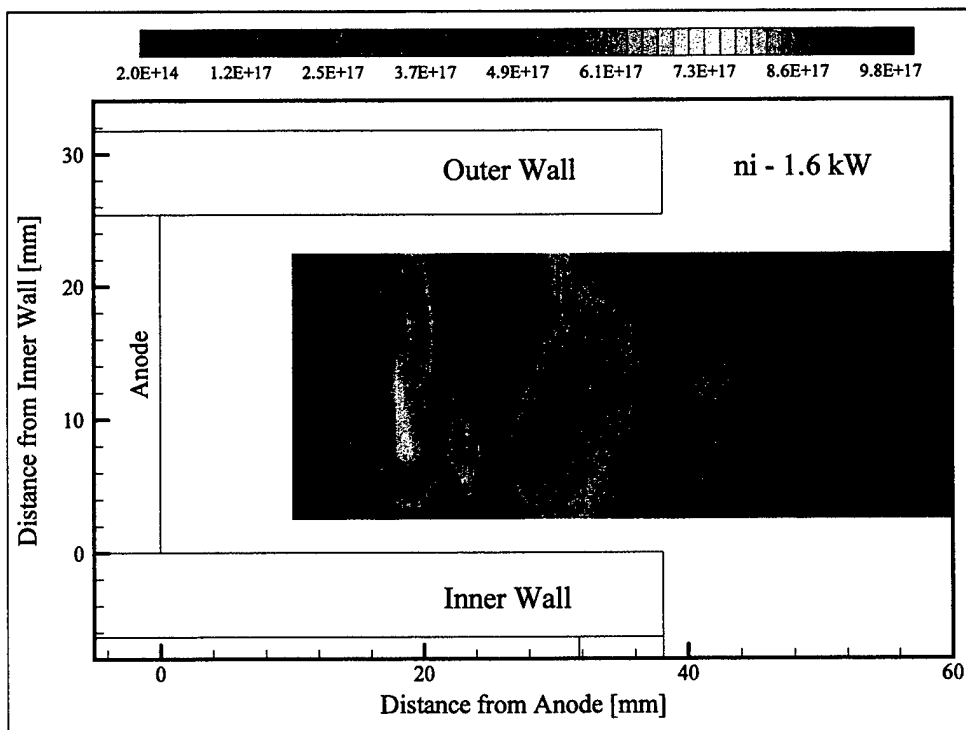


Figure 5.87 Ion number density contours, 1.6 kW. Units are in m^{-3} .

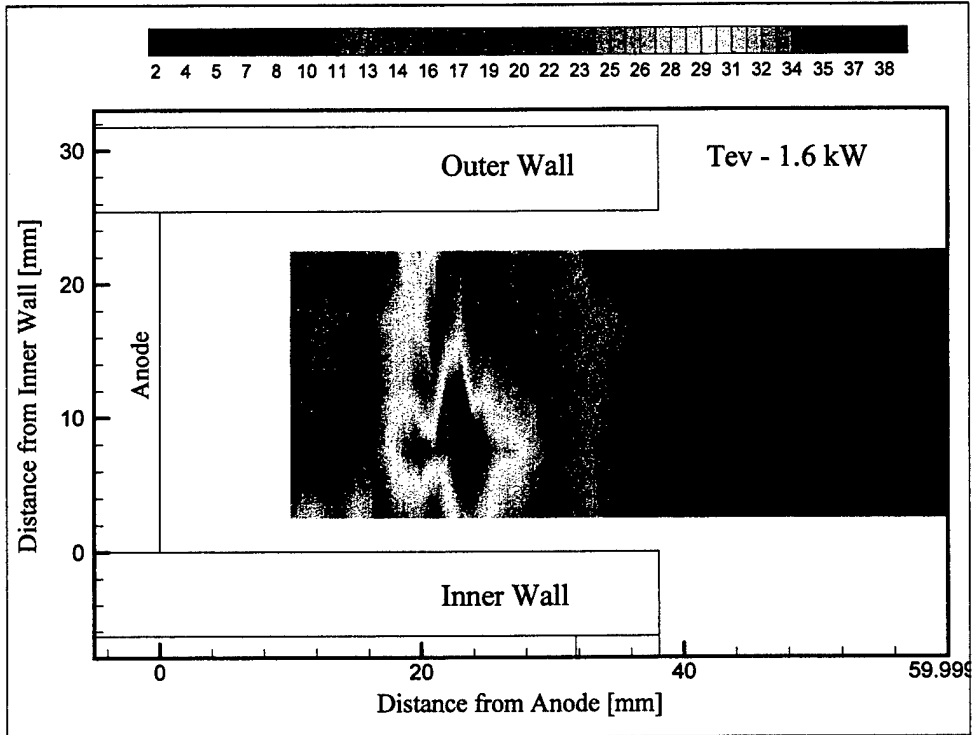


Figure 5.88 Electron temperature contours, 1.6 kW. Units are in eV.

The ion number density contour plot of Figure 5.87 illustrates the most striking feature of the 1.6 kW operating condition. The data exhibit, with the exception of the inner wall region, a double-axial-peak structure indicating two regions of ionization. The primary zone occurs quite far upstream of the exit plane (~20 mm) while the second occurs much closer to the exit plane (~32 mm). Referring to Figure 5.88, it can be seen that this primary ionization zone closely corresponds spatially with the peak electron temperature. The electron temperature begins to decrease considerably in the vicinity of the secondary peak, implying a different ionization mechanism. From the potential and magnetic field profiles, it was determined that this second ionization zone corresponds approximately to the location of high electron drift velocity, i.e. the Hall current. The Hall current will be

presented in more detail in Section 6.1. Figure 5.89 shows the axial profile of electron azimuthal energy.

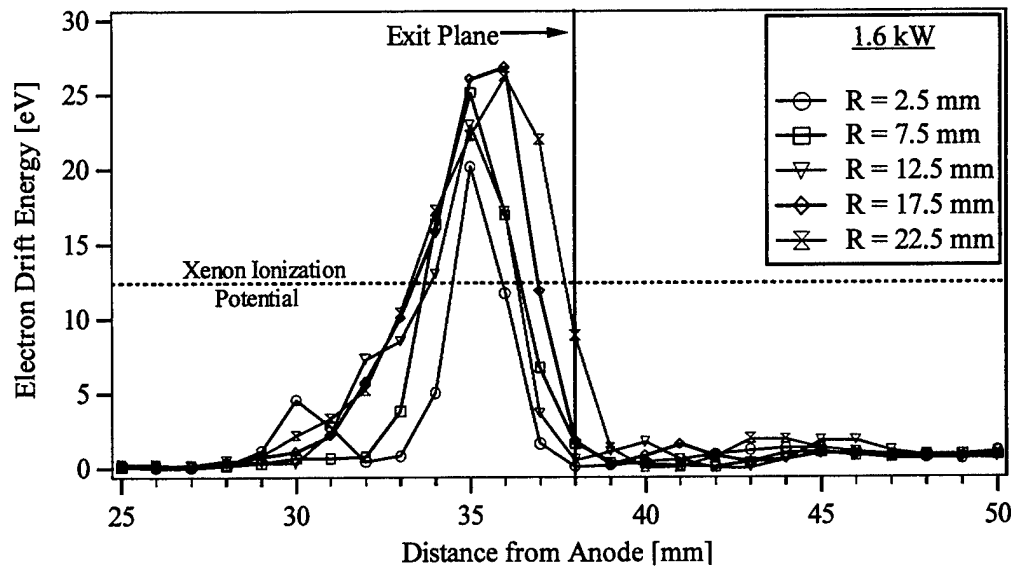


Figure 5.89 Electron drift energy profiles, 1.6 kW.

Drift energy is computed from the $\mathbf{E} \times \mathbf{B}$ drift velocity. The peak energy corresponds roughly to the spatial location of the secondary ionization zone shown by the local density increase near the exit plane in Figure 5.87.

Hall thrusters ideally operate such that ionization and acceleration occur at the same location, near the exit plane of the thruster. This keeps ion losses to the walls at a minimum, increasing the performance of the thruster and reducing material erosion. The location of a main ionization peak far upstream of the exit plane helps to explain the lower efficiency of the P5 at low power. The ionization and acceleration zones are far apart and ions formed at this location see very little axial acceleration. This is evidenced by the low potential gradient in the primary ionization region. The result is a large loss of

ions to the walls of the discharge channel. This is supported by observations of the erosion patterns in the P5 that show erosion of the boron nitride starting approximately 20 mm from the anode and extending to the end of the channel. While the P5 is run at a number of different power levels, a majority of its run time has been accrued at the 1.6 kW condition.

As stated previously, Hall thrusters ideally ionize and accelerate in the same location, near the exit plane. This behavior is observed at 3 kW and will be discussed in the next section. An explanation for the considerably different density profiles of the 1.6 kW case can be found by examining more closely the mechanisms of ion formation, paying particular attention to how thruster operating conditions vary from those at 3 kW. Recall from the description of the thruster physics that the electrons gain energy from the applied accelerating voltage as they travel upstream to the anode. Conversely, they experience energy losses through collisions with heavy particles (ions and neutrals) and with the channel walls. Thus it is expected that electron temperature will be low outside the thruster where electrons are first emitted from the cathode. Moving toward the anode, temperature will rise as electrons gain energy through interaction with the electric field then plateau and drop as they lose energy via heavy particle and wall collisions. Temperature magnitude and its peak location will be determined by a complicated balance between the various energy loss/gain mechanisms. Discharge voltage and magnetic field configuration for the two cases are essentially the same; the major difference occurs in the mass flow rate. At 1.6 kW, the mass flow rate is roughly half, with a correspondingly lower neutral particle density. As a result, the electrons

experience fewer collisions and their net energy gain is larger. This explains the higher temperatures compared to the 3 kW case. However, it is the collisions that provide a mechanism for electron transport across magnetic field lines, referred to as a “random-walk” process. The question then is why the temperature peak, and hence ionization, occurs so far upstream. A possible explanation is that at higher temperatures, the electrons are trapped less effectively by the radial magnetic field. Thus electron transport depends less on collisions at low flow rates than at high. The net effect is that electron transport increases, electron temperature is larger, and the peak occurs further upstream.

In contrast to the 1.6 kW case, data at 3 kW show a single ionization zone close to the acceleration region. The number density profiles follow the electron temperature, which is expected as the high temperature electrons are the main ionizing mechanism. Figures 5.90 and 5.91 show the ion number density and electron temperature contours.

It can be seen clearly that density peaks at an axial position of approximately 32 mm. Referring back to the plasma potential profiles, this corresponds to the beginning of the main potential gradient. Obviously, this significantly reduces ion losses to the walls of the discharge channel since the ions are accelerated out of the thruster almost immediately after being formed. This would account for the increased efficiency compared to the 1.6 kW condition.

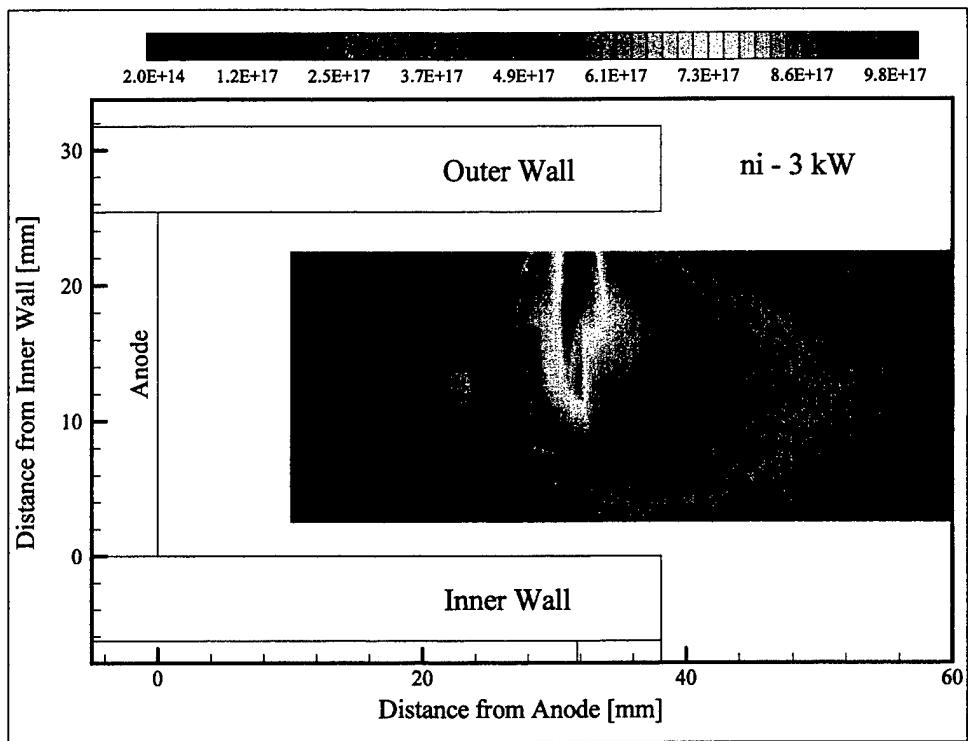


Figure 5.90 Ion number density contours, 3 kW. Units are in m^{-3} .

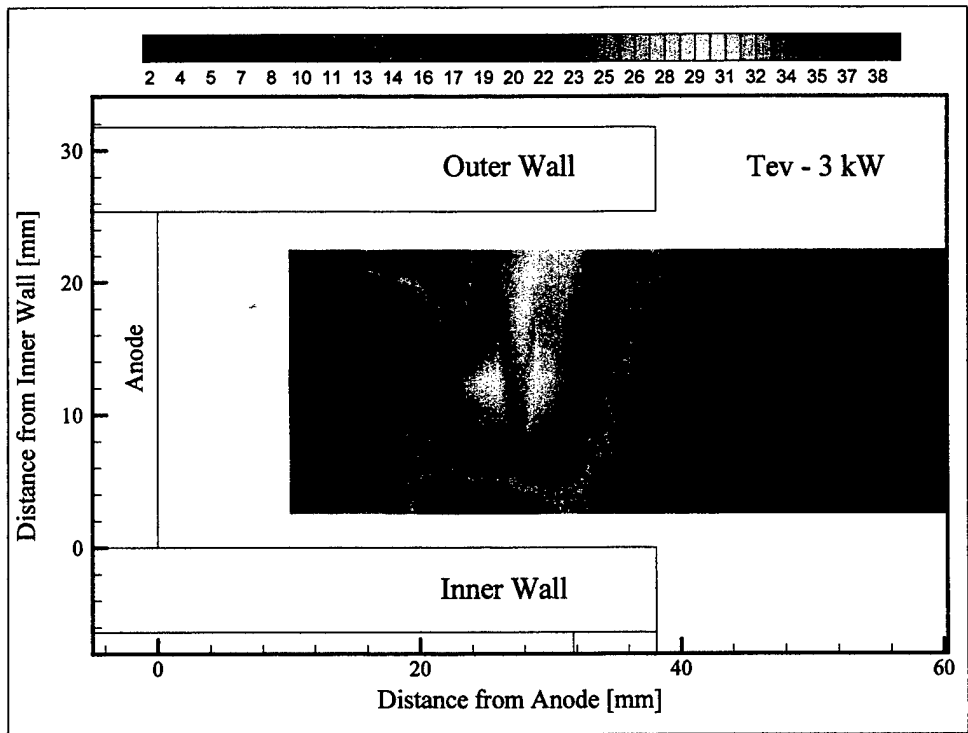


Figure 5.91 Electron temperature contours, 3 kW. Units are in eV.

An interesting feature of the number density profile along the channel centerline, as shown in Figure 5.78, is the small secondary peak at the exit plane. As in the 1.6 kW case, the energy of the Hall current electrons is computed and the results are displayed in Figure 5.92.

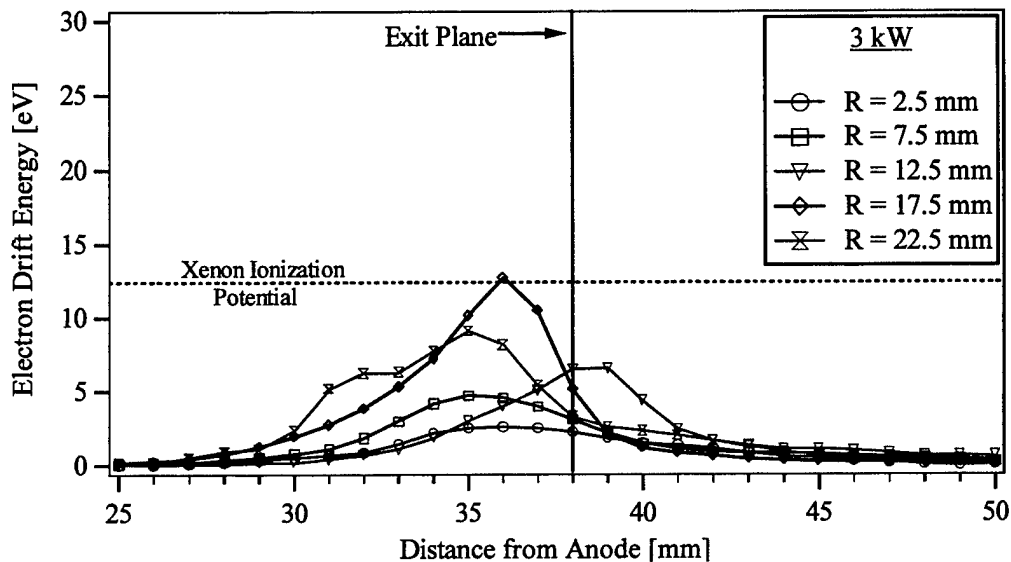


Figure 5.92 Electron drift energy profiles, 3 kW.

The electron drift energy peak for the centerline data corresponds very closely to the secondary density peak in Figure 5.78. If only single collisions are assumed, the drift energy appears too low to account for this additional ionization. However, the electron drift velocity is two orders of magnitude greater than the ion velocity. In the time it takes the relatively slow moving ions to traverse the acceleration zone, the electrons will have completed many cycles around the discharge channel. This greatly increases the probability of multiple collisions and offers an explanation for the secondary peak in Figure 5.78. The obvious question, then, is why this effect is not observed in the rest of

the 3 kW data. Referring back to Figures 5.76 – 5.80, the primary peak for the density data occurs several millimeters upstream of the exit plane (~35-36 mm), coinciding with the peak electron drift energy (with the exception of the centerline data) in Figure 5.92. The contribution of the Hall current would then be obscured by the primary ionization from electrons with a large thermal temperature.

References for Chapter 5

¹ Hutchinson, I.H., *Principles of Plasma Diagnostics*. New York, Cambridge University Press, 1987.

² Williams, G.J., Smith, T.B., Gulczinski, F.S., Beal, B.E., Gallimore, A.D., Drake, R.P., "Laser Induced Fluorescence Measurements of Ion Velocities in the Plume of a Hall Effect Thruster," AIAA-99-2424, 35th AIAA / ASME / SAE / ASEE Joint Propulsion Conference, Los Angeles, CA, June 20-24, 1999.

³ Hargus, W.A., Cappelli, M.A., "Interior and Exterior Laser-Induced Fluorescence and Plasma Potential Measurements on a Laboratory Hall Thruster," AIAA-99-2721, 35th AIAA / ASME / SAE / ASEE Joint Propulsion Conference, Los Angeles, CA, June 20-24, 1999.

⁴ Baranov, V.I., Nazarenko, Y.S., Petrosov, V.A., Vasin, A.I., Yashnov, Y.M., "Energy Balance and Role of Walls in ACDE," IEPC-97-060, 25th International Electric Propulsion Conference, Cleveland, OH, August 1997.

⁵ Ahedo, E., Martinez-Sanchez, M., "One-Dimensional Plasma Structure in Hall Thrusters," AIAA-98-8788, 34th AIAA / ASME / SAE / ASEE Joint Propulsion Conference, Cleveland, OH, July 13-15, 1998.

⁶ Kim, V., "Main Physical Features and Processes Determining the Performance of Stationary Plasma Thrusters," *Journal of Propulsion and Power*, Vol. 14, No. 5, 1998, 736-743.

CHAPTER 6

INTERNAL AND NEAR FIELD DATA ANALYSIS

6.1 Hall Current

Figures 5.61 – 5.70 in Chapter 5 show the Hall current density measured directly using a planar probe. These measurements indicate a total Hall current magnitude consistent with that calculated from measured plasma parameters, to be presented below. However, the peak Hall current does not correspond to the maximum in the electric field as expected. Upon further consideration, it was determined that the planar collection electrode should have been biased at the plasma potential rather than being allowed to float¹. The floating potential of the probe is determined by a balance of the flux of charged particles to the probe such that the net current is zero; the probe potential, when oriented to collect the Hall current, differed from that when the Hall current was absent. Further, a double probe was used and the planar electrode was actually biased several tens of volts relative to the floating potential. The end result is that the potential of the planar probe was not well defined and even had it been, it most likely was not at plasma potential everywhere in the channel. Thus, for the remainder of this chapter, the Hall current calculated from the measured plasma parameters will be used.

As discussed earlier, the azimuthal motion of the electrons, the Hall current, is a consequence of the crossed electric and magnetic field configuration. This motion is the cumulative effect, averaged over many gyroradii, of small variations induced in each cycle of the electrons cyclotron motion by the electric field. The drift velocity can be calculated from the known electric and magnetic field magnitudes and is defined by Equation 6-1.

$$\mathbf{V}_{ExB} = \frac{\mathbf{E} \times \mathbf{B}}{B^2} = \frac{E_j B_k - E_k B_j}{B^2} \approx \frac{E_j}{B_k} \quad \text{Eq. 6-1}$$

In Equation 6-1, the axial magnetic field and the radial electric field are both small and the second term in the numerator is dropped. Using the ion number density, and assuming quasineutrality, the Hall current density is then computed according to Equation 6-2.

$$j_{ExB} = n_i q V_{ExB} \quad \text{Eq. 6-2}$$

The resulting Hall current density is shown in Figures 6.1 and 6.2.

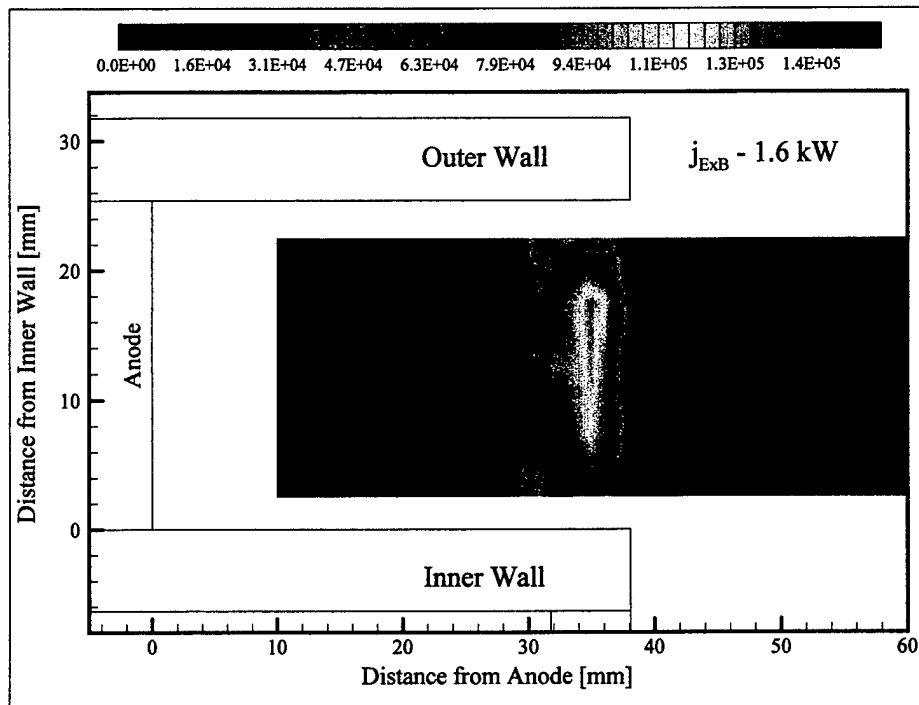


Figure 6.1 Hall current density calculated from measured electric and magnetic fields, 1.6 kW. Units are in A/m².

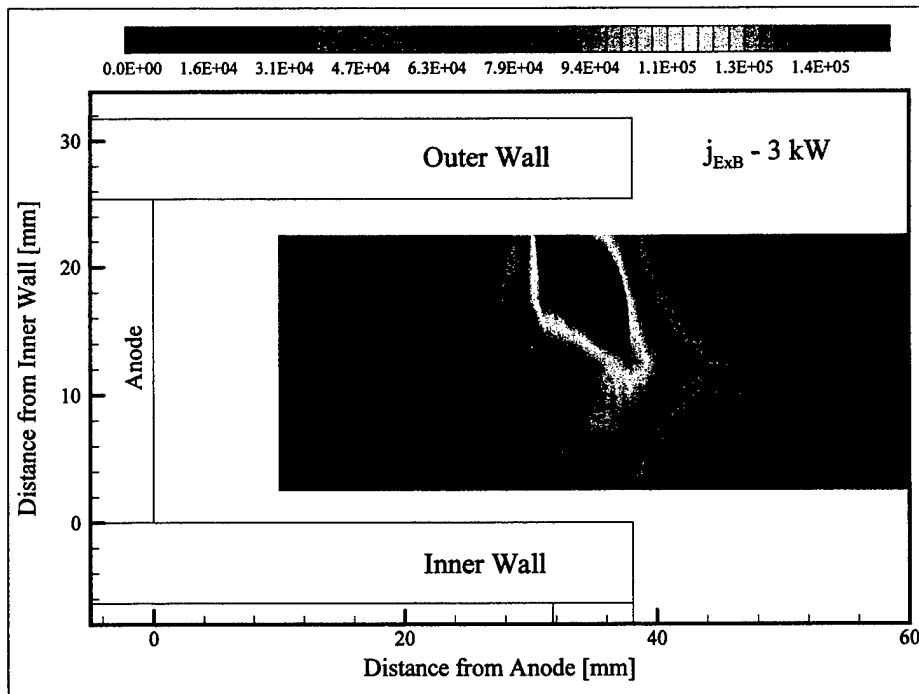


Figure 6.2 Hall current density calculated from measured electric and magnetic fields, 3 kW. Units are in A/m².

Integrating the Hall current over the domain, a total Hall current can be computed. These values are summarized in Table 6-1 and show the total Hall current to be several times the thruster discharge current. Included for comparison are the directly measured Hall currents from Section 5.1.4. The measured values are 27 and 43% higher than the computed Hall current when considering only the data upstream of the exit plane, a consequence of the measured Hall current having its peak further upstream. Extending the domain out to 60 mm, where both sets of data show the Hall current decreasing to a negligible level, the measured and computed values, at both conditions, agree to within approximately 15%. It is interesting to note that the current ratios for the measured values (at 38 and 60 mm) are nearly identical for both operating conditions.

		$I_{Hall} = n_i q A \frac{\mathbf{E} \times \mathbf{B}}{ B ^2}$		Measured I_{Hall}	
		38 mm (Exit Plane)	60 mm	38 mm (Exit Plane)	60 mm
1.6 kW	Hall Current [A]	14.6	25.1	18.5	21.4
	Current Ratio (I_{Hall}/I_D)	2.7	4.6	3.4	4.0
3 kW	Hall Current [A]	23.3	34.6	33.3	40.2
	Current Ratio (I_{Hall}/I_D)	2.3	3.5	3.3	4.0

Table 6-1 Total Hall current calculations at 1.6 and 3 kW.

6.2 Self-Fields

One of the questions associated with the Hall current is if, and to what extent, it modifies the plasma. The self-field generated by this current is of particular interest as it may significantly alter the magnetic field structure and hence the operation of the thruster². The discharge channel was divided into a rectangular mesh with a cell size of 1 mm by 5 mm. The Hall current in a given cell was computed using the current density from Figures 6.1 and 6.2 and the cell area. The Hall current in a given cell was approximated as current flowing in a long straight wire allowing the self-field to be computed using the Biot-Savart law shown in Equation 6-3

$$\mathbf{B} = \frac{\mu_0 \mathbf{I}}{2\pi r_I} \quad \text{Eq. 6-3}$$

where \mathbf{B} is the resulting self field, \mathbf{I} is the Hall current, and r_I is the distance between the approximated wire and another point in the computational domain. The resulting self-field was further broken down into its axial and radial components. Figure 6.3 illustrates the domain.

An iterative approach was used to obtain the self-field throughout the domain. The static magnetic field and electric field were used to compute an initial Hall current. This current was used to compute the resulting self-field in the plasma. The self-field was then added to the static magnetic field and the Hall current recalculated. This process

was repeated until the calculated self-field converged. Figures 6.4 – 6.7 show the computed axial and radial magnetic self-fields for the 1.6 and 3 kW cases.

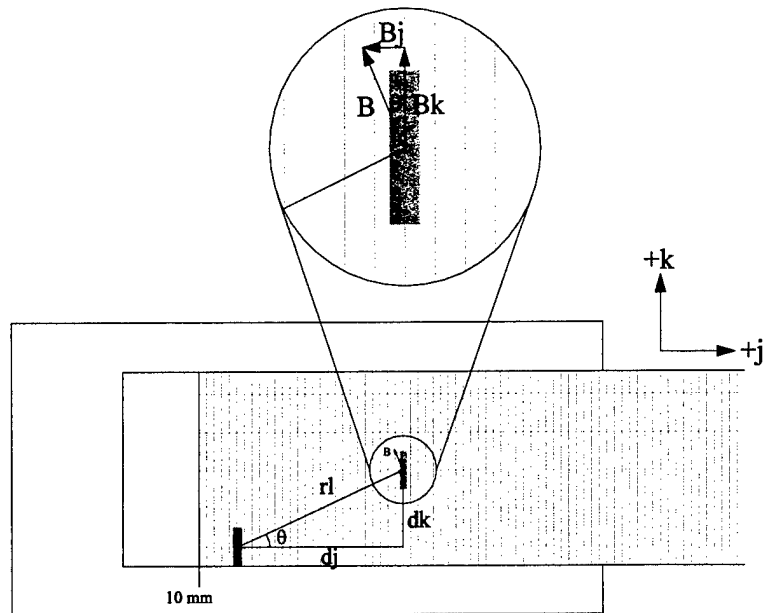


Figure 6.3 Calculation of self magnetic fields in the P5 discharge channel.

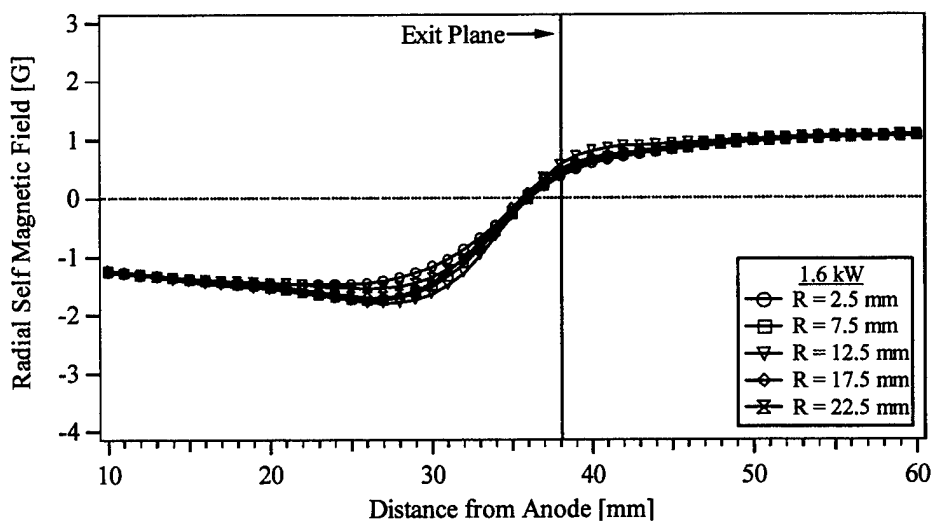


Figure 6.4 Radial self magnetic field from computed Hall current, 1.6 kW.

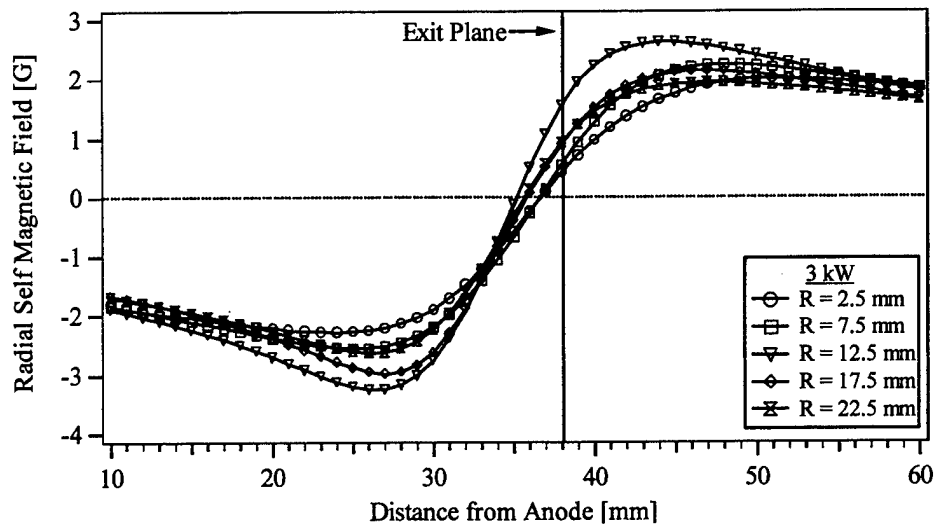


Figure 6.5 Radial self magnetic field from computed Hall current, 3 kW.

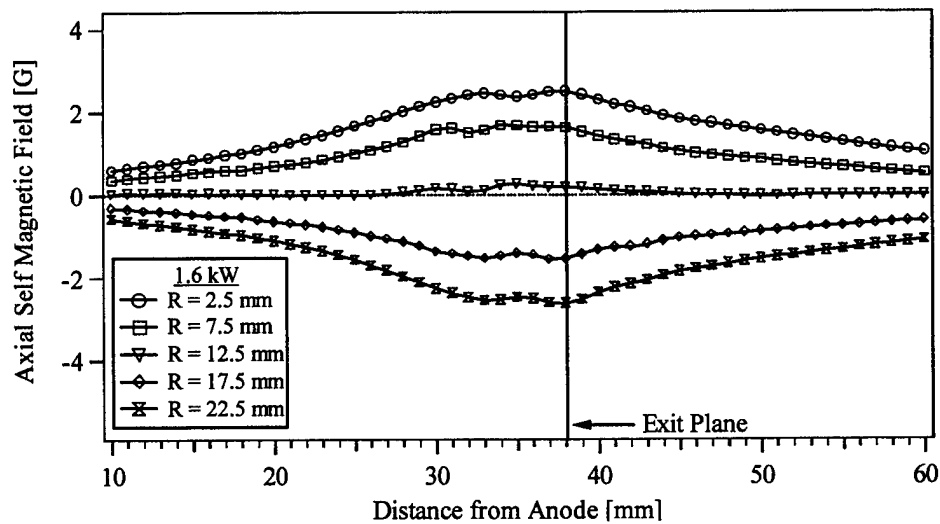


Figure 6.6 Axial self magnetic field from computed Hall current, 1.6 kW.

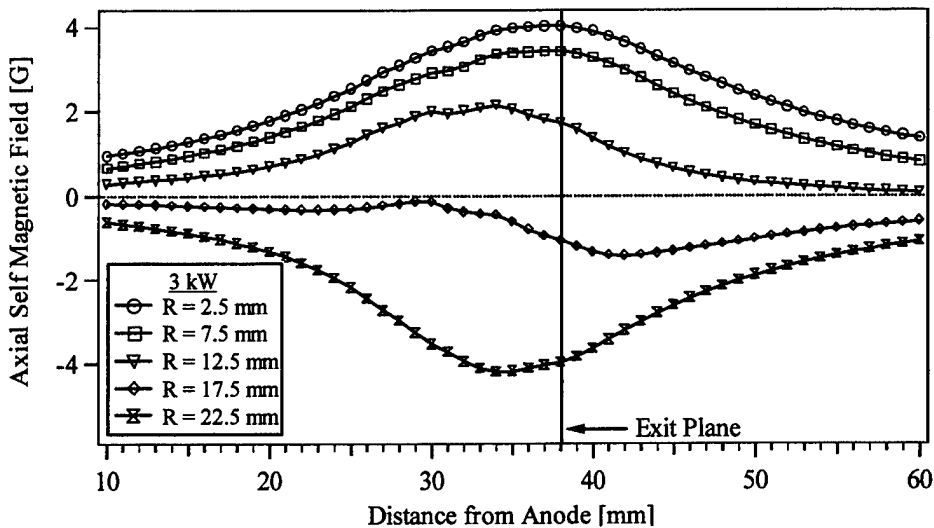


Figure 6.7 Axial self magnetic field from computed Hall current, 3 kW.

The results of the self-field calculations show that the Hall current does not contribute any substantial change to the static field. However, as was shown in Table 6-1, Section 6.1, the total Hall current is several times the magnitude of the discharge current. As Hall thrusters are scaled up in power, more specifically higher current, the Hall current is expected to reach hundreds of amps. At these levels, the Hall current may significantly alter the configuration of the magnetic field during thruster operation, especially since scaling laws suggest that the applied magnetic field will drop with increasing thruster size³.

6.3 Hall Parameter

As its name, and the preceding discussion, implies, the Hall current plays a significant role in thruster operation. A measure of the relative importance of the Hall current is the

Hall parameter. The electron Hall parameter is defined as the ratio of the electron cyclotron frequency and the total electron collision frequency.

$$\Omega \equiv \frac{\omega_e}{\nu_t} \quad \text{Eq. 6-4}$$

The electron cyclotron frequency is always positive and is written

$$\omega_e = \frac{|q|B}{m} \quad \text{Eq. 6-5}$$

Physically, the Hall parameter relates the axial and azimuthal electron transport in the thruster. For the case where $\Omega \gg 1$, the electrons complete many cycles of their cyclotron motion before undergoing a collision. Thus they will have a large **E**x**B** drift and their motion will be predominantly azimuthal. In the other extreme, $\Omega \ll 1$, the electrons will complete few cycles before undergoing a collision. The effect of this collision is to interrupt the electron's cyclotron motion, essentially forcing it to start its motion again from rest. Therefore, the electrons develop little or no azimuthal motion.

The electron collision frequency consists of three possible particle interactions: electron-electron, electron-ion, and electron-neutral. Jahn indicates that for ionization fractions starting well below 1%, the electron-ion coulomb collision frequency dominates⁴. This

analysis will include all three components. The general form of the collision frequency is written in terms of a collision cross section, Q :

$$\nu = nQ\bar{v} \quad \text{Eq. 6-6}$$

where n is the heavy particle number density, and \bar{v} is the relative particle velocity, taken to be the electron thermal velocity.

$$\bar{v} = \left(\frac{8\kappa T_e}{\pi m} \right)^{1/2} \quad \text{Eq. 6-7}$$

Chen provides a formula for the electron-ion collision cross section⁵,

$$Q_{ei} = \frac{\pi q^4}{(4\pi\epsilon_0)^2 E^2} \ln \Lambda \quad \text{Eq. 6-8}$$

where E is the kinetic energy of the electrons,

$$E = \frac{1}{2} m \bar{v}^2 \quad \text{Eq. 6-9}$$

and Λ is the plasma parameter.

$$\Lambda = 12\pi m_i \lambda_D^3 = \frac{12\pi}{n_i^{1/2}} \left(\frac{\epsilon_0 T_{ev}}{q} \right)^{3/2} \quad \text{Eq. 6-10}$$

Chen indicates that the electron-electron collision frequency is on the same order as the electron-ion collision frequency and provides an approximation of its magnitude

$$\nu_{ee} \approx 2.5\nu_{ei} \quad \text{Eq. 6-11}$$

The electron-neutral collision frequency is determined using the experimental data of Brode⁶. Figure 6.8 shows the collisional probability as a function of the square root of the electron temperature.

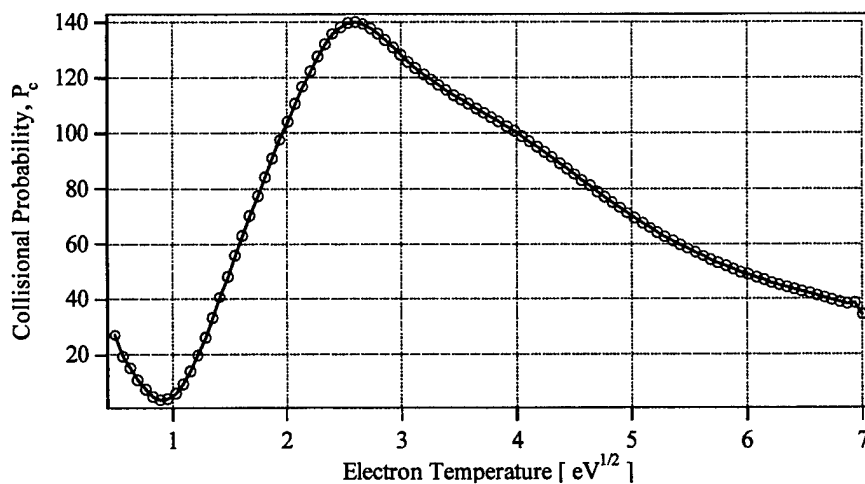


Figure 6.8 Collisional probability as a function of the square root of electron temperature.

The relationship between collision probability and collision cross section is then given by:

$$Q_{en} = 2.83 \times 10^{-21} P_c \quad \text{Eq. 6-12}$$

The final result is that the electron Hall parameter can be written in terms of the electron collision frequencies and magnetic field.

$$\Omega = \frac{qB}{m(\nu_{ei} + \nu_{ee} + \nu_{en})} \quad \text{Eq. 6-13}$$

Figures 6.9 and 6.10 illustrate the relative magnitudes of the components of the total electron collision frequency. Electron collisions with the discharge channel walls cannot be calculated. However, the numerical simulation results of Koo⁷, to be presented later in the text, do include a wall collision term, which is included for reference.

Figures 6.9 and 6.10 show that, at both conditions, electron-neutral collisions are the dominant mechanism (by 1-2 orders of magnitude) through the majority of the channel. Near the exit plane, the various electron collision terms approach the same order of magnitude.

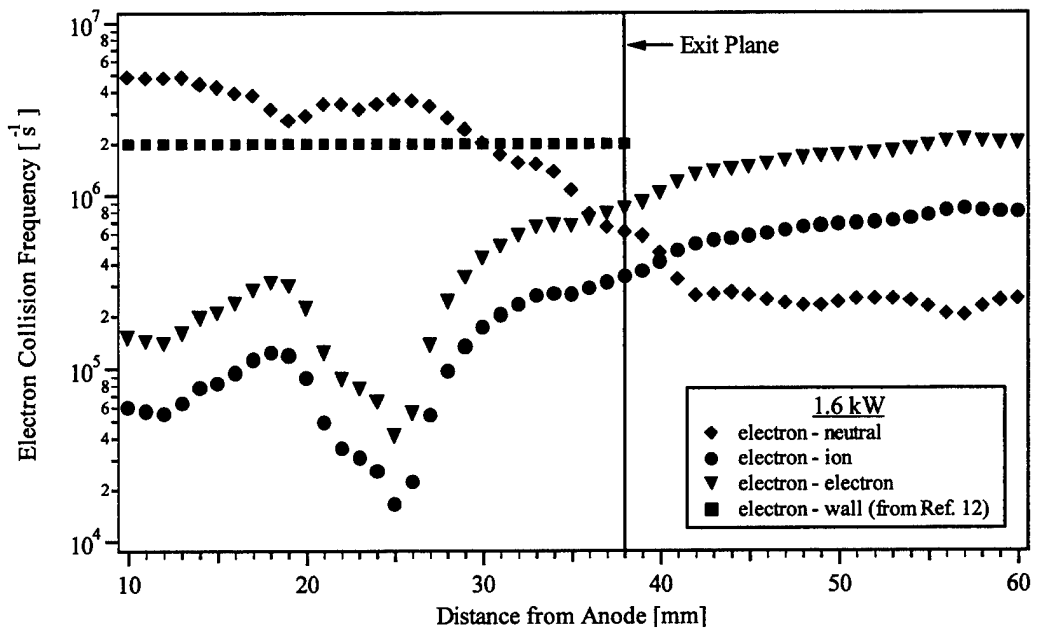


Figure 6.9 Electron collision frequency components, 1.6 kW.

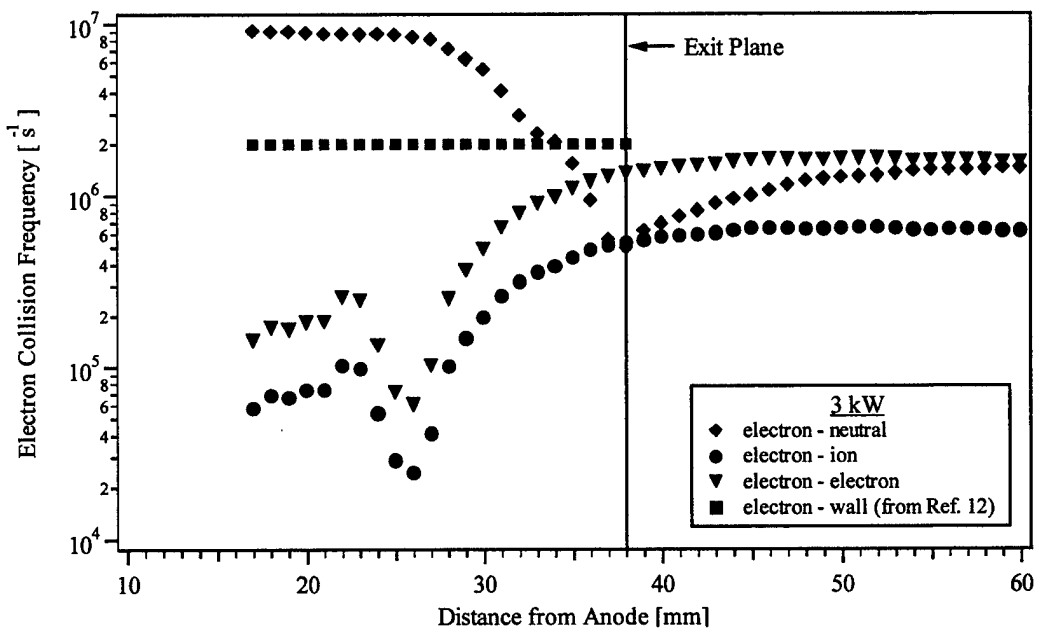


Figure 6.10 Electron collision frequency components, 3 kW.

Figure 6.11 shows the computed ionization fraction for both operating conditions. The ionization fraction meets or exceeds 1% nearly everywhere in the channel for both cases. This is in contrast to Jahn's assumption that coulomb collisions should dominate when the ionization fraction exceeds 1%.

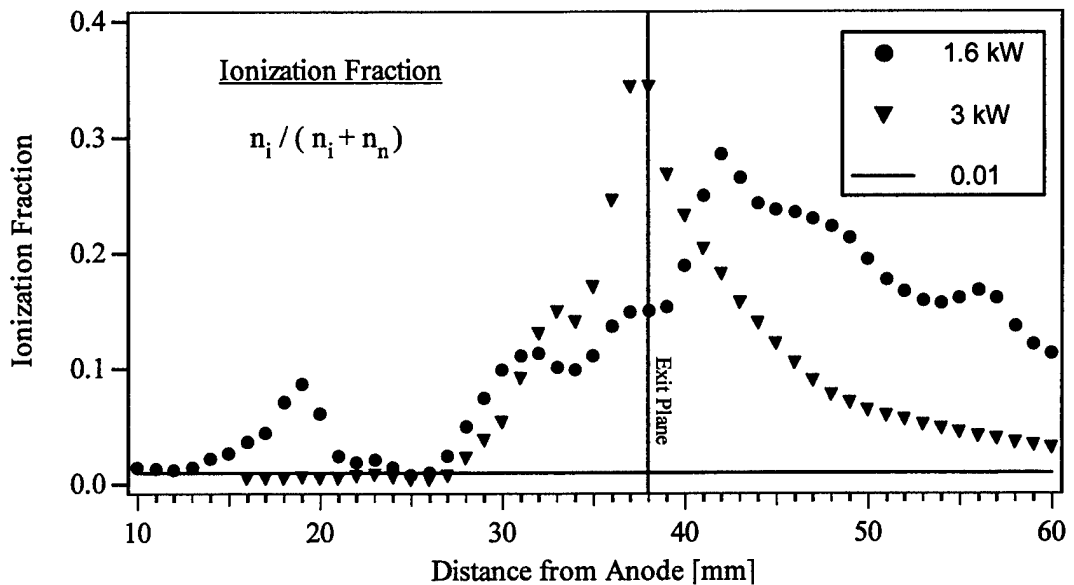


Figure 6.11 Computed ionization fraction profiles in the P5.

An alternative to the classical approach presented above is to calculate the Hall parameter from directly measured quantities: electric field, magnetic field, electron temperature, number density and current density. Equation 6-14 provides the starting point for this analysis using a generalized Ohm's law, which relates the current density vector to the applied fields and plasma parameters in an internally self-consistent manner.

$$\mathbf{j} = \bar{\sigma}(\mathbf{E} + \mathbf{V} \times \mathbf{B}) - \frac{\Omega}{B} (\mathbf{j} \times \mathbf{B} - \nabla P_e) \quad \text{Eq. 6-14}$$

Here $\bar{\sigma}$ is the conductivity tensor, specified for a coordinate system in which \mathbf{B} defines the orientation of the \hat{z} -axis, and is given by Equation 6-15

$$\bar{\sigma} = \sigma_0 \begin{bmatrix} \frac{1}{1+\Omega^2} & -\frac{\Omega}{1+\Omega^2} & 0 \\ \frac{\Omega}{1+\Omega^2} & \frac{1}{1+\Omega^2} & 0 \\ 0 & 0 & 1 \end{bmatrix} \quad \text{Eq. 6-15}$$

While the magnetic field vector is often treated as being essentially radial, it does possess an axial component in the current reference frame. Therefore, in order to use the above form of the conductivity tensor, it is necessary to perform a coordinate transformation. Figure 6.12 illustrates the relationship between the two coordinate systems.

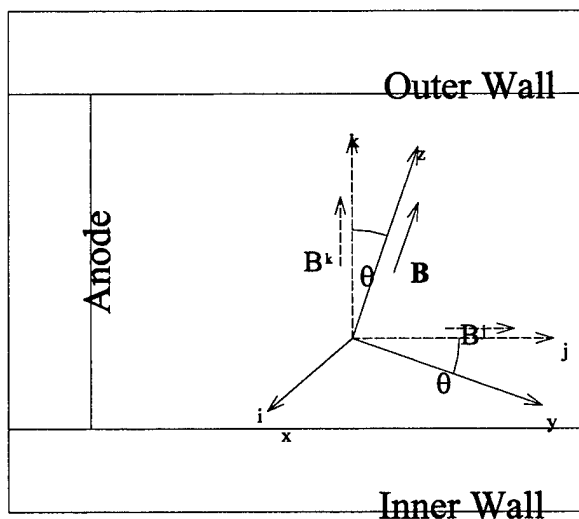


Figure 6.12. Coordinate transformation for Hall parameter measurements.

The i-j-k frame is the original coordinate system in which the probe measurements were made, while the x-y-z frame is the new coordinate system defined by the orientation of the magnetic field vector. A transformation matrix can then be written in order to convert vector quantities to the new frame and is given by Equation 6-16.

$$\bar{T} = \begin{bmatrix} 1 & 0 & 0 \\ 0 & \cos\theta & -\sin\theta \\ 0 & \sin\theta & \cos\theta \end{bmatrix} \quad \text{Eq. 6-16}$$

Here, the frame rotation angle, θ , is defined by the components of the magnetic field vector in the original coordinate system.

$$\tan\theta = \frac{B_j}{B_k} \quad \text{Eq. 6-17}$$

The first step in the Ohm's law analysis is to write the x and y components of the electron current density.

$$j_x = \sigma_0 \left(\frac{1}{1+\Omega^2} \right) (V_y B_z) - \sigma_0 \left(\frac{\Omega}{1+\Omega^2} \right) (E_y - V_x B_z) - \frac{\Omega}{B_z} (j_y B_z) \quad \text{Eq. 6-18}$$

$$j_y = \sigma_0 \left(\frac{\Omega}{1+\Omega^2} \right) (V_y B_z) + \sigma_0 \left(\frac{1}{1+\Omega^2} \right) (E_y - V_x B_z) - \frac{\Omega}{B_z} \left(j_y B_z - \frac{\partial P_e}{\partial y} \right) \quad \text{Eq. 6-19}$$

Next the two equations are solved for the scalar conductivity, σ_0 . Note also that in this coordinate frame, the electron velocity in the x-direction, V_x , is the $\mathbf{E} \times \mathbf{B}$ drift velocity and can be written

$$V_x = \frac{E_y}{B_z} \quad \text{Eq. 6-20}$$

Therefore, the second term in both equations can be dropped.

$$\sigma_0 = \frac{j_x + \Omega j_y}{\left(\frac{1}{1+\Omega^2}\right)V_y B_z - \left(\frac{\Omega}{1+\Omega^2}\right)(E_y - V_x B_z)} = \frac{j_x + \Omega j_y}{\left(\frac{1}{1+\Omega^2}\right)V_y B_z} \quad \text{Eq. 6-21}$$

$$\sigma_0 = \frac{j_y - \Omega j_x - \frac{\Omega}{B_z} \frac{\partial P_e}{\partial y}}{\frac{\Omega}{1+\Omega^2} V_y B_z + \frac{1}{1+\Omega^2} (E_y - V_x B_z)} = \frac{j_y - \Omega j_x - \frac{\Omega}{B_z} \frac{\partial P_e}{\partial y}}{\left(\frac{\Omega}{1+\Omega^2}\right)V_y B_z} \quad \text{Eq. 6-22}$$

Combining the two equations for scalar conductivity, a quadratic expression for the electron Hall parameter results

$$\Omega^2 + \Omega \left(2 \frac{j_x}{j_y} + \frac{1}{j_y B_z} \frac{\partial P_e}{\partial y} \right) - 1 = 0 \quad \text{Eq. 6-23}$$

the solution for which is

$$\Omega = -\frac{1}{2} \left(2 \frac{j_x}{j_y} + \frac{1}{j_y B_z} \frac{\partial P_e}{\partial y} \right) \pm \frac{1}{2} \left[\left(2 \frac{j_x}{j_y} + \frac{1}{j_y B_z} \frac{\partial P_e}{\partial y} \right)^2 + 4 \right]^{1/2} \quad \text{Eq. 6-24}$$

In this equation, the current densities and electron pressure are related to the measured quantities through the coordinate transformation tensor, $\bar{\bar{T}}$:

$$j_x = j_i \quad \text{Eq. 6-25}$$

$$j_y = j_j \cos \theta \quad \text{Eq. 6-26}$$

$$\frac{\partial P_e}{\partial y} = \frac{\partial P_e}{\partial j} \sin \theta + \frac{\partial P_e}{\partial k} \cos \theta \quad \text{Eq. 6-27}$$

$$P_e = n_i \kappa T_e \quad \text{Eq. 6-28}$$

Generally, the electron pressure term is considered negligible and dropped from the Hall parameter expression. Additionally, it is assumed that the electron Hall parameter is large, $\Omega \gg 1$.

The end result of these assumptions is a simplified version of the Hall parameter inferred from the generalized Ohm's law.

$$\Omega = 2 \frac{j_x}{j_y} \quad \text{Eq. 6-29}$$

The negative sign has been dropped since the axial electron current density, j_z , is in the negative direction. Figures 6.13 and 6.14 show the resulting Hall parameter values. The semiempirical Bohm⁸ value is included for comparison. This value evolved from Bohm's attempts to describe anomalously large diffusion in plasmas with magnetic fields and is obeyed in a large variety of experimental plasmas.

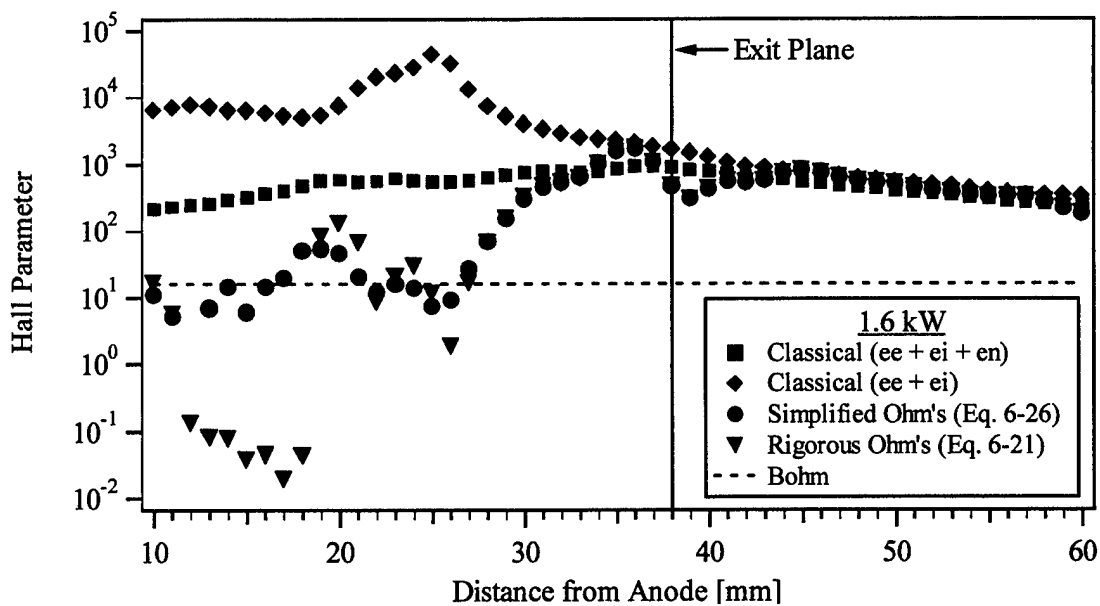


Figure 6.13 Electron Hall parameter, 1.6 kW.

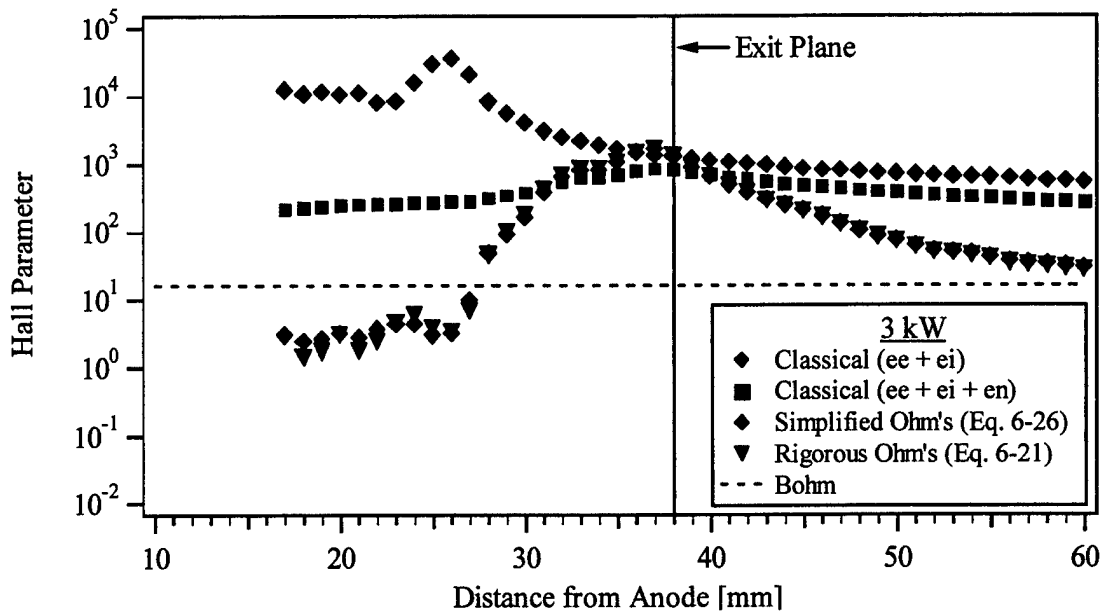


Figure 6.14 Electron Hall parameter, 3 kW.

In general, the pressure term in the Ohm's law analysis is negligible. The exception is the region nearest the anode at 1.6 kW, where the pressure term reduces the Hall parameter considerably. Everywhere else, the two Ohm's law analyses are essentially identical. At 1.6 kW, the Hall parameter is on the order of 10-20 near the anode, agreeing well with the Bohm value of 16. Coincident with the start of the acceleration zone at 30 mm, the Hall parameter begins to increase, with a maximum value of approximately 1000. This peak occurs a few millimeters upstream of the exit plane, which is to be expected since this is the location of the peak electric field and thus, maximum Hall current density.

The 3 kW data are very similar to the 1.6 kW data. Electron-neutral collisions dominate inside the channel. The classical Hall parameter is several orders of magnitude larger than the inferred (Ohm's law) value, which is about an order of magnitude less than the

Bohm value. At a position of approximately 27 mm, the inferred and classical values begin to converge. As in the 1.6 kW case, the inferred Hall parameter peaks at a value of approximately 1000, a few millimeters upstream of the exit plane; again, coincident with the peak Hall current density. Downstream of the exit plane, in contrast to the 1.6 kW case, the classical and inferred values diverge, with the inferred Hall parameter approaching the Bohm value.

Of particular interest is the comparison between the classical and Ohm's law Hall parameters. The two values differ considerably for both cases in the channel but show very good agreement near, and for the 1.6 kW case, downstream of the exit plane. An obvious explanation for this difference in the channel would be the wall collisions, which were not taken into account. An electron-wall collision frequency can be calculated based on the collision frequency necessary to account for the difference in the classical and inferred Hall parameters. These computed wall collision frequencies are shown in Figure 6.15.

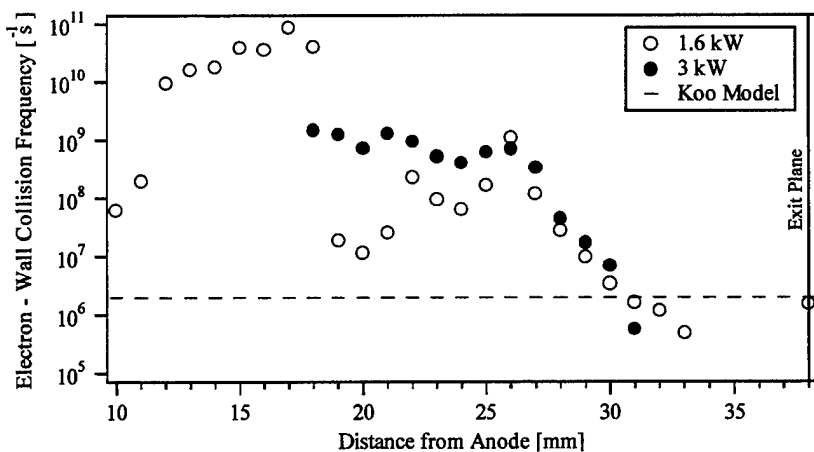


Figure 6.15 Calculated electron-wall collision frequency. This is the wall collision frequency necessary to account for the difference between the classical and inferred Hall parameters.

From Figure 6.15, it can be seen that the computed wall collision frequency is considerably larger than that assumed in Koo's 2D model⁷. Stanford⁹ has performed similar analyses on their own laboratory Hall thruster and concluded that in addition to the wall collisions, plasma turbulence plays a significant role in electron transport. Omission of this turbulence effect may explain the large wall collision frequency values obtained in Figure 6.15.

6.4 Thrust

Thrust is traditionally measured using a thrust stand, which obviously provides no information on the mechanism of thrust production. Given the presence of both electric and magnetic fields in the Hall thruster, the question of whether plasma acceleration is electrostatic (i.e. electric body forces) or electromagnetic (i.e. interaction of magnetic fields and plasma currents) is often raised. Interestingly, it can be shown through a fairly simple analysis, and with the correct assumptions, that both approaches are essentially the same.

6.4.1 Electrostatic Analysis

In the electrostatic analysis, we consider the motion of individual particles and their behavior in the presence of electric and magnetic fields. This motion is described by the Lorentz force equation, Equation 6-30.

$$\mathbf{F} = q(\mathbf{E} + \mathbf{V} \times \mathbf{B})$$

Eq. 6-30

Making the simplifying assumption that the magnetic field is radial and the electric field is axial (this is not strictly true throughout the entire discharge channel and near-field region of the thruster; however, the majority of the acceleration is confined to a region centered several millimeters upstream of the exit plane and in this region the magnetic and electric fields are essentially radial and axial, respectively), the component of force directed along the thruster axis can be written

$$F_y = q(E_y - V_x B_z) \quad \text{Eq. 6-31}$$

It is already known that the net force on the electrons is zero; the $\mathbf{E} \times \mathbf{B}$ drift velocity, $V_x = E_y / B_z$, was derived from this equation using that very assumption (The electron drift is a cumulative effect over many gyroradii. During each gyroperiod, the electron experiences acceleration in a given direction over part of its orbit, which reverses as it, gyrates about the magnetic field. Over many gyroperiods, the averaged acceleration, and hence the net force, is zero). The ions, on the other hand, are essentially unmagnetized, having gyroradii larger than the discharge channel dimensions. As a result, they develop no azimuthal motion. Thus the force on a single ion is simply

$$F_y = |q|E_y \quad \text{Eq. 6-32}$$

The thrust is then the sum of the force on all the ions in each volumetric element, k, throughout the thruster discharge.

$$T = \sum_k |q| n_i^k E_y^k V^k \quad \text{Eq. 6-33}$$

6.4.2 Electromagnetic Analysis

Rather than consider the motion of discrete particles, the ions and electrons can each be treated as a fluid. Further, the ion and electron fluid equations can be combined to form a single fluid model of the plasma referred to as the equations of magnetohydrodynamics (MHD). The full set of MHD equations consists of mass, momentum, and charge conservation equations, and a generalized Ohm's law.

The MHD equations are an ideal starting point for the electromagnetic analysis of the Hall thruster because we are interested in the interaction of the currents driven in the plasma with the applied magnetic field. The MHD momentum equation, also called the force equation, expresses the volumetric body force (F/∇) on the plasma and is given by

Equation 6-34.

$$\mathbf{F} = -\nabla P + \rho_c \mathbf{E} + \mathbf{j} \times \mathbf{B} \quad \text{Eq. 6-34}$$

The electron pressure term is small compared to the $\mathbf{j} \times \mathbf{B}$ term over most of the discharge channel. Additionally, the quasineutrality assumption means there is no net charge imbalance ($\rho_c = 0$). Therefore, the axial body force density can be written

$$\frac{F_y}{V} = -j_x B_z \quad \text{Eq. 6-35}$$

As in the previous section, note that the ions are unmagnetized; thus the azimuthal current density in Equation 6-35 is composed entirely of the drifting electrons. Rewriting the current density, $j_x = qn_i V_x$, and recalling that the electron drift velocity is simply $V_x = E_y / B_z$, the body force density is

$$\frac{F_y}{V} = -qn_i E_y \quad \text{Eq. 6-36}$$

Summing over each volumetric element in the thruster discharge and noting that, for electrons, $-q = +|q|$, the total thrust can be written

$$T = \sum_k |q| n_i^k E_y^k V^k \quad \text{Eq. 6-37}$$

Comparing Equations 6-33 and 6-37, we see that the electrostatic and electromagnetic analyses yield the same results. Figure 6.16 is a cut-away view of the thruster and

illustrates the annular volumetric elements used to calculate thrust from the measured plasma parameters.

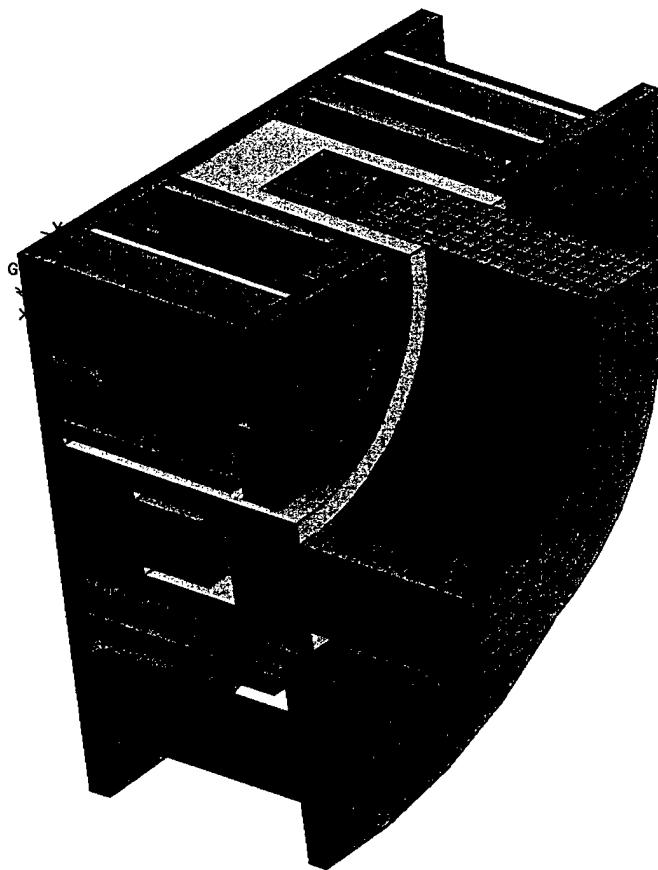


Figure 6.16. Three dimensional cut-away view of the P5. Thrust is determined by summing the force in each annular volumetric element.

Figures 6.17 and 6.18 show axial profiles of the calculated thrust at five radial positions for the 1.6 and 3 kW levels. The total calculated thrust is also shown and illustrates where the majority of the thrust is generated.

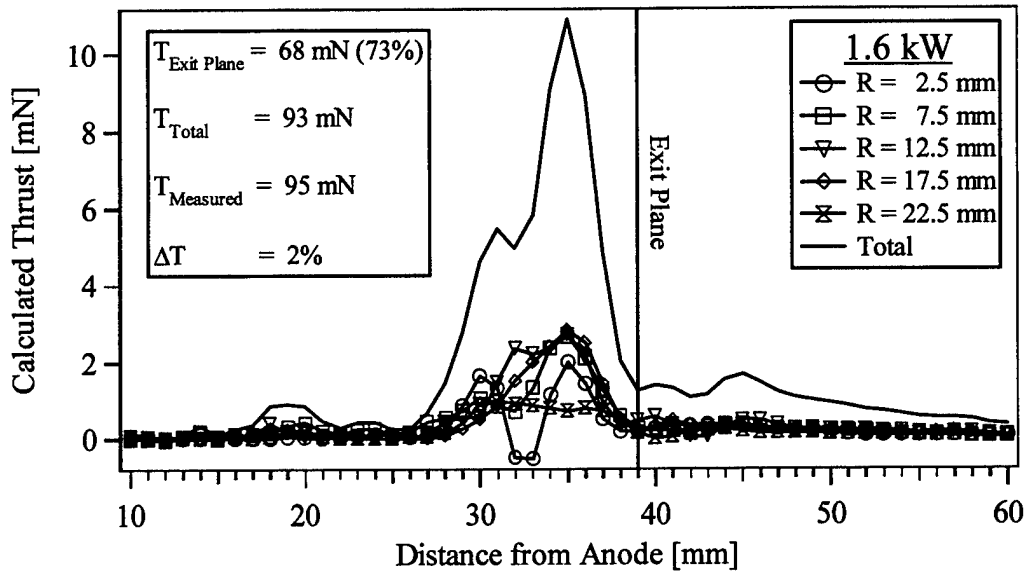


Figure 6.17 Calculated thrust from directly measured plasma parameters at 1.6 kW. 73% of the total calculated thrust is developed inside the discharge channel. The total calculated thrust was within 2% of the thrust measured using a thrust stand.

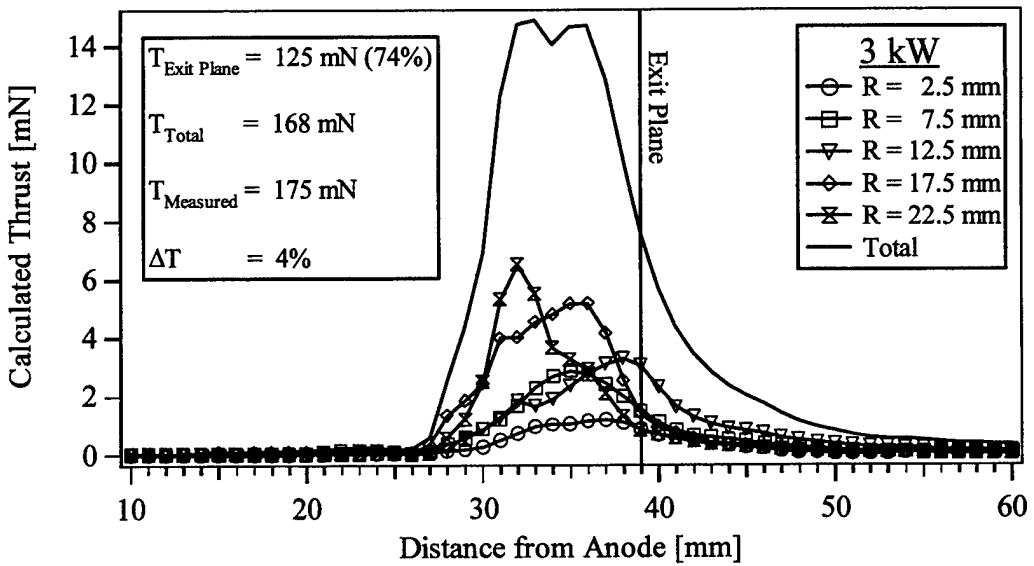


Figure 6.18 Calculated thrust from directly measured plasma parameters at 3 kW. 74% of the total calculated thrust is developed inside the discharge channel. The total calculated thrust was within 4% of the thrust measured using a thrust stand.

6.4.3 Jet Thrust

A third approach to calculating thrust is to use the ion velocities inferred from the plasma potential measurements and write the total momentum of the ions, referred to as the jet thrust, shown in Equation 6-38.

$$J_T = n_i M A V_i^2$$

Eq. 6-38

Figures 6.19 and 6.20 show the inferred ion velocities, which agree very well with independent LIF measurements².

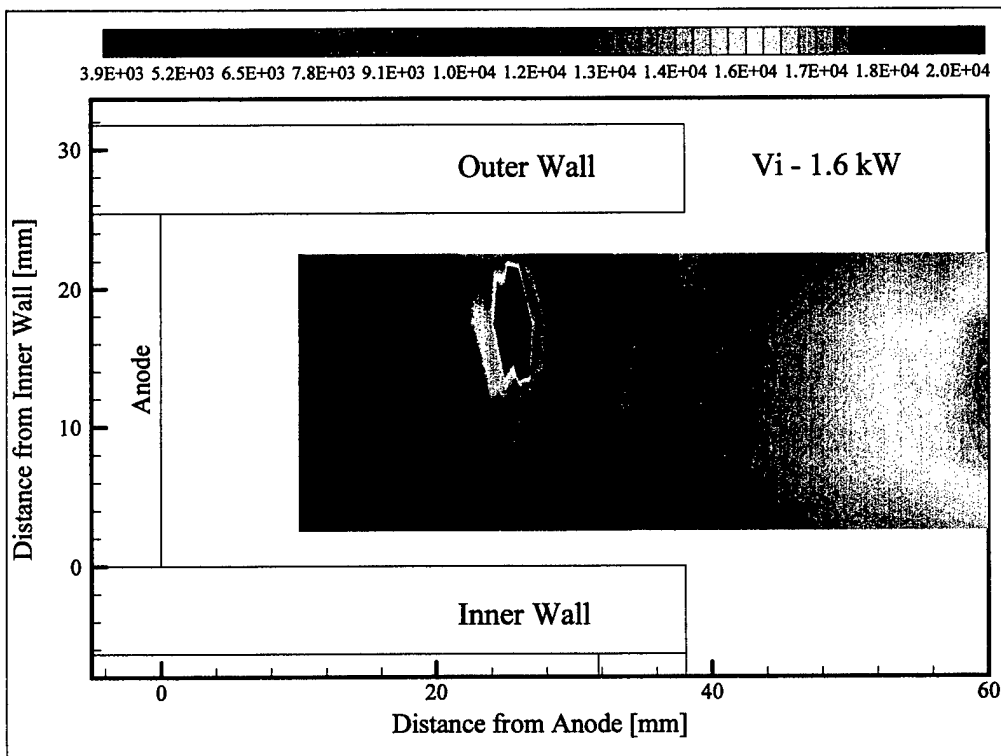


Figure 6.19 Calculated ion velocity, 1.6 kW.

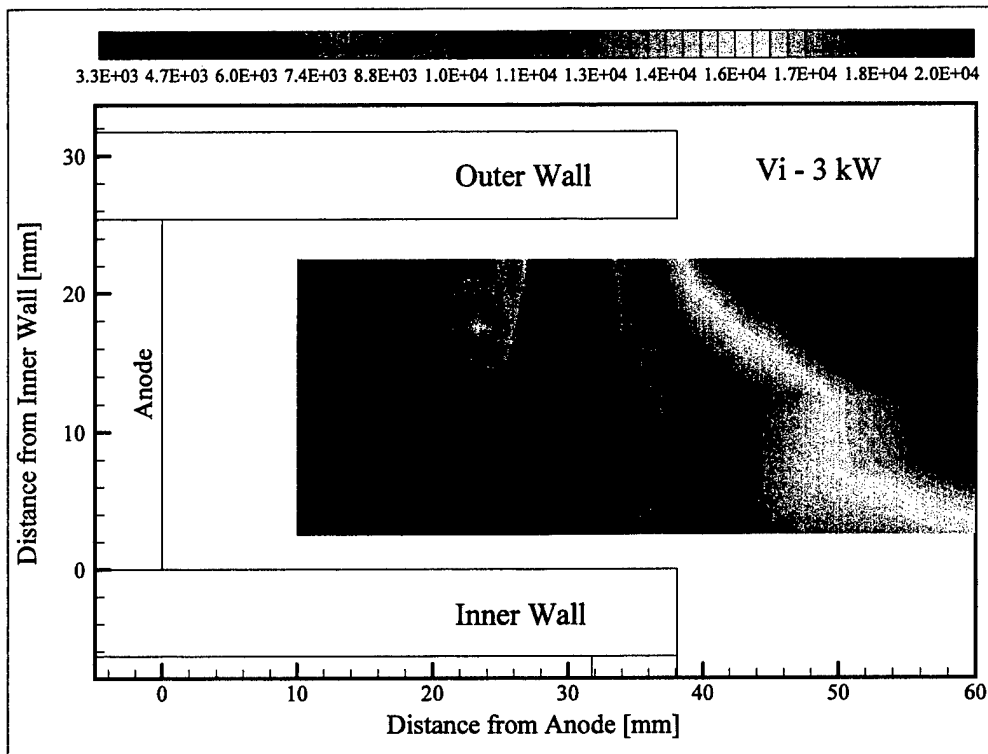


Figure 6.20 Calculated ion velocity, 3 kW.

Table 6-2 below summarizes the various thrust calculations as well as the thrust measured directly using an inverted-pendulum thrust stand.

		$J_T = n_i M A V_i^2$		$T = j x B = n_i q E \nabla$		Thrust Stand
		38 mm (Exit Plane)	60 mm	38 mm (Exit Plane)	60 mm	
1.6 kW	Thrust [mN]	70	94	68	93	95
	Total Thrust Fraction	0.74	0.99	0.72	0.98	-
3 kW	Thrust [mN]	124	169	125	168	175
	Total Thrust Fraction	0.71	0.97	0.71	0.96	-

Table 6-2 Comparison of calculated and measured thrust data.

All three thrust values show excellent agreement. Both the jet thrust and the jxB calculation yield total thrust values within 4% of the total measured value. Further, the thrust calculations provide information not available from the thrust stand. Thrust data at the exit plane indicate that nearly 30% of the total thrust is generated outside of the thruster.

6.5 Beam Current

Beam current is that component of the total discharge current attributed to the ions and can be estimated from the ion number density (Figures 5.87 and 5.90) and the calculated ion velocity values (Figures 6.19 and 6.20). The beam current is computed according to Equation 6-39, where A is the annular cross section area of the discharge channel and it is assumed all ions are singly charged.

$$I_B = n_i q V_i A \quad \text{Eq. 6-39}$$

Beam current can also be computed from Faraday probe data. The Faraday probe measures ion current density along a constant radius arc in a horizontal plane passing through the centerline of the thruster. This is illustrated in Figure 6.21, which is a top view of the thruster and probe. The cathode is positioned at the outer edge of the pole piece, at the 2 o'clock position when facing the thruster exit. Ion current density was measured in 1° increments at 0.5 m and 1.0 m at both operating conditions. Figure 6.22 shows the profiles of ion current density as a function of angle.

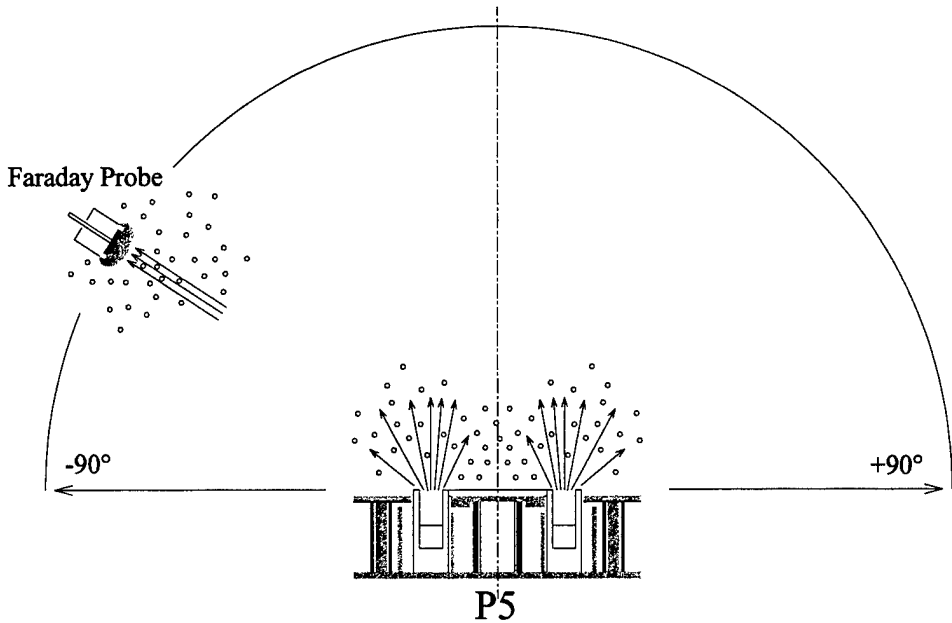


Figure 6.21 Top view of thruster illustrating its orientation with respect to the Faraday probe. The probe collection surface is aligned with the center of the thruster and is swept 180° through a constant radius arc.

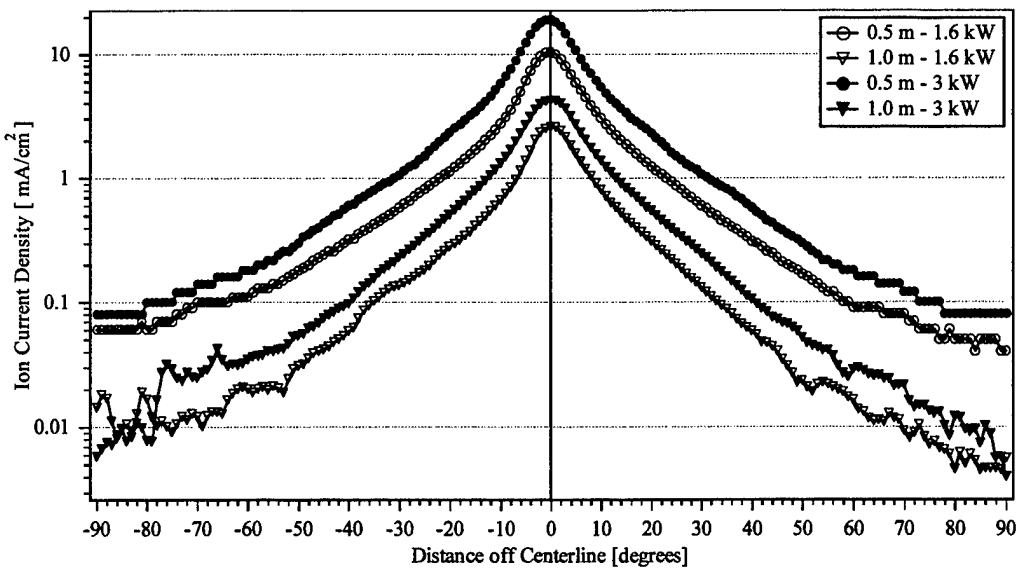


Figure 6.22 Ion current density, 0.5 m and 1 m from thruster exit plane, at 1.6 kW and 3 kW.

Total beam current is obtained by integrating the curves of Figure 6.22 according to Equation 6-40.

$$I_B = 2\pi a^2 \int_0^{\pi/2} j_B \sin(\theta) d\theta \quad \text{Eq. 6-40}$$

Results of the beam current calculations are summarized in Table 6-3.

		Faraday Probe				Electrostatic Probes	
		0.5 m		1.0 m		38 mm (Exit Plane)	60 mm
		0 → π/2	0 → -π/2	0 → π/2	0 → -π/2		
1.6 kW	Beam Current [A]	5.40	5.44	4.71	4.86	4.08	4.04
	Discharge Current Fraction	1.00	1.01	0.87	0.90	0.76	0.75
3 kW	Beam Current [A]	10.20	9.74	8.48	8.63	8.09	5.52
	Discharge Current Fraction	1.02	0.97	0.85	0.86	0.81	0.55

Table 6-3 Comparison of beam current measurements using a Faraday probe and flux calculated from plasma parameters.

The results from the ion number density and velocity data measured via electrostatic probes (Langmuir and emissive) include calculations at two locations. The data at the thruster exit plane indicate that the beam current is 76 – 81% of the total discharge voltage. The data at 60 mm agrees at 1.6 kW but indicates a considerably smaller discharge current fraction, 55%, at 3 kW. This is to be expected as an increasing number of ions are no longer confined to the annular channel and have begun to diverge; the

calculated flux of ions fails to account for these ions and thus under predicts the beam current. The data at the exit plane is a more accurate representation of the beam current and will be referenced exclusively for the remainder of this discussion.

In general, Table 6-3 shows that the Faraday probe data at 1.0 m agree reasonably well with the electrostatic probe data at the exit plane. They differ by approximately 12 % at 1.6 kW and by only 4% at 3 kW, which is well within the experimental uncertainty due to the ion number density. Further both sets of data show beam current values close to 80% of the discharge current, which is the value generally presumed for Hall thrusters. This agreement between independent diagnostics provides additional confidence in the electrostatic probe data. At 0.5 m, the Faraday probe beam current is 100% of the discharge current at both power levels, a significant increase over the expected 80% value.

The large beam currents from the Faraday probe are not unexpected. In practice, Faraday probes tend to overestimate the total beam current¹⁰. Results from previous experiments involving different thrusters and experimental facilities have indicated beam currents as large as 200% of the discharge current. The reason for this is the presence of low-energy charge exchange (CEX) ions. These CEX ions originate both within the plume (neutral xenon from the thruster) and at the plume boundaries (ambient background gas resulting from a non-ideal vacuum). To see how this contributes to an overprediction of the total beam current, consider a Faraday probe some distance from and facing the thruster. Figure 6.21 is a top view of the thruster showing the plane in which the Faraday probe is

swept through a constant radius arc, centered at the thruster face on thruster centerline. Long arrows indicate “fast” beam ions while the low-energy CEX ions are denoted by randomly placed circles. The bulk of the beam ions are directed along the thruster axis and these dominate the current density measurements near centerline. At large angles, the density of beam ions, as well as their velocity, drops considerably and the CEX ions contribute a larger fraction to the current density.

CEX ions are produced when a “fast” ion interacts with a “slow” neutral. Total momentum is conserved and the result is a “slow” ion and a “fast” neutral. A cursory examination seems to indicate that the measured current density should be artificially low; current density is proportional to the product nV and the CEX process essentially depopulates the “fast” ions, replacing them with an equal number of “slow” ions. The apparent discrepancy can be explained by recognizing that the collection of beam ions and CEX ions by the Faraday probe differ considerably. Figure 6.23 illustrates the distribution of the two ion species and their motion with respect to the probe.

Beam ions, having been accelerated through a substantial potential, have a large directed velocity. Only those “fast” ions collimated along the axis of the Faraday probe will be collected and contribute to the measured current. CEX ions, on the other hand, have very low energy and an essentially random velocity distribution. Thus, for the CEX ions, the Faraday probe acts as a planar Langmuir probe, “pulling in” CEX ions through the sheath from all directions. This preferential collection of CEX ions is responsible for the anomalously large beam current commonly seen.

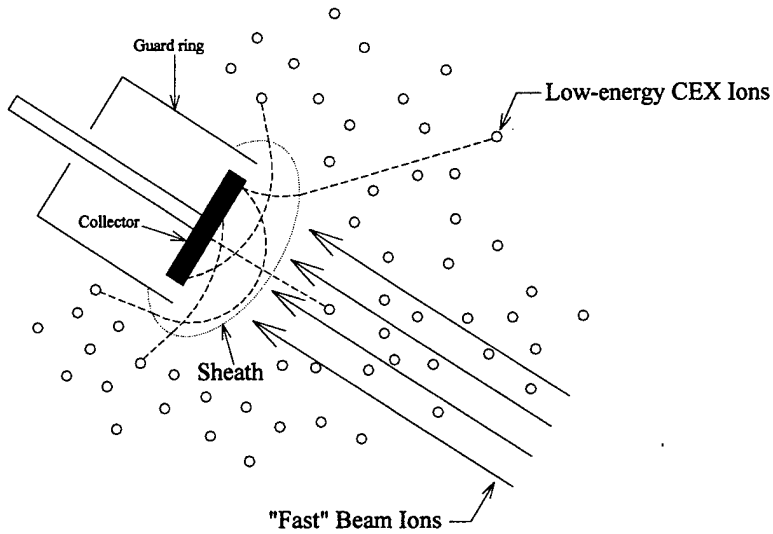


Figure 6.23 Ion current collection with a Faraday probe. Only “Fast” beam ions collimated with the probe collector surface contribute to the total current. CEX ions have low-energy and an essentially random velocity distribution. Thus, for these ions, the Faraday probe behaves like a planar Langmuir probe, preferentially collecting CEX ions from a much larger surrounding area. The net result is an artificially large beam current.

Returning to the P5 results, this effect is not observed in the 1.0 m data and only to a limited extent in the 0.5 m data. The reason for this is not entirely clear. One possibility is the way in which the data was integrated to get a total beam current. This was tested by analyzing both P5 and SPT-140¹⁰ data using the same algorithm and the results for each did not change; P5 beam currents at 3 kW were ~ 100% and ~ 85% of the discharge current at 0.5 m and 1.0 m, respectively, while the SPT-140 beam current at 3 kW and 1.0 m was ~ 170% of the discharge current. Another possible explanation for the discrepancy is the probe design. The above referenced data were both obtained in the PEPL facility at the same background pressure, operating conditions, and probe distance, and using the same instrumentation. The two Faraday probes had identical collector size and material but differed in that the SPT-140 probe had a slightly different guard ring

configuration with a ceramic insulator between the guard ring and the collector. SPT-140 measurements at 4.5 kW performed at NASA GRC, using a probe identical to that used for the P5 at PEPL, yielded a beam current $\sim 111\%$ of the discharge current¹⁰. The effect of a different probe is difficult to quantify due to a difference in background pressure in the two facilities (9.1×10^{-6} at NASA GRC versus 1.6×10^{-5} at PEPL), which would affect the contribution from ambient CEX ions. However, even accounting for a reduction in CEX ion current resulting from the lower background pressure at NASA GRC, the measured beam current is much larger than the expected.

A related issue is the apparent difference between measured beam current at 0.5 m and 1.0 m. Beam current at 0.5 m was approximately 100% of the discharge current at both power levels, dropping to approximately 75 – 80% of the discharge current at 1.0 m. One possibility is that this effect is a manifestation of higher order CEX collisions (triple, double, and single ion interactions) in the thruster plume. Gulczinski¹¹ measured ion species fractions in both the near- and far-field of the P5 at 1.6 kW. The results are summarized in Table 6-4.

	Species Fraction	
	0.1 m	0.75 m
Xe ⁺	0.698	0.925
Xe ⁺⁺	0.231	0.068
Xe ⁺⁺⁺	0.052	0.007
Xe ⁺⁺⁺⁺	0.019	-

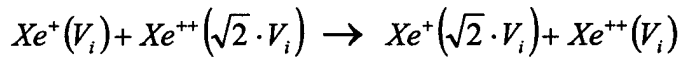
Table 6-4 Species fractions of multiply charged xenon ions in the plume of the P5¹¹.

The specific charge exchange processes cannot be determined from the data in Table 6-3.

However, the important thing to recognize is that there is a significant population of multiply charged ions undergoing CEX collisions. This can account for the variation in beam current at the two radial positions, 0.5 m and 1.0 m. Taking a very simple example, assume a population of n double ions and n single ions. The single ions are accelerated through a given potential giving them a velocity V_i . The double ions will have undergone twice the acceleration of a single ion, giving them a velocity $\sqrt{2}V_i$ (assuming both are created in the same region of the thruster). Thus the current density measured by the probe will be

$$j_0 = nqV_i + n(2q)\sqrt{2}V_i = 3.83nqV_i \quad \text{Eq. 6-41}$$

If each double ion then undergoes a CEX collision with a single ion, the net result is a double ion with velocity V_i , and a single ion with velocity $\sqrt{2}V_i$.



It is important to note that, unlike the CEX collisions involving neutrals, the resultant products here retain a large directed velocity and remain well collimated.

Thus the current density is now

$$j_f = n(2q)V_i + nq\sqrt{2V_i} = 3.41nqV_i \quad \text{Eq. 6-42}$$

Comparing the current density before and after the CEX collisions

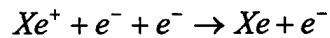
$$\frac{j_f}{j_0} = 0.89 \quad \text{Eq. 6-43}$$

we see that the measured current density drops by approximately 11%. Note that this analysis does not apply to the beam currents calculated from electrostatic probe data in Table 6-1 as those values assumed all ions were singly charged.

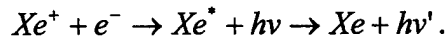
The actual CEX collision processes are much more complicated than this simple example implies, involving additional CEX reactants and products. Further, the data in Table 6-4 correspond to different locations than for the Faraday probe. However, the trend is clearly a reduction in the population of multiply charged ions with increasing distance from the thruster and this would account for the drop in observed beam current.

A second possible explanation for the decrease in measured beam current is ion-electron recombination, whereby ions recombine with free electrons reducing their charge state.

There are two possible mechanisms for ion-electron recombination. The first is a three-body collisional process



and the second is a radiative process



The contribution of these two processes is reflected in the bulk recombination coefficient α , which is composed of the individual collisional and radiative terms¹²

$$\alpha_c = 1.1 \times 10^{-20} \cdot T_{eV}^{-9/2} \quad \text{Eq. 6-44}$$

$$\alpha_c = 3.0 \times 10^{-16} \cdot \frac{T_{eV}^{-3/4}}{n_e} \quad \text{Eq. 6-45}$$

At 1.6 kW, the conditions in the plume of the P5 are very similar to those in the SPT-100, thus the results of King's analysis are applicable here¹³. Assuming an electron temperature of 1 eV and electron density of $2 \times 10^{16} \text{ m}^{-3}$, he showed that the recombination time in the thruster plume is greater than 260 s. LIF¹⁴ measurements of the P5 indicate ions exit the thruster with a velocity of $1.2 \times 10^4 \text{ m/s}$ yielding a transit time through the

plume (1 m downstream) of approximately 80 μ s. Thus it is obvious that the reduction of ion charge states through recombination is a negligible effect.

6.6 Comparison with Numerical Simulation

One of the current goals of Hall thruster research is to generate accurate models of the plasma discharge. With accurate models, new thruster designs and configurations can be tested without the time and expense associated with physically building and testing thrusters. The data presented in this thesis are invaluable in validating these models. This section presents the results of a time-dependent, 2D code developed by Koo. The time-averaged results of the model are compared directly with the experimental data of Chapter 5. The analysis here will be limited to the 3 kW case. This model continues to be refined and details of its development can be found in the literature⁷.

Thruster dimensions, magnetic field configuration, mass flow rate and discharge voltage are the user specified inputs; the model then predicts discharge current, number density, electron temperature, and plasma potential data in the discharge channel of the thruster. In addition, it computes thruster performance characteristics: thrust, specific impulse, and efficiency. It is important to note that the model's input discharge voltage is specified with respect to ground, while the direct measurement of discharge voltage is with respect to cathode. Note also that the model computes the discharge current rather than having it specified as an input parameter. Thus the specified power level for a particular simulation will differ from that of a comparable set of thruster data. For example, at 3 kW, thruster discharge voltage with respect to the cathode is 300 V but only 277 V with

respect to ground (since the cathode floats approximately 22 V below ground). Converting to a cathode referenced voltage, simulated power is 2.8 kW, the remaining 0.2 kW difference resulting from an underprediction of the discharge current. The results of the model for the 3 kW case are summarized, along with measured values, in Table 6-5.

	2-D Model	Direct Measurements
Mass Flow Rate [sccm]	113	110
Discharge Voltage [V]	275	300
Discharge Current [A]	9.4	10
Thruster Power [W]	2.6	3.0
Beam Current Fractior [A]	94	85
Thrust [mN]	178	175
Specific Impulse [s]	1652	1670
Efficiency [%]	56	51

Table 6-5 Comparison of numerical and experimental thruster operating parameters and performance values for the P5. Efficiency predictions vary from experimental values by 5% while both specific impulse and thrust agree within 2%.

As can be seen, the model predicts quite well the performance characteristics of the P5 operating at 3 kW. Efficiency values vary by only 5% while both thrust and specific impulse agree to within 2%. These variations are on the same order as the uncertainty in thrust stand measurements (-2/+8 mN).

Of more immediate concern are the two dimensional profiles of plasma parameters inside the thruster. Figures 6.24 and 6.25 are the predicted and measured contours of the plasma potential at 3 kW (2.6 kW), respectively.

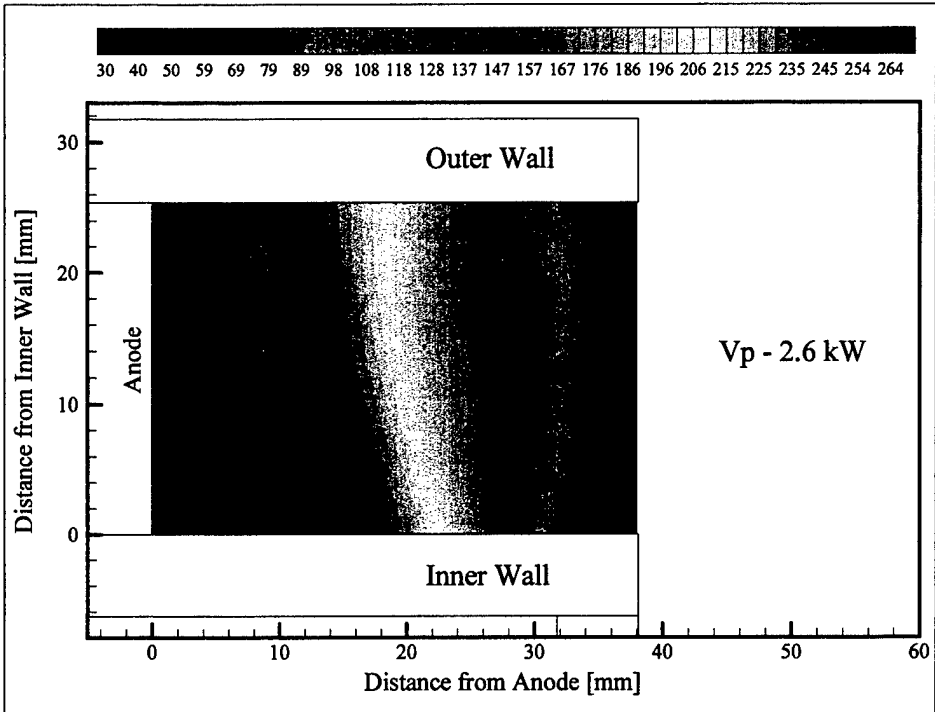


Figure 6.24 Plasma potential contours, predicted, 2.6 kW.

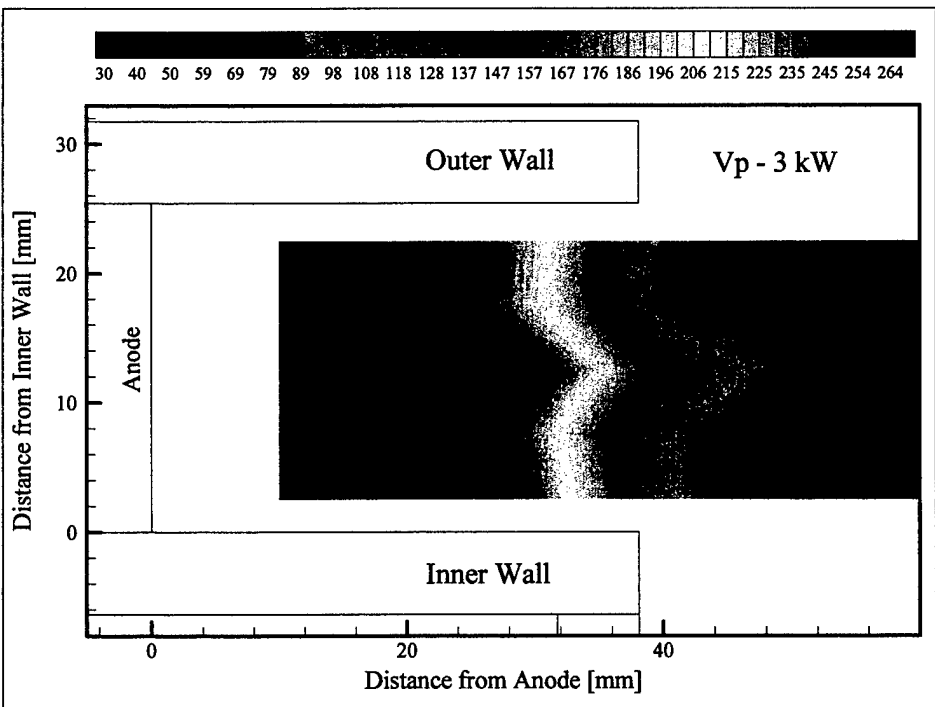


Figure 6.25 Plasma potential contours, measured, 3 kW.

As discussed at the beginning of the chapter, the entire potential drop in the P5 does not occur in the channel. Depending on the radial location, fully one-half to one-third of the potential drop takes place downstream of the thruster exit. This is considerably different from the 2D predictions in Figure 6.24. This is due to the particular boundary conditions imposed in the model where the exit plane is fixed at ground potential. Thus the full potential drop is artificially forced to occur within the channel. This makes it difficult to directly compare the predicted and measured potential data but some limited comparisons may be drawn. It was observed that the plasma potential remained nearly constant over the first 75 % of the channel in the P5. If, instead of using the channel length as a reference, we consider the distance over which the total potential drop occurs, the extent of constant potential is approximately 30 – 40%. This agrees closely with the predicted plasma potential, which remains nearly constant over the same 30 – 40% of its total drop. Based on this same reasoning, it should be possible to directly compare the strength of the electric field, which is the change in potential over a given distance. Referring back to Figure 5.81b, the average electric field peak measured across the discharge channel is approximately 16.6 V/mm. The same calculation for the predicted potential data yields 16.5 V/mm. One aspect of the potential data that the model does not predict is the prominent jet structure on centerline.

Figures 6.26 and 6.27 show the predicted and measured ion number density at 3 kW.

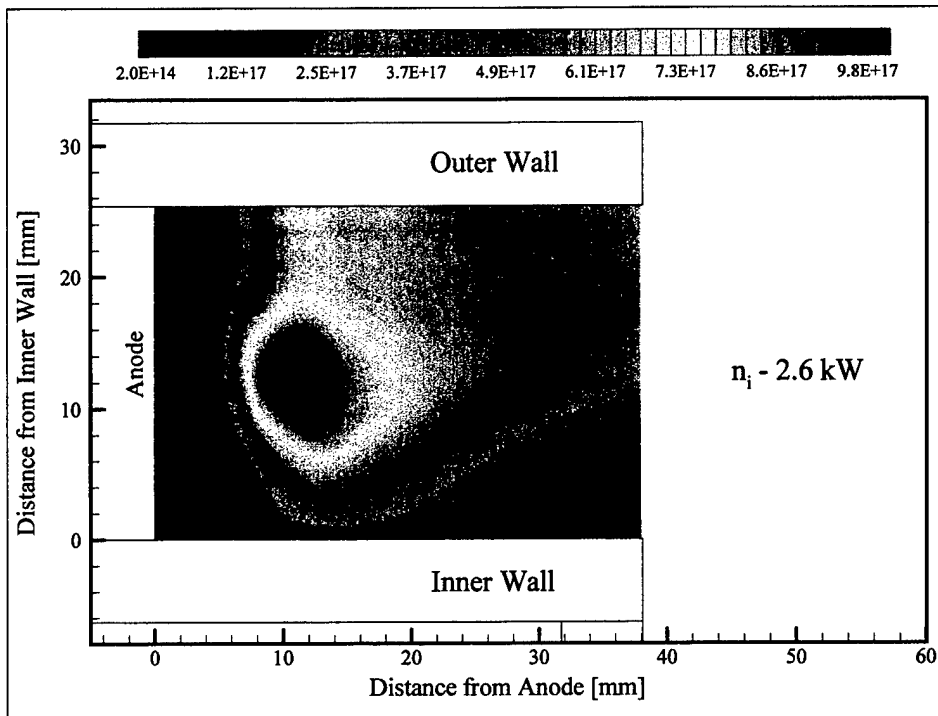


Figure 6.26 Ion number density, predicted, 2.6 kW.

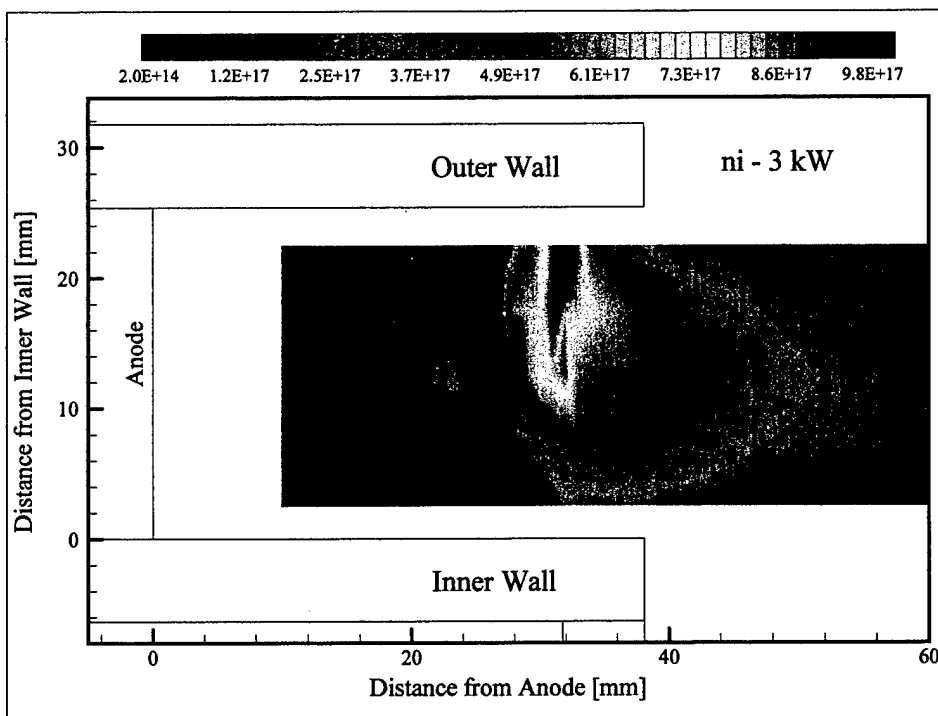


Figure 6.27 Ion number density, measured, 3 kW.

As was the case with the potential data, the exit plane boundary condition makes direct comparisons difficult. However, one puzzling aspect of the measured density profiles is the observed radial asymmetry; ions seem to preferentially exist along the outer wall of the channel. While the predicted ion density shows a peak centered in the channel, the same sort of asymmetry is apparent.

Because of their mass, ions are essentially unmagnetized and experience no drift motion associated with the magnetic field. They are, however, susceptible to electric fields in the plasma. A sufficiently strong radial field, directed toward the outer wall, could account for the observed density profile. Figure 6.28 shows the magnitude of the radial electric field, calculated from the plasma potential measurements, at 3 kW.

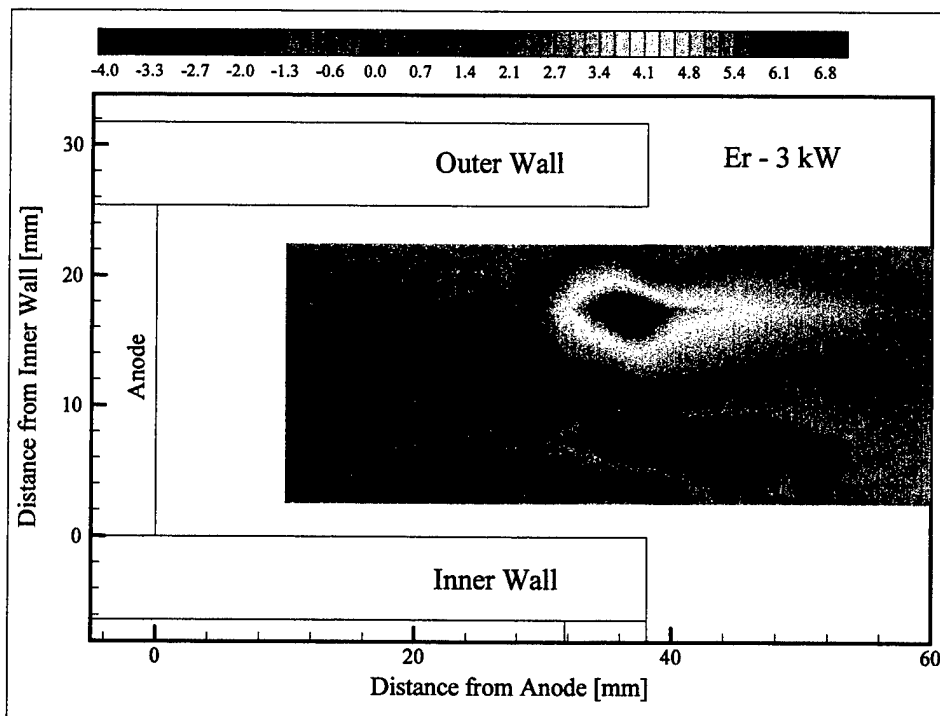


Figure 6.28 Radial electric field, 3 kW.

From Figure 6.28, it can be seen that there is a radial electric field, near the outer wall and oriented in that direction. However, there is also a radial field oriented toward the inner wall. This implies that ions experience both an inner and outward radial acceleration of similar magnitude; but there is no observed ion concentration along the inner wall suggesting that the radial field is not responsible, at least not solely, for the ion density asymmetry. Further, the ion density profiles of Figure 6.27 show the main concentration of ions occurring at an axial position of 32 mm. The radial electric field only becomes substantial downstream of this position.

If there are no forces acting on the ions causing them to migrate to the outer wall, then it stands to reason that they were created there to begin with. This is supported quite well, as has been seen, by the electron temperature measurements, indicating electrons with a high thermal temperature along the outer wall. Additionally, Hall current calculations indicate a large Hall current along the outer wall (Section 6.1), coincident with the peak ion density. This explains the asymmetry of the ion density but raises the additional question as to the origin of the Hall current asymmetry. Recall that the Hall current is proportional to the drift velocity of the electrons, which is in turn proportional to the ratio of the axial electric field to the radial magnetic field. The potential data of Figure 6.25 indicate that the potential, and hence the axial electric field, are symmetric about the channel centerline. The radial magnetic field, on the other hand, is considerably lower along the outer wall, as shown below in Figure 6.29.

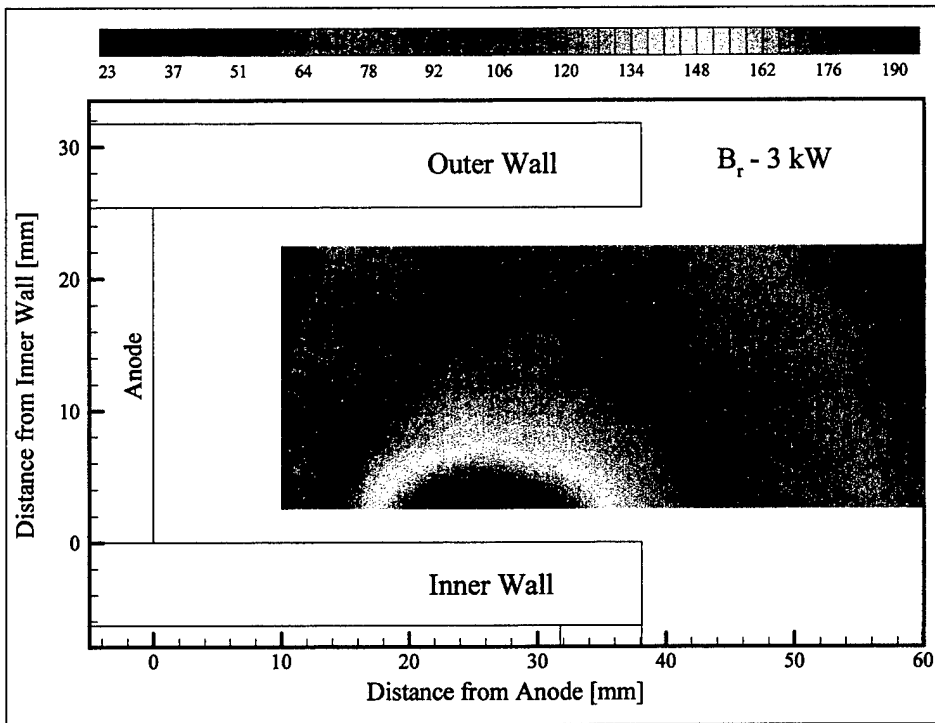


Figure 6.29 Radial magnetic field contours for the P5 at the 3 kW condition. The radial field has a maximum along the inner wall and decreases across the channel.

Therefore, a reasonable hypothesis is that it is the magnetic field that causes an asymmetric Hall current zone, which in turn creates an ionization zone along the outer wall. Unfortunately, this doesn't seem to explain the high electron temperatures found along the outer wall (ionization is an energy loss mechanism for the electrons; further, it is expected that the electron population would be dominated by lower-energy secondary electrons from the ceramic walls). As is often the case with plasmas, it may be prohibitively difficult to try and analyze the observed phenomena in terms of a cause and effect relationship. As an alternative, consider the single-fluid MHD equation of motion, which describes the combined plasma effects in a self-consistent manner.

$$\mathbf{u} \circ \nabla \mathbf{u} = \frac{1}{\rho} (\mathbf{j} \times \mathbf{B} - \nabla P) \quad \text{Eq. 6-46}$$

There is very little bulk electron or ion motion in the radial direction and so we can ignore the radial component of the term on the left hand side of Equation 6-46. Making use of Maxwell's equation

$$\nabla \times \mathbf{B} = \mu_0 \mathbf{j} \quad \text{Eq. 6-47}$$

the Hall current term can be written as

$$\mathbf{j} \times \mathbf{B} = \left(\frac{1}{\mu_0} (\nabla \times \mathbf{B}) \right) \times \mathbf{B} = (\mathbf{B} \circ \nabla) \mathbf{B} - \left(\frac{\mathbf{B}^2}{2\mu_0} \right) \quad \text{Eq. 6-48}$$

If it is assumed that the magnetic field lines are essentially straight and parallel (this is a weak assumption, at best, but is reasonably true in the region of interest. Further, it is understood that the results offer only the grossest qualitative approximation), the radial component of Equation 6-49 simplifies to

$$\frac{\partial}{\partial r} \left(P + \frac{\mathbf{B}^2}{2\mu_0} \right) = 0 \quad \text{Eq. 6-49}$$

Equation 6-49 tells us that, in the radial direction, the plasma pressure balances the magnetic pressure. This would explain the high temperature, high density region along the outer wall, coincident with the low magnetic field region, since plasma pressure is proportional to the product of particle density and temperature.

It is clear that ion losses to the walls of the discharge channel reduce the efficiency of the thruster and increase material erosion, lowering thruster lifetime. The above analysis suggests that a symmetric magnetic field, high along the walls and low along the centerline of the channel, would confine the plasma to the center of the channel and reduce ion-wall interaction.

It is interesting to consider how this magnetic field configuration might manifest itself in the structure of the plume. A common feature of Hall thrusters is the high density core on thruster centerline; both visual inspection and probe based measurements (particularly Faraday probes) reflect this focusing of ions along the thruster axis. Appendix A contains an expanded data set for the P5 that shows this high density core. Gulczinski¹¹ has speculated that, in the P5, certain charge exchange products at high angles come from ions that have been accelerated from the opposite side of the thruster. This suggests that the ions leaving the channel are being over-focused and that better performance might be achieved by increasing the effective focal length of the ions. This conclusion is further supported by Faraday probe data from the SPT-140, a state-of-the-art thruster currently undergoing life-testing at AFRL¹⁰. Figure 6.30 shows ion current density at 1 m for the P5 and for the SPT-140¹⁰. At 1 m on centerline, the P5 shows the typical high-density

core, whereas the SPT-140 has a double-peak structure, indicative of a highly collimated ion beam exiting an annular discharge chamber. Considering the P5 results and the SPT-140 data, it seems apparent that by focusing ions along the channel centerline, as opposed to the thruster centerline, a more collimated ion beam, and hence more efficient thruster, could be achieved.

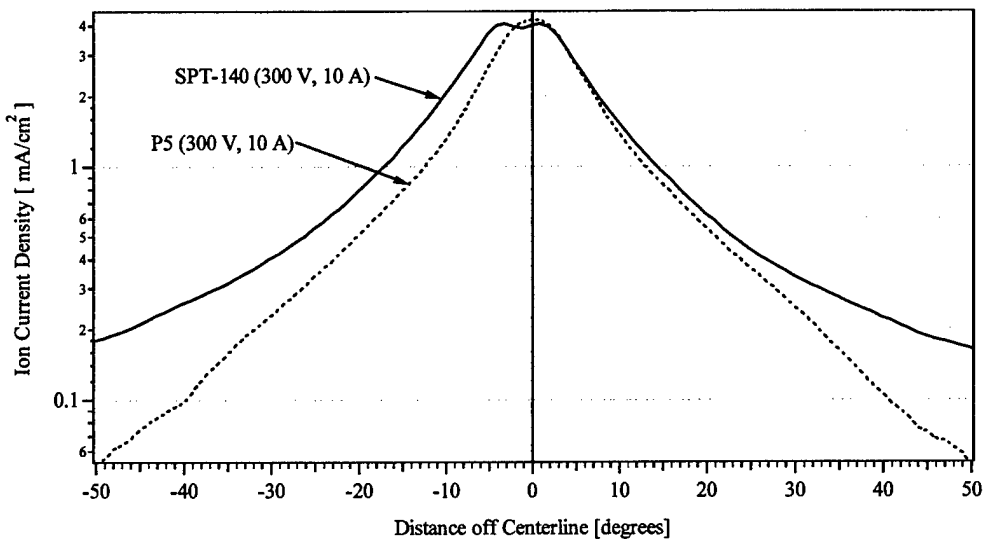


Figure 6.30 Ion current density profiles for the P5 and the SPT-140¹⁰. The wide, double-peak of the SPT-140 profile indicates a more highly collimated ion beam compared to the focused beam of the P5.

References for Chapter 6

¹ Bugrova, A.I., "Probe Measurements of Drift Current in a Hall Accelerator," *Soviet Physics-Technical Physics*, Vol. 30, No. 6, June 1985, pp. 610-612.

² Peterson, P., Haas, J., Hofer, R., Gallimore, A., "Experimental Investigation of Hall Thruster Magnetic Field Topography," ICOPS 2000-4A07, 27th IEEE International Conference on Plasma Science, New Orleans, LA, June 2000.

³ Maslenikov, N.A., Russian Electric Propulsion Seminar, Massachusetts Institute of Technology, 1991.

⁴ Jahn, R.G., The Physics of Electric Propulsion, McGraw-Hill Book Company, New York, 1968.

⁵ Chen, F.F., Introduction to Plasma Physics and Controlled Fusion, Plenum Press, New York, 1984.

⁶ Brown, A., Basic Data of Plasma Physics, McGraw-Hill Book Company, New York, 1959.

⁷ Koo, J., Boyd, I., Haas, J., Gallimore, A., "Computation of the Internal Flow of a 2kW-Class Hall Thruster," to be presented at the 37th AIAA/ASME/SAE/ASEE Joint Propulsion Conference Salt Lake City, Utah, July, 2001.

⁸ Bohm, D. in *The characteristics of Electrical Discharges in Magnetic Fields*, edited by A. Guthrie and R.K. Wakerling, McGraw, New York, 1949.

⁹ Meezan, N.B., Cappelli, M.A., "Electron Density Measurements for Determining the Anomalous Electron Mobility in a Coaxial Hall Discharge Plasma," AIAA-2000-3420, 36th AIAA / ASME / SAE / ASEE Joint Propulsion Conference, Huntsville, AL, July 16-19, 2000.

¹⁰ Fife, J.M., Hargus, W.A., Jaworske, D.A., Sarmiento, C., Mason, L., Jankovsky, R., Snyder, J.S., Malone, S., Haas, J.M., Gallimore, A.D., "Spacecraft Interaction Test results of the High Performance Hall System SPT-140," AIAA-2000-3521, 36th AIAA / ASME / SAE / ASEE Joint Propulsion Conference, Huntsville, AL, July 16-19, 2000.

¹¹ Gulczinski, F.S., *Examination of the Structure and Evolution of Ion Energy Properties of a 5 kW Class Laboratory Hall Effect Thruster at Various Operational Conditions*, Ph.D. Thesis, University of Michigan Department of Aerospace Engineering, University Microfilms International, 1999.

¹² Anders, A., "Recombination of a Xenon Plasma Jet," *Contrib. Plasma Phys.* Vol. 27, No. 5, 1987, pp. 373-398.

¹³ King, L.B., *Transport Property and Mass Spectral Measurements in the Plasma Exhaust Plume of a Hall-Effect Space Propulsion System*, Ph.D. Thesis, University of Michigan Department of Aerospace Engineering, University Microfilms International, 1998.

¹⁴ Williams, G.J., Smith, T.B., Gulczinski, F.S., Beal, B.E., Gallimore, A.D., Drake, R.P., "Laser Induced Fluorescence Measurements of Ion Velocities in the Plume of a Hall Effect Thruster," AIAA-99-2424, 35th AIAA / ASME / SAE / ASEE Joint Propulsion Conference, Los Angeles, CA, June 20-24, 1999.

CHAPTER 7

SUMMARY AND FUTURE WORK

This thesis has attempted to expand the current knowledge of Hall thruster physics. This chapter summarizes the results of the previous sections and suggests directions for further research.

7.1 Summary of Experimental Results and Data Analysis

7.1.1 HARP

A high speed positioning system for internal probing of the Hall thruster was developed. The HARP was capable of inserting and removing electrostatic probes in less than 100 ms. Thruster perturbation, indicated by discharge current variations, was not eliminated entirely but was reduced considerably. Discharge current perturbation did not exceed 15% of nominal and remained below 10% for the majority of measurements. Probe lifetime was extended indefinitely; probes were not visibly damaged or destroyed by the plasma during the course of data collection.

7.1.2 P5

The P5 laboratory model Hall thruster was designed and constructed through a joint effort between the University of Michigan Plasmadynamics and Electric Propulsion Laboratory (PEPL) and the Air Force Research Laboratory (AFRL). The P5 is an SPT-type thruster, having ceramic discharge channel walls. The P5 was thoroughly tested and characterized at PEPL and was shown to have performance characteristics comparable to those of commercial thrusters then available. The size of the P5 was a compromise between providing adequate probe access (the larger the thruster, the easier to insert probes and the better the resolution) and facility capabilities (a larger thruster requires greater pumping speed).

7.1.3 Propellant Acceleration

At both power levels considered, plasma potential profiles indicated an acceleration zone that began approximately 10 mm upstream of the exit plane and extended several centimeters downstream. 75% of propellant acceleration occurred over this first 10 mm; the remaining acceleration occurred outside the thruster. At 1.6 kW, the plasma potential was very uniform across the width of the channel; at 3 kW, the potential profile on the channel centerline was shifted downstream several millimeters and a “jet” structure developed. LIF¹ measurements at the exit plane showed axial ion velocity was radially uniform at both 1.6 and 3 kW. While not reflecting the asymmetry of the potential profiles at 3 kW, LIF measurements did indicate a 50% increase in radial ion velocity,

compared to the 1.6 kW case; this is consistent with the curvature of the equipotential contours at 3 kW.

7.1.4 Propellant Ionization

Two populations of electrons were identified: High temperature, thermal electrons and high-energy, drifting electrons. At low power, a primary ionization zone was observed far upstream of the exit plane corresponding to high temperature electrons. A secondary zone occurred near (upstream of) the exit plane and corresponded to a region of high energy, drifting electrons - the Hall current. Ions formed in this primary zone experienced very little axial acceleration (as evidenced by the plasma potential profiles) and had a high rate of loss to the walls. The majority of the thrust at this power level was generated from ions resulting from the interaction of the neutral propellant with the Hall current near the exit plane. The primary ionization far upstream of the exit plane, and subsequent loss to the walls, resulted in a lower observed efficiency at low power.

At higher power, the plasma density exhibited a single axial peak near the exit plane. Both the high temperature thermal and high energy drifting electrons occupied a region several millimeters upstream of the exit plane, near the outer wall. For the most part, the contribution to ionization from the individual electron populations could not be distinguished. However, the ion density profile along the centerline had two peaks; one corresponding spatially to the high temperature electrons and one corresponding to the Hall current. This indicated that the Hall current still contributed to propellant ionization at higher power levels.

7.1.5 Role of Hall Current

From the profiles of ion current density, it was clear that the Hall current contributed to the ionization of the propellant. The self magnetic fields created by the Hall current in the thruster discharge were calculated using experimental data. At the power levels considered in this thesis, the axial and radial self-field magnitudes did not exceed several Gauss. This was negligible compared to the applied fields, which were several hundred Gauss. However, the data showed that the Hall current magnitude was 3-5 times that of the discharge current. If this trend continues as Hall thrusters are scaled to higher current, the self-fields generated by the drifting electrons could become large enough to significantly alter the applied magnetic field.

7.1.6 Thruster Macro-Properties

Using the internal plasma data, macro-properties of the thruster were calculated and compared to directly measured values. Electrostatic and electromagnetic analyses of thrust were shown to reduce to identical equations with the correct assumptions. The calculated and directly measured thrust (using a thrust stand) were shown to agree within 5%. Further, it was shown that approximately 75% of the total thrust was developed inside the discharge channel.

Beam current was calculated using ion number density measurements and ion velocity at the exit plane. Beam current fractions (ratio of beam current to discharge current) from internal data were shown to be approximately 76 and 81% of the discharge current at

both 1.6 and 3 kW. Faraday probe data indicated a beam current fraction of approximately 100% and 87% of discharge current at 0.5 m and 1 m, respectively. This difference between Faraday and probe based measurements is well within the 50% uncertainty associated with the ion number density. This is also considerably lower than similar measurements for other thrusters and facilities, which generally show beam current fractions much greater than 100%. It was hypothesized that low-energy charge exchange ions, the result of fast beam ions interacting with slow background neutrals, were preferentially collected at large angles off centerline, appearing as additional beam current. The difference in the P5 Faraday probe data at the two radial positions was attributed to depopulation of higher order ionic charge states as the ions transited the plume.

7.1.7 Experimental – Numerical Comparison

The experimental data were compared to a two dimensional numerical model of the Hall thruster. Efficiency predictions varied from directly measured values by 5% while both specific impulse and thrust varied by less than 2%. Due to the nature of the boundary conditions imposed by the model, a direct, quantitative comparison with experimental data was not possible. However, time-averaged number density from the model reflected the most important feature of the experimental data; the shift in the plasma to a location along the outer wall, opposite the magnetic field peak. This behavior was explained by an analysis of the MHD equations, which showed that for the conditions in the Hall thruster, the plasma pressure is balanced by the magnetic pressure. Faraday probe data from the SPT-140, a state-of-the-art thruster, showed a double-peak structure on

centerline, indicative of a well collimated ion beam. It was surmised that the improved performance of the SPT-140 was a direct result of focusing the plasma along the channel centerline, as opposed to the thruster centerline, as in the P5.

7.2 Future Work

The research reported on here has provided a wealth of information on the internal plasma characteristics of the Hall thruster. Of particular importance was the development and implementation of a high-speed probing system to enable, for the first time, interrogation with minimal perturbation to the thruster. While a necessary and important contribution to the field, this body of work is by no means comprehensive or complete. It has provided a solid starting point for further research into many areas of Hall thruster physics. Several items of particular importance are discussed below.

7.2.1 Additional Thruster Conditions

The number of thruster operating conditions investigated in this work were limited due to the practical considerations associated with completing this thesis. Hall thrusters are currently being scaled up to higher powers, both high current and high voltage. Future work should include data sets at constant discharge current to determine the effect of increasing voltage.

7.2.2 Internal LIF

The electrostatic probes employed in this work did not provide ion velocities, which were needed for beam current calculations and probe end-effect corrections. The 1D model of Section 4.4.2 provided only a gross approximation of axial ion velocities. LIF measurements in the channel would provide much more accurate information, in both the axial and radial directions. Radial velocity would provide a check on the radial plasma potential profiles.

7.2.3 Plasma Magnetic Field Measurements

The effect of the Hall current on the applied magnetic field was investigated and determined to be negligible at the conditions considered. A better approach would be to measure the magnetic field profiles directly during thruster operation; preliminary attempts at these measurements² have suggested that the Hall current may alter the applied magnetic field. A comparison with vacuum field values would determine the impact of the Hall current on the applied field; additionally, plasma field measurements could be used to verify the magnitude and spatial structure of the Hall current.

7.2.4 Next Generation Hall Thruster

Ultimately, the goal of this, and other, Hall thruster research is to enable the design of thrusters with improved performance characteristics. The experimental and numerical ion number density profiles presented here, combined with Faraday probe data for the P5 and the SPT-140, have provided direction for the next generation P5. This new thruster,

with a radial magnetic field structure symmetric about the channel centerline, is currently under construction. It will be thoroughly characterized using HARP and its associated diagnostics.

References for Chapter 7

¹ Williams, G.J., Smith, T.B., Gulczinski, F.S., Beal, B.E., Gallimore, A.D., Drake, R.P., "Laser Induced Fluorescence Measurements of Ion Velocities in the Plume of a Hall Effect Thruster," AIAA-99-2424, 35th AIAA / ASME / SAE / ASEE Joint Propulsion Conference, Los Angeles, CA, June 20-24, 1999.

² Peterson, P., Haas, J., Hofer, R., Gallimore, A., "Experimental Investigation of Hall Thruster Magnetic Field Topography," ICOPS 2000-4A07, 27th IEEE International Conference on Plasma Science, New Orleans, LA, June 2000.

APPENDICES

Additional ion number density, electron temperature, and plasma potential data were obtained beyond the confines of the discharge channel and the axial profiles are presented below. Contour plots incorporating the entire data set (from thruster centerline to the outer edge of the front pole piece) are included.

Appendix A

Ion number density profiles beyond the radial confines of the discharge channel

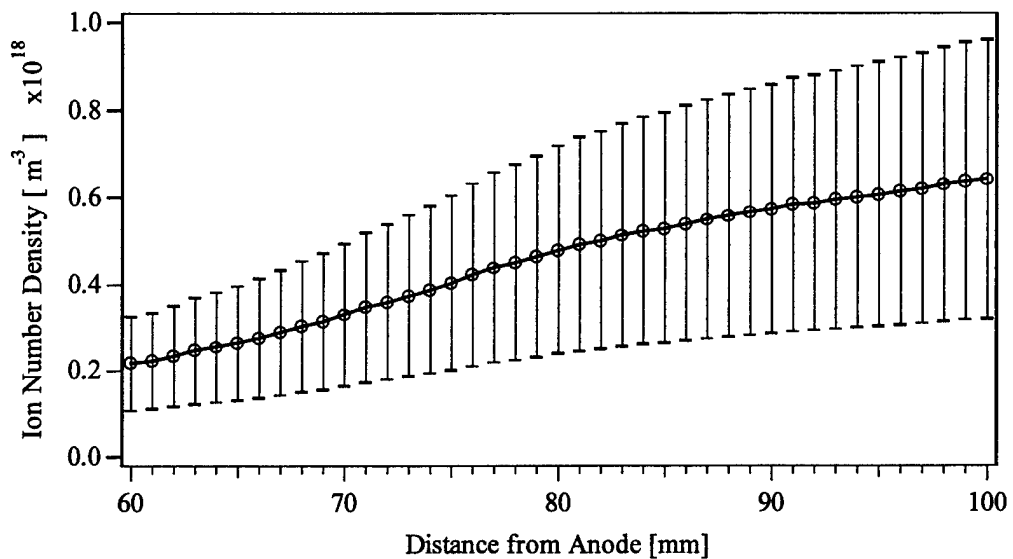


Figure A. 1 Ion number density, 1.6 kW, $R = -61$ mm.

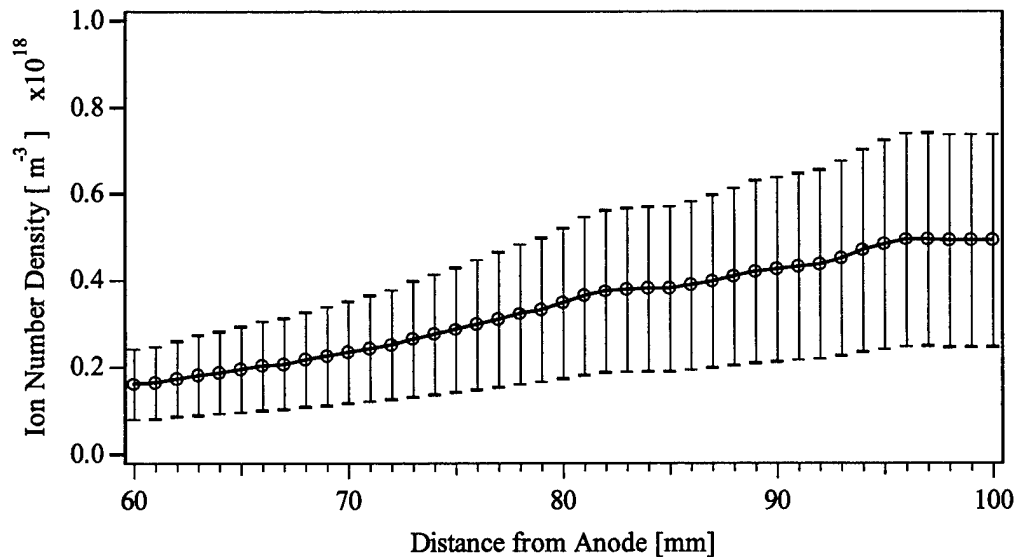


Figure A. 2 Ion number density, 1.6 kW, $R = -54.7$ mm.

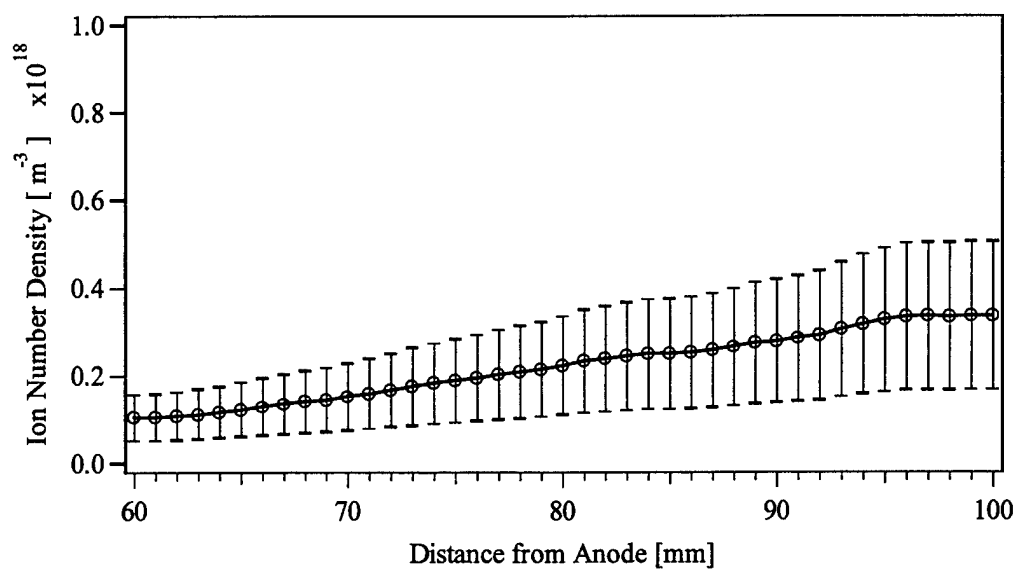


Figure A. 3 Ion number density, 1.6 kW, R = -48.3 mm.

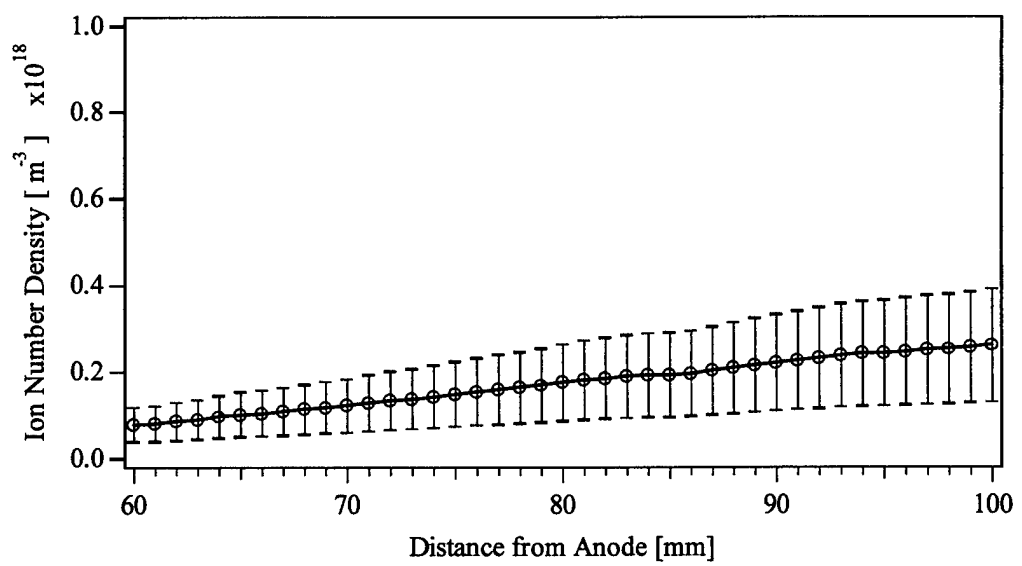


Figure A. 4 Ion number density, 1.6 kW, R = -42 mm.

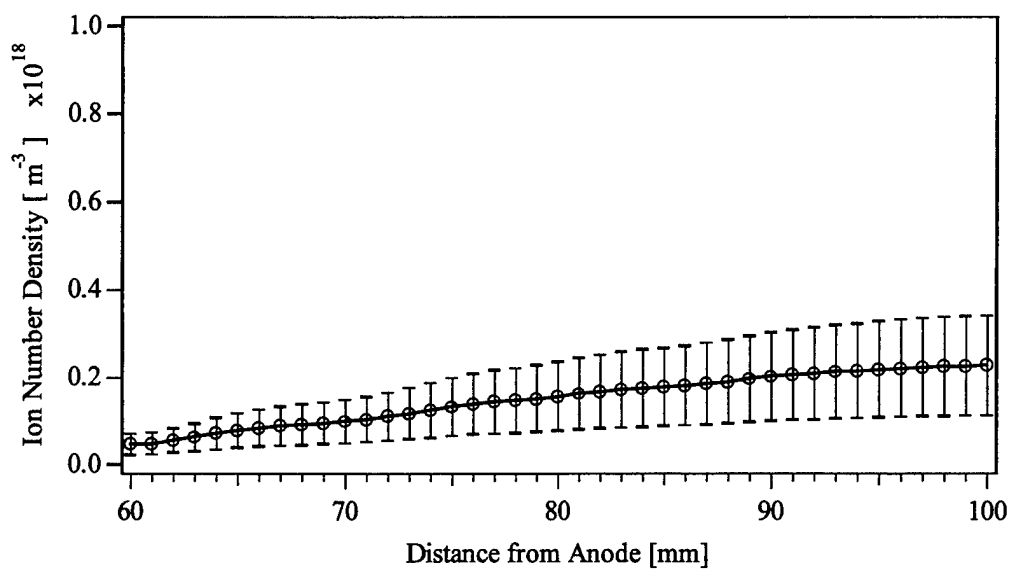


Figure A. 5 Ion number density, 1.6 kW, R = -35.6 mm.

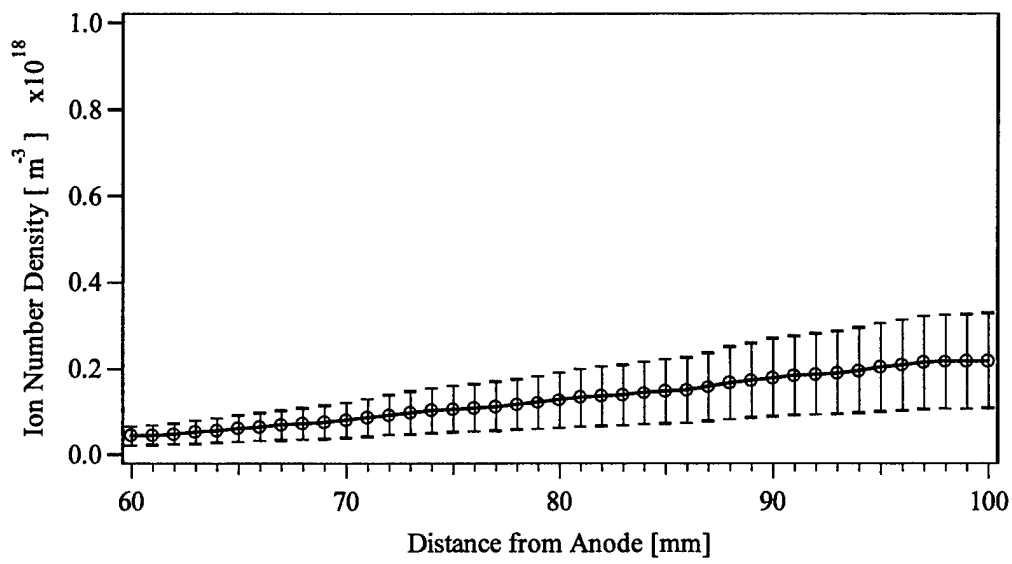


Figure A. 6 Ion number density, 1.6 kW, R = -29.3 mm.

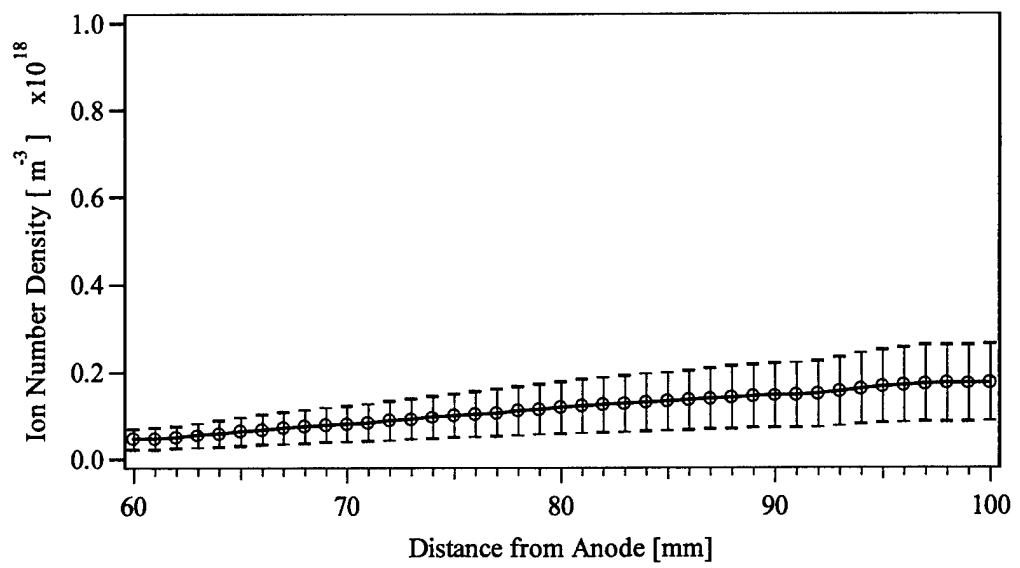


Figure A. 7 Ion number density, 1.6 kW, R = -22.9 mm.

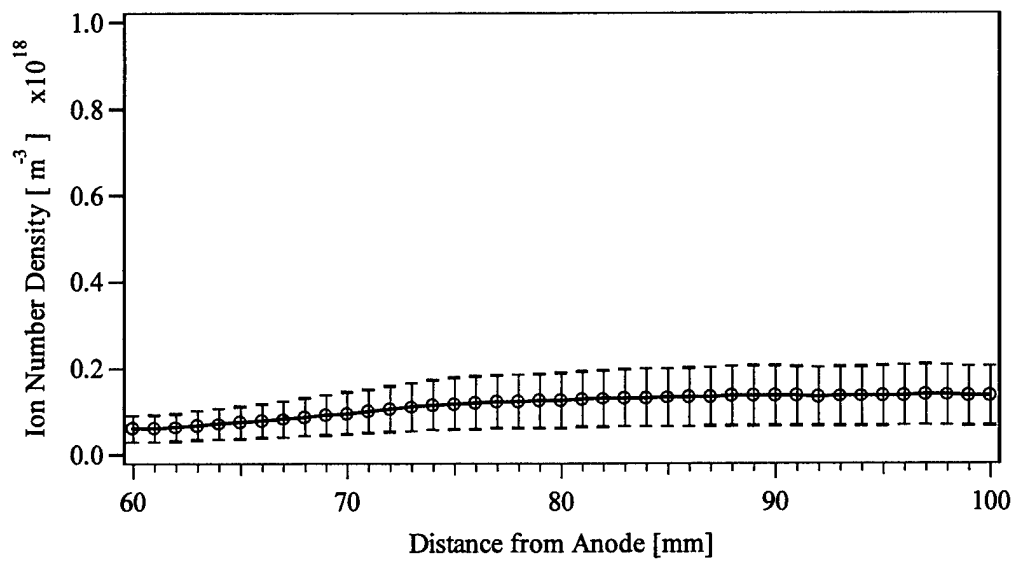


Figure A. 8 Ion number density, 1.6 kW, R = -16.6 mm.

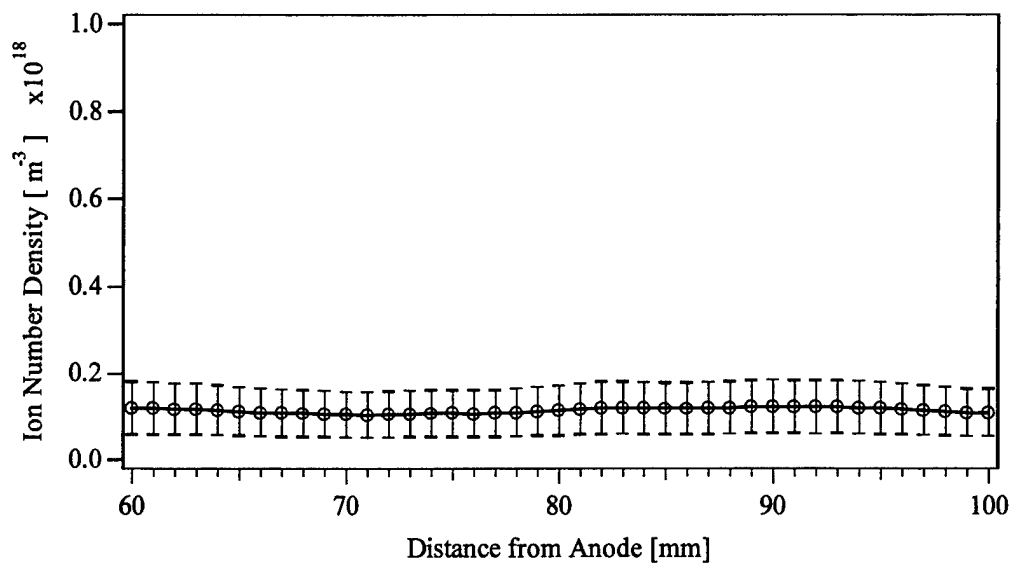


Figure A. 9 Ion number density, 1.6 kW, R = -10.2 mm.

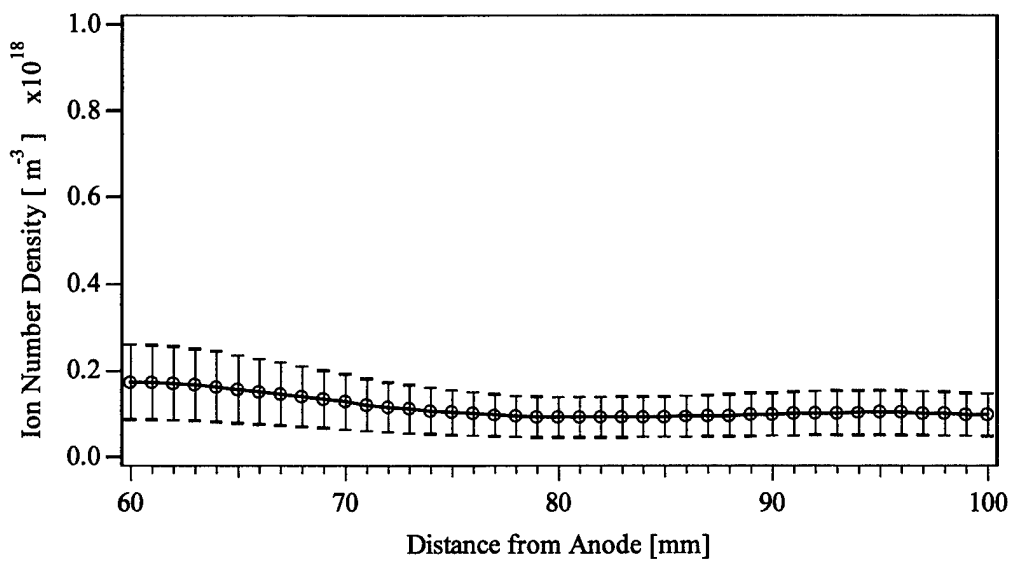


Figure A. 10 Ion number density, 1.6 kW, R = -3.9 mm.

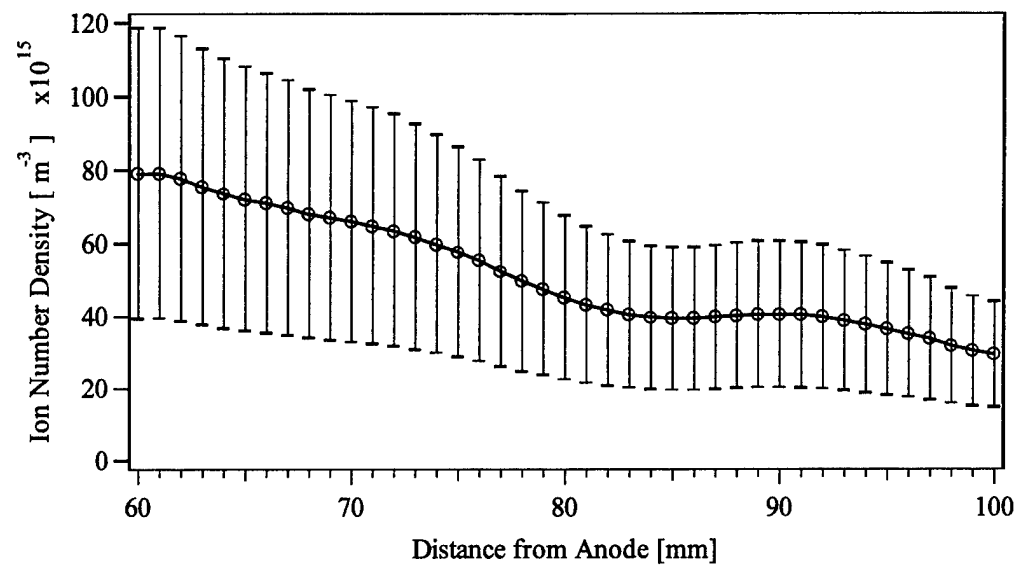


Figure A. 11 Ion number density, 1.6 kW, $R = 29.2$ mm.

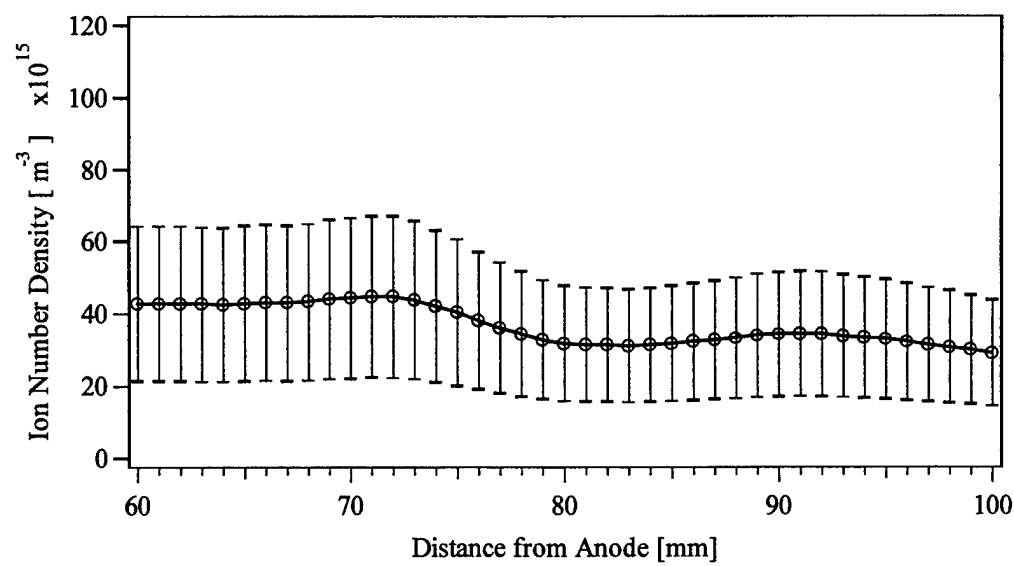


Figure A. 12 Ion number density, 1.6 kW, $R = 35.5$ mm.

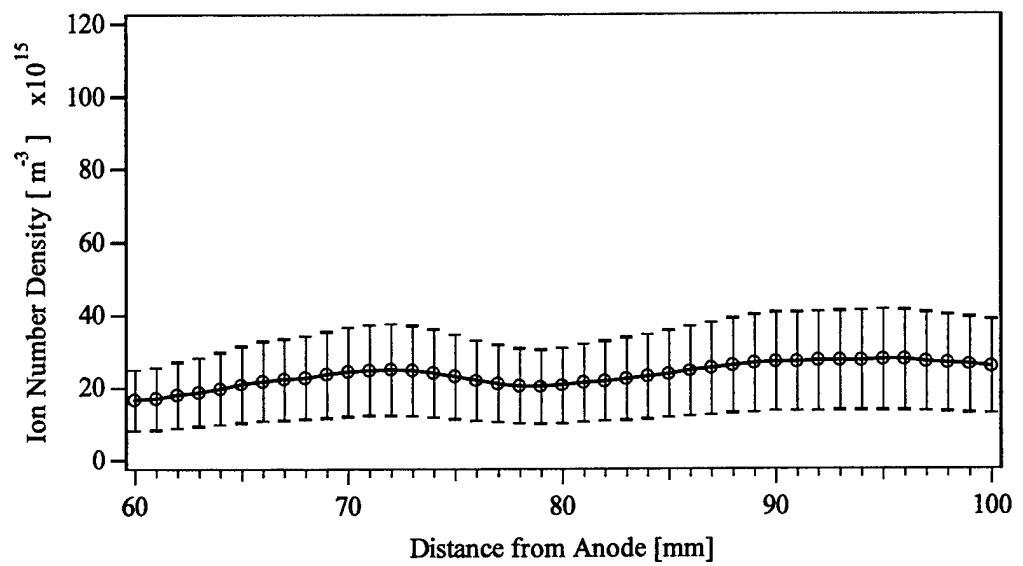


Figure A. 13 Ion number density, 1.6 kW, R = 41.9 mm.

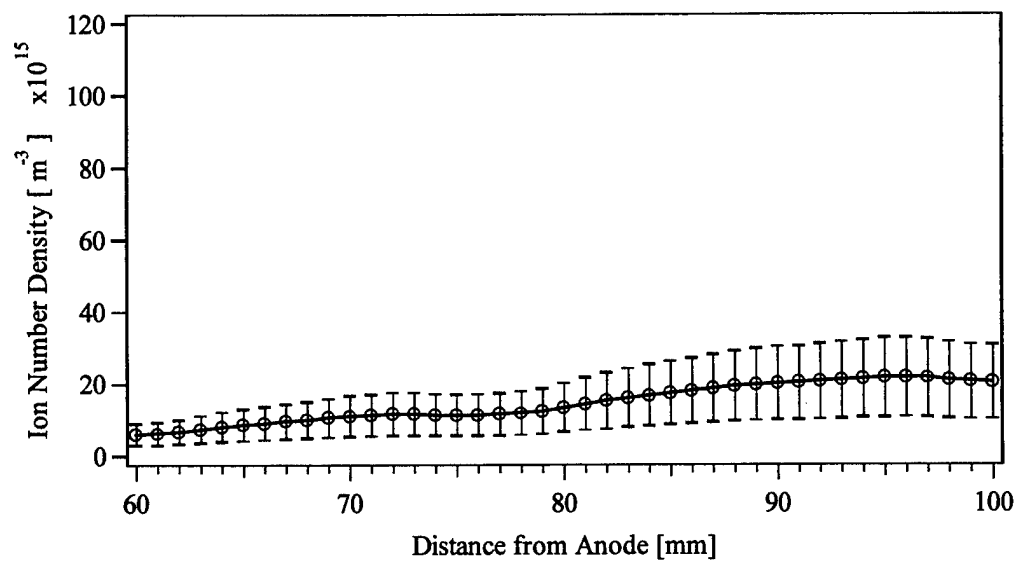


Figure A. 14 Ion number density, 1.6 kW, R = 48.2 mm.

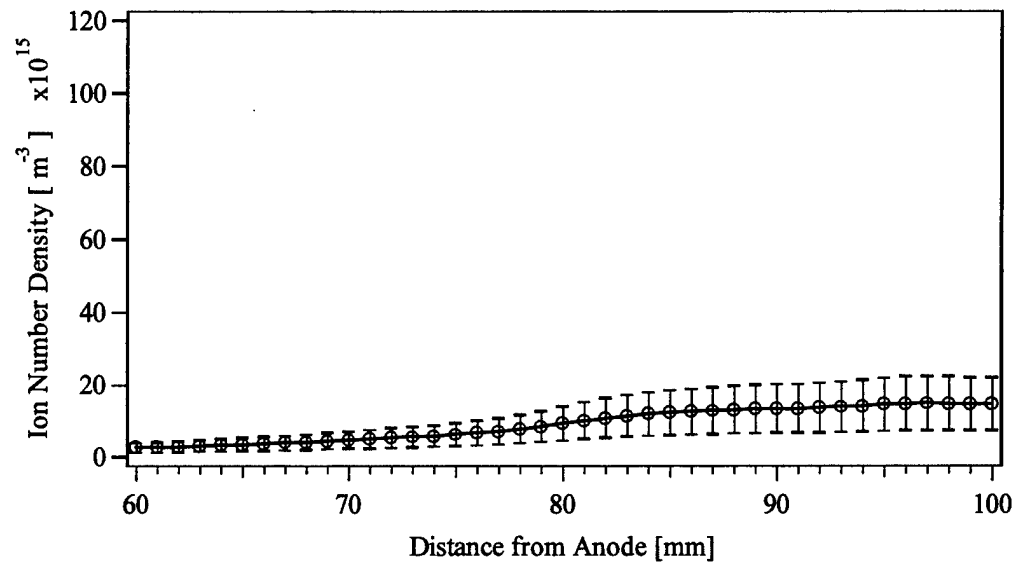


Figure A. 15 Ion number density, 1.6 kW, R = 54.6 mm.

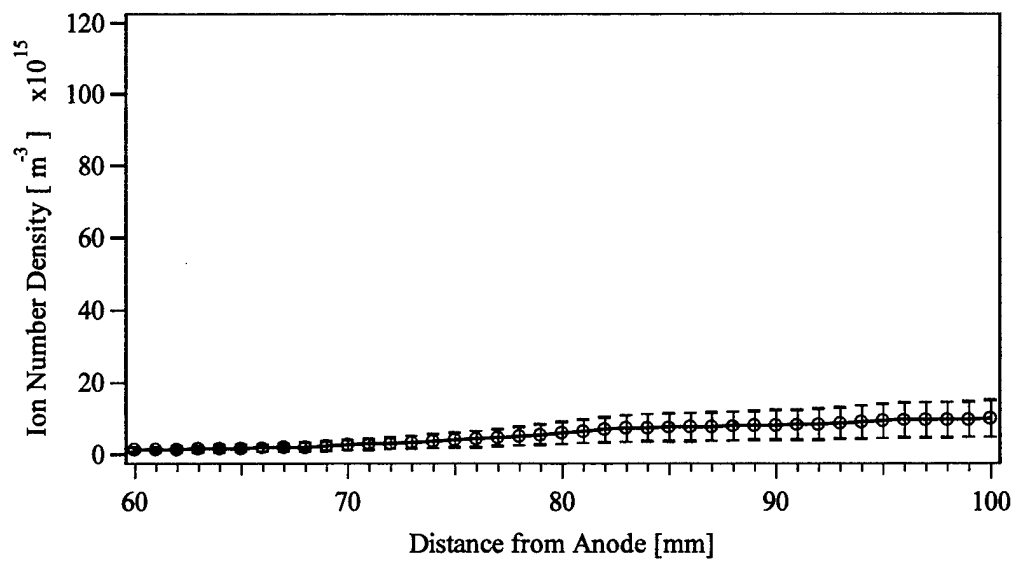


Figure A. 16 Ion number density, 1.6 kW, R = 60.9 mm.

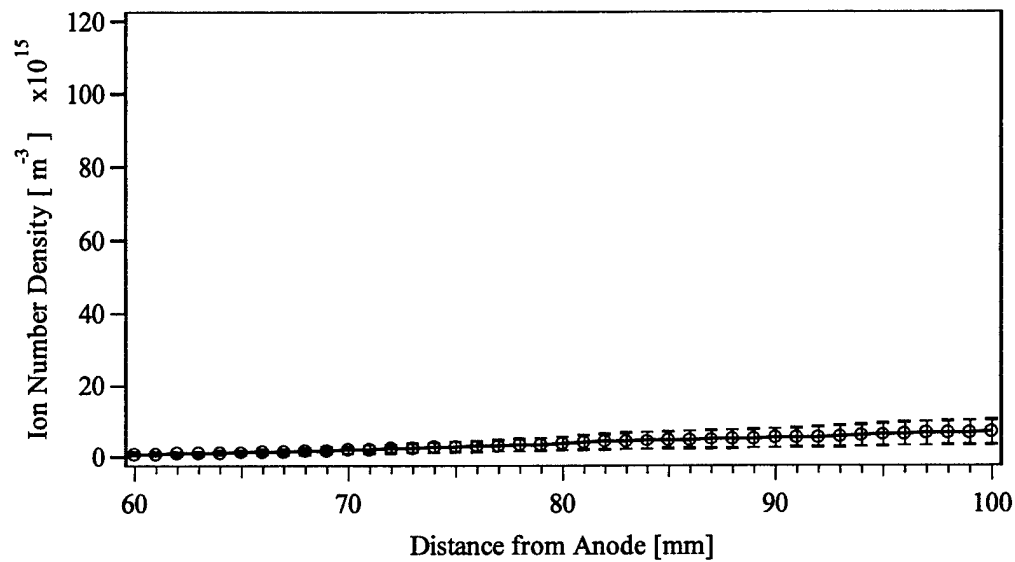


Figure A. 17 Ion number density, 1.6 kW, R = 67.3 mm.

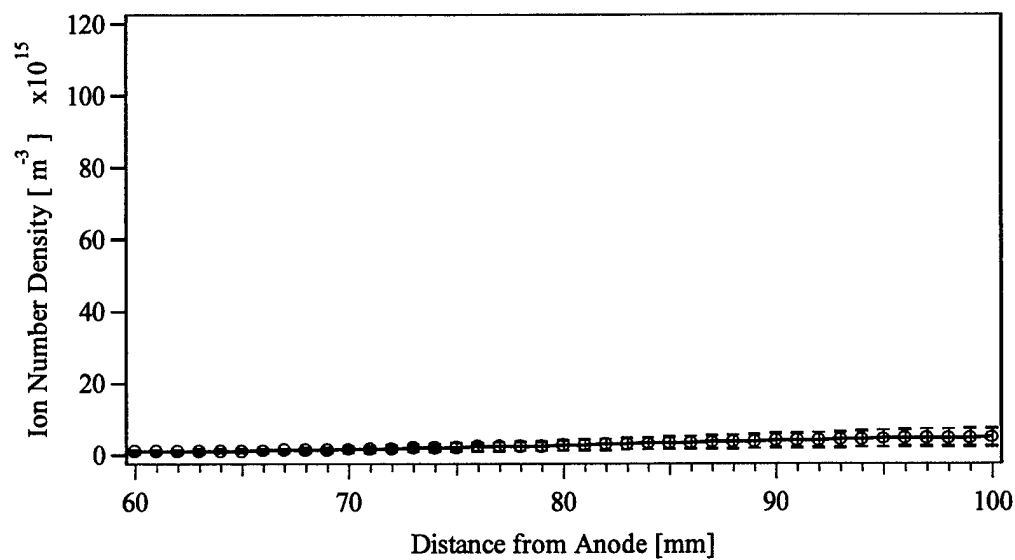


Figure A. 18 Ion number density, 1.6 kW, R = 73.6 mm.

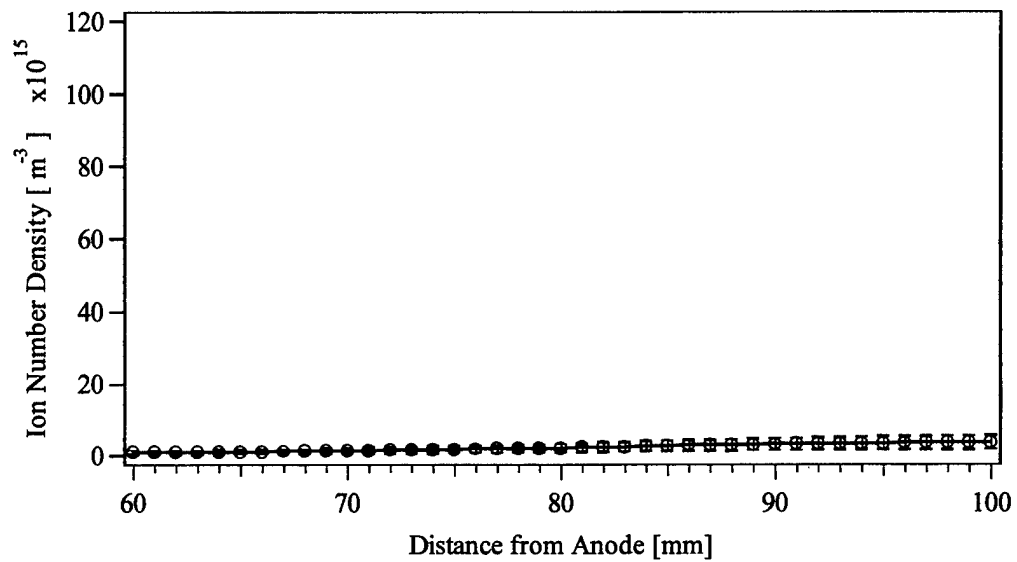


Figure A. 19 Ion number density, 1.6 kW, R = 80 mm.

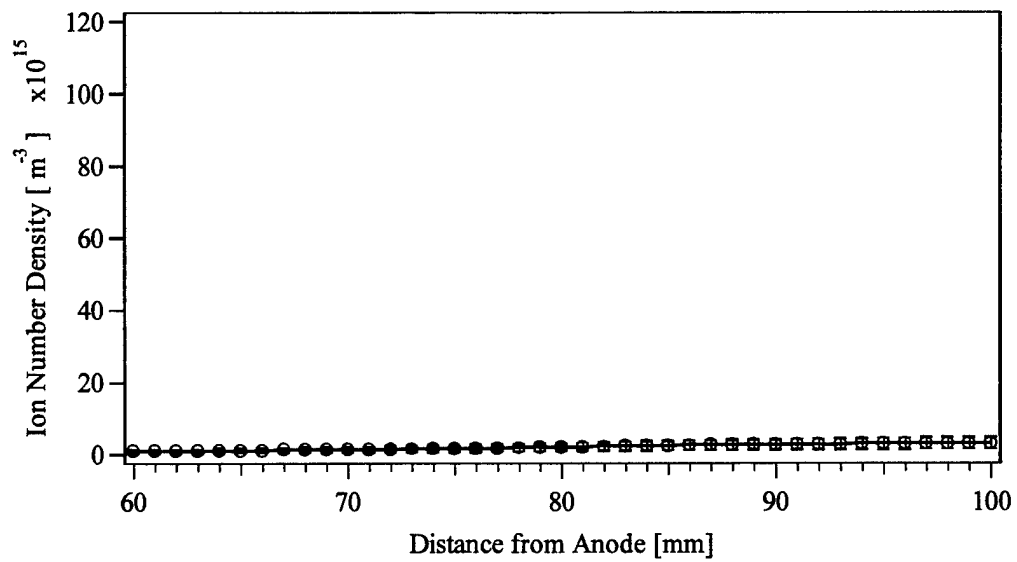


Figure A. 20 Ion number density, 1.6 kW, R = 86.3 mm.

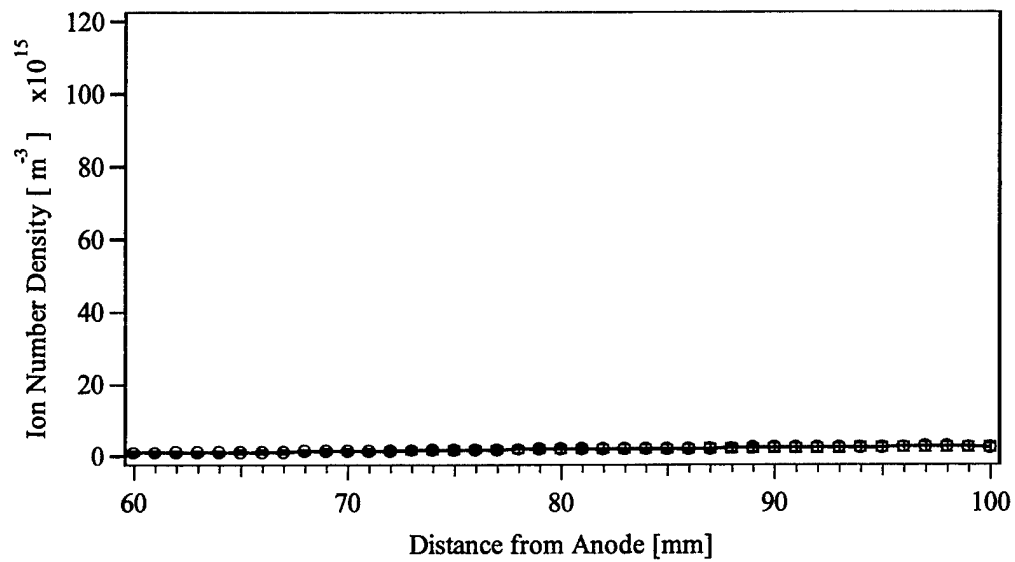


Figure A. 21 Ion number density, 1.6 kW, R = 92.7 mm.

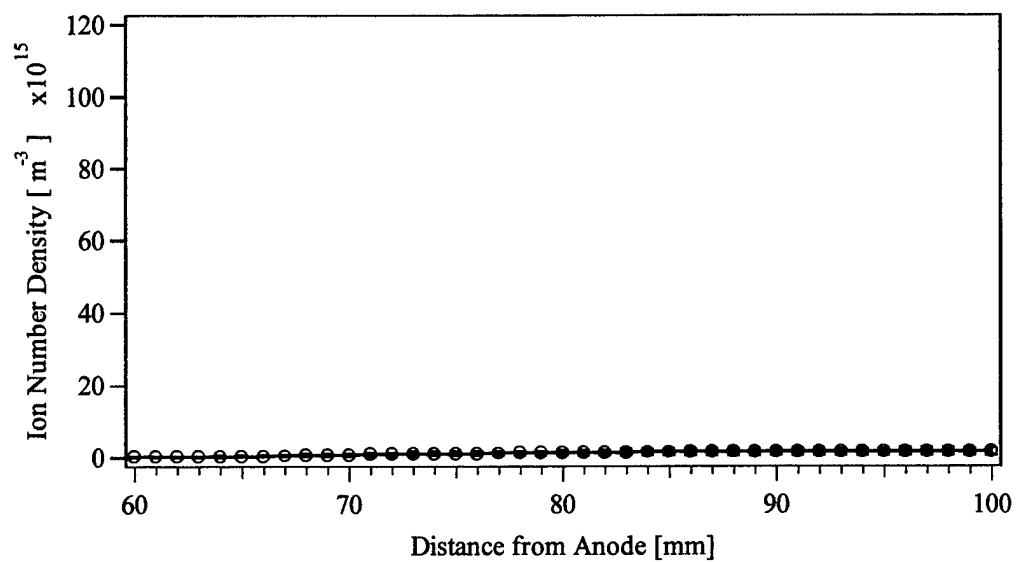


Figure A. 22 Ion number density, 1.6 kW, R = 99 mm.

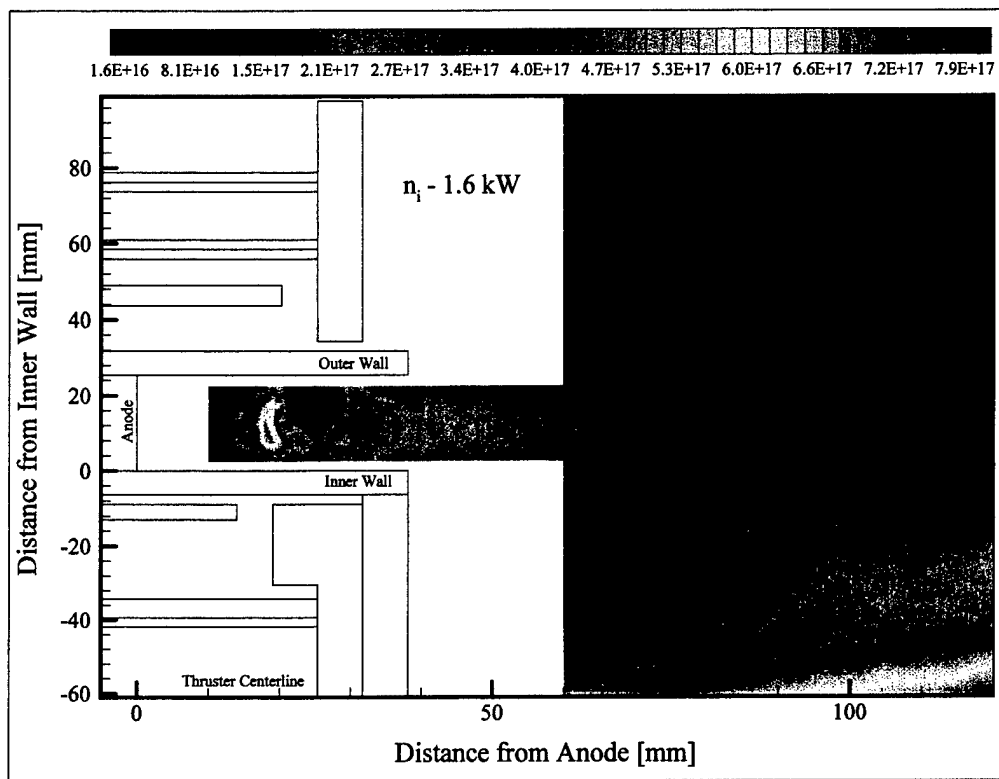


Figure A. 23 Ion number density contours, 1.6 kW. The high-density core along centerline shows the focusing of the ions.

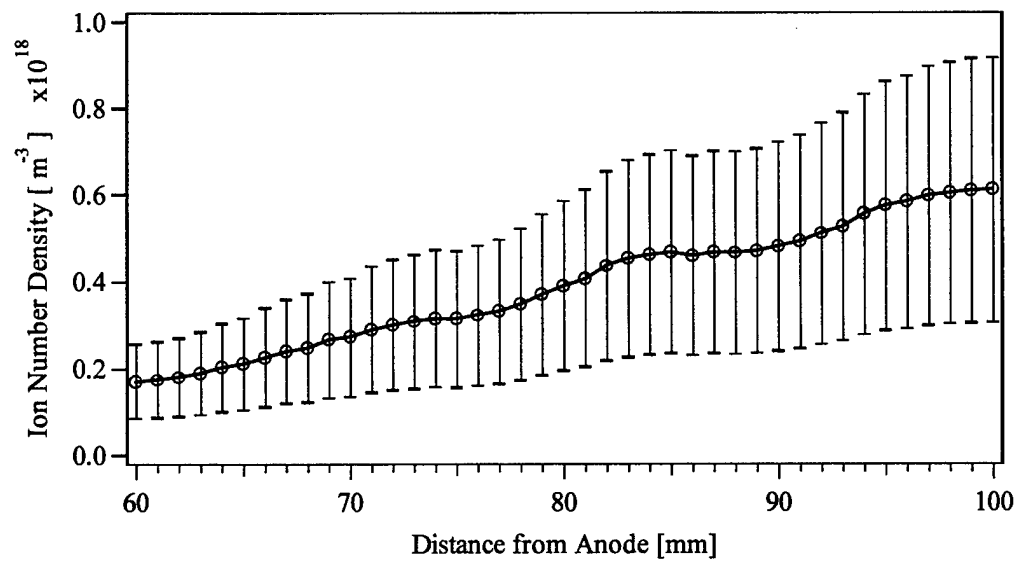


Figure A. 24 Ion number density, 3 kW, R = -61 mm.

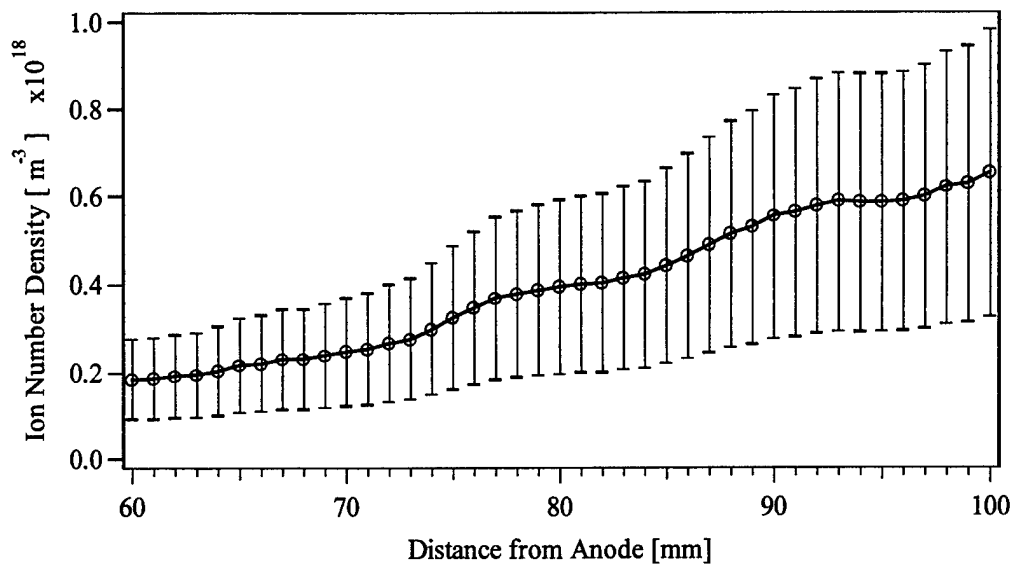


Figure A. 25 Ion number density, 3 kW, R = -54.7 mm.

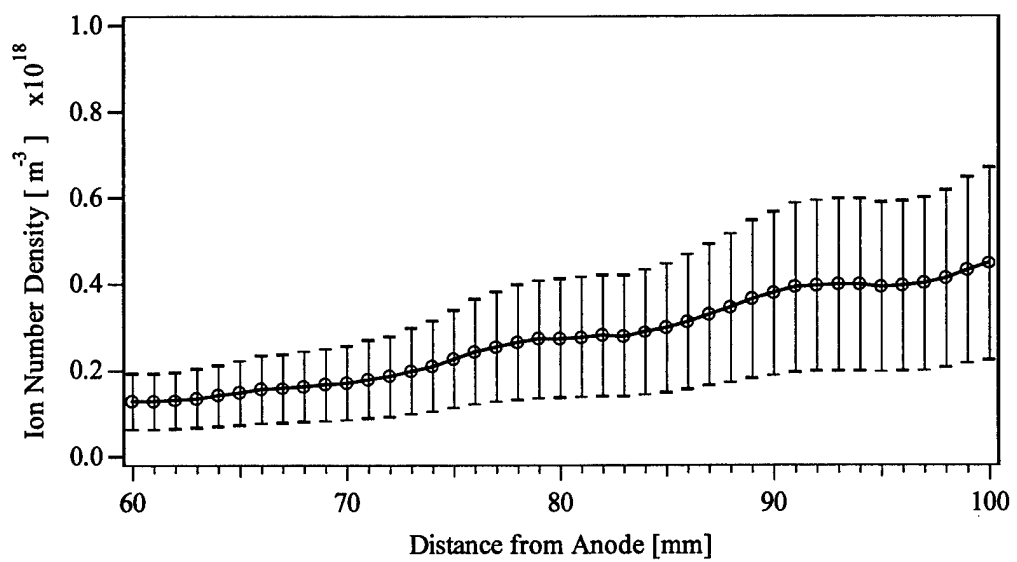


Figure A. 26 Ion number density, 3 kW, R = -48.3 mm.

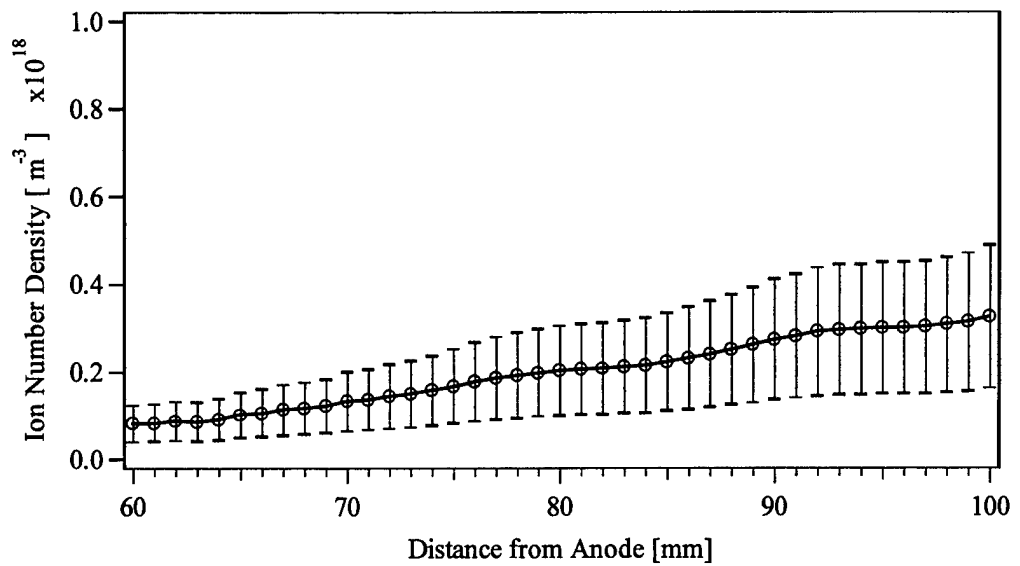


Figure A. 27 Ion number density, 3 kW, R = -42 mm.

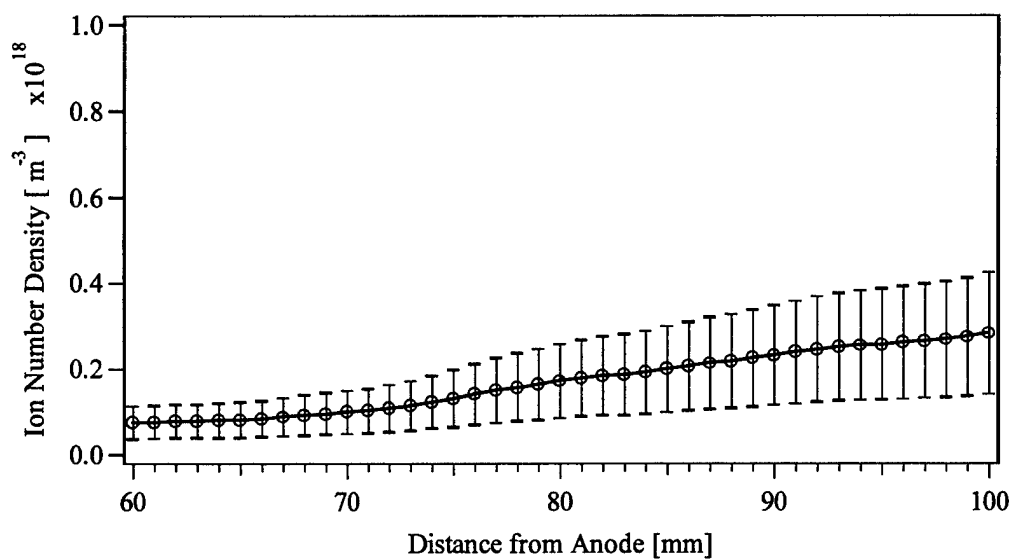


Figure A. 28 Ion number density, 3 kW, R = -35.6 mm.

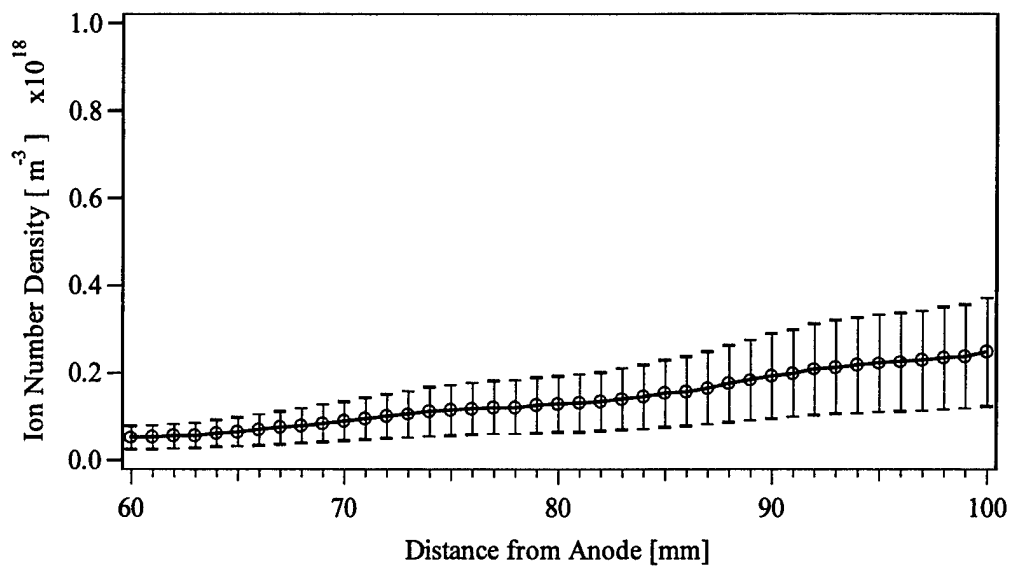


Figure A. 29 Ion number density, 3 kW, $R = -29.3$ mm.

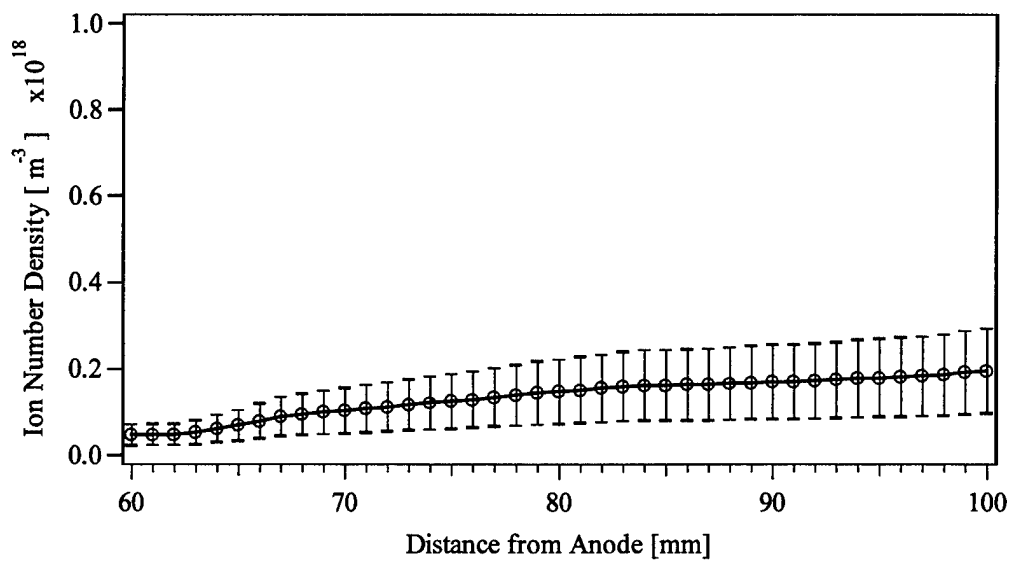


Figure A. 30 Ion number density, 3 kW, $R = -22.9$ mm.

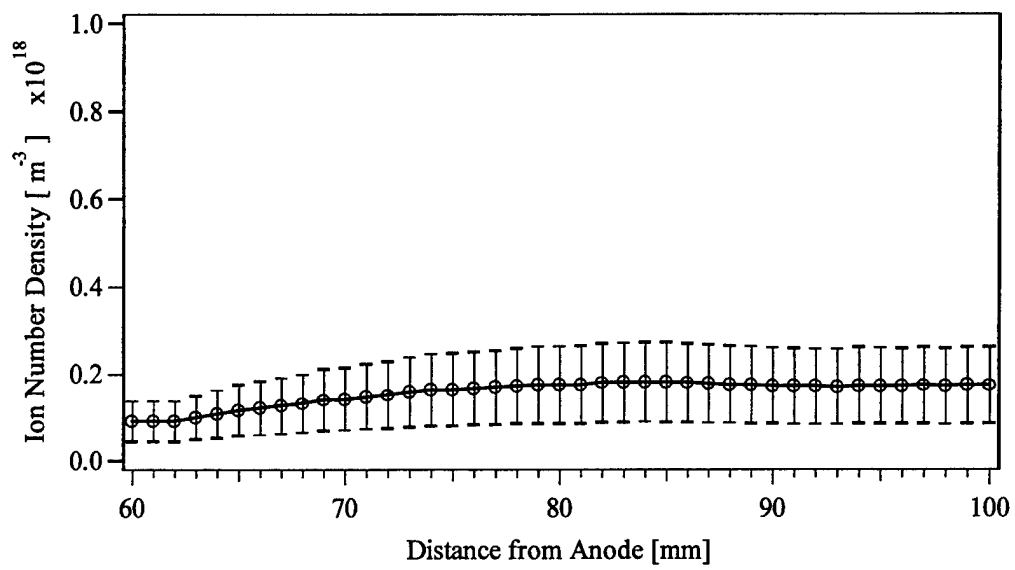


Figure A. 31 Ion number density, 3 kW, R = -16.6 mm.

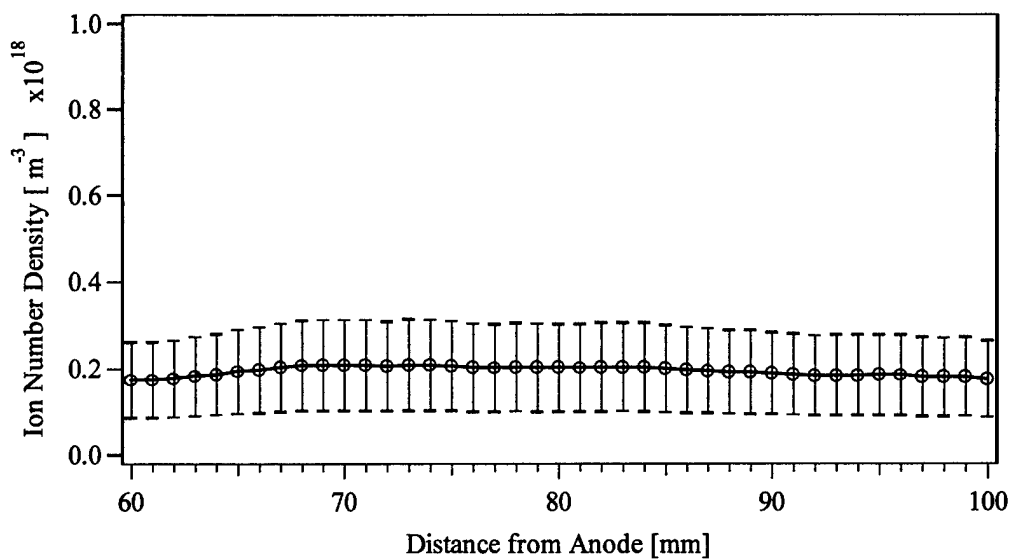


Figure A. 32 Ion number density, 3 kW, R = -10.2 mm.

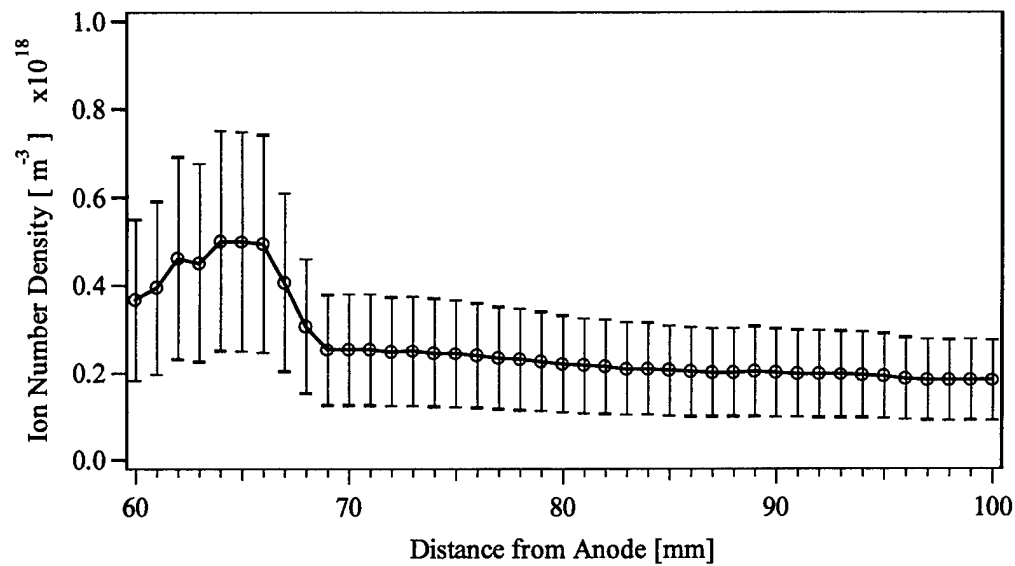


Figure A. 33 Ion number density, 3 kW, R = -3.9 mm.

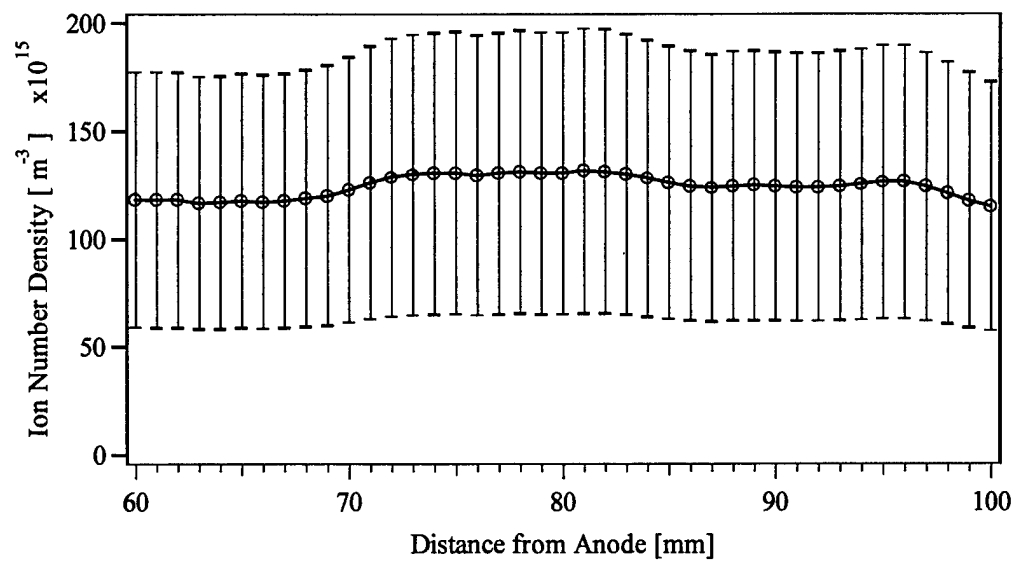


Figure A. 34 Ion number density, 3 kW, R = 29.2 mm.

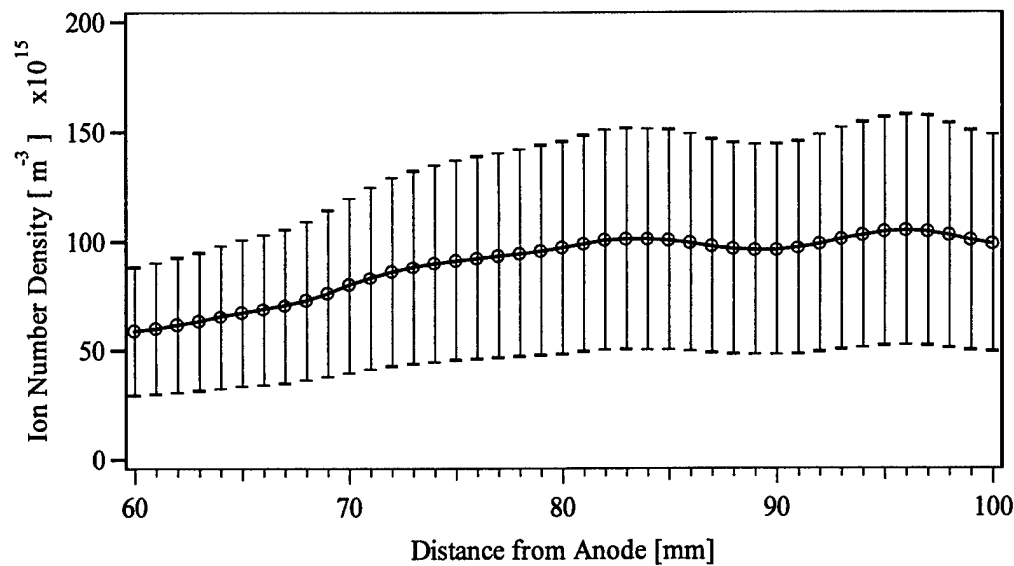


Figure A. 35 Ion number density, 3 kW, R = 35.5 mm.

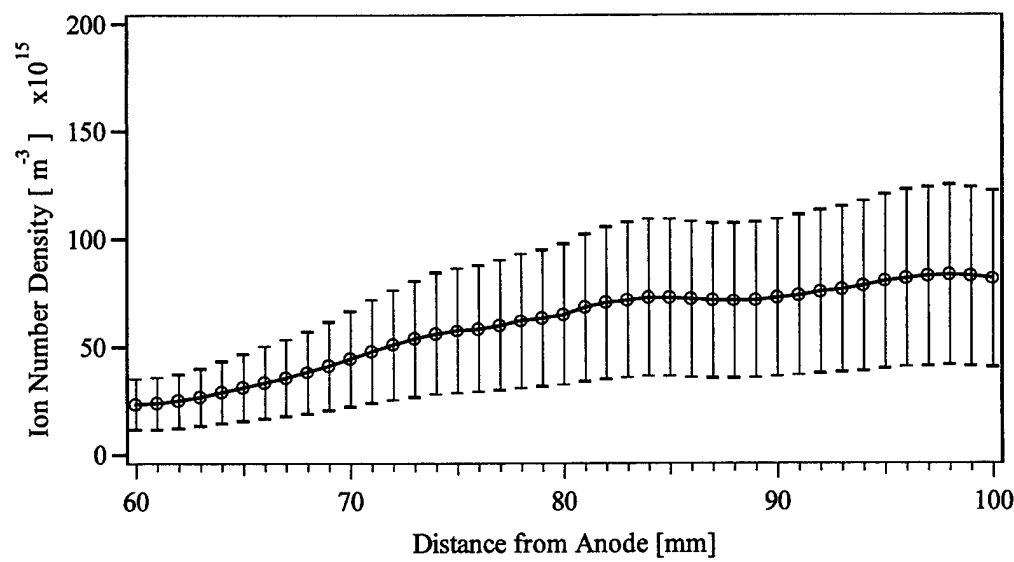


Figure A. 36 Ion number density, 3 kW, R = 41.9 mm.

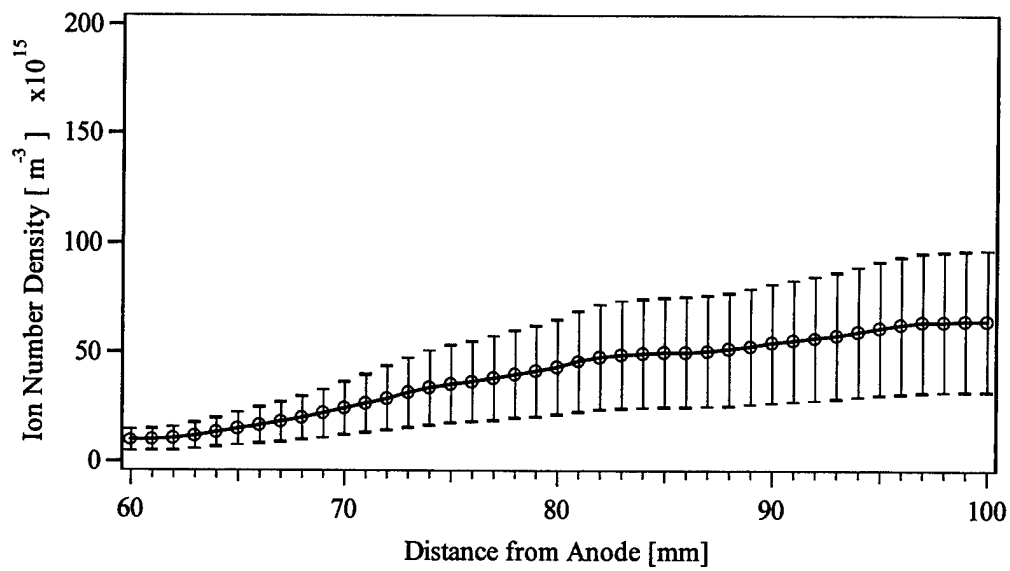


Figure A. 37 Ion number density, 3 kW, R = 48.2 mm.

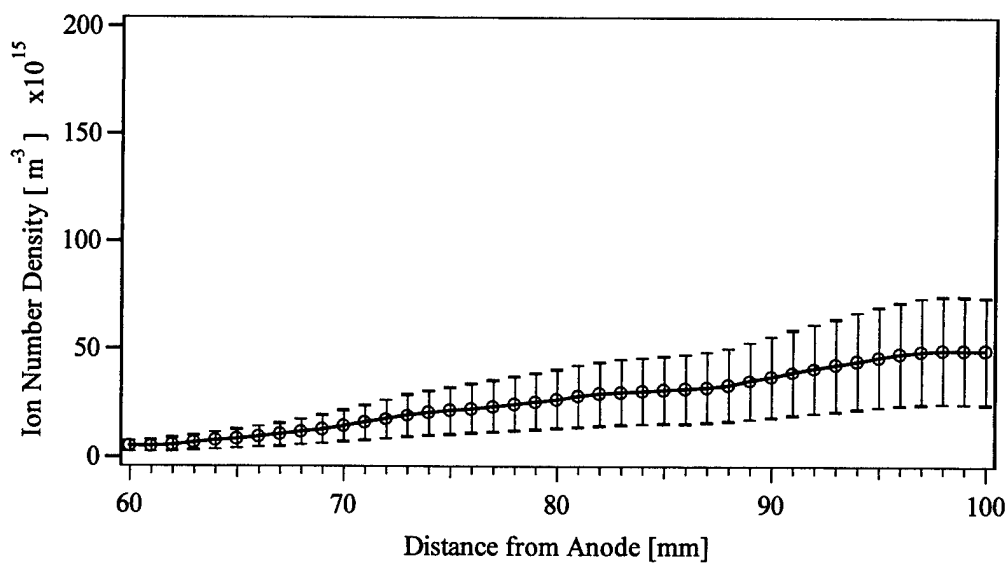


Figure A. 38 Ion number density, 3 kW, R = 54.6 mm.

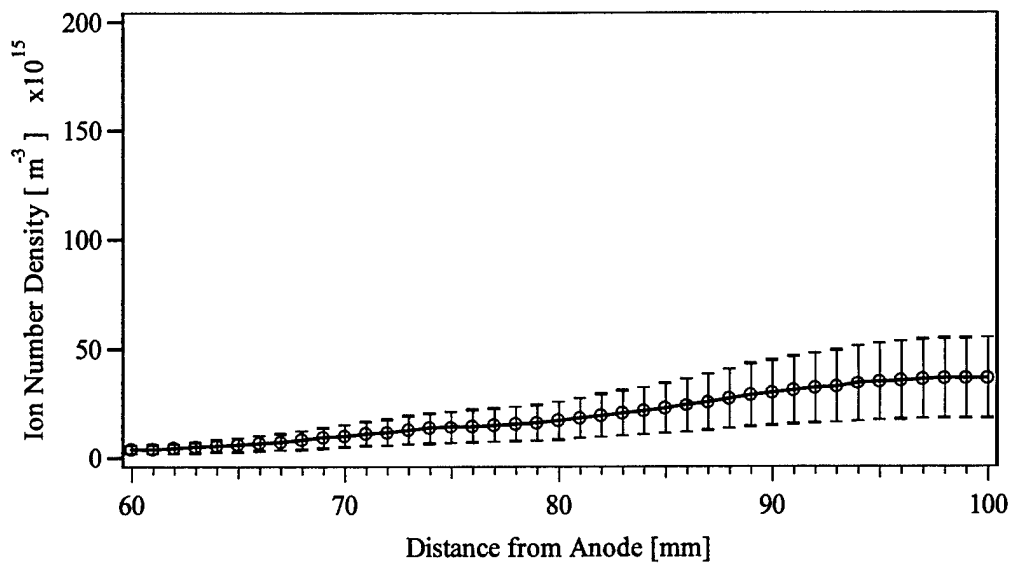


Figure A. 39 Ion number density, 3 kW, R = 60.9 mm.

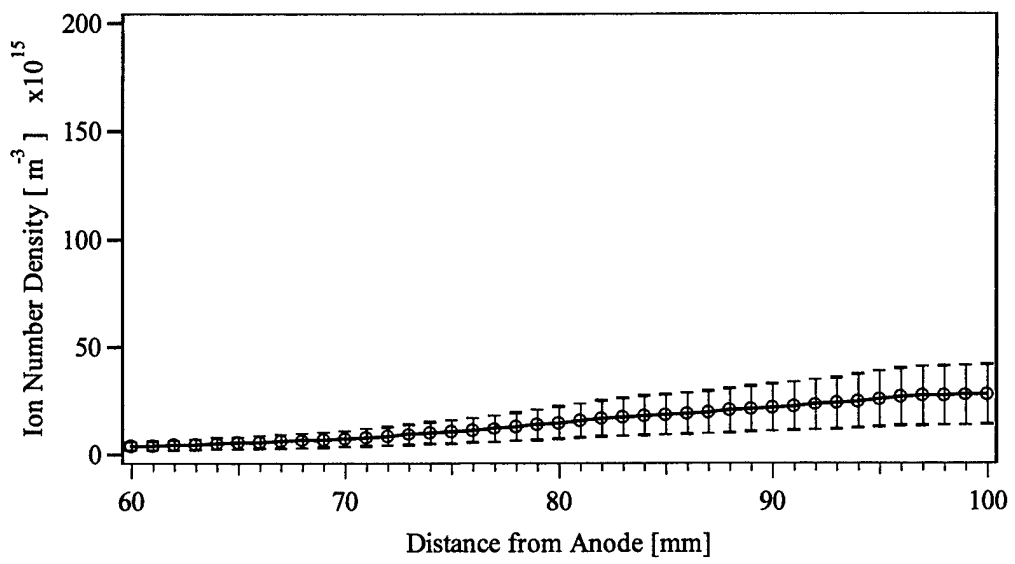


Figure A. 40 Ion number density, 3 kW, R = 67.3 mm.

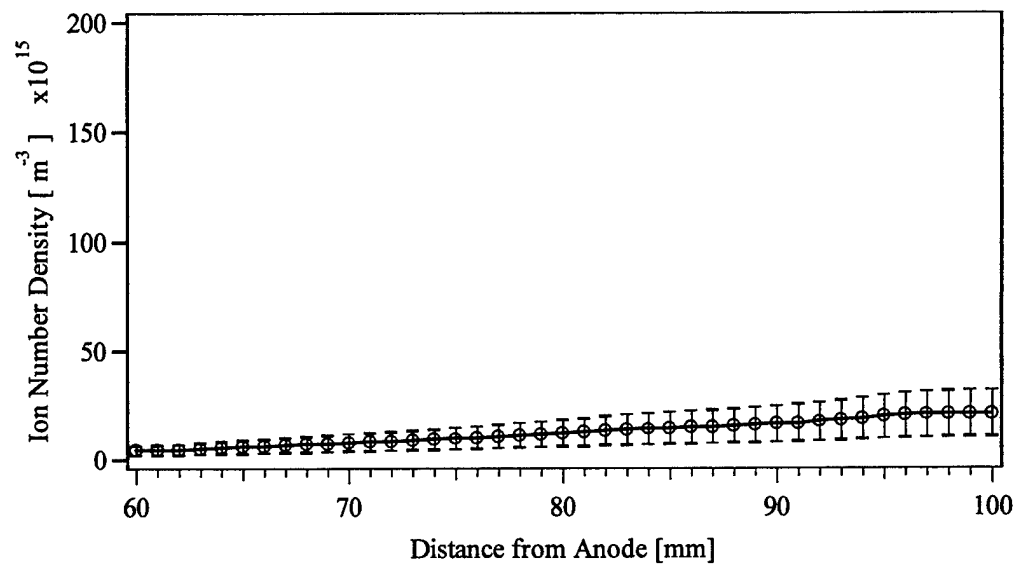


Figure A. 41 Ion number density, 3 kW, R = 73.6 mm.

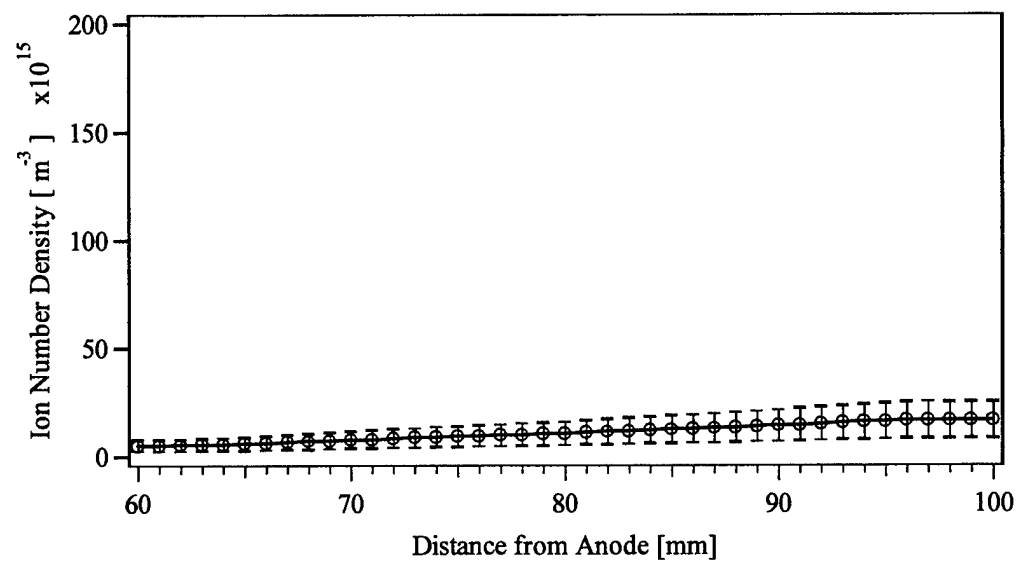


Figure A. 42 Ion number density, 3 kW, R = 80 mm.

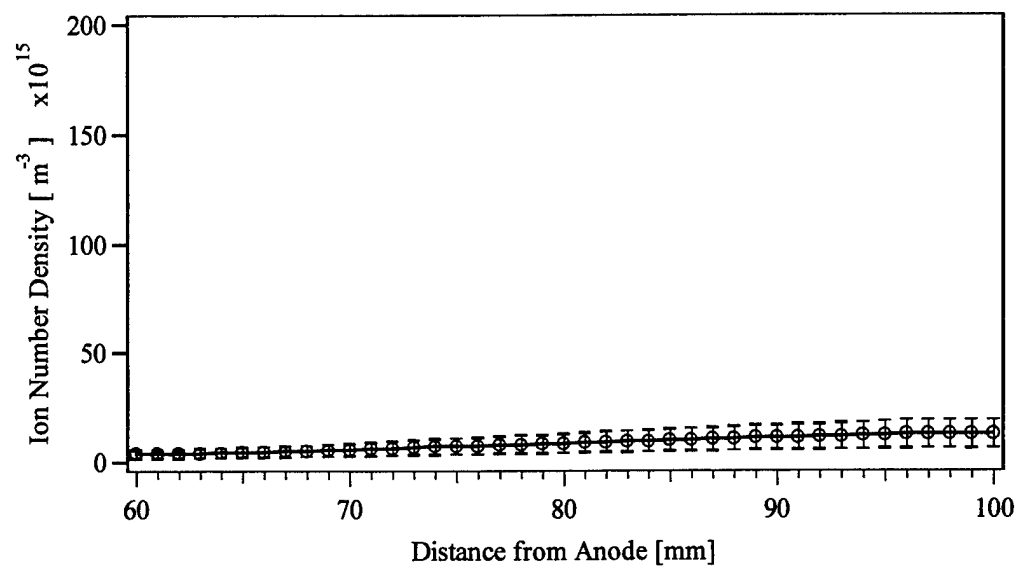


Figure A. 43 Ion number density, 3 kW, R = 86.3 mm.

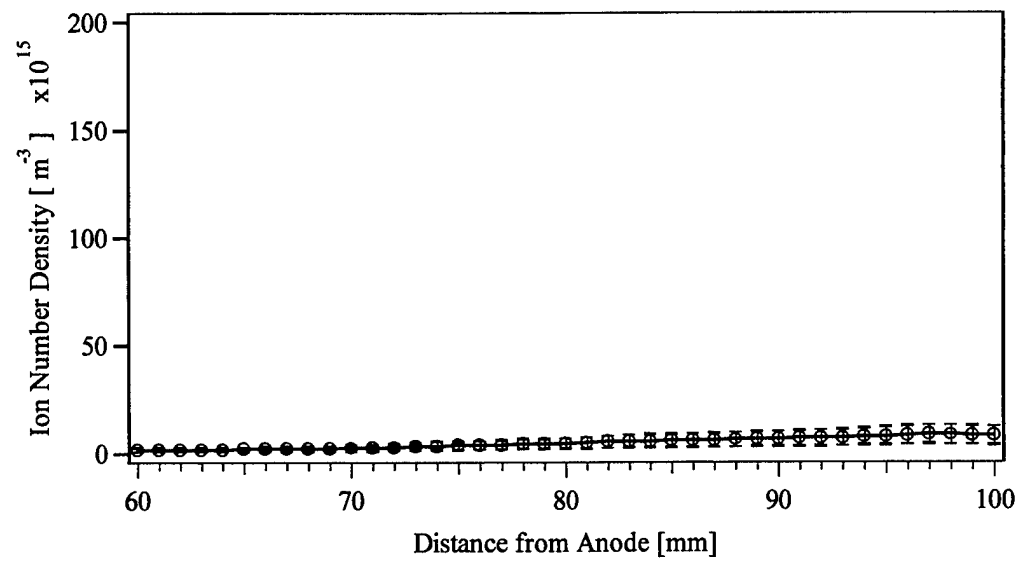


Figure A. 44 Ion number density, 3 kW, R = 92.7 mm.

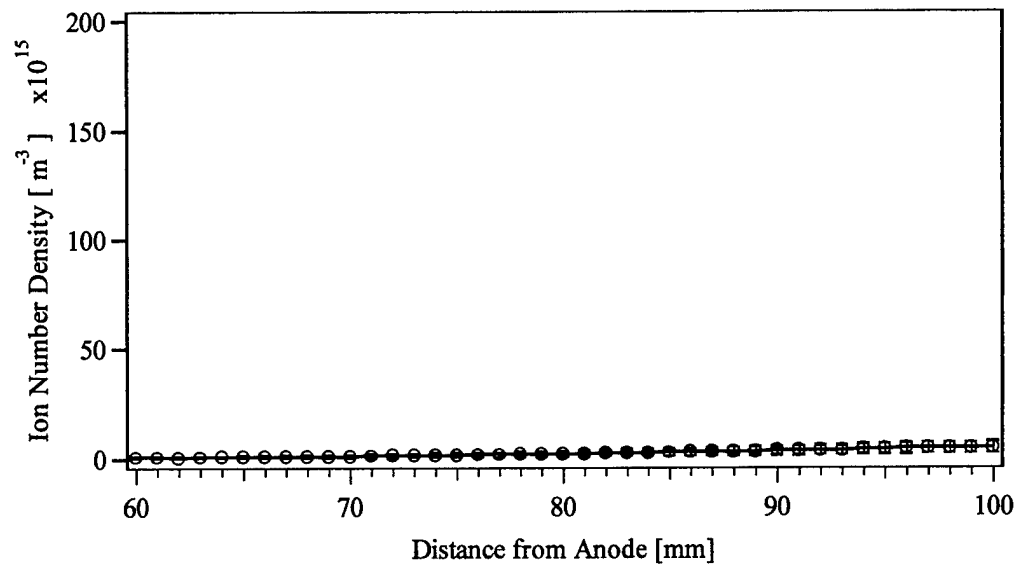


Figure A. 45 Ion number density, 3 kW, R = 99 mm.

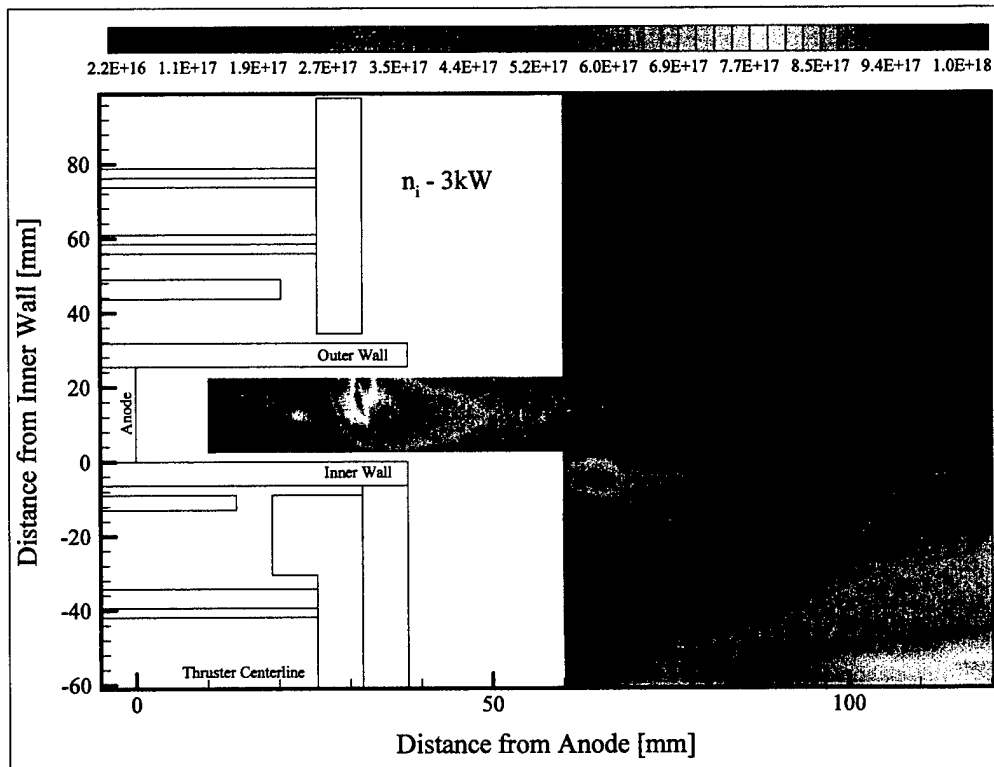


Figure A. 46 Ion number density contours, 3 kW. Note the high-density core resulting from ions being focused along the thruster centerline.

Appendix B

Electron temperature profiles beyond the radial confines of the discharge channel

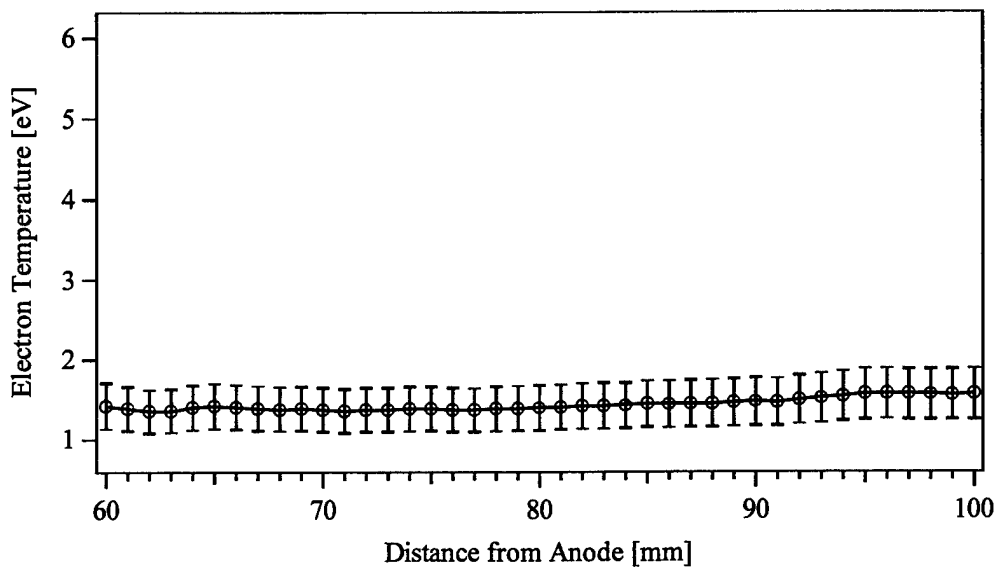


Figure B. 1 Electron temperature, 1.6 kW, $R = -61$ mm.

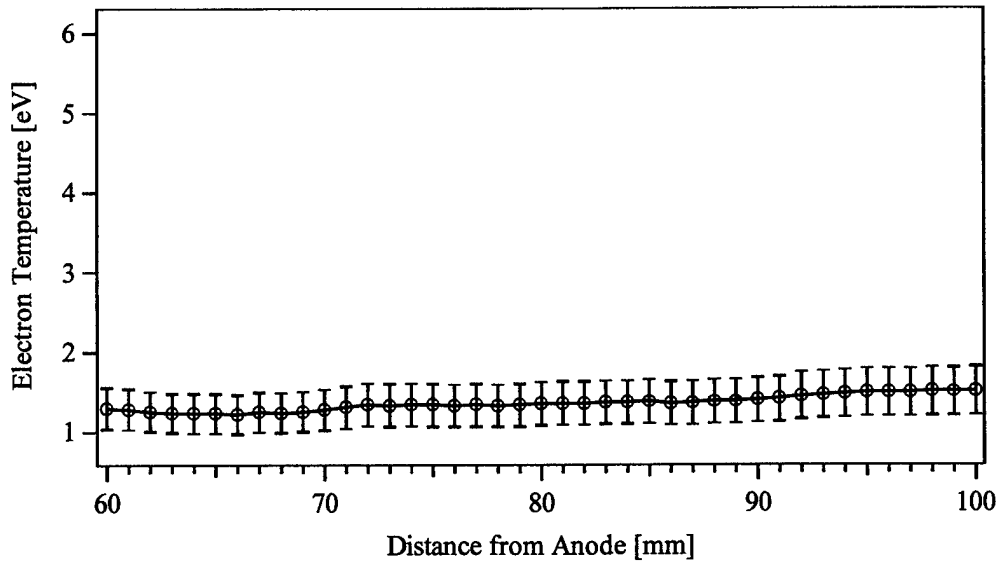


Figure B. 2 Electron temperature, 1.6 kW, R = -54.7 mm.

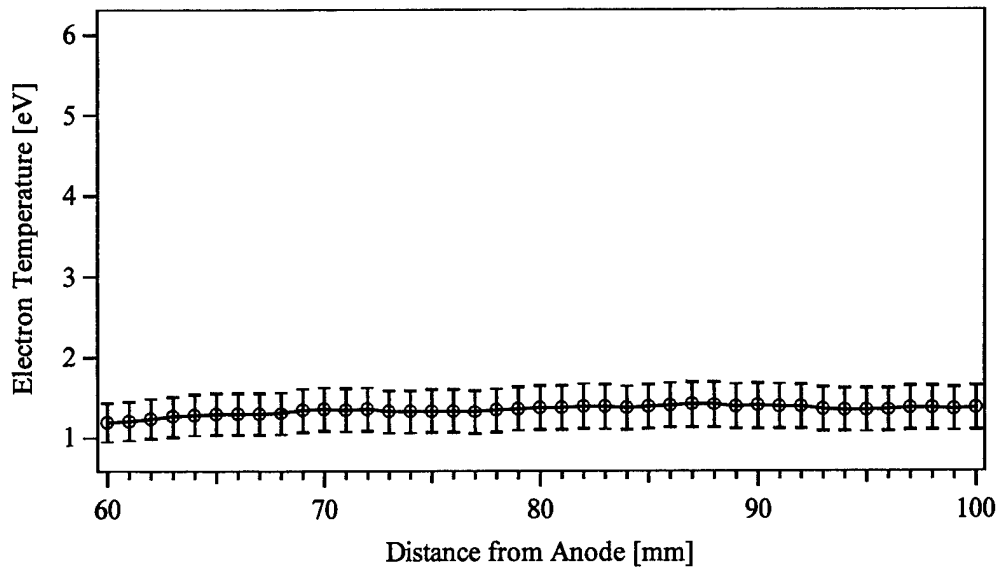


Figure B. 3 Electron temperature, 1.6 kW, R = -48.3 mm.

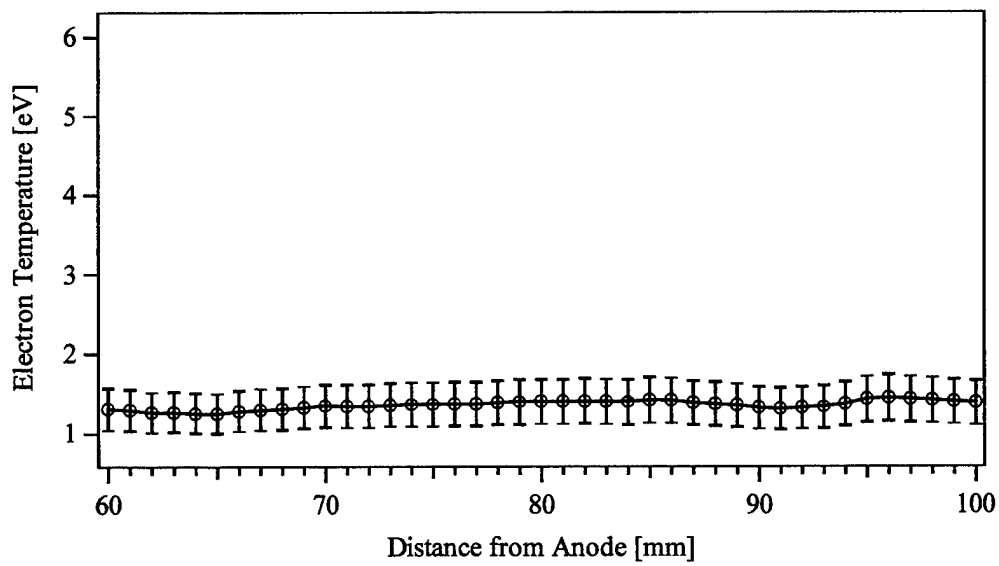


Figure B. 4 Electron temperature, 1.6 kW, R = -42 mm.

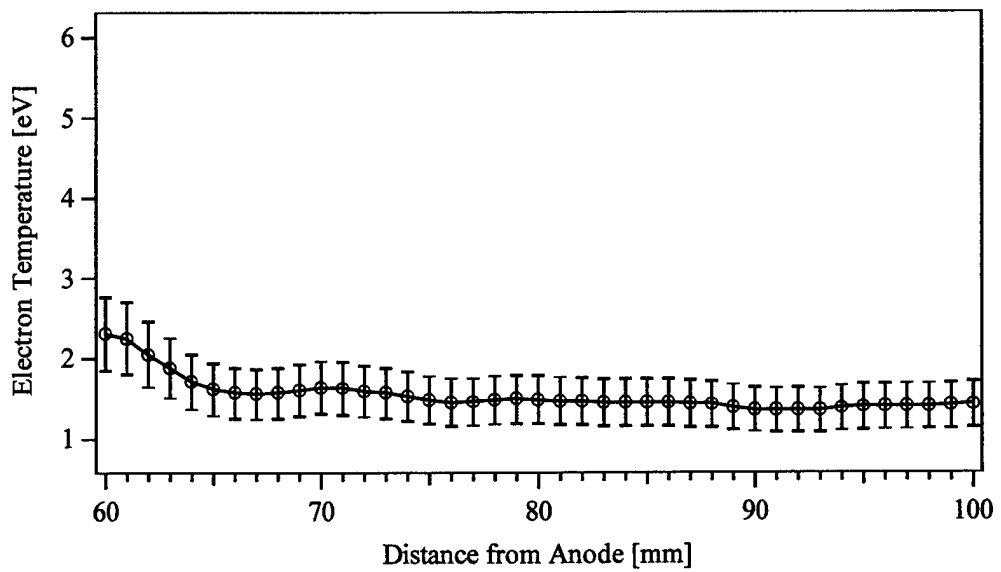


Figure B. 5 Electron temperature, 1.6 kW, $R = -35.6$ mm.

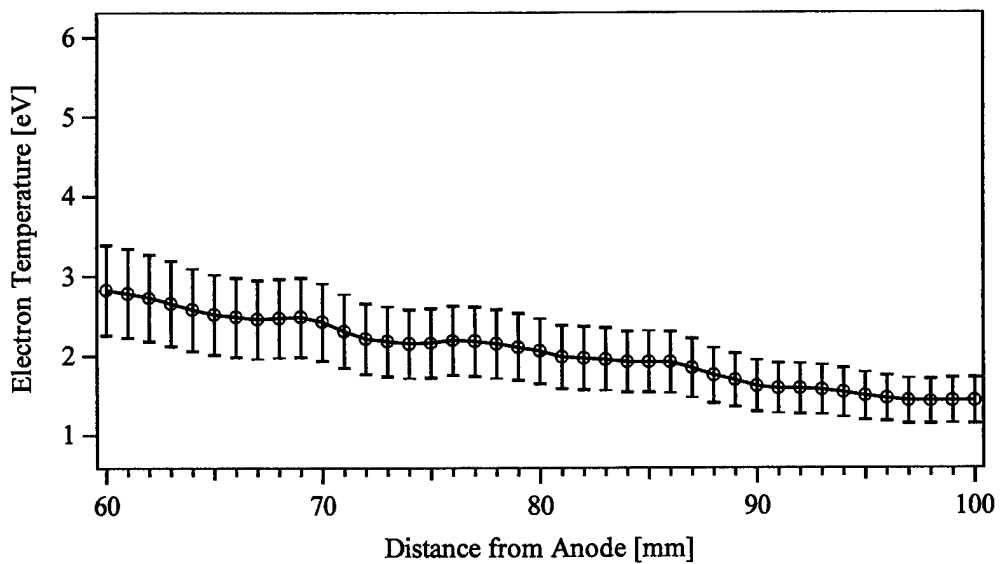


Figure B. 6 Electron temperature, 1.6 kW, $R = -29.3$ mm.

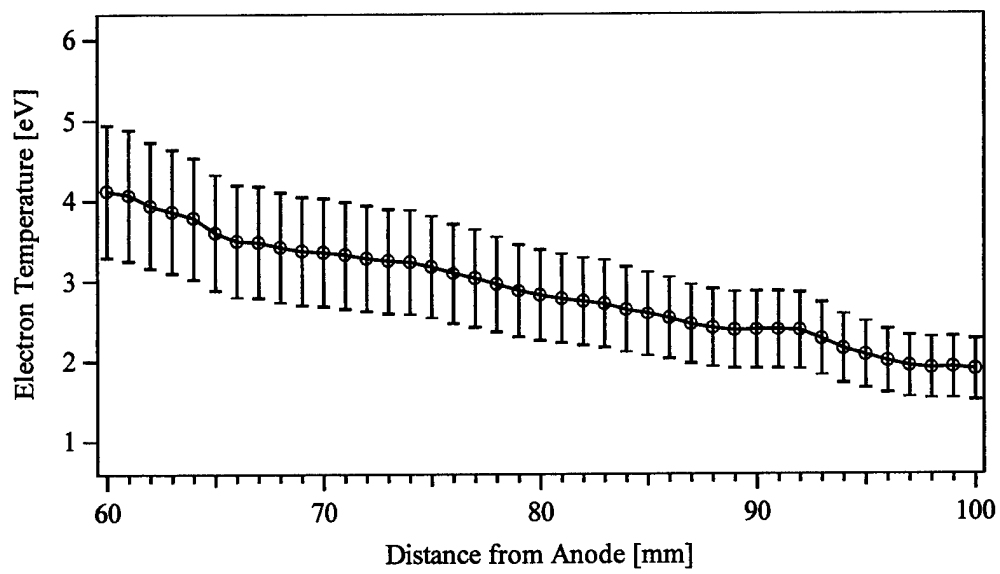


Figure B. 7 Electron temperature, 1.6 kW, $R = -22.9$ mm.

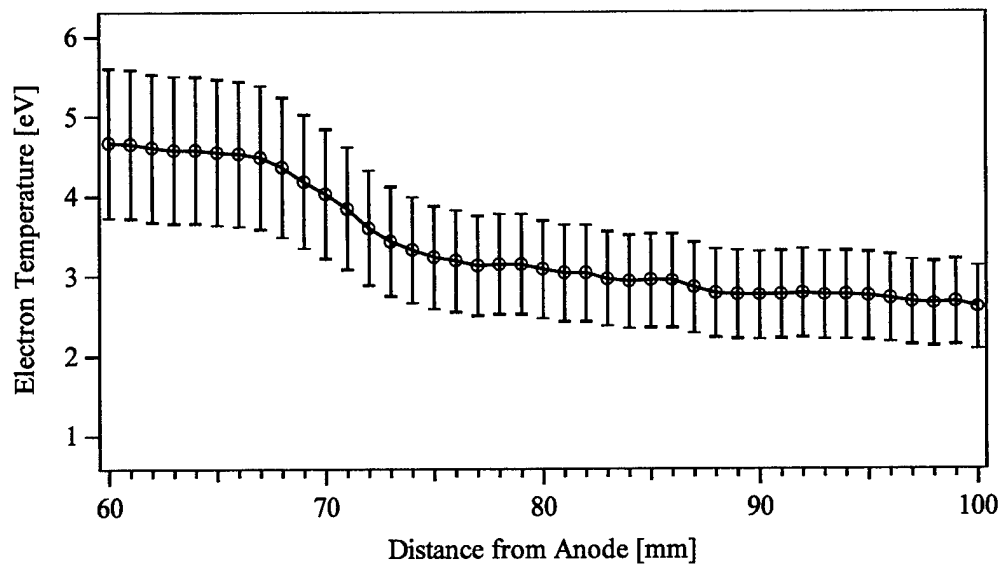


Figure B. 8 Electron temperature, 1.6 kW, $R = -16.6$ mm.

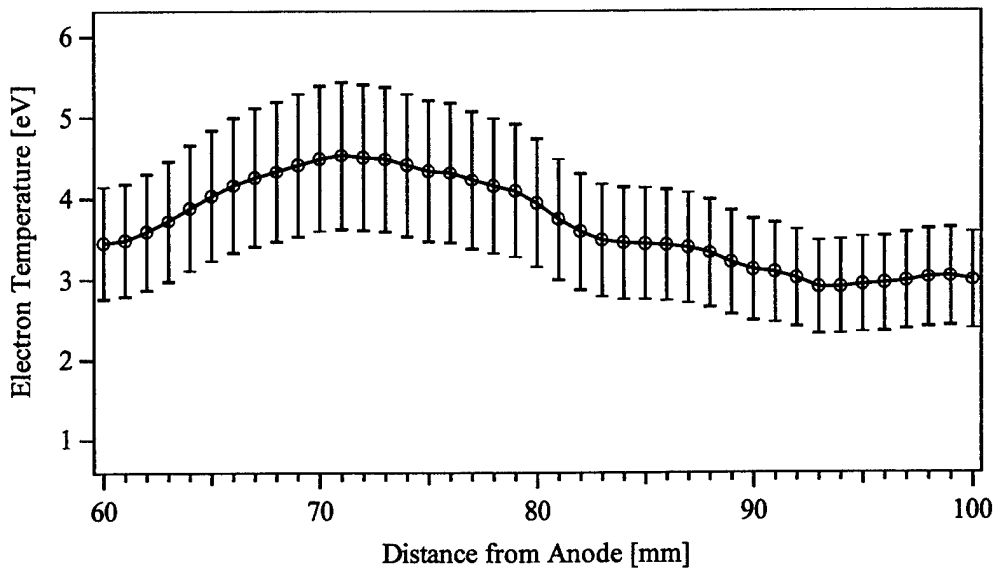


Figure B. 9 Electron temperature, 1.6 kW, $R = -10.2$ mm.

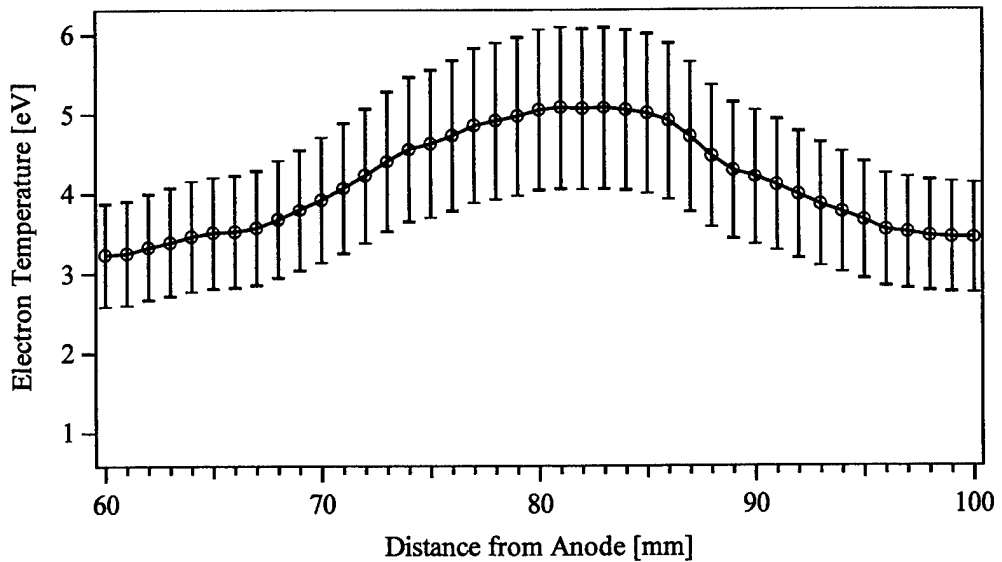


Figure B. 10 Electron temperature, 1.6 kW, $R = -3.9$ mm.

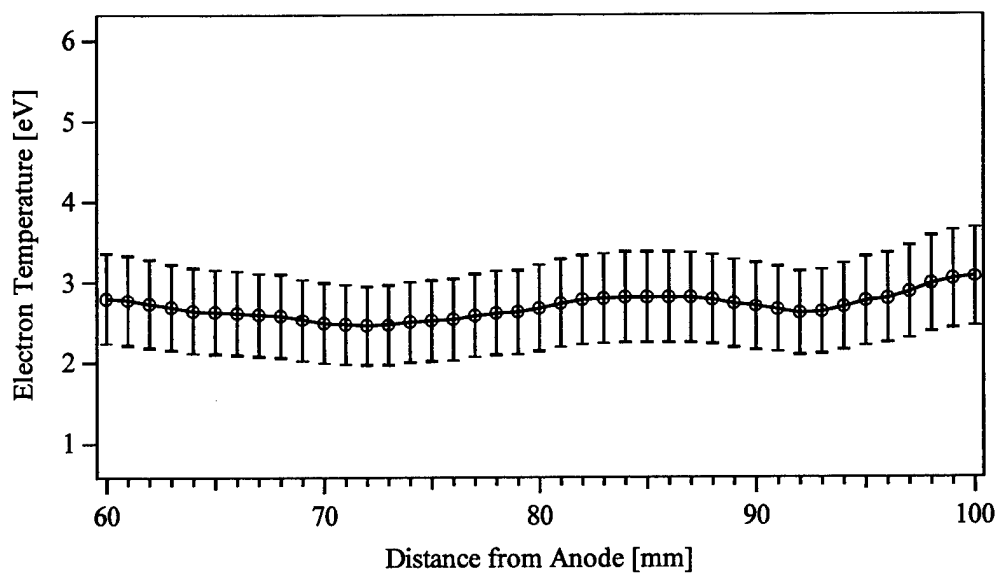


Figure B. 11 Electron temperature, 1.6 kW, $R = 29.2$ mm.

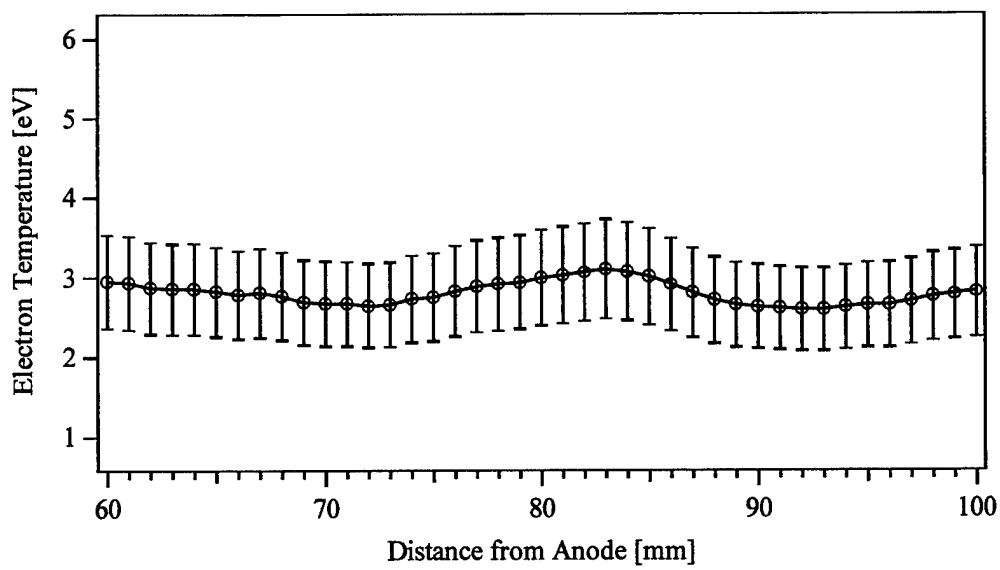


Figure B. 12 Electron temperature, 1.6 kW, $R = 35.5$ mm.

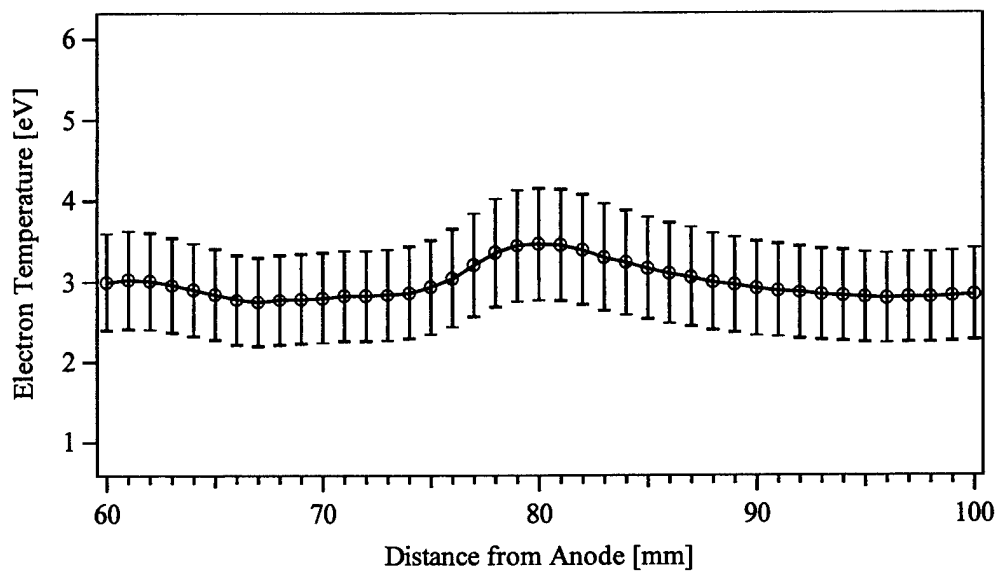


Figure B. 13 Electron temperature, 1.6 kW, $R = 41.9$ mm.

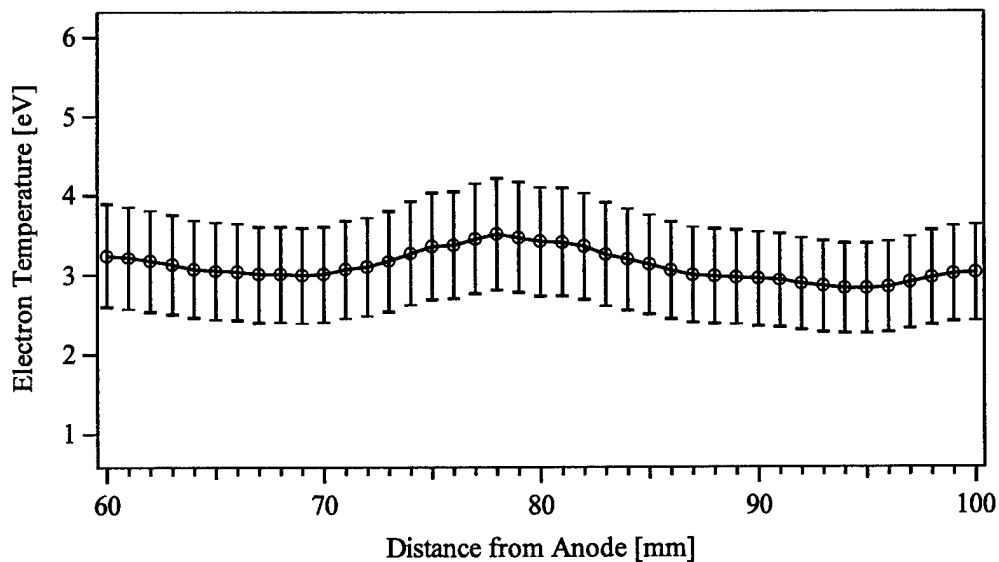


Figure B. 14 Electron temperature, 1.6 kW, $R = 48.2$ mm.

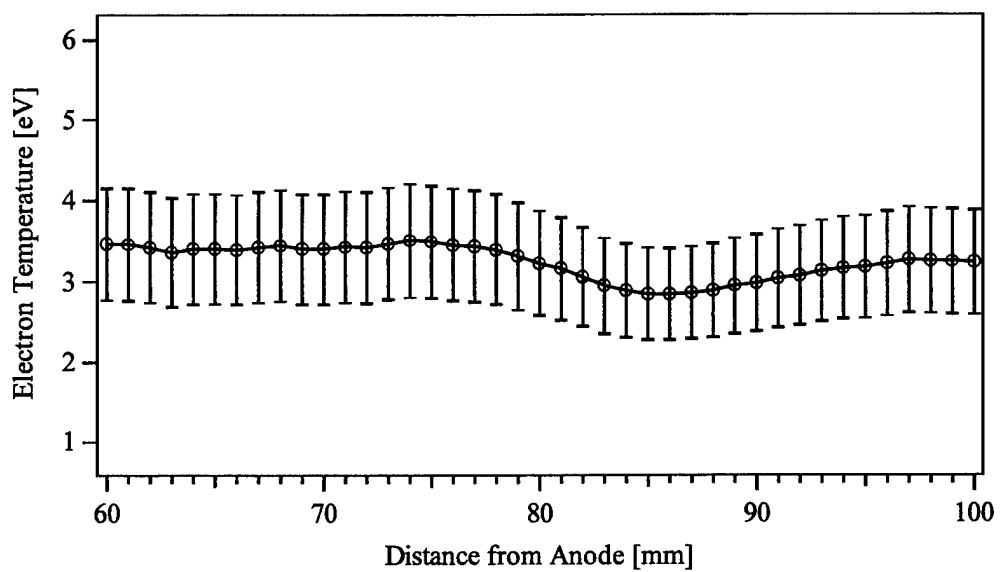


Figure B. 15 Electron temperature, 1.6 kW, $R = 54.6$ mm.

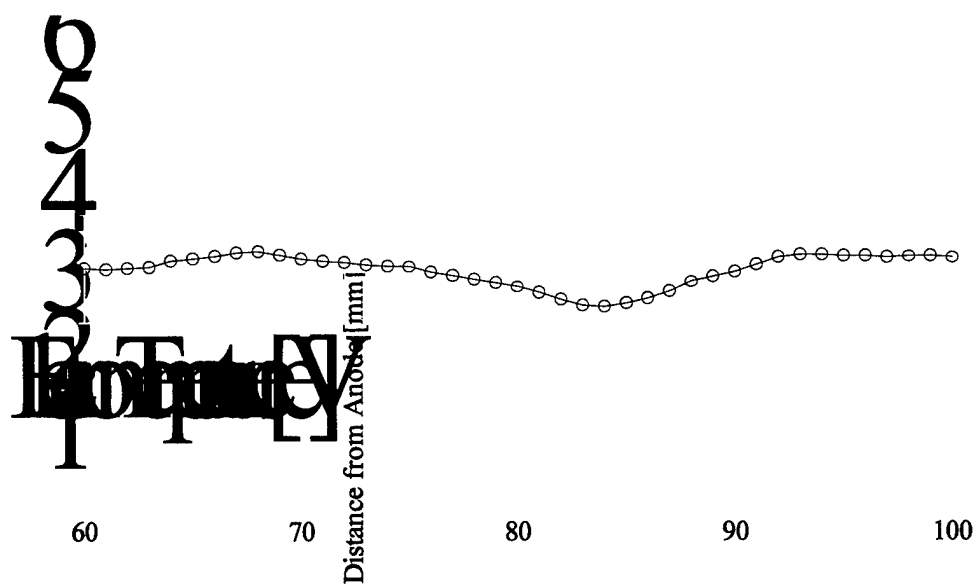


Figure B. 16 Electron temperature, 1.6 kW, $R = 60.9$ mm.

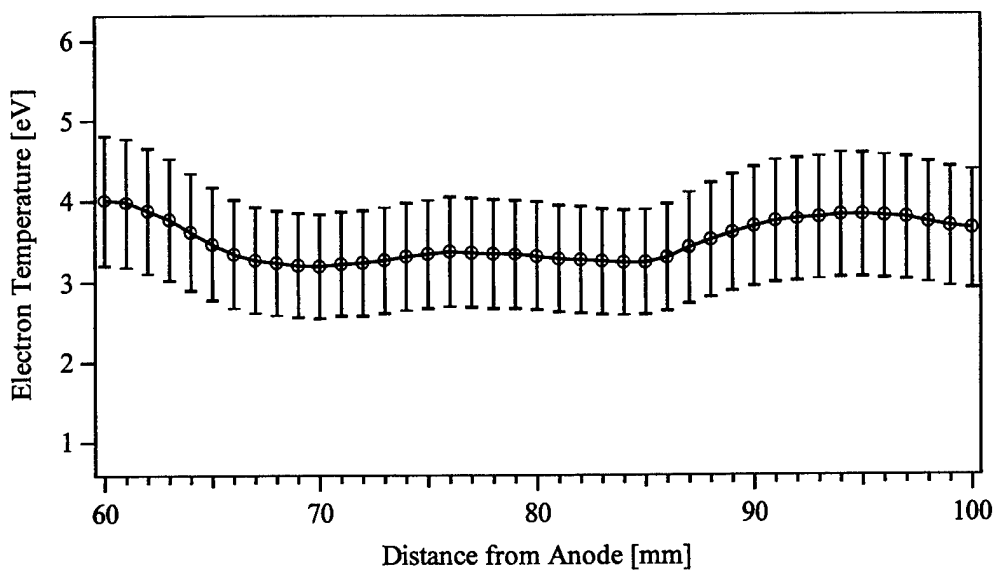


Figure B. 17 Electron temperature, 1.6 kW, $R = 67.3$ mm.

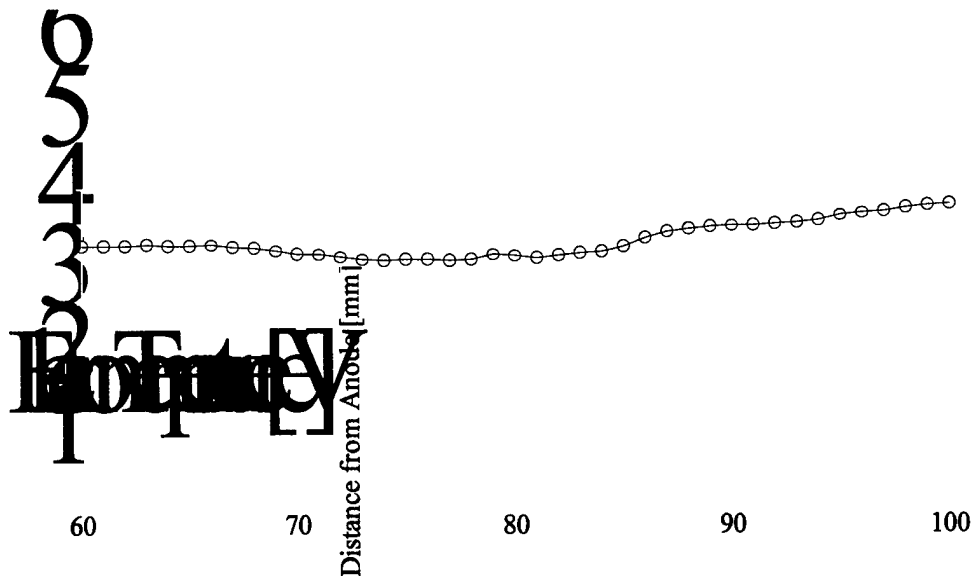


Figure B. 18 Electron temperature, 1.6 kW, $R = 73.6$ mm.

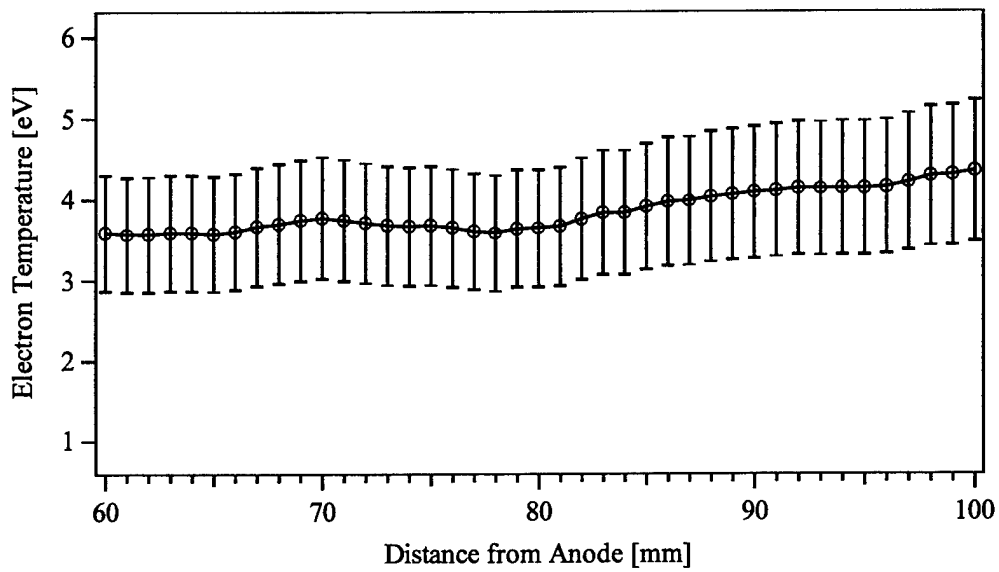


Figure B. 19 Electron temperature, 1.6 kW, $R = 80$ mm.

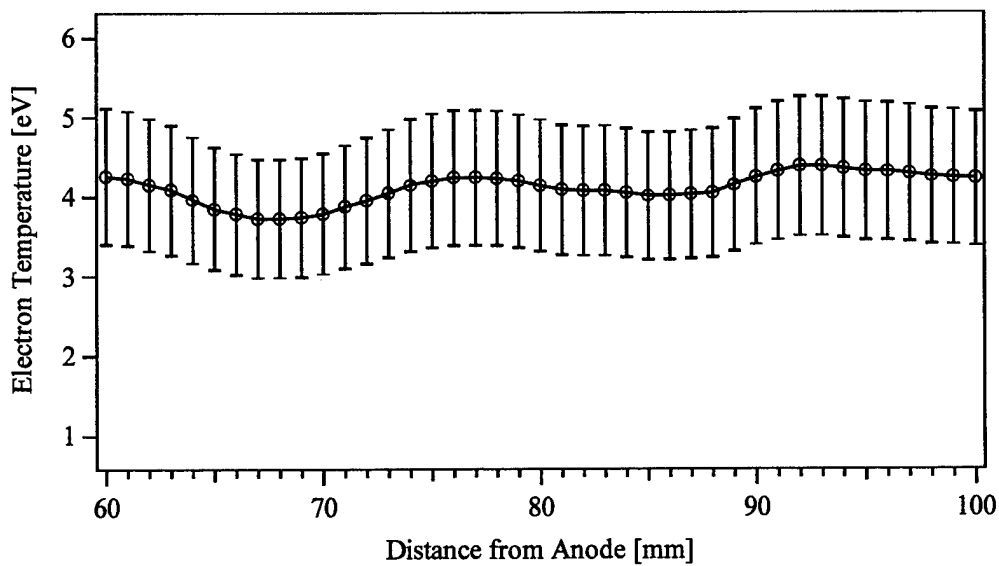


Figure B. 20 Electron temperature, 1.6 kW, $R = 86.3$ mm.

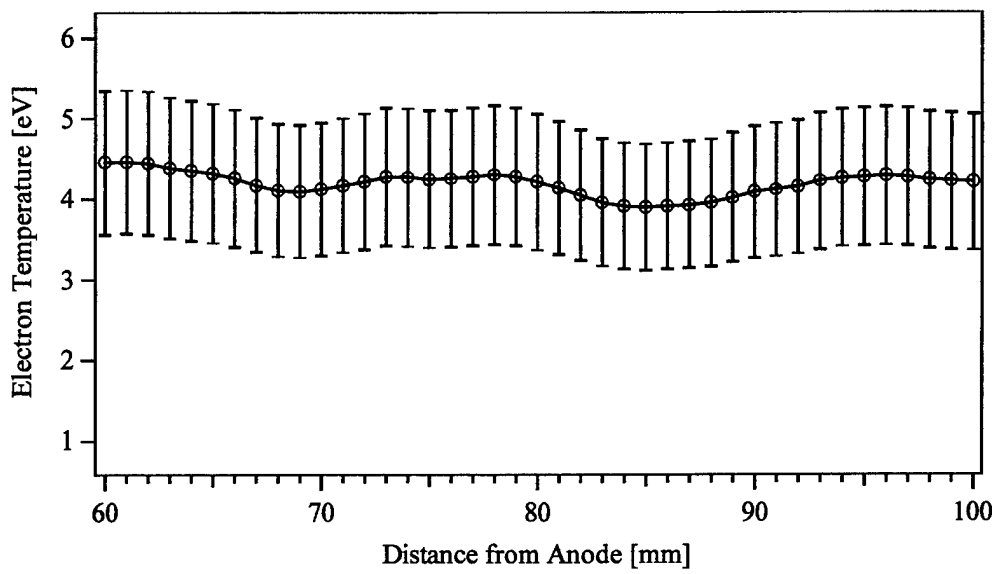


Figure B. 21 Electron temperature, 1.6 kW, $R = 92.7$ mm.

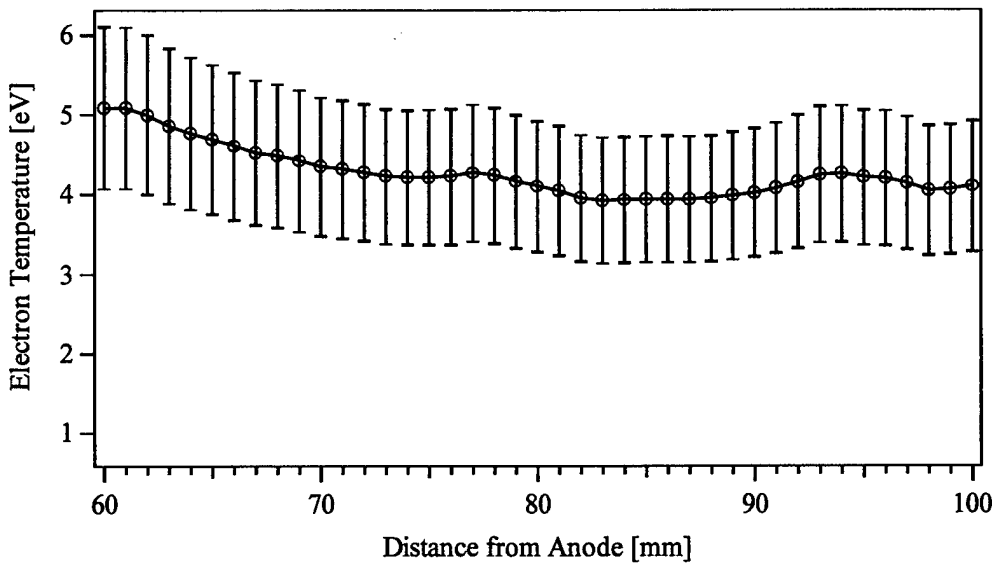


Figure B. 22 Electron temperature, 1.6 kW, $R = 99$ mm.

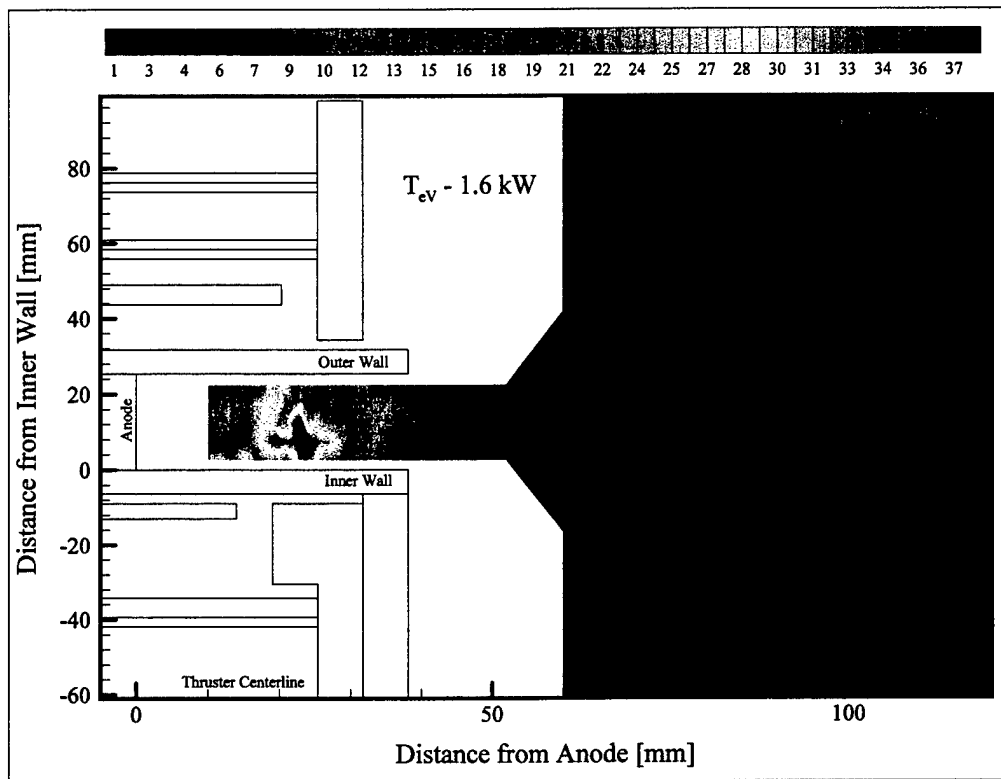


Figure B. 23 Electron temperature contours, 1.6 kW. Maximum temperature is approximately 38 eV and occurs 20 – 25 mm from the anode.

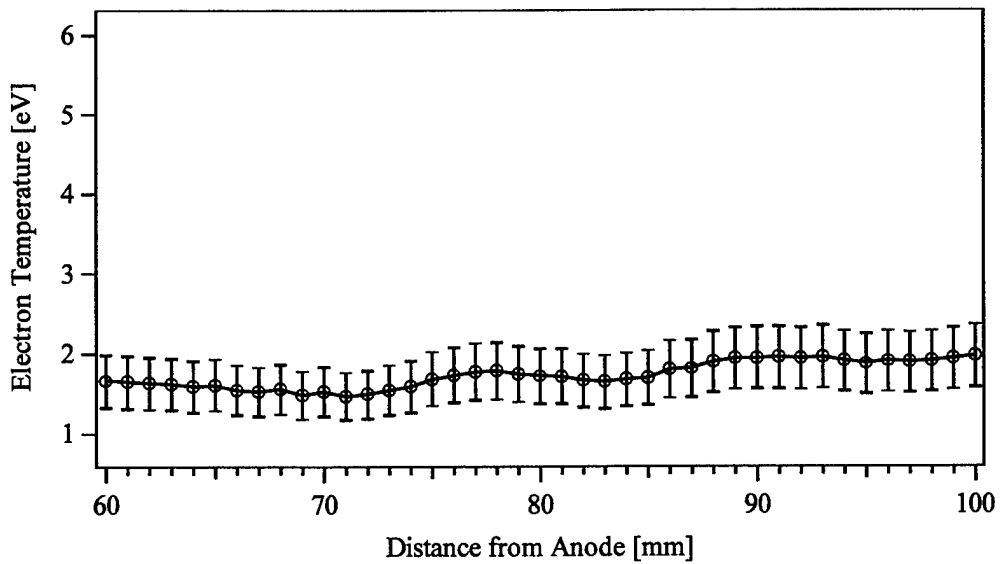


Figure B. 24 Electron temperature, 3 kW, R = -61 mm.

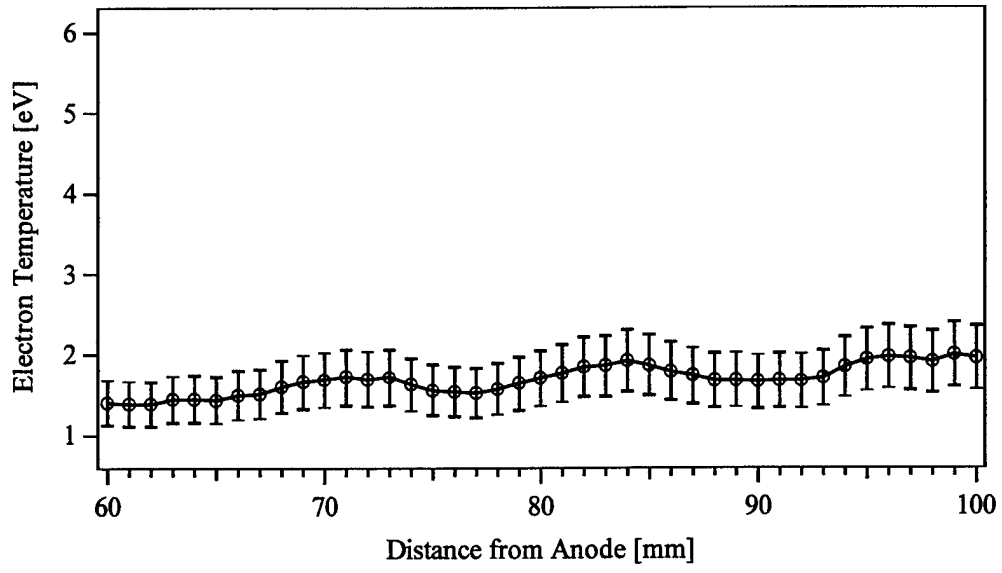


Figure B. 25 Electron temperature, 3 kW, $R = -54.7$ mm.

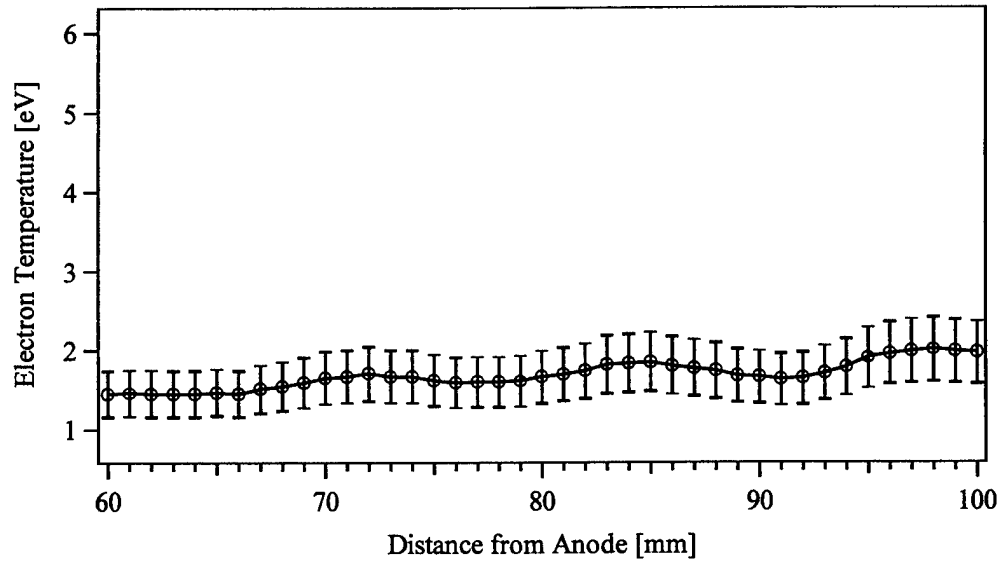


Figure B. 26 Electron temperature, 3 kW, $R = -48.3$ mm.

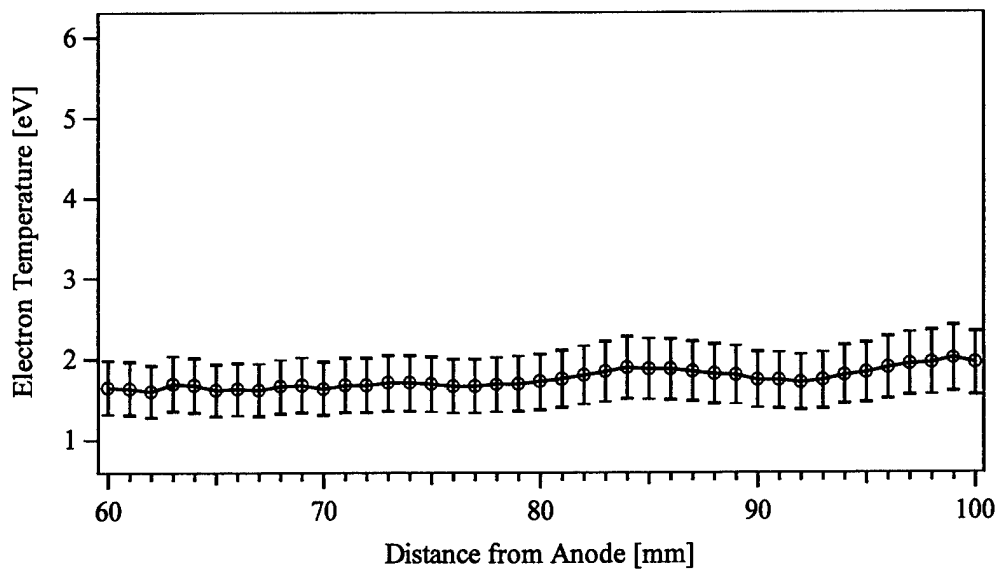


Figure B. 27 Electron temperature, 3 kW, $R = -42$ mm.

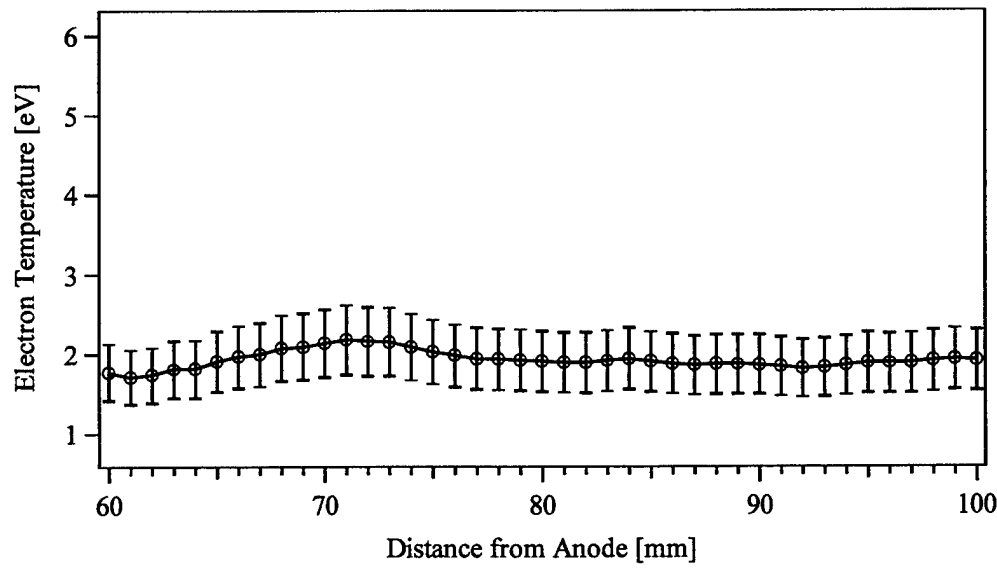


Figure B. 28 Electron temperature, 3 kW, $R = -35.6$ mm.

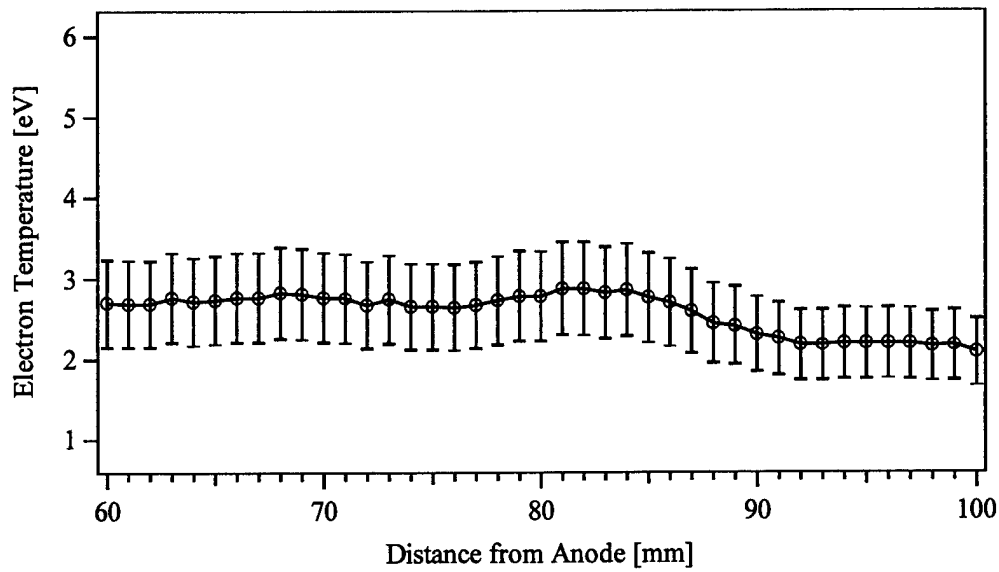


Figure B. 29 Electron temperature, 3 kW, $R = -29.3$ mm.

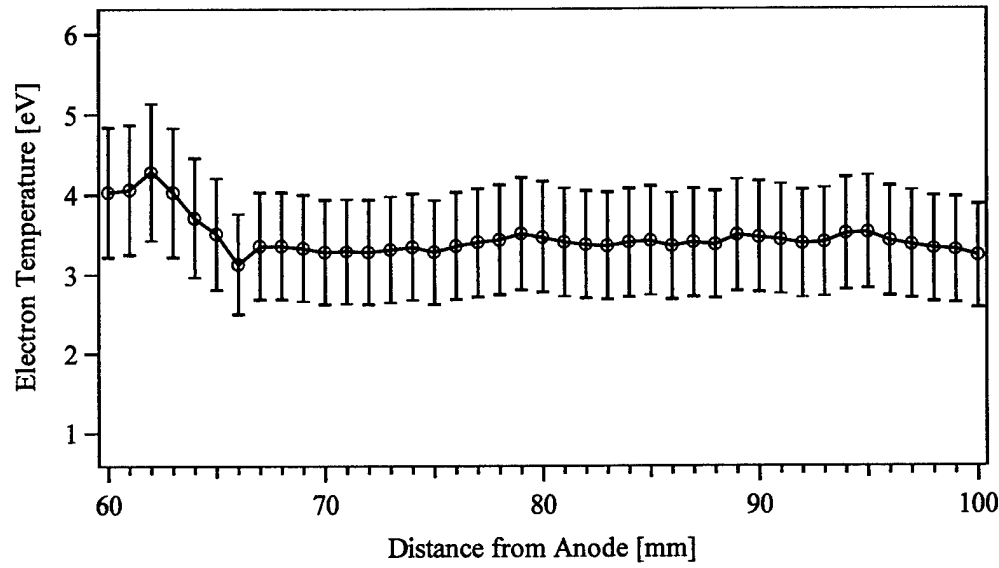


Figure B. 30 Electron temperature, 3 kW, $R = -22.9$ mm.

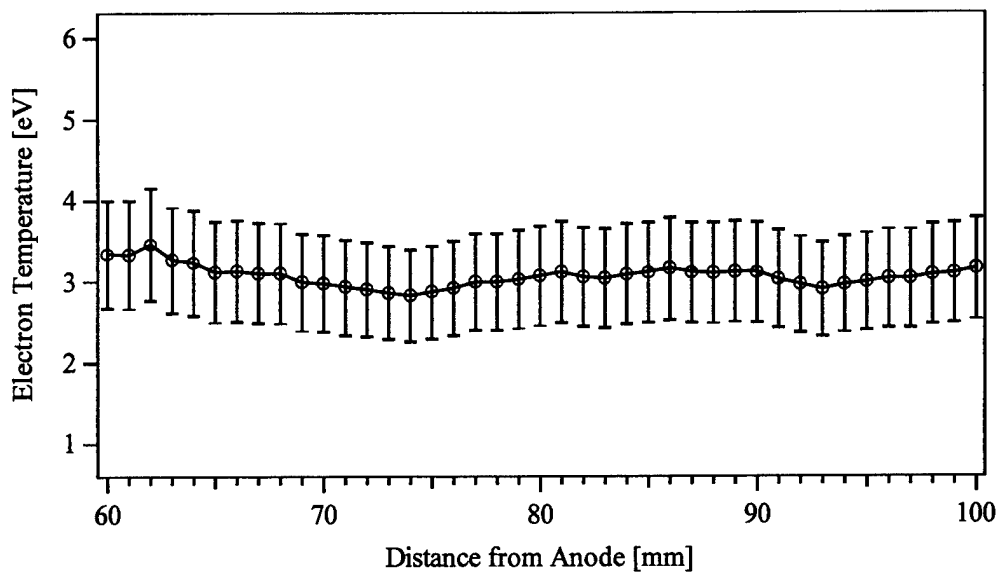


Figure B. 31 Electron temperature, 3 kW, $R = -16.6$ mm.

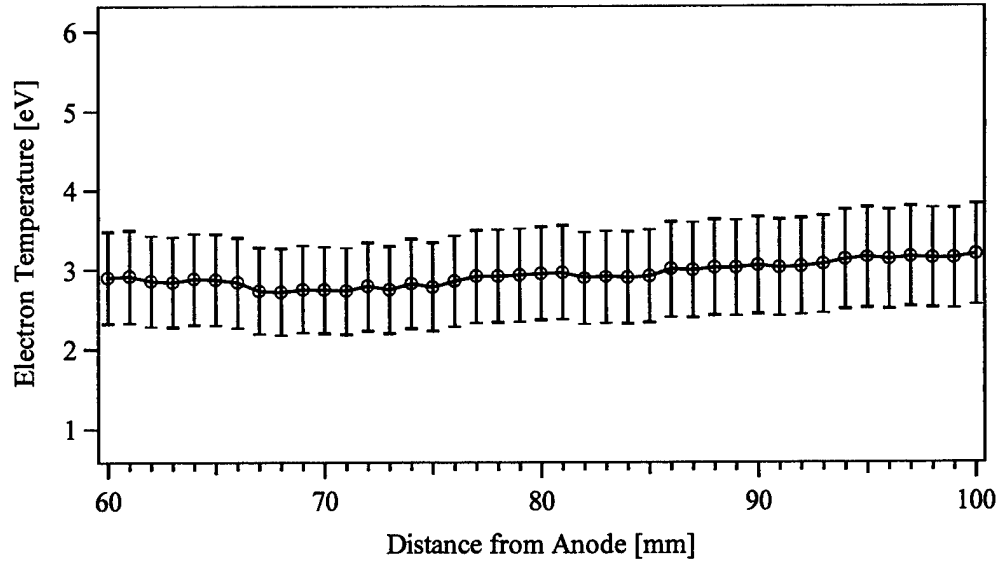


Figure B. 32 Electron temperature, 3 kW, $R = -10.2$ mm.

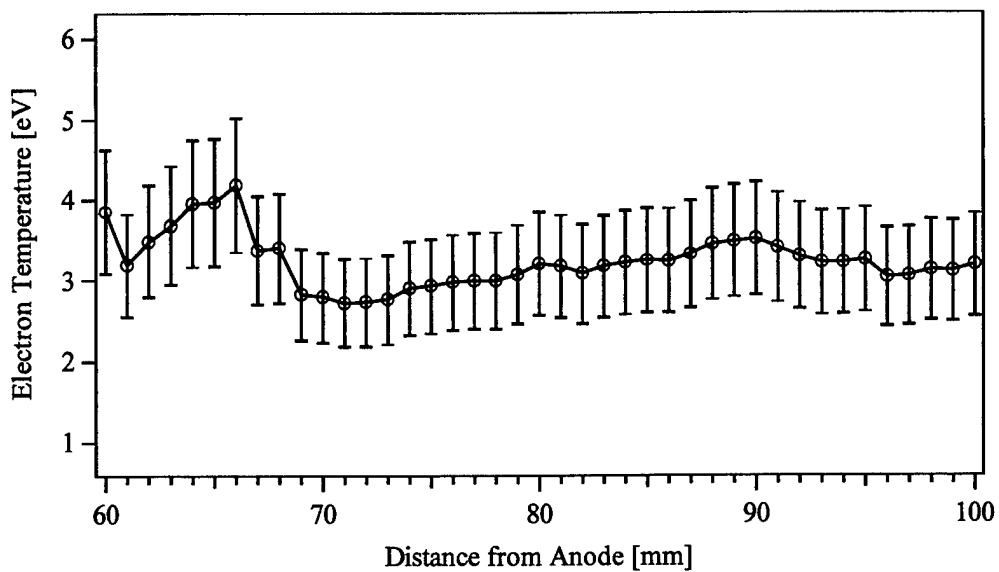


Figure B. 33 Electron temperature, 3 kW, $R = -3.9$ mm.

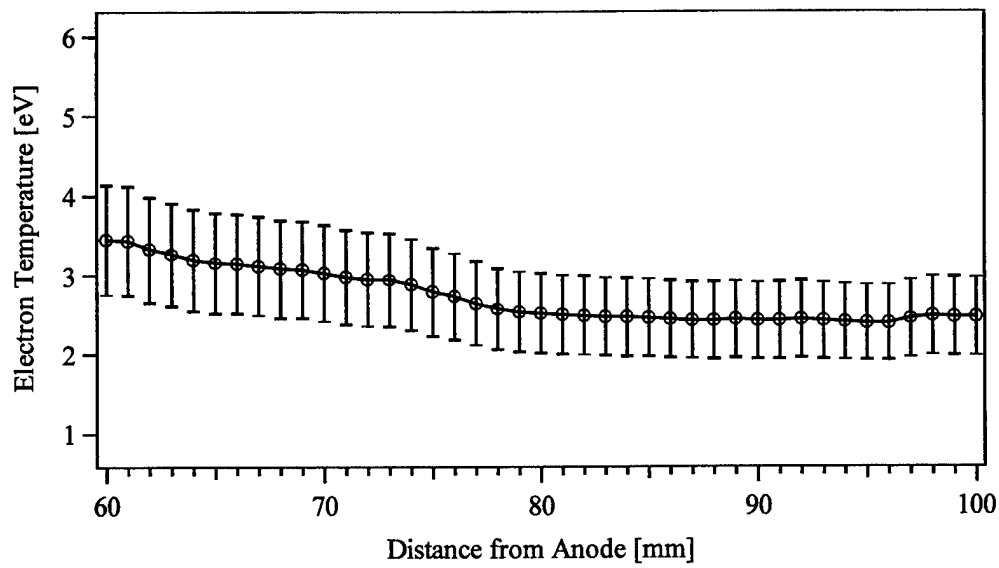


Figure B. 34 Electron temperature, 3 kW, $R = 29.2$ mm.

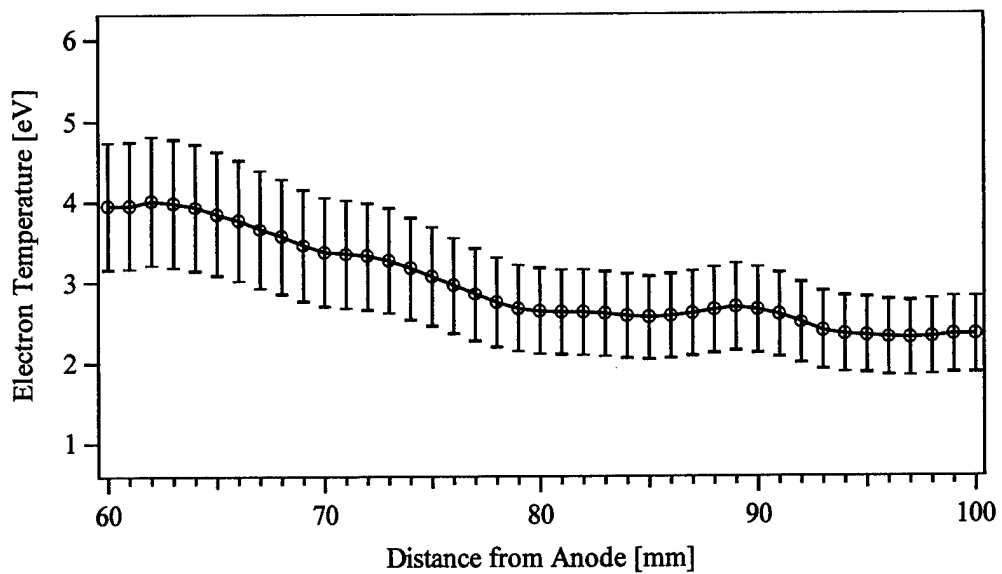


Figure B. 35 Electron temperature, 3 kW, $R = 35.5$ mm.

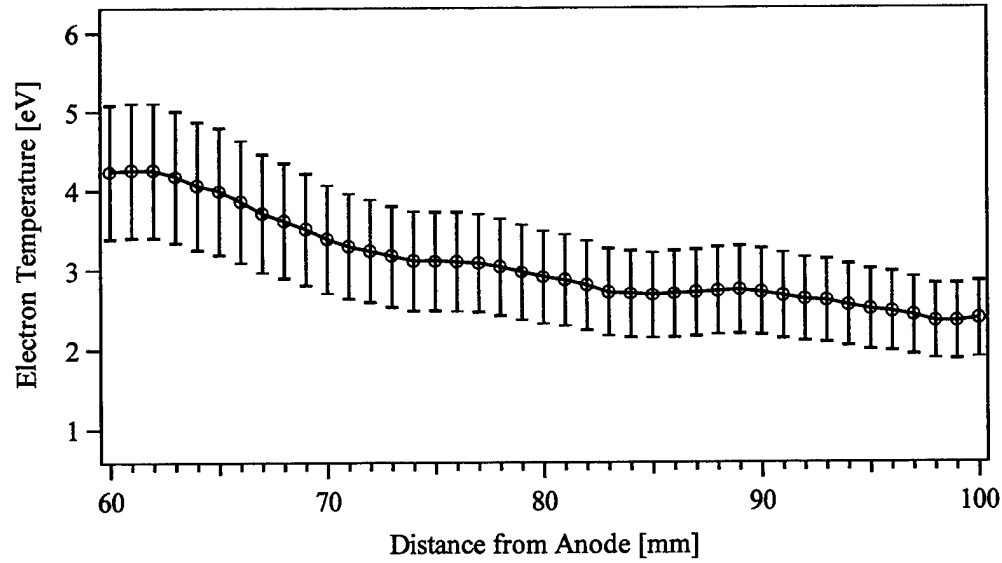


Figure B. 36 Electron temperature, 3 kW, $R = 41.9$ mm.

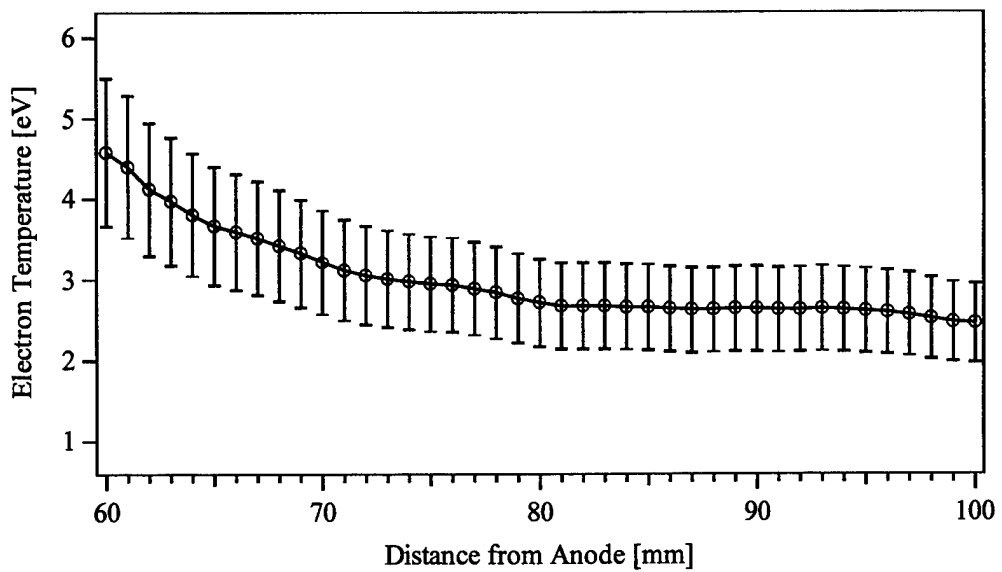


Figure B. 37 Electron temperature, 3 kW, $R = 48.2$ mm.

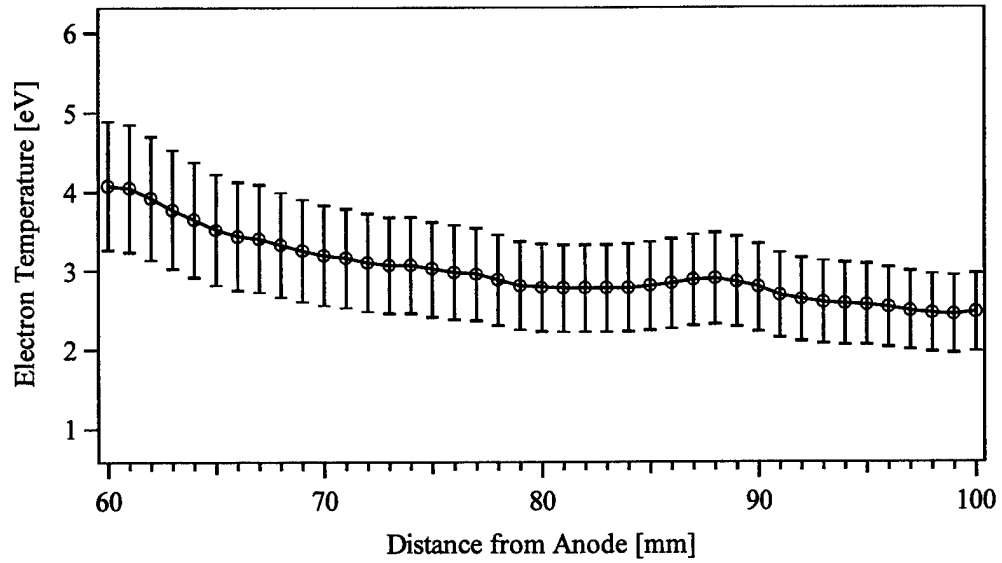


Figure B. 38 Electron temperature, 3 kW, $R = 54.6$ mm.

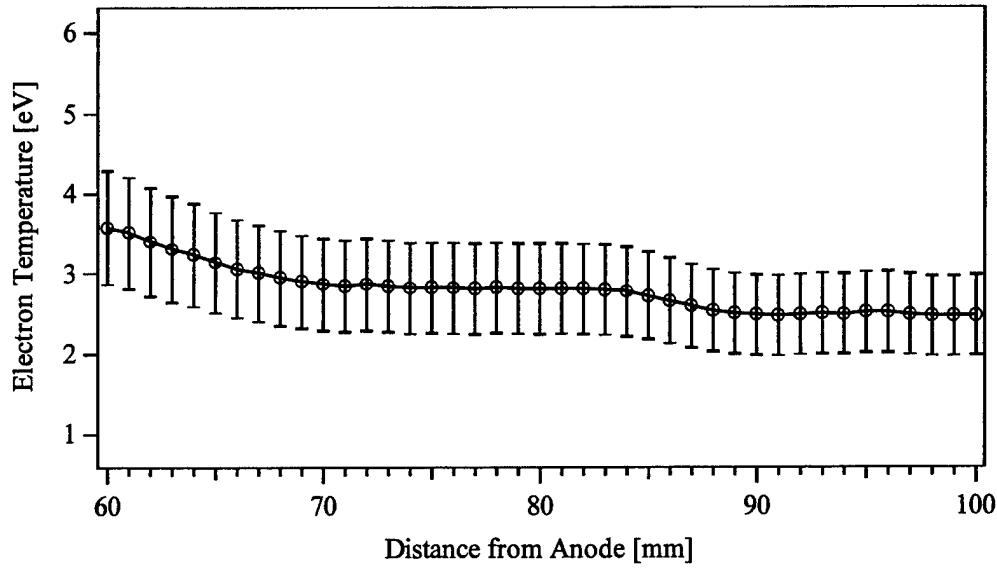


Figure B. 39 Electron temperature, 3 kW, $R = 60.9$ mm.

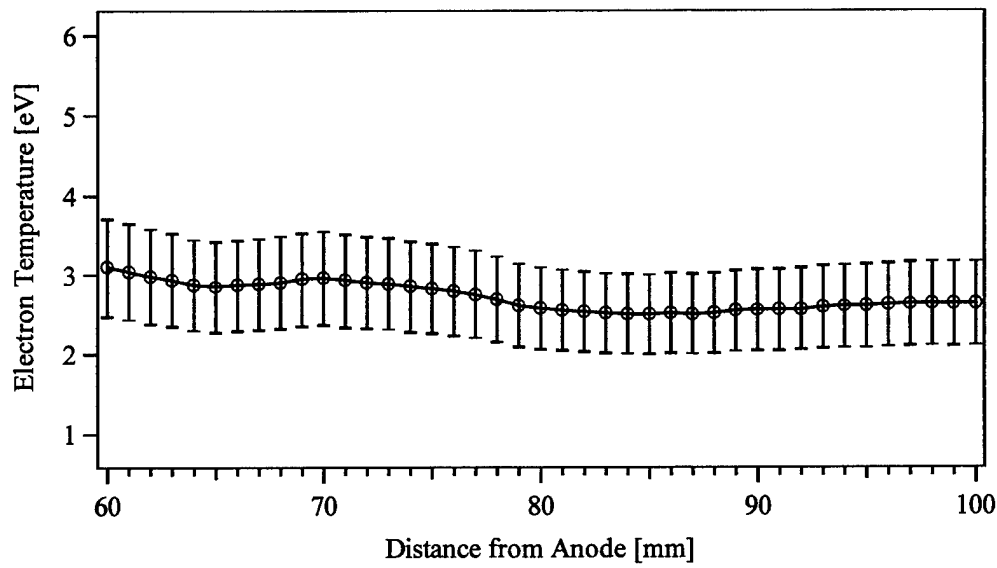


Figure B. 40 Electron temperature, 3 kW, $R = 67.3$ mm.

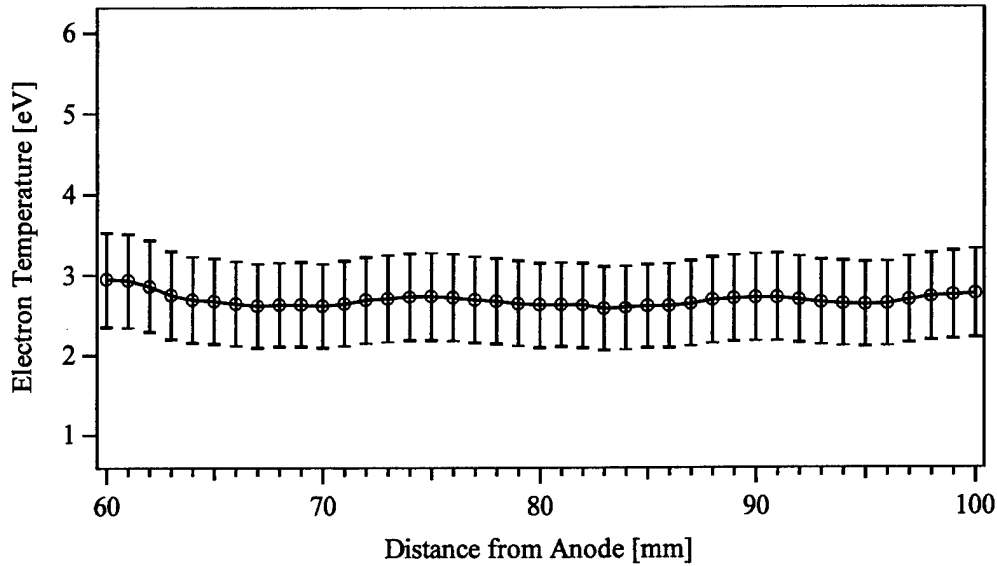


Figure B. 41 Electron temperature, 3 kW, $R = 73.6$ mm.

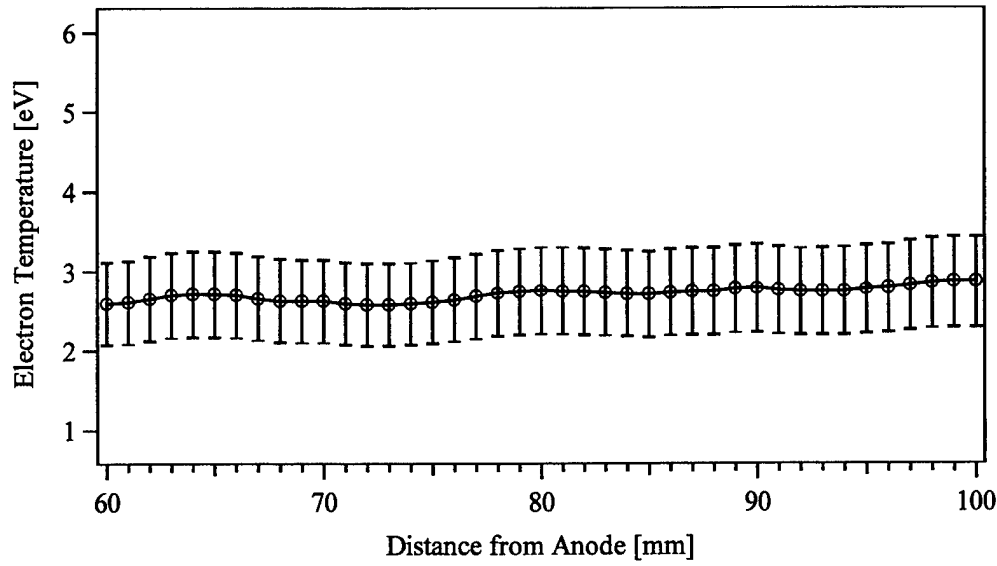


Figure B. 42 Electron temperature, 3 kW, $R = 80$ mm.

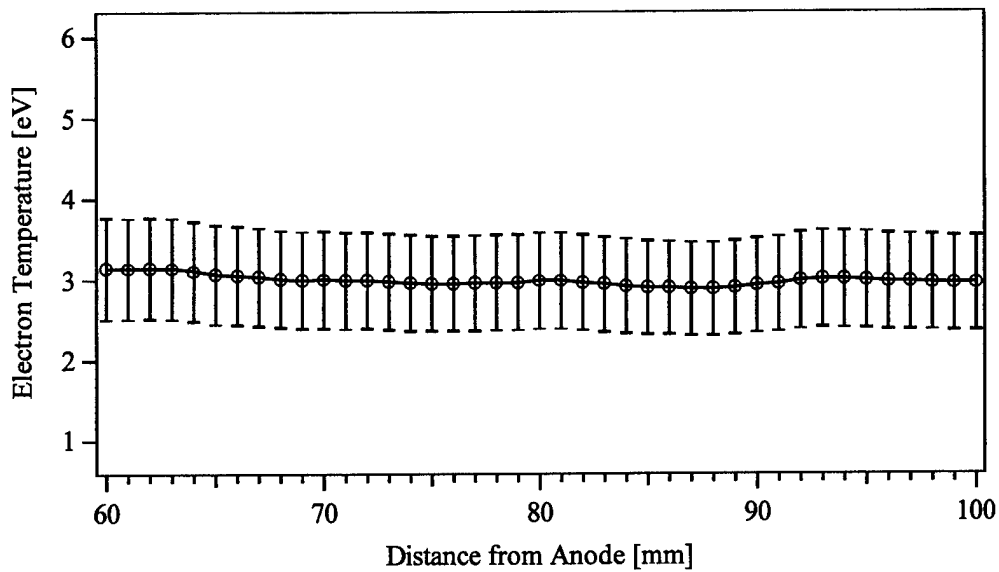


Figure B. 43 Electron temperature, 3 kW, $R = 86.3$ mm.

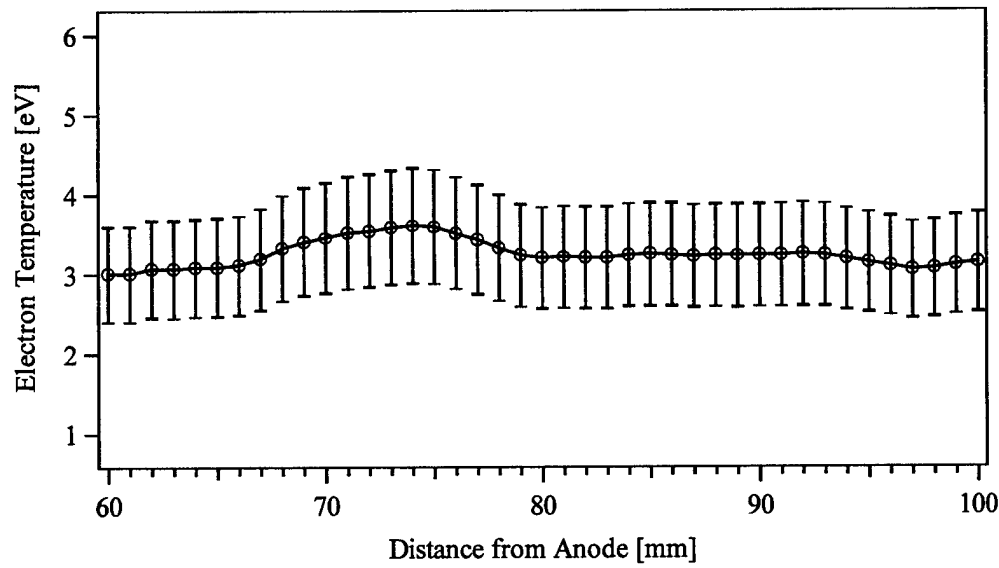


Figure B. 44 Electron temperature, 3 kW, $R = 92.7$ mm.

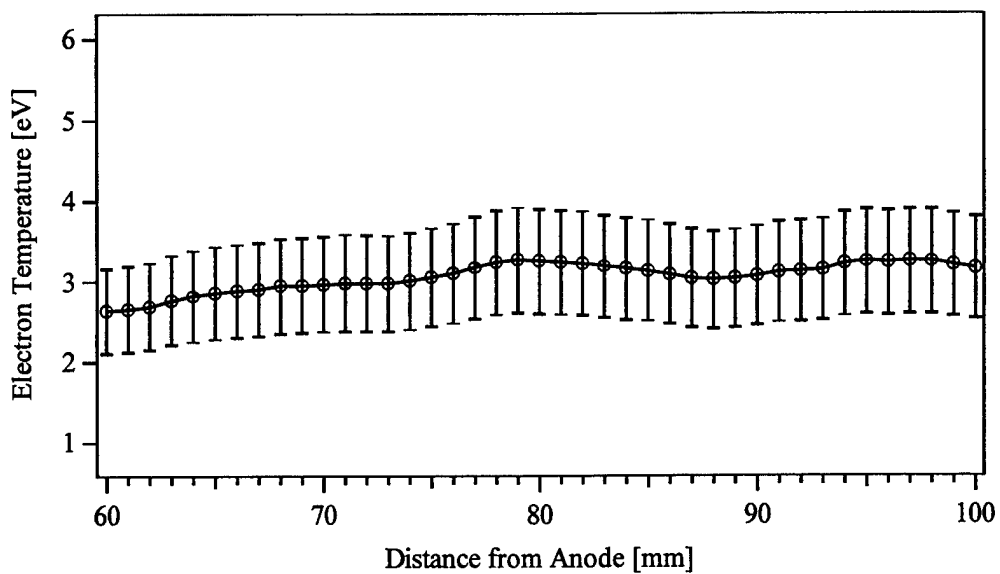


Figure B. 45 Electron temperature, 3 kW, R = 99 mm.

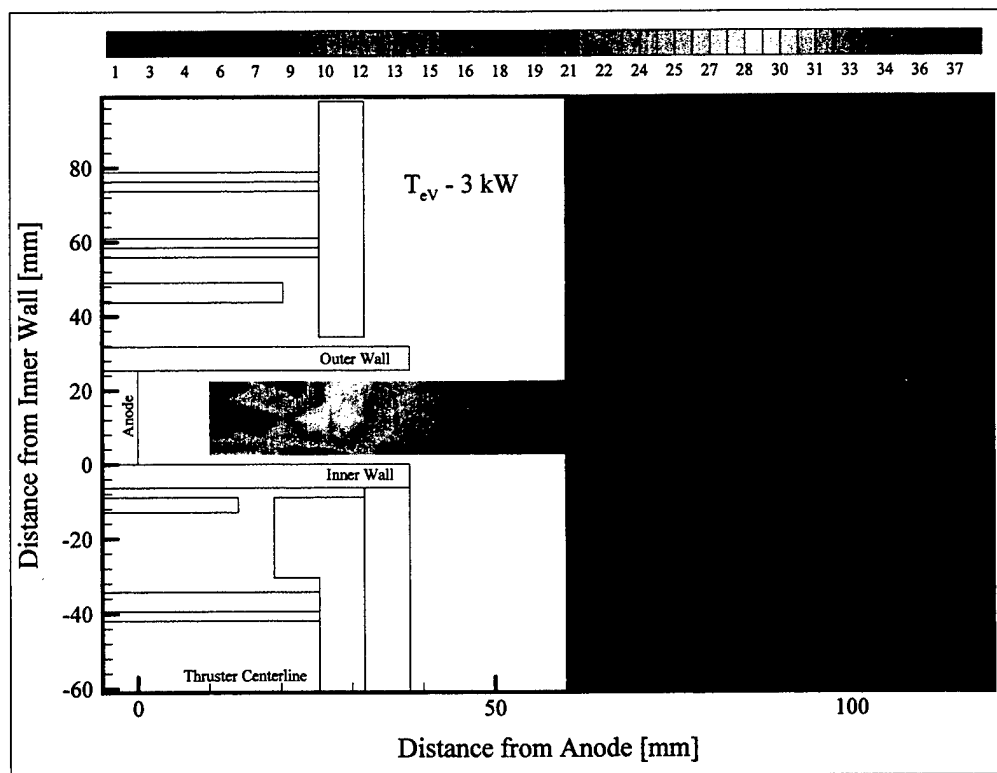


Figure B. 46 Electron temperature contours, 3 kW. Maximum temperature is approximately 30 eV and occurs 20 – 25 mm from the anode.

Appendix C

Plasma potential profiles beyond the radial confines of the discharge channel

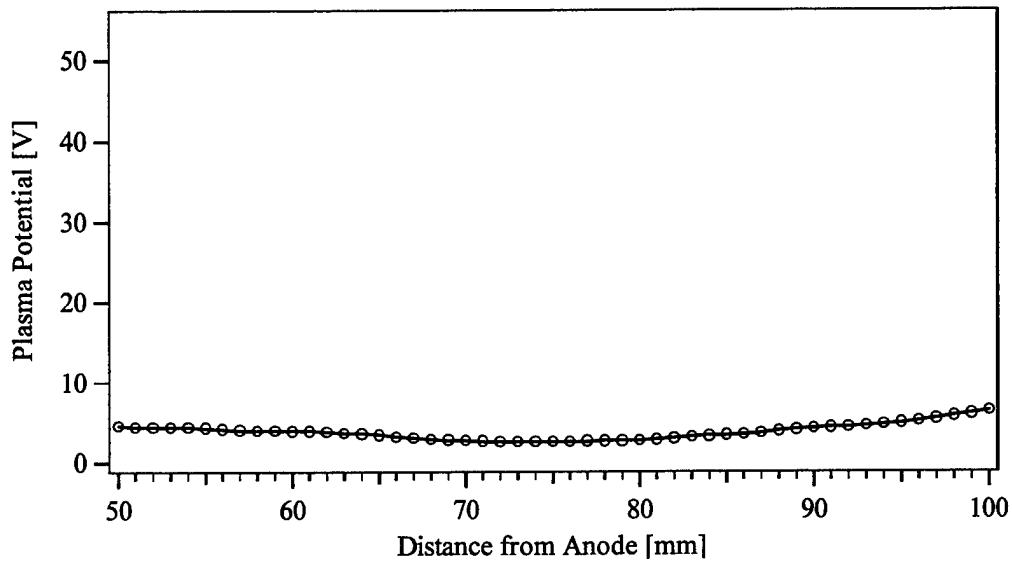


Figure C. 1 Plasma potential, 1.6 kW, $R = -10.2$ mm.

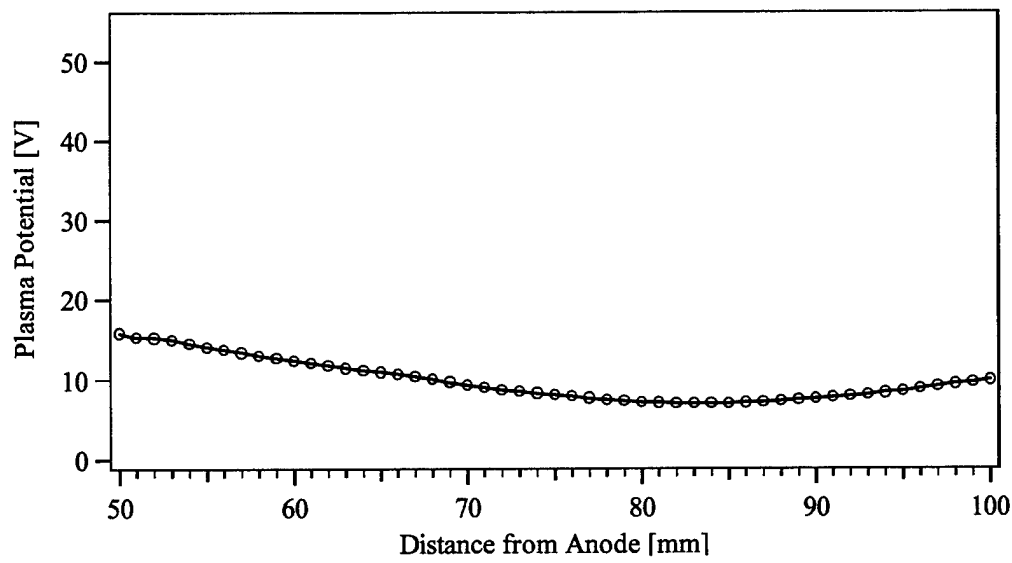


Figure C. 2 Plasma potential, 1.6 kW, $R = -3.9$ mm.

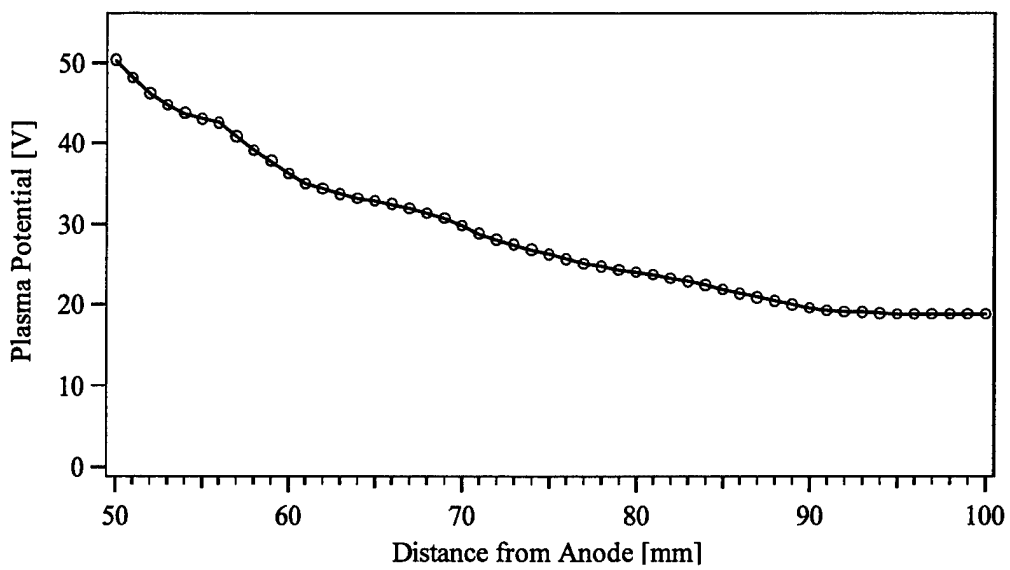


Figure C. 3 Plasma potential, 1.6 kW, $R = 27.9$ mm.

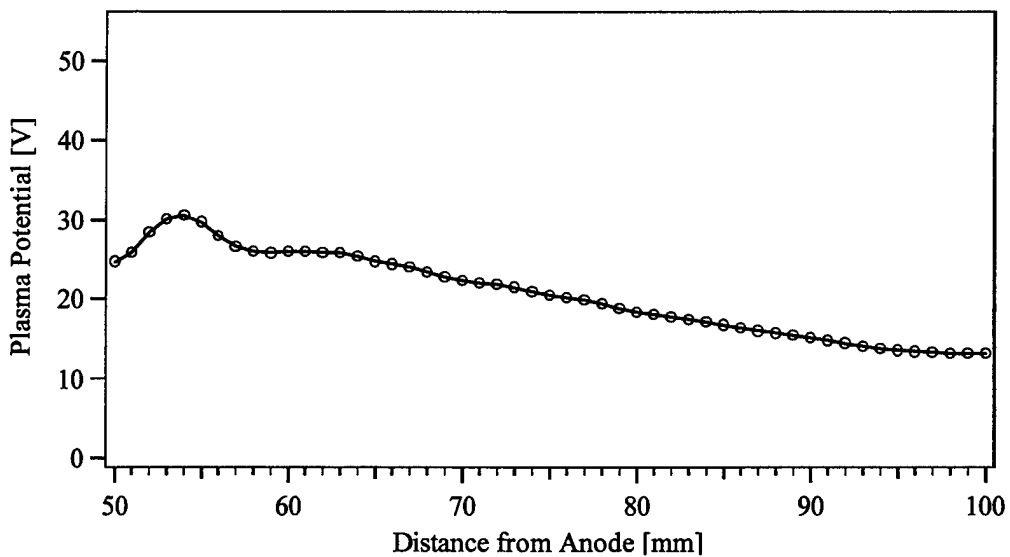


Figure C. 4 Plasma potential, 1.6 kW, $R = 34.3$ mm.

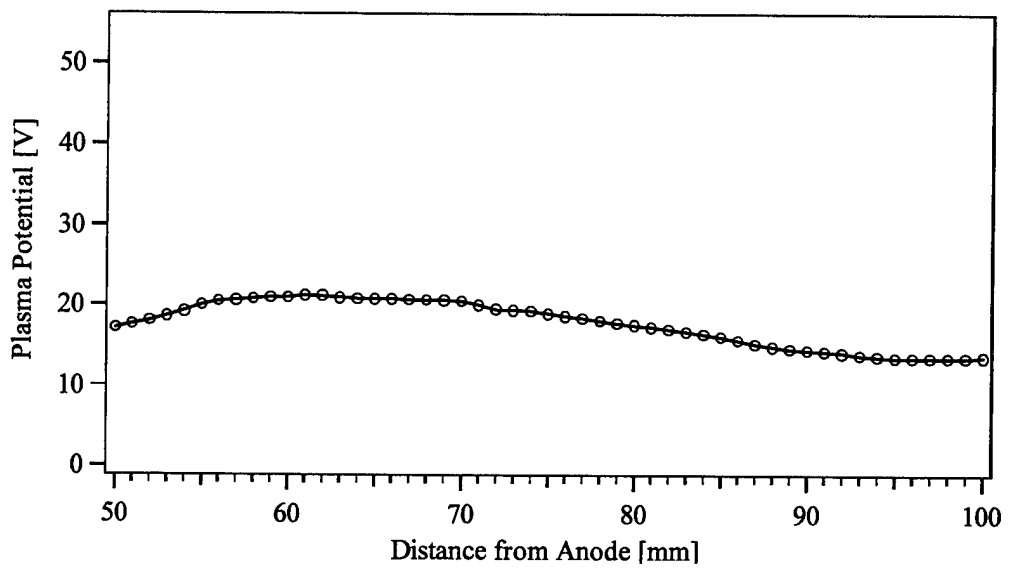


Figure C. 5 Plasma potential, 1.6 kW, $R = 40.6$ mm.

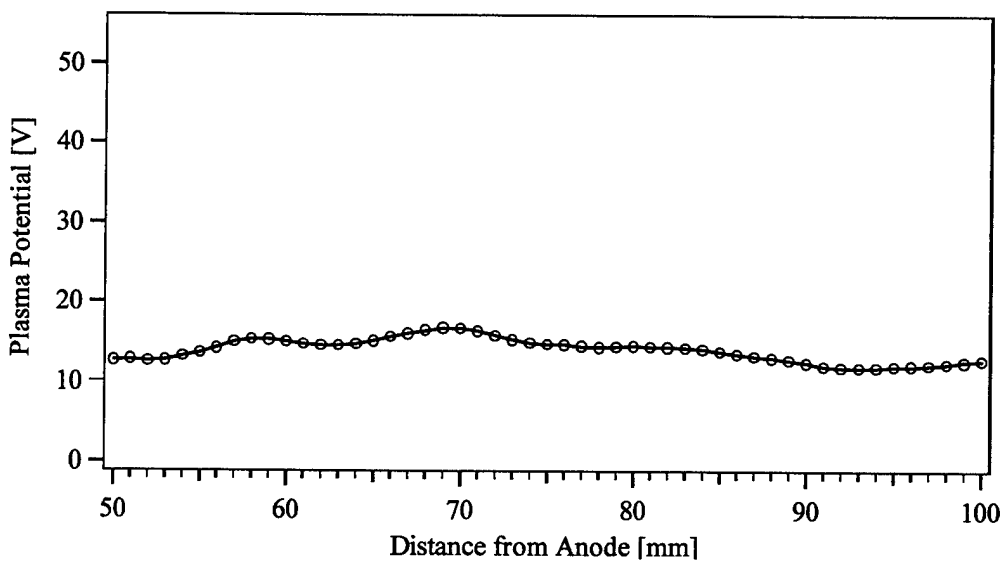


Figure C. 6 Plasma potential, 1.6 kW, $R = 47.0$ mm.

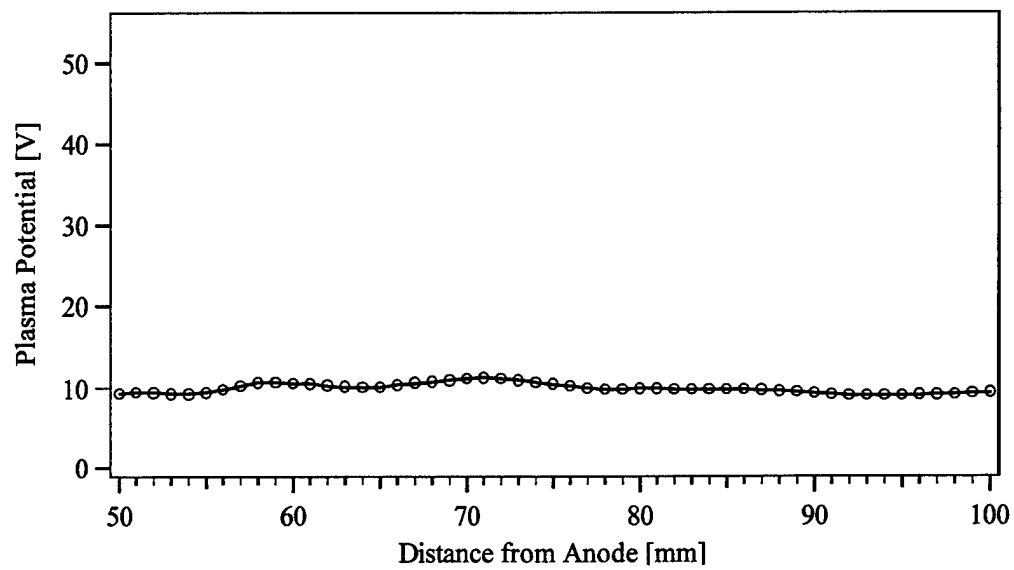


Figure C. 7 Plasma potential, 1.6 kW, R = 53.3 mm.

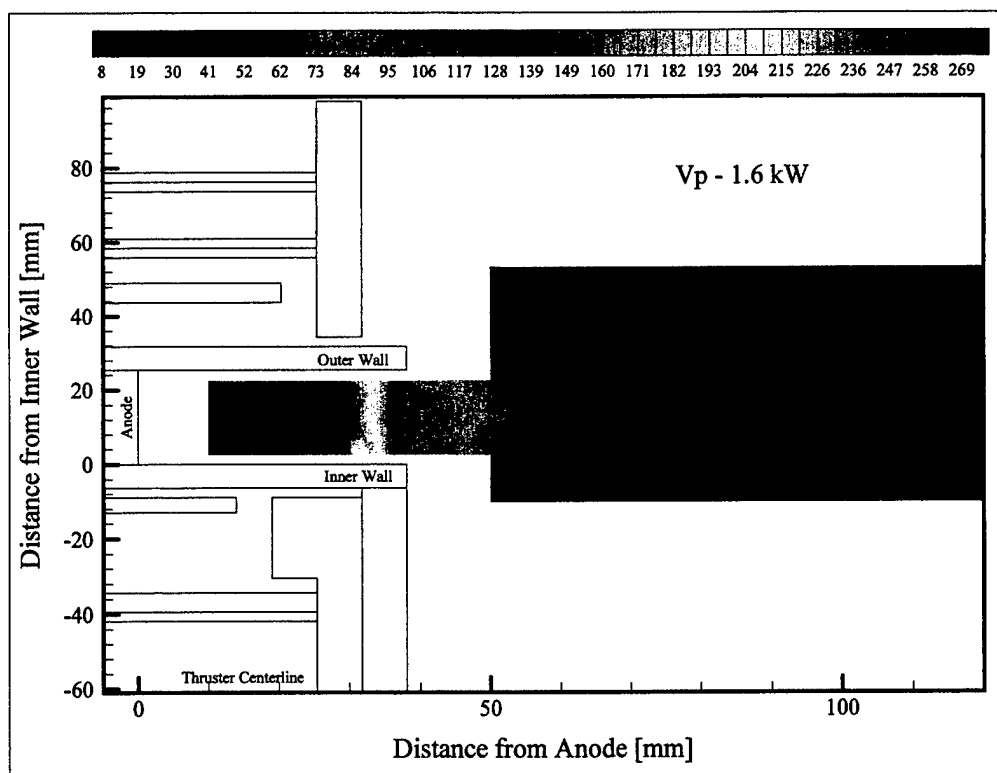


Figure C. 8 Plasma potential contours, 1.6 kW.

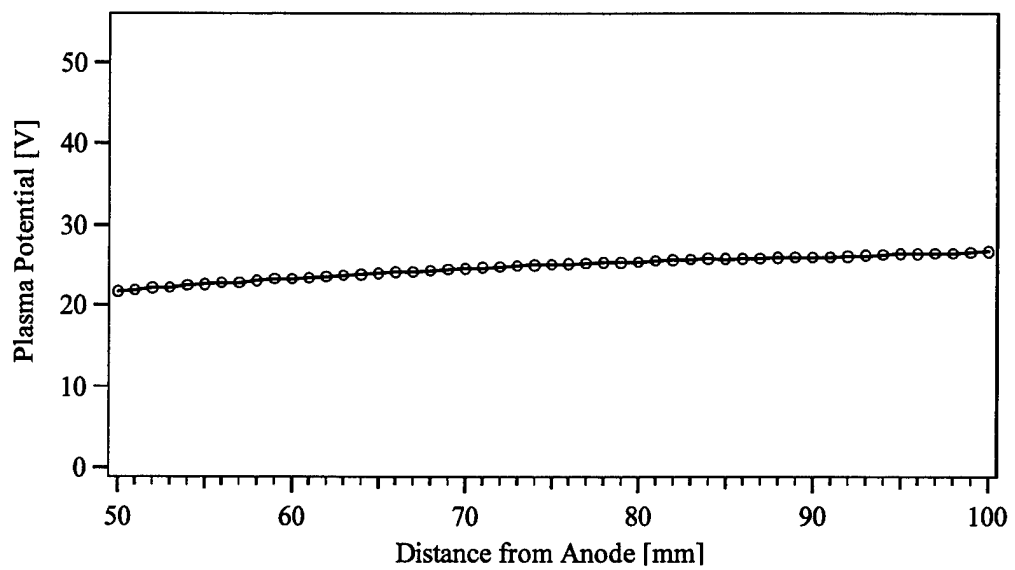


Figure C. 9 Plasma potential, 3 kW, $R = -61$ mm.

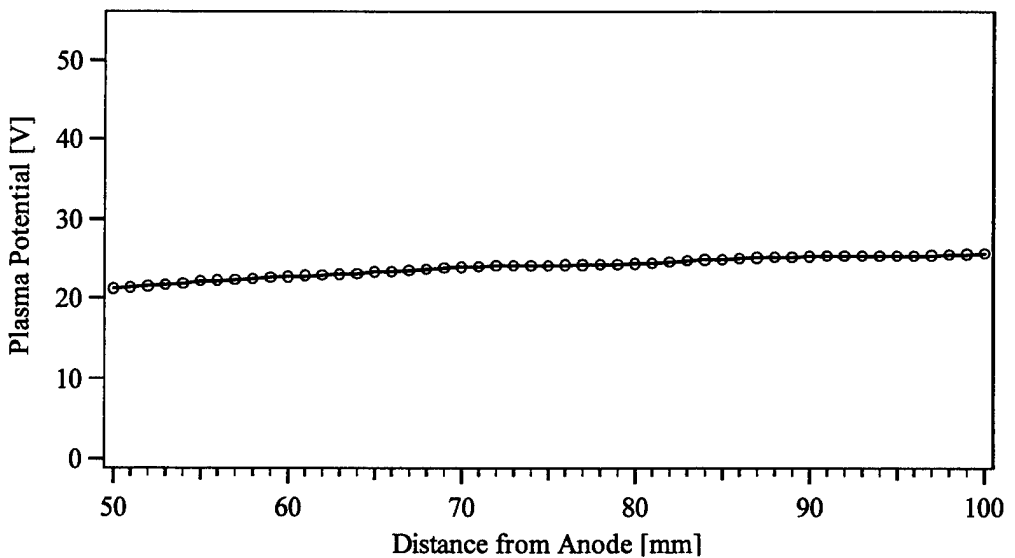


Figure C. 10 Plasma potential, 3 kW, $R = -48.3$ mm.

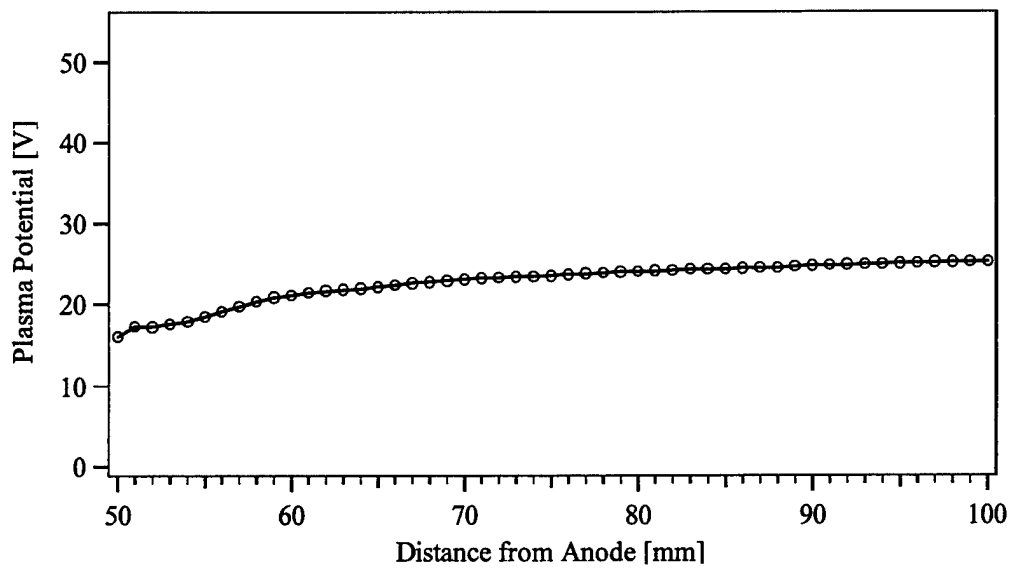


Figure C. 11 Plasma potential, 3 kW, $R = -35.6$ mm.

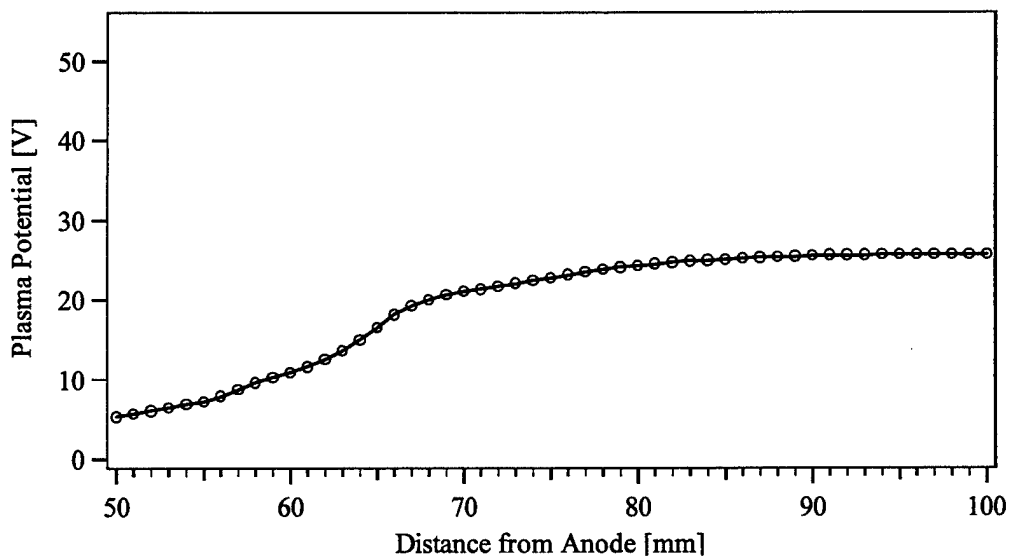


Figure C. 12 Plasma potential, 3 kW, $R = -22.9$ mm.

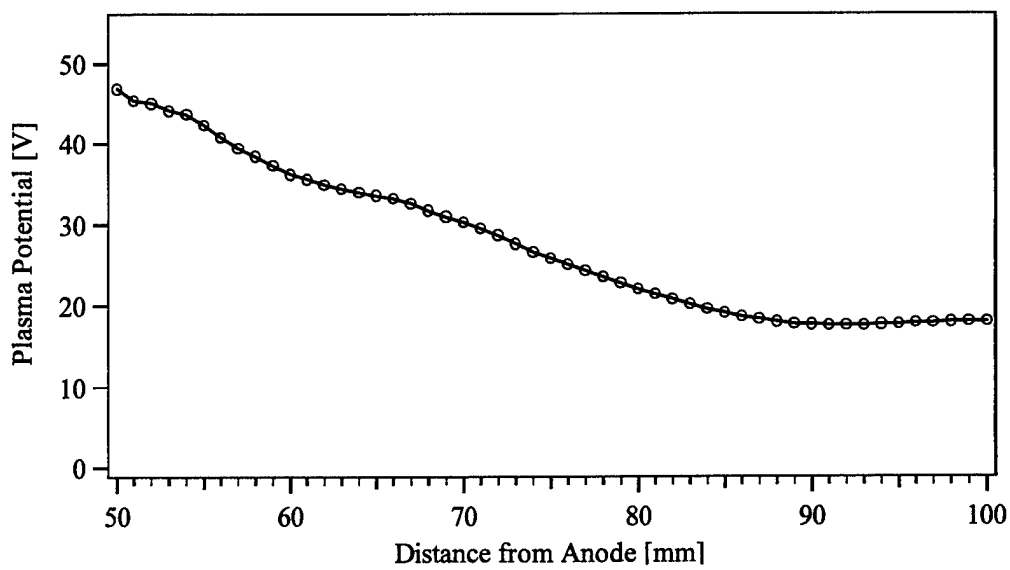


Figure C. 13 Plasma potential, 3 kW, $R = 27.9$ mm.

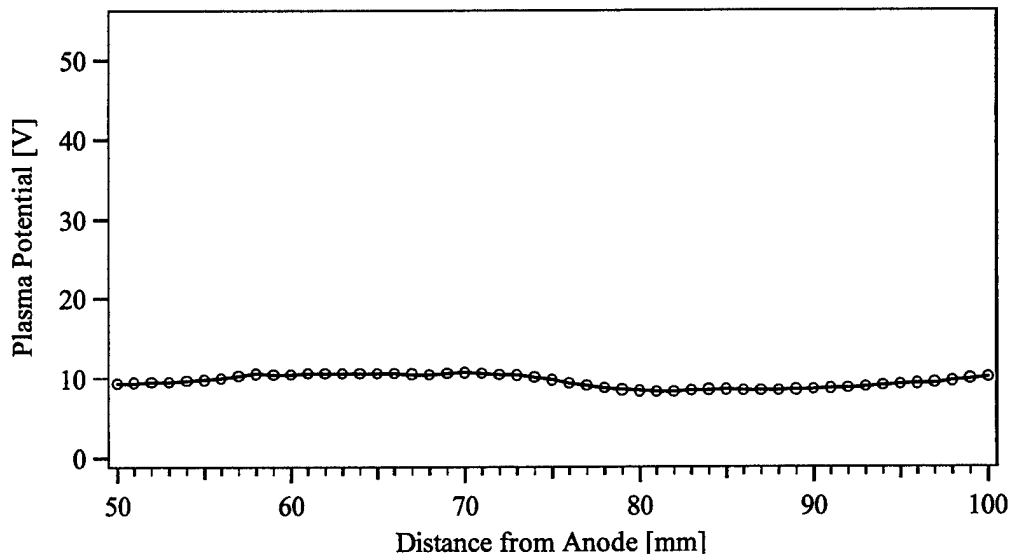


Figure C. 14 Plasma potential, 3 kW, $R = 53.3$ mm.

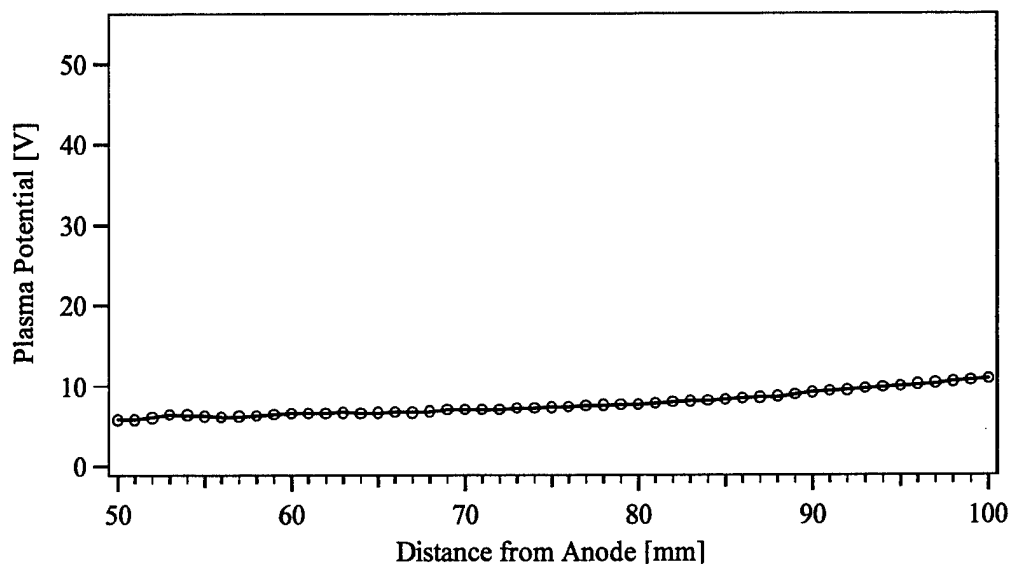


Figure C. 15 Plasma potential, 3 kW, $R = 78.7$ mm.

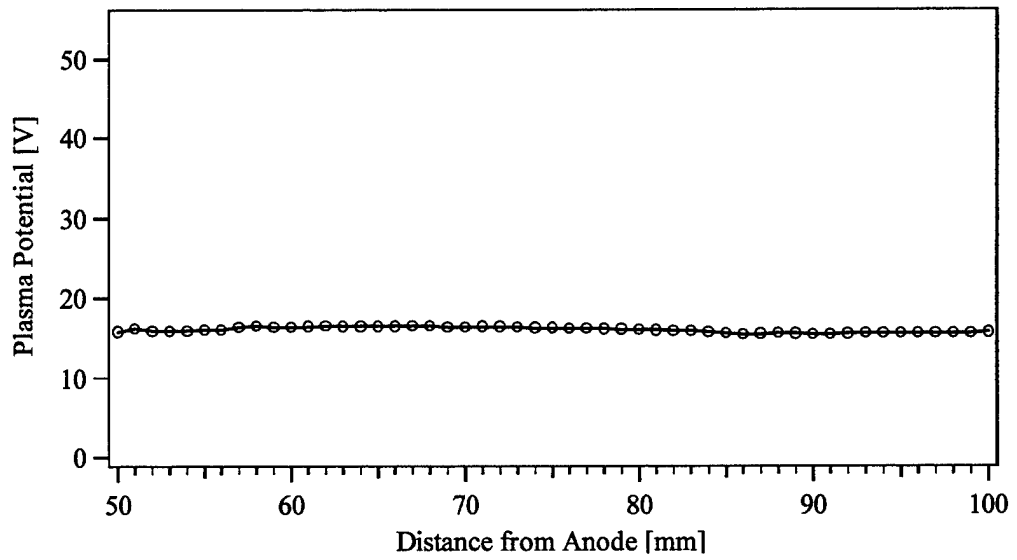


Figure C. 16 Plasma potential, 3 kW, $R = 104.1$ mm.

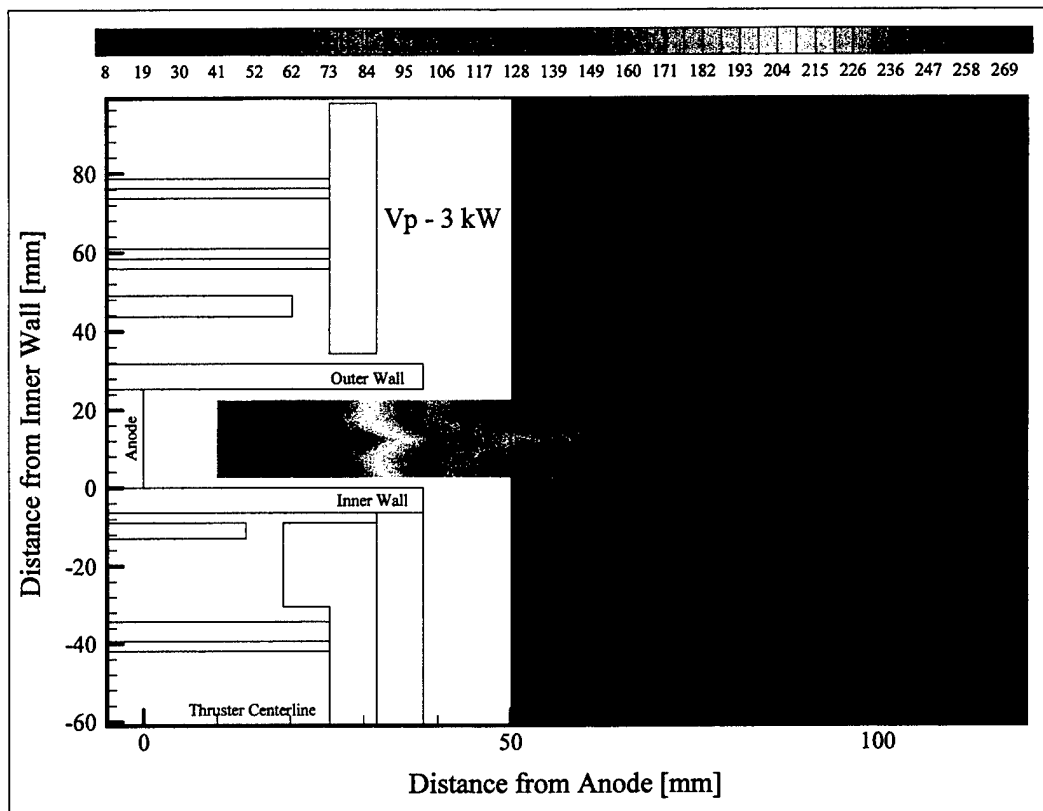


Figure C. 17 Plasma potential contours, 3 kW.